

**FINITE ELEMENT SIMULATION OF NONLINEAR
FREE SURFACE WAVES**

A THESIS

Submitted by

V. SRIRAM

for the award of the degree

of

DOCTOR OF PHILOSOPHY



**DEPARTMENT OF OCEAN ENGINEERING
INDIAN INSTITUTE OF TECHNOLOGY MADRAS
CHENNAI – 600 036**

APRIL 2008

THESIS CERTIFICATE

This is to certify that the thesis entitled "**FINITE ELEMENT SIMULATION OF NONLINEAR FREE SURFACE WAVES**" submitted by **V. SRIRAM** to the Indian Institute of Technology Madras, for the award of the degree of **DOCTOR OF PHILOSOPHY** is a bonafide record of research work carried out by him under our supervision. The contents of this thesis, in full or in parts, have not been submitted to any other Institute or University for the award of any degree or diploma.

Research Guides

(Dr. S.A. SANNASIRAJ)

(Prof. V. SUNDAR)

Place: Chennai - 600 036

Date:

**DEDICATED TO
MY BELOVED PARENTS
&
GRAND MASTER CHOA KOK SUI**

ACKNOWLEDGEMENTS

The author is very much thankful to his research supervisors, Dr. S.A. Sannasiraj and Prof. V. Sundar for their excellent guidance, support and patience to listen. Their constructive conversations, friendly behaviour and their unique way made him to realise the hidden research talents. The author heartily acknowledges their constant encouragements throughout the course of the research study. The author wishes to thank Dr. K. Murali for his valuable suggestions during the initial period of the research.

Many thanks are to the doctoral committee members Prof. R. Sundaravadivelu (Head), Prof. C.P. Vendhan (M.S. to Ph.D. conversion – Chairman), Dr. K. Murali, Prof. K. Srinivasan and Prof. S. Vengadesan for their critical evaluation and creative suggestions.

The author wishes to thank DAAD (German Academic Exchange Service) for providing short term fellowship to carry out the part of the research work at University of Wuppertal, Germany. The author is grateful to Prof. A. Schlenkhoff for all the necessary help in making the experiments possible with in a short span of time. The author also thanks Prof. T. Schlurmann, of University of Hannover, Germany for providing ample space in his lab to carry out a part of the studies at short notice.

The author wishes to thank all the unknown reviewers of the publications made in the journal and conferences for their critical comments and suggestion that improved the quality of the present work drastically.

The author always remembers his friends Mr. Sankar, Mr. Nasar, Dr. Balaji, Mr. Rajasekaran, Mr. Krishnakumar, Mr. Behera, Mr. Sabapathy, Mr. Vadhagiri, Mr. Kumaresh, Mrs. Chitra, Mrs. Muthuchelvi, Mr. Vinooth and Mr. Anand, with whom

the author have cherished some joyous moments and refreshing exchanges during his stay at IITM Campus. Thanks also to Suresh and Preetha for their valuable assistance.

Of all the students, who helped him in Germany, author would like to mention Dr. Mario, Mr. Daniel and Mr. Arndt for their valuable support during the difficult times in experiments. Thanks also to Ms. Melanie, administrative officer, Germany, for all the administrative help during the author stay. The author life in Germany would never been enjoyable without the company of his friends Ms. Garima Jain, Mr. Sivakumar, Mr. Anoop, Mr. Vignesh, Mr. Vaidheeswaran and Mr. Basheer. Thanks are to Mr. Rajan and family for their help during authors' stay at Germany.

The author would like to acknowledge the help rendered by his friends Mr. Sathish Kumar, Mr. P. Balaji, Ms. Jayashree, Ms. Swetha and Ms. Priyadharshini for their constant support and suggestions during the times in taking the crucial decisions.

The author wishes to extend his utmost thanks to his sisters, Mrs. V. Usha Devi and Mrs. V. Janaagi, for their love and continuous support. Finally, the thesis would have never been in this shape without lovely efforts from the author parents Mr. SP. Venkatachalam and Mrs. V. Valliammai. Their invaluable companionship, warmth, strong faith in the author's capabilities has always helped to be assertive in difficult times. Their optimistic and enlightening boosts have made this involved research task a pleasant journey.

Divine Energy and Divine Power blessings be with all.

V. Sriram

ABSTRACT

KEY WORDS: numerical wave tank, nonlinear waves, finite element method, velocity calculation method, mesh moving strategies, solitary and cnoidal waves, continental shelf, vertical wall, submerged bar, PIV measurement, wavelet transformation, numerical wave absorber, sloshing.

The estimation of forces and responses due to the nonlinearities in ocean waves is vital in the design of offshore structures, as these would result in the extreme loads. Simulation of such events in a laboratory is quite laborious. Even for the preparation of the driving signals for the wave paddle, one needs to resort to mathematical models. In order to achieve this task, numerical tool plays a major role. The time domain simulation of nonlinear waves has received considerable attention, in which a mixed Eulerian and Lagrangian (MEL) formulation has been solved using Finite Element Method (Wu and Eatock Taylor, 1994). Most of the conventional methods need the free surface to be smoothed or regridded at a particular/every time step of the simulation due to Lagrangian characteristics of motion even for a short time. This would introduce numerical diffusion of energy in the system. In order to minimize this effect, the present study aims at fitting the free surface using a cubic spline approximation with a Finite Element approach for discretising the domain.

The validation of the simulations in the past studies has been evaluated based on qualitative analysis or the relative errors. However, none of them, in fact, reveal the existence of phase difference if any, between the numerical simulation and laboratory generation of nonlinear waves. In this present study, the simulation of nonlinear waves by applying existing velocity calculation methods viz., global projection, mapped finite difference, least squares and the proposed cubic spline method has been compared with the experimental measurements. The wavelet analysis has been carried

out, which gives a better understanding between the numerical and the experimental results with respect to the time-frequency space, compared to the conventional Fourier transformation. The analyses of the simulated regular and cnoidal waves reveal that least squares and cubic spline give identical results and the application of cubic spline approach leads to a higher phase difference for steeper waves. The present study has shown that the existence of the phase difference is not found at the primary wave period under consideration but at a higher mode. In addition, the comparison of kinematics of numerical simulation of solitary waves with that from PIV measurements is reported. The developed model has also been compared with the experimental measurements carried out in three different wave tanks (namely, IITMadras, India; University of Hannover, Germany and University of Wuppertal, Germany).

The developed model based on structured mesh has been extended to accommodate unstructured mesh in order to deal wave interaction with complex objects (like, cylinders, floating bodies). An efficient mesh moving method has been adopted for the regeneration of unstructured mesh at every time step. Since this method is similar to Arbitrary Lagrangian and Eulerian approach, it is called as Semi-Arbitrary Lagrangian and Eulerian (SALE/Semi-ALE) method. The spring analogy concept is used to move the mesh at every time step. The adoption of improved segment method as well as the improved vertex method of the spring analogy leads to accurate results, provided the spring stiffness is taken care off contrary to the results reported by Sudharsen *et al.* (2001).

On the application of the present numerical model to investigate the interactions with the submerged obstacles, it is found that by using cubic spline the dispersive characteristics are not predicted well compared to the experimental measurements for

very steep waves. The phenomenon of three wave split-up of solitary wave during its propagation over an uneven bottom topography is successfully established. Wave transmission and reflection over a vertical step introduced in the bottom topography are in good agreement with the experimental results from Seabra-Santos *et al.* (1987). The interaction of the solitary wave with a vertical wall for different wave steepness has been analysed. The reflected shape of the profile is in good agreement with the observation made by Fenton and Rienecker (1982) and an increase in wave celerity is observed.

The motion of sloshing waves under random excitation in the sway and heave modes has also been simulated using the present model. The sloshing due to the simulated random excitation with different peak frequencies relative to the natural sloshing frequency has been subjected to frequency domain analysis. The results showed that irrespective of peak excitation frequency, the spectral peaks appear at the natural frequencies of the system and the maximum magnitude appears close to the natural frequency for the sway excitation. In the case of heave excitation, even though, the maximum sloshing appear at the natural frequencies, the magnitude of the spectral peak remains same for different excitation frequency.

Finally, the developed algorithms are extended to three-dimensional tank, wherein, an efficient combined wave absorber having mixed boundary conditions and damping zone along with grid stretching is introduced to dampen the highly nonlinear waves.

The details of the background on the numerical modelling with detailed procedures on velocity calculation methods including new algorithms, comparison of the simulation with experiments and the applicability of the formulation are presented in this thesis.

TABLE OF CONTENTS

	Page
ACKNOWLEDGEMENTS	i
ABSTRACT	iii
TABLE OF CONTENTS	vi
LIST OF TABLES	xi
LIST OF FIGURES	xii
NOTATIONS	xxii
 CHAPTER 1 INTRODUCTION	
1.1 Background	1
1.2 Importance of Ocean Waves	2
1.3 Present Study.....	3
1.4 Applications of the Present Study.....	3
1.5 Organization of the Thesis.....	4
1.6 Summary.....	6
 CHAPTER 2 REVIEW OF LITERATURE	
2.1 General	9
2.2 Mathematical Model.....	9
2.2.1 Numerical grid	10
2.2.2 Mixed eulerian and lagrangian method.....	12
2.2.3 Finite element based MEL.....	13
2.3 Wave Propagation.....	15
2.4 Shallow Water Waves.....	17
2.5 Simulation of Sloshing Waves.....	20
2.6 Objective and Scope of the Study	22
2.7 Summary.....	23
 CHAPTER 3 NUMERICAL MODELLING	
3.1 General	25

Table of Contents (continued)		Page
3.2	Governing Equation.....	25
3.3	Boundary Conditions.....	26
3.4	Mixed Eulerian-Lagrangian Scheme.....	29
3.5	Finite Element Formulation.....	30
3.6	Velocity Calculation Methods.....	32
3.6.1	General	32
3.6.2	Global projection method.....	34
3.6.3	Least squares method.....	34
3.6.4	Mapped finite difference.....	36
3.6.5	Cubic spline.....	37
3.7	Mesh Generation.....	39
3.8	Numerical Time Integration.....	40
3.9	Smoothing/Regridding Techniques.....	43
3.10	Algorithm	43
3.11	Unstructured Mesh Implementation.....	44
3.11.1	Dynamic mesh moving.....	44
3.11.2	Vertex method.....	46
3.11.3	Segment method.....	47
3.11.4	Improved vertex/segment method.....	48
3.11.5	Node table connectivity.....	49
3.11.6	Vertical velocity estimation.....	50
3.12	Validation.....	53
3.12.1	General	53
3.12.2	Steep standing waves in a container.....	53
3.12.3	Error analysis.....	54
3.13	Summary.....	56
 CHAPTER 4 NUMERICAL WAVE TANK SIMULATION		
4.1	General	68
4.2	Simulation using Wave Paddle: Structured Mesh.....	68
4.2.1	General	68
4.2.2	Mesh independent study.....	69

Table of Contents (continued)		Page
4.2.3	Simulation of medium steep waves.....	70
4.2.4	Simulation of steep waves.....	71
4.2.5	Simulation of solitary waves.....	73
4.3	Comparison with Experimental Measurements.....	74
4.3.1	Wave focusing.....	74
4.3.2	Cnoidal waves.....	74
4.3.3	Solitary waves.....	76
4.4	Quantitative Comparison.....	79
4.4.1	General.....	79
4.4.2	Experimental details.....	81
4.4.3	Regular waves.....	82
4.4.4	Cnoidal waves.....	85
4.4.5	Solitary waves and PIV measurements.....	87
4.5	Unstructured Mesh.....	89
4.5.1	General.....	89
4.5.2	Comparison with structured mesh : Interpolation techniques.....	90
4.5.3	Comparison with structured mesh : Mesh moving strategies.....	90
4.5.4	GP method and its improvement.....	91
4.5.5	Comparison between different velocity calculation methods.....	92
4.6	Summary.....	92
 CHAPTER 5 APPLICATIONS OF NONLINEAR WAVE SIMULATION		
5.1	General	134
5.2	Wave Propagation Model.....	134
5.2.1	General	134
5.2.2	Interaction with submerged bar I.....	135
5.2.3	Interaction with submerged bar II.....	136
5.3	Solitary Waves and its Interaction.....	137
5.3.1	Split-up of solitary waves.....	137
5.3.2	Propagation of solitary waves over step.....	139
5.3.3	Propagation of solitary waves over smooth slope.....	140
5.3.4	Solitary wave interaction with vertical wall.....	141

Table of Contents (continued)		Page
5.4	Wave Interaction with Rectangular Object.....	144
5.5	Wave Interaction with a Submerged Cylinder.....	145
5.6	Simulation of Sloshing Waves.....	146
5.6.1	General	146
5.6.2	Mathematical formulation.....	147
5.6.3	Input generation.....	150
5.6.4	Regular wave excitation.....	152
5.6.5	Random wave excitation.....	156
5.7	Summary.....	158

CHAPTER 6 3-DIMENSIONAL NUMERICAL WAVE TANK

6.1	General.....	197
6.2	Mathematical Formulation.....	197
6.3	Mesh Generation.....	202
6.4	Mesh Orientation Study.....	203
6.5	Wave Absorber.....	205
6.5.1	General	205
6.5.2	Mixed boundary condition.....	208
6.5.3	Damping zone.....	210
6.5.4	Mesh stretching.....	211
6.5.5	Proposed wave absorber for the present study.....	212
6.6	Regridding Method.....	213
6.7	Comparison with 2-D Tank.....	213
6.8	Long Time Simulation: Wave Absorber.....	214
6.8.1	Monochromatic wave.....	214
6.8.2	Bi-chromatic wave.....	215
6.9	Summary.....	216

CHAPTER 7 SUMMARY AND CONCLUSIONS

7.1	Summary.....	232
7.2	Conclusions.....	233
7.2.1	Simulation of nonlinear waves using wave paddle.....	233
7.2.2	Nonlinear wave propagation.....	235

Table of Contents (continued)	Page
7.2.3 Solitary wave propagation and its interactions.....	235
7.2.4 Simulation of sloshing waves.....	236
7.2.5 3-D Numerical wave tank.....	237
7.3 Suggestions for Future Studies.....	238
APPENDIX A MOVING LEAST SQUARES.....	240
APPENDIX B ANALYTICAL SOLUTION FOR FREE SLOSHING..	244
APPENDIX C SOLITARY AND CNOIDAL WAVE SIMULATIONS	248
APPENDIX D WAVELET TRANSFORMATIONS	253
REFERENCES	260
PUBLICATIONS BASED ON THIS THESIS	272

LIST OF TABLES

Table	Title	Page
3.1	Node Connectivity Table.....	58
4.1	Tested Solitary Wave Characteristics.....	94
4.2	Wavelet Phase Angle for the Test Case T = 1.92s, H = 0.04m, D = 0.613m (R1). [XWT1 and WTC1: EXP-CS , XWT2 and WTC2: EXP-LS , WP1 @ 4.8495m; WP2 @ 20.146m; WP3 @ 25.136m; WP4 @ 30.425m; WP5 @ 40.406m; WP6 @ 50.609m].....	94
4.3	Wavelet Phase Angle for the Test Case T = 1.92s, H = 0.2m, D = 0.621m (R2). [XWT1 and WTC1: EXP-CS , XWT2 and WTC2: EXP-LS , WP1 @ 4.8495m; WP2 @ 20.146m; WP3 @ 25.136m; WP4 @ 30.425m; WP5 @ 40.406m; WP6 @ 50.609m].....	95
4.4	Wavelet Phase Angle for the Test Case T = 6.4s, H = 0.03m, D = 0.619m (CN1). [XWT1 and WTC1: EXP-CS , XWT2 and WTC2: EXP-LS , WP1 @ 4.8495m; WP2 @ 20.146m; WP3 @ 25.136m; WP4 @ 30.425m; WP5 @ 40.406m; WP6 @ 50.609m].....	95
4.5	Wavelet Phase Angle for the Test Case T = 6.4s, H = 0.3m, D = 0.62m (CN2). [XWT1 and WTC1: EXP-CS , XWT2 and WTC2: EXP-LS , WP1 @ 4.8495m; WP2 @ 20.146m; WP3 @ 25.136m; WP4 @ 30.425m; WP5 @ 40.406m; WP6 @ 50.609m].....	96
4.6	Wavelet Phase Angle for the Test Case T = 3.2s, H = 0.2m, D = 0.621m (CN3). [XWT1 and WTC1: EXP-CS , XWT2 and WTC2: EXP-LS , WP1 @ 4.8495m; WP2 @ 20.146m; WP3 @ 25.136m; WP4 @ 30.425m; WP5 @ 40.406m; WP6 @ 50.609m].....	96
5.1	Simulated Input Wave Parameters in a Water Depth of 0.5m...	160
5.2	Comparison with the Bousinessq Model for Wave Speed in Split-up Waves. C_{nwt} – Numerical Celerity, C_{bou} – Boussinessq Celerity ($C_{Bou} = \sqrt{g(h+H)}$).....	160

LIST OF FIGURES

Figure	Title	Page
1.1	The Relative Amount of Energy Available in the Ocean Surface.....	7
1.2	A Physical Illustration of Various Wave Profiles.....	7
1.3	Extreme Nonlinear Waves Noticed in the Deep Water at Gulf Stream, Charleston	8
2.1	Flow Chart Showing the Progress of the Finite Element Method.....	24
3.1	Computational Domain with Specified Boundaries.....	58
3.2	General Procedure for the Wave Simulation.....	59
3.3	Node Configuration for Calculating Vertical Velocity	59
3.4	Cubic Spline Approximation using Five Nodes	59
3.5	Typical Nodal Variation for a Cosine Free Surface Elevation	60
3.6	Typical Mesh Structure using Linear 3-Noded Triangular Element...	60
3.7	Time Updating Procedure.....	61
3.8	Flow Chart of the Simulation	61
3.9	Physical Interpretation of Springs Connected to ‘i’th node to its neighbours such as ‘j’	62
3.10	Mesh with Node Numbering	62
3.11	Physical Interpretation to Calculate Vertical Velocity	62
3.12	Physical Representation to Find the Group of Nodes	64
3.13	Time History of the Free Surface Profile at the Center of the Container for a Wave Steepness, $H/\lambda = 0.05$ [----Analytical (upto 2 nd order); ♦♦♦ GP; ——— CS].....	64
3.14	Time History of the Free Surface Profile at the Center of the Container for a Wave Steepness, $H/\lambda = 0.1$ [----- Analytical (upto 2nd order) ; ♦♦♦ GP; ——— CS].....	65
3.15	Time History of the Free Surface Profile at the Center of the Container for a Wave Steepness $H/\lambda = 0.033$ [---- Analytical (upto 2nd order); ——— CS].....	65
3.16	Relative Energy Error (δE_i) while using GP Method.....	66

List of Figures (Continued)	Page
3.17 Comparison of Relative Energy Error (δE_t) [----- Analytical Solution (upto 2 nd order); ♦♦♦ Westhuis (2001); ——— CS].....	66
3.18a Relative Energy Loss (∇E_t) with respect to Second order Analytical Solution [♦-♦-♦ Westhuis (2001); ——— CS].....	67
3.18b Relative Energy Loss (∇E_t) with respect to Second order Analytical Solution [♦-♦-♦ GP; ——— CS].....	67
4.1 Comparison between Nonlinear and Linear Wave Simulation at 12m from the Wave Paddle for a Wave Steepness, $H/\lambda = 0.0036$ [——— Nonlinear Wave; ♦♦♦ Linear Wave].....	97
4.2 Comparison between Nonlinear and Linear Wave Simulation at 12m from the Wave Paddle for a Wave Steepness, $H/\lambda = 0.046$ [——— Nonlinear Wave; ♦♦♦ Linear Wave].....	97
4.3 Free Surface Elevation at 12m from the Wave Paddle for a Wave Steepness, $H/\lambda = 0.046$ [♦♦♦ Wu and Eatock Taylor (1995); ——— Present Simulation].....	98
4.4a Mesh Convergence for the Spatial Resolution for 15, 25, 30 and 40 Nodes per Wavelength.....	98
4.4b Mesh Convergence for the Temporal Resolution of 15, 30, 40 and 50 Time Steps per Wave Period	99
4.5 Free Surface Profile at 20s along the Length of the Tank [----- LS; ——— CS; ----- MFD].....	99
4.6 Time History at 12m from the Wave Paddle [----- LS; ——— CS; - ----- MFD; ——— GP].....	99
4.7 Free Surface Elevation near the Wave Paddle showing Instability after 17s [----- LS; ——— CS; ----- MFD].....	100
4.8a Mesh Structure near the Wave Paddle at 2s	100
4.8b Mesh Structure near the Wave Paddle showing Node Movement around 18s	100
4.9 Free Surface Elevation near the Wave Paddle after Increasing the Number of Nodes to 825 [----- LS; ——— CS; ----- MFD].....	100
4.10 Free Surface Elevation along the Length of the Tank for a Wave Steepness of 0.7 [----- LS; ——— CS; ----- MFD].....	101
4.11 Time History at the Center of the Tank [----- LS; ——— CS; ----- MFD].....	101

List of Figures (Continued)	Page
4.12 Time History at a) 2m and b) 5m from the Wave Paddle [----- LS; —— CS; ----- MFD].....	101
4.13a Paddle Displacement for the Simulation of Transient Wave Packet...	102
4.13b Time History Comparison at Various Locations [•••••Experiments (Claus and Steinhagen, 1999); ----- LS; —— CS; ----- MFD]	103
4.14a Paddle Displacement for the Simulation of Cnoidal Waves	104
4.14b Time History Comparison at Various Locations [••••• Experiments (Jeong, 2003); ----- Numerical (Jeong, 2003); —— CS].....	104
4.15 Velocity Vector Plot along the Length of the Tank at 80s	105
4.16 Relative Error along the Length of the Tank.....	106
4.17 Comparison of the Numerical Simulation of Free Surface Profile at 15.7m from the Wave Paddle with the Experimental Measurements (Yim <i>et al.</i> 2004) for a Wave Height of 0.24m in a 0.8m Water Depth	106
4.18 Comparison of Numerical Simulation with Present Experimental Measurements at 3m for $H/h=0.1$ [••••• Experiments; —— Numerical].....	107
4.19 Comparison of Numerical Simulation with Experimental Measurements with Corrected Water Depth at Various Distances of 3m, 8m and 9m from the Wave Paddle for $H/h = 0.1$ [••••• Experiments; —— Numerical].....	107
4.20 Comparison of Numerical Simulation with Experimental Measurements with Corrected Water Depth at Various Distances of 3m, 8m and 9m from the Wave Paddle for $H/h = 0.075$ [••••• –Experiments; —— Numerical].....	108
4.21 Variation of Wave Speed with respect to Wave Steepness	108
4.22 View of the Flume at University of Hannover, Germany	109
4.23 View Showing the Glass Flume at University of Wuppertal, Germany.....	109
4.24 PIV Set-up and Light Settings	110
4.25 Input Velocity and Time History Comparisons to Simulate a Regular Wave with a Steepness of 0.01 [R1: ••••• EXP; ----- LS; —— CS].....	111

List of Figures (Continued)		Page
4.26	Fourier and Wavelet Spectrum for R1 [WP1 @ 4.895m; WP6 @ 50.609m].....	112
4.27	Cross Wavelet Transform and Wavelet Coherence between Numerical Approaches and Experiment for the Time History near to the Wave Paddle [R1].....	113
4.28	Input Velocity and Time History Comparisons to Simulate a Regular Wave with a Steepness of 0.047 [R2: ●●●●● EXP; ---- LS; ——— CS].....	114
4.29	Fourier and Wavelet Analysis for Time History near the Wave Paddle [R2].....	115
4.30	Fourier and Wavelet Analysis for the Time History far away from the Paddle [R2].....	116
4.31	Input Velocity and Time Histories Comparison to Simulate a Cnoidal Wave of Ursell Parameter 30 [CN1: ●●●●● EXP; ---- LS; ——— CS].....	117
4.32	Fourier and Wavelet Analysis for Time History far away from the Paddle [CN1].....	118
4.33	Input Velocity and Time History Comparison to Simulate a Cnoidal Wave of Ursell Number 307 [CN2: ●●●●● EXP; ---- LS; ——— CS].....	119
4.34	Fourier and Wavelet Analysis for the Time History far away from the Paddle [CN2].....	120
4.35	Input Velocity and Time Histories Comparison to Simulate a Cnoidal Wave of Ursell Number 41 [CN3: ●●●●● EXP; ---- LS; ——— CS].....	121
4.36	Fourier and Wavelet Spectrum for Time History near to the Paddle [CN3].....	122
4.37	Comparison of Time Histories for Solitary Waves [●●●●● EXP; ——— Numerical].....	123
4.38	Snap Shots of the Water Flowing through the Side Walls.....	124
4.39	Generated Signal [————] and the Tuned Signal [●●●●●] to the Wave Paddle to Generate the same Wave Height [$H/h = 0.1$].....	124
4.40	Comparison of Time Histories for Solitary Waves with Modified Input Signal [●●●●● EXP; ---- LS; ——— CS].....	125

List of Figures (Continued)	Page
4.41 Velocity Comparison at the Crest of the Solitary Waves for Various H/h Ratio [●●● Experiments; ○○○ LS; ▲▲▲ CS].....	126
4.42 Snapshots of the Image from CCD High Speed Camera before Processing [Sampling Interval is 2ms].....	127
4.43 Spatial Velocity Information of Solitary Waves obtained from PIV Measurement (Top) and Numerical Simulation (Bottom) for $H/h = 0.5$	128
4.44 Wave Profile at 15s along the Length of the Tank [●●●●● Structured Mesh; ——— MLS; ----- Shape Function].....	129
4.45a Wave Time History at 5m [●●●●●●● Structured Mesh; ——— MLS; --- ----- Shape Function].....	129
4.45b Zoomed in View of Fig. 4. 45a	129
4.46a Free Surface Profile along the Length of the Tank at 15s for Different Mesh Moving Strategies.....	130
4.46b Time Histories at 5m from the Wave Paddle for Different Mesh Moving Strategies	130
4.47 Snapshot of the Mesh Movement using Vertex Method at 10s.....	130
4.48 Comparison between Structured and Unstructured Code for a Stroke of the Wave Paddle, $0.05h$ [●●●●● Unstructured; ——— Structured]...	131
4.49 Time History Comparison using Different Velocity Calculation Methods for Transient Wave Packet Simulation	132
4.50 Moved Mesh at the Focusing Point [Segment Method].....	133
5.1 Experimental Setup of Beji and Battjes (1993).....	161
5.2 Comparison of the Free Surface Elevation with the Experimental Measurements of Beji and Battjes (1994) at Seven Different Position in the presence of a Submerged Bar	162
5.3 Mesh Configuration at a particular Time Step near the Trapezoidal Obstacle along the Length of the Tank (5m to 18m).....	163
5.4 Experimental Setup of Ohyama <i>et al.</i> (1995).....	164
5.5 Free Surface Profile and the Mesh Configuration when the Wave Reaches the Deeper Water Region from the Shallow Water Region...	164

List of Figures (Continued)	Page
5.6 Comparison of Numerical Simulation with Experimental Measurements. Left Side Figures are at Station 3 and Right Side Figures are at Station 5 [ooooExperiments (Ohyama <i>et al.</i> 1995); ——— CS; ----- LS].....	165
5.7 Comparison of the Free Surface Profile with the Bousinessq Theory at $t = 80s$ over a constant Water Depth.....	166
5.8 Free Surface Profile at Time 20s, 40s, 80s and 119s along the Length of the Tank	166
5.9 Space – Time Plot showing the Splitting of Solitary Waves while Propagating into Shallower Water Depths (h_0) [$h = 0.5m$; $H = 0.1m$].....	167
5.10 Free Surface Profile at $t = 119s$ While Solitary Wave Propagates into Shallow Water Depths [$h = 0.5m$; $H = 0.1m$].....	169
5.11 Dimensions of the Wave Tank with the Location of the Numerical Wave Gauges	170
5.12 Discretisation of the Step using Triangular Elements.....	170
5.13 Transmission Coefficient over Obstacles of Different Relative Height [———— First Order Shallow Water Wave Theory; (+) First, (\diamond) Second and (\square) Third Transmitted Wave of Experiments (Seabra-Santos <i>et al.</i> 1987); (\bullet) First, (\blacklozenge) Second and (\blacksquare) Third Transmitted Wave of Numerical Simulation].....	171
5.14 Reflection Coefficient for Different Relative Obstacle Height [————First Order Shallow Water Wave Theory; +++ Experiments (Seabra-Santos <i>et al.</i> 1987); ooo Numerical].....	172
5.15 Propagation of the Solitary Wave over a Smooth Slope, (c) and (d) are the zoomed in view of the Rectangle Marked in (a) and (b) respectively	173
5.16 Vertical Wall Run-up due to Different Wave Steepness	174
5.17 Maximum Horizontal Force on the Vertical Wall due to Different Wave Steepness	174
5.18 Reflected Shape of the Profile for Different Steepness:(a) $H/h = 0.1$, (b) $H/h = 0.2$, (b) $H/h = 0.3$, (c) $H/h = 0.4$, (d) $H/h = 0.5$, [——— Incident Wave;----- Reflected Wave].....	175
5.19a Variation of the change in Wave Elevation ($\Delta\eta$) with respect to Wave Steepness	176

List of Figures (Continued)	Page
5.19b Variation of change in Wave Celerity (ΔC) with respect to Wave Steepness	176
5.20a Pressure Time History on the Vertical Wall at the Still Water Level [From Left to Right: $H/h = 0.1; 0.198; 0.293; 0.383; 0.4699; 0.5533$].	177
5.20b Pressure Time History at the Bottom of the Vertical Wall [From Left to Right: $H/h = 0.1; 0.198; 0.293; 0.383; 0.4699; 0.5533$].	177
5.21 Force Time History on the Vertical Wall [From Left to Right: $H/h = 0.1; 0.198; 0.293; 0.383; 0.4699; 0.5533$].	178
5.22 Typical Mesh Configuration in the Presence of a Rectangular Object	178
5.23 Comparison of Free Surface Profile between Two Different Wave Heights with a Rectangular Object [----- $H/\lambda = 0.015$; —— $H/\lambda = 0.075$].	179
5.24 Initial Mesh Structure with Cylinder Generated using GAMBIT and Refined using ICEM-CFD	180
5.25 Comparison of the Wave Profiles with and without the Cylinder [---- without Cylinder; —— with Cylinder].	180
5.26 Force Time Histories of Component F_a [----- x Component; —— z Component].	181
5.27 Force Time Histories of Component F_b [----- x Component, —— z Component].	182
5.28 Sloshing Wave Tank Model Domain	183
5.29 Free Surface Profiles over the Length for $\omega_h = 0.999 \omega_1$ and $a_h = 0.0018$ after every 2s Interval [—— Numerical; ----- Analytical]...	184
5.30 Free Surface Elevation at the Left Wall due to Regular Horizontal Excitation at a Frequency, $\omega_h = 0.7 \omega_1$ (a) $a_h \omega_h^2 = 0.0036g$; (b) $a_h \omega_h^2 = 0.036g$ [—— Present Numerical; ●●● Numerical (Frandsen, 2004)].	185
5.31 Power Spectra of Waves at the Left Corner of the Wall due to Horizontal Excitation, $a_h = 0.005h$ [$T_1 = 2\pi / \omega_1$].	186
5.32 Movement of the Generated Mesh during a Horizontal Excitation after every 5s Interval for $a_h = 0.005h$ and $\omega_h = \omega_1$, Number of Nodes in x Direction is 31 and in z Direction is 13.	187

List of Figures (Continued)	Page
5.33 Bar Chart showing the Magnitude of Different Spectral Peaks of Sloshing Waves due to Horizontal Excitation with Frequencies[$\omega_2=1.5 \omega_1$; $\omega_3=1.8 \omega_1$; $\omega_5=2.334 \omega_1$].....	188
5.34 Free Surface Elevation at the Left Wall due to Regular Vertical Excitation of Frequency, $\omega_v=0.789 \omega_1$, $a_v \omega_v^2=0.5g$. a) $\varepsilon=0.0014$ b) $\varepsilon=0.288$ [—— Present Numerical; ●●● Numerical (Frandsen, 2004)].....	189
5.35 Power Spectra of Free Surface Sloshing Waves at the Left Corner of the Wall due to Regular Vertical Excitation for an Initial Steepness of 0.014, $a_v = 0.005h$ [$T_1 = 2\pi / \omega_1$].....	190
5.36 Power Spectra of Free Surface Sloshing Waves at the Left Corner of the Wall due to Regular Vertical Excitation for an Initial Steepness of 0.288, $a_v = 0.005h$ [$T_1 = 2\pi / \omega_1$].....	191
5.37a Typical Excitation Spectrum with $H_s= 0.01h$ and $\omega_p = \omega_1$	192
5.37b Displacement Generated from the Spectrum Fig. 5.37 a.....	192
5.37c Free Surface Elevation at the Left Corner of the Wall due to Horizontal Motions Prescribed by Fig. 5.37b	193
5.37d Free Surface Elevation at the Left Corner of the Wall due to Vertical Motions Prescribed by Fig. 5.37b.....	193
5.38 Spectra of Free Surface Sloshing Waves at the Left Corner of the Wall due to Horizontal Random Excitation of $H_s=0.006h$ [$T_1 = 2\pi / \omega_1$].....	194
5.39 Spectra of Free Surface Sloshing Waves at the Left Corner of the Wall due to Vertical Random Excitation for an Initial Steepness of 0.014 and $H_s=0.006h$ [$T_1 = 2\pi / \omega_1$].....	195
5.40 Spectra of Free Surface Sloshing Waves at the Left Corner of the Wall due to Vertical Random Excitation for an Initial Steepness of 0.288 and $H_s=0.006h$ [$T_1 = 2\pi / \omega_1$].....	196
6.1 Representation of 3-D Numerical Wave Tank with Prescribed Boundary Conditions.....	217
6.2 Nodal Configuration for Least Squares Principle	218
6.3 Division of Hexahedron to Six Tetrahedrons.....	219
6.4 Velocity Potential Contours along the Length of the 2-D Tank	220

List of Figures (Continued)		Page
6.5a	Mesh Type I along with the Velocity Potential Contours in a 3-D Tank.....	220
6.5b	Velocity Potential along y/h at $z/h = -0.045$ [Mesh Type I].....	221
6.5c	Velocity Potential across z/h for all the y/h Values [Mesh Type I]....	221
6.6a	Mesh Type II along with the Velocity Potential Contours	222
6.6	(b) Velocity Potentials along y/h at $z/h = -0.045$ m (c) Velocity Potential across z/h for all y/h Values [Mesh Type II, — NY+1=6; -----NY+1 = 12; - . - . - NY+1 = 16;•-•-• 2-D].....	222
6.7a	Mesh Type III along with the Velocity Potential Contours.....	223
6.7	(b) Velocity Potentials along y/h at $z/h = -0.045$ m (c) Velocity Potential across z/h for all y/h Values [Mesh Type III, — NY+1=6; -----NY+1 = 12; - . - . - NY+1 = 16;•-•-• 2-D].....	223
6.8a	Mesh Type IV along with the Velocity Potential Contours	224
6.8	(b) Velocity Potentials along y/h at $z/h = -0.045$ m (c) Velocity Potential across z/h for all y/h Values [Mesh Type IV, — NY+1=6; -----NY+1 = 12; - . - . - NY+1 = 16;•-•-• 2-D].....	224
6.9	Representation of Mesh Stretching in x - z Direction	225
6.10	Time History at 0.5m from the Wave Paddle [••• 2-D; — 3-D].....	225
6.11	Time History at 3.572m from the Wave Paddle [••• 2-D; — 3-D].	226
6.12	Space Profile at Time 11.995s [••• 2-D; — 3-D].....	226
6.13	Snapshot of the Mesh Configuration during the Wave Simulation	227
6.14	Space – Time Profile showing the Absorption Efficiency for a Wave Steepness of 0.082 [Right Side of the Black Line is the Absorption Zone].....	228
6.15	Time History at 0.5m from the Wave Paddle [----- Long Tank, 15.1m; —Short Tank, 6.69m].....	228
6.16	Time History at 3.572m from the Wave Paddle [-----Long Tank, 15.1m; — Short Tank, 6.69m].....	229
6.17	Wave Profile at Time 10.995s [----- Long Tank, 15.1m; — Short Tank, 6.69m].....	229
6.18	Wave Profile at Time 14.995s [----- Long Tank, 15.1m; — Short Tank, 6.69m].....	230

List of Figures (Continued)	Page
6.19 Absorption Coefficient against Wave Steepness for various Wave Frequency [Beach Length = λ ; Mesh Stretching Coefficient = 1.03].	230
6.20 Time History before the Beach [----- Long Tank; —— Short Tank].....	231
6.21 Space Profile at 15s [----- Long Tank; —— Short Tank].....	231
6.22 Space Profile at 25s [----- Long Tank; —— Short Tank].....	231

NOTATIONS

English symbols

a	wave amplitude
A_{ij}	global domain matrix
A_{∞}	far end surface boundary
A_B	bottom surface boundary
A_p	piston surface boundary
A_w	wall surface boundary
B	breadth
B_i	global boundary matrix
b	height of the obstacle
C	wave celerity
C_a	absorption coefficient
D	depth of the object
E	total energy
E_2	energy in the second order analytical solution
F	force
f	frequency
f	functional value
g	acceleration due to gravity
h	water depth
H	wave height
H_s	significant wave height
i, j	index numbers
k	wave number($k = 2\pi/\lambda$)
K_r	reflection coefficient
K_t	transmission coefficient
L	length of the tank
L_{beach}	length of the beach
L_{eff}	effective length of the beach
M	sink term
n	total number of nodes

N_i	shape function
N_w	number of wave components
NX	number of nodes in the x direction
NY	number of nodes in the y direction
NZ	number of nodes in the z direction
O	origin
S	stroke of the wave paddle
t	time
T	wave period
u	horizontal velocity
U	velocity vectors
U_r	Ursell parameter ($U_r = H\lambda^2/h^3$)
v	translation velocity
V	volume domain
w	vertical velocity
W_i	weight function
X	displacement vectors
x	x-axis direction
$x_{,l}$	partial differentiation of x w.r.t. l
X''	horizontal acceleration
x_p	wave paddle displacement
\dot{x}_p	wave paddle velocity
y	y- axis direction
$y_{,l}$	differentiation of y w.r.t. l
z	z- axis direction
$z_{,l}$	differentiation of z w.r.t. l
Z''	vertical acceleration

Greek symbols

$\Delta\eta$	decrease in wave elevation
Δc	increase in Celerity
Δt	time step
Φ	total velocity potential.

Γ_B	bottom boundary
Γ_∞	far end boundary
Γ_s	free surface boundary
Γ_p	piston boundary
ζ_0	non-physical wave elevation
Ω	2-D fluid domain
α_z	mesh parameter
χ, Ψ	stiffness factors
δ	displacement vector
δE	relative energy error
δx	horizontal spacing
ε	wave steepness
ϕ	nodal potential
$\phi_{,l}$	partial differentiation of ϕ w.r.t. l
γ	mesh stretching
γ	mesh stretching
η	water surface elevation
φ	velocity potential in moving coordinates
κ	stiffness of the spring
λ	wave length
$\nu(x)$	damping coefficient
π	constant (=3.1415)
ρ	density
σ	wave angular frequency (rad/sec)
τ	translation parameter
ω_b	damping frequency
ω_h, ω_v	excitation frequencies in horizontal (h) and vertical (v) directions
ω_n	sloshing modal frequencies (rad/sec), $n = 1, 2, \dots$
ω_p	peak excitation frequency (rad/sec)
ξ	mapped coordinates in x direction
Ψ	wavelet basis function

ζ	mapped coordinates in z direction
Υ	scaling factor
$\nabla\phi$	fluid velocity
∇E	relative energy loss

Operators

$\delta/\delta t$	derivative in vertical direction
$\partial/\partial t$	local partial derivative
∇^2	Laplace operator
D/Dt	substantial derivative

Abbreviations

2-D	2-Dimensional
3-D	3-Dimensional
ABPC	Adam Bashforth Predictor and Corrector
BEM	Boundary Element Method
bfd	Backward Finite Difference
BOU	Boussinesq
CCD	Charged Coupled Device
CPU	Central Processing Unit
CS	Cubic Spline
CWT	Continuous Wavelet Transformation
EXP	Experiments
FEM	Finite Element Method
FOV	Field of View
FT	Fourier Transform
GP	Global Projection Method
LS	Least squares
MFD	Mapped Finite Difference
MLS	Moving Least Squares
NODETAB	Node connectivity table algorithm
NWT	Numerical Wave Tank
PIV	Particle Image Velocimetry

RK	Runge-Kutta
STFT	Short Time Fourier Transform
TRIFIND	Finding triangle algorithm
VOF	Volume of Fluids
WT	Wavelet Transformation
WTC	Wavelet Coherence
XWT	Cross Wavelet Transformation

CHAPTER 1

INTRODUCTION

1.1 BACKGROUND

Different environmental loads that impart on the marine structures are due to wind, waves, currents, earthquake and ice. Of these, the hydrodynamic loads due to wind waves are the most important that induces cyclic loading that may lead to fatigue type of failure of structures if not properly incorporated in their design. With the advancement in the development of ocean wave modelling and remote sensors, the information on ocean waves are abundantly available these days. However, it is necessary to get the reliable information about the behaviour of loadings on the offshore systems due to ocean waves. The ocean surface propagates enormous amount of energy in the form of waves, tsunami, seiche and other types of waves. The relative energies of these waves differ from each other as they are formed by different disturbing forces acting over the sea surface. Ocean surface waves are generally classified based on the disturbing forces, restoring forces and their period. The amount of energy that is possessed by each type of waves on the ocean surface with respect to the period of wave is illustrated in Fig. 1.1. Among all the types of waves, the wind generated ocean waves dominate in terms of the total relative energy and are of great concern to engineers/scientists/planners. The wave form moves forward with a significant amount of energy from its origin, the properties of which keep varying. Based on the ratio of water depth (h) and wave length (λ), the wind waves are classified as deep water ($h/\lambda > 0.5$), intermediate water ($0.05 < h/\lambda < 0.5$) and shallow water ($h/\lambda < 0.05$) waves. Cnoidal and solitary waves fall in the category of shallow water waves. The

profiles of different types of waves discussed above are shown in Fig. 1.2. Thus, under-prediction of the ocean wave information will lead to failure of the structure and the over-prediction may give rise to uneconomical design.

1.2 IMPORTANCE OF OCEAN WAVES

Waves generated by wind or storm travel from the deep ocean towards the shore during which wave deforms (refraction, diffraction, reflection and shoaling). An offshore structure in deep sea experiences the extreme wave action and strong wave-wave interaction, while a coastal structure in the shallower region experiences loading due to the deformed waves due to refraction or diffraction or a combination of both. In either of the above cases, the waves behave as a nonlinear, highly dispersive and transient in nature. A typical photo of an extreme wave event that occurred at Gulf Stream, Charleston is shown in Fig. 1.3. Such a huge wave causes high impact loads on the ship and induces instability to the ship motion if not properly considered in the design. For example, the case of an oil cargo ship, sloshing in the container due to the ship motions may impart higher forces on the tank walls, which eventually lead to its capsizing.

The physical and numerical modeling of nonlinearity, particularly in extreme waves or shallow water waves are the important field of research for the design of the marine structures. Thus, the contribution to the analysis and the design of many complex structures and the nonlinear engineering problems such as slamming, ringing, ship stability phenomenon is to simulate and investigate these highly nonlinear waves that exist in nature.

1.3 PRESENT STUDY

Studies on the behaviour of waves and wave structure interaction problems in the marine environment have been topics of great interest over the past few decades with an increase in the necessity for exploration and exploitation of the ocean resources. Prior to the construction of marine structures, their performance needs to be evaluated either through numerical simulation or through physical model tests. Till early eighties, emphasis has been in understanding the behavior of marine structures more through physical model tests that require large hydrodynamic testing facilities with well controlled wave generation system. Due to the rapid progress in the computational power over the last two decades, numerical simulations of hydrodynamic process through the development of Numerical Wave Tank (NWT) have become increasingly important. NWT has the flexibility of reproducing several scenarios of predefined wave characteristics and their interaction with structures within hours or minutes, which, otherwise in the case of physical model tests might take several days or even months.

1.4 APPLICATIONS OF THE PRESENT WORK

The rapid increase in the marine applications, the real accurate prediction of hydrodynamic loads has become increasingly important for the design. For example, to minimize the wave energy transmission, a submerged trapezoidal structure or a submerged breakwater is often deployed in coastal areas. The presence of such structures is felt by the wave while propagating over them due to which the waves get deformed, with a significant nonlinear energy transfer among different wave frequencies.

The coastal structures that experience nonlinear wave interaction are usually studied using the shallow water theory. One such wave is the solitary waves, the interaction of

which on structures in general and in particular, on porous breakwaters or seawall has been a topic in which researchers have been focusing their attention. The solitary wave can also be approximated to the characteristics of a tsunami. Due to the recent Indian Ocean tsunami 2004, this topic has become much more important particularly in addressing the run-up on the sloping beaches due to steep shallow water waves including that of a tsunami/solitary waves. An important component of tsunami disaster prevention measure is to understand how a tsunami propagates from the deep to shallow waters. Since field observations of tsunamis are difficult to quantify except at the coast, the experimental and numerical investigation are becoming more important. Thus, the nonlinear wave simulation has the flexibility to reproduce the wave characteristics that exhibit in the deep water and shallow water as close as possible.

Apart from NWT, the need for numerical modelling arises due to the significant importance of the higher order effects due to sloshing waves which are nonlinear in which case, neither the linear nor the second order potential considerations are enough to simulate steep waves. This will be useful in various engineering problems like earthquake excitation on the liquid tank, spacecraft and the liquid cargo ship container.

1.5 ORGANISATION OF THE THESIS

Chapter 1 gives a brief introduction to the different types of ocean waves, the importance of the understanding the nonlinear waves and the need for the numerical modeling of such waves and their interaction with structures.

Chapter 2 details the review of the literature related to the present study showing the various numerical approaches for the simulation of nonlinear waves with an emphasis on the simulation using Finite Element Method on which the present study is based on. Past

numerical works and the approaches used by different investigators are briefed. The literature related to wave propagation, solitary wave interaction with structures, sloshing phenomenon along with the motivation for the present study are highlighted.

Chapter 3 explains the numerical modeling to simulate the nonlinear free surface waves. The finite element formulation and the different velocity calculation methods are projected along with the proposed velocity calculation method. The procedures involved in implementing unstructured mesh to the developed model based on structured mesh are described. Dynamic mesh moving strategies are discussed briefly in the context of nonlinear wave structure interaction.

Chapter 4 deals with the efficacies of the different velocity calculation methods on the simulation of nonlinear waves from small to high steep waves. The different velocity calculation methods have been validated with measurements at IITMadras, India, University of Wuppertal and University of Hannover, Germany. Further, quantitative comparisons are reported for the difference in wave phase speed between numerical and experiments by adopting wavelet transformation.

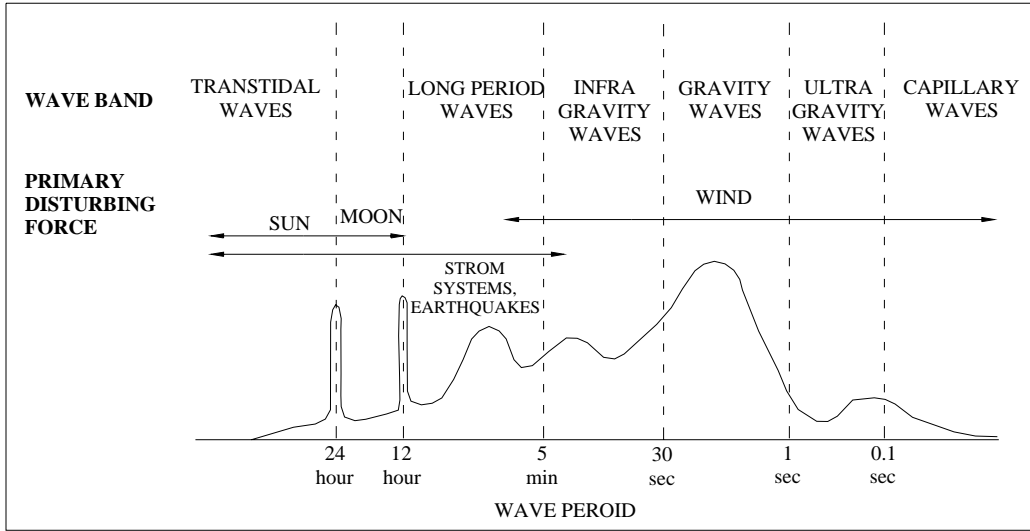
Chapter 5 presents the typical applications of the developed model to the wave interaction with submerged bar, surface-piercing object and a submerged cylinder near the free surface. The solitary wave interaction with the continental shelf and a vertical wall are explored in detail. This chapter also shows an insight into the physical behavior of the sloshing waves when a container undergoes regular excitation and how the sloshing behaviour changes due to the random excitation. The spectral analyses for the different excitation modes are presented and discussed.

Chapter 6 depicts the development of three dimensional numerical wave tank. The mathematical formulation and studies on the mesh orientation are projected. The implementation of an efficient wave absorber described with mixed boundary conditions and damping zone along with the grid stretching techniques are put forth for long time wave simulation.

Chapter 7 summarises the present study and the salient conclusions drawn from the study are highlighted.

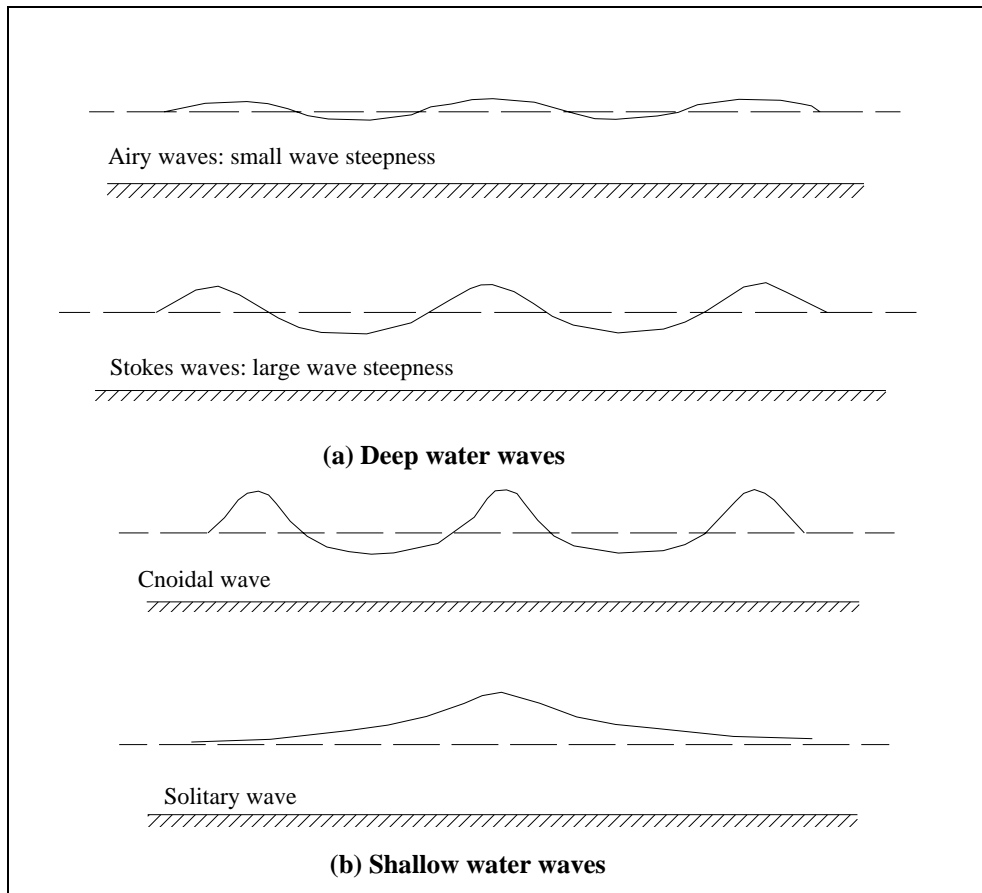
1.6 SUMMARY

The application of the nonlinear waves is wide. This is quite useful in obtaining reliable information about the type of loading that exert on the offshore or coastal structures. The simulation of very steep waves and its interaction with the structures has received considerable attention by researchers. Although important contribution on the subject of the nonlinear waves has been made over the last two decades, work on fully nonlinear numerical simulation and the various associated problems pose many challenges for the researchers even today. In order to address these problems, the present study deals with the development a numerical model, its validation and its application to field problems. The details of the organization of this thesis have been discussed in this chapter.



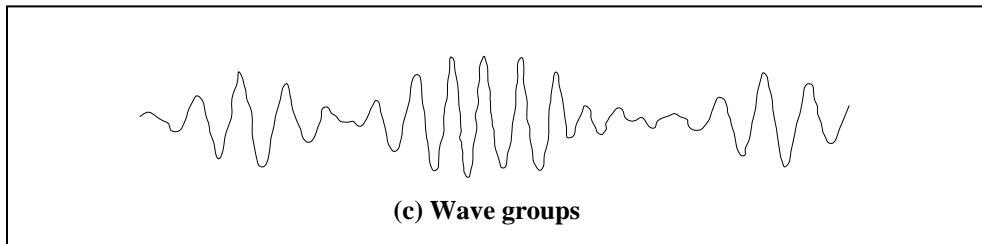
(Source : Kinsman, 1965)

Fig. 1.1 The Relative Amount of Energy Available in the Ocean Surface



(Source : Chakrabarti, 1987)

Fig. 1.2 A Physical Illustration of Various Wave Profiles



(Source : Chakrabarti, 1987)

Fig. 1.2 Contd.



(Source: <http://www.underwatertimes.com>)

Fig. 1.3 Extreme Nonlinear Waves Noticed in the Deep Water at Gulf Stream, Charleston

CHAPTER 2

REVIEW OF LITERATURE

2.1. GENERAL

The understanding on the studies in past on the steep waves are highly nonlinear waves of transient nature. The interaction of steep waves with the marine structure and kinematics of such waves is absolutely essential. For over the past three decades, the simulation of nonlinear waves and their interactions have been studied through the physical, analytical and numerical models. Although physical modelling replicates the phenomenon of steep waves accurately, it is quite tedious. Hence, researchers focused on the theoretical tools. The exact solution from the analytical model is possible with ease for definite domain shape and linearised boundary conditions. It is appreciable to solve the analytical model for the interaction of steep waves with simple geometries like vertical, horizontal cylinders but is difficult to derive for the irregular geometries and moving objects. In the case of numerical simulation, the domain equations can be approximated with the prescribed boundary conditions for any complex shape including moving boundaries. Each of the existing modelling approaches has its own merits and demerits and hence each approach depends upon the problem under consideration. This chapter focuses on the different numerical techniques.

2.2. MATHEMATICAL MODEL

For the simulation of free surface flows, various numerical techniques are available. The review on the free surface flows applied in the field of ocean engineering by Yeung

(1982), Schwartz and Fenton (1982), Tsai and Yue (1996), Scardovelli and Zaleski (1999) will provide a clear picture of the different numerical modelling techniques with the advantages and disadvantages of each of the methods. The reviews of the different techniques are given below.

2.2.1. Numerical Grid

One of the important criteria that govern the accuracy of the numerical solution is the adopted meshing strategy. The literature review of mathematical model based on the numerical grid is classified as follows,

Fixed mesh: The method based on fixed mesh is also called as surface capturing technique. It is classified under two types,

- a. **Marker methods**, where the free surface markers are used to capture the interface at the fixed mesh. These marker particles are used to locate the phases. This surface marker method was used by Unverdi and Tryggvason (1992). A modified marker and cell algorithm based on finite difference scheme has been developed to investigate the interactions of fully nonlinear waves with the two or three dimensional arbitrary structure by Park *et al.* (2003).
- b. **Volume of fluid (VOF)** solves the problem of updating the volume fraction field ' D ' given the fixed mesh, the velocity field ' u ', and the field ' d ' at the previous step. In two dimensions, the interface is considered to be continuous, piecewise smooth line. The problem of its reconstruction is that of finding an approximation to the section of the interface in each cut cell, by knowing only the volume fraction ' D ' in that cell and in the neighbouring cells. The simplest method is SOLA-VOF is that of Hirt and Nichols (1981). Clauss and Habel (2000) used the

commercial package StarCD to study the interaction with the artificial reefs for coastal protection. Clauss *et al.* (2004) used FLUENT to simulate the highly nonlinear transient waves and has shown good comparison with laboratory data. The free surface has been tracked via VOF on solving the Reynolds average Navier-Stokes equation.

Meshfree method: Meshfree or grid free methods are formed due to the problems caused by fixed or moving grids, in part or in complete. It has been adopted in the Boundary integral method (BIM) and Particle in cell (PIC) method (Harlow, 1964). Coupling of these two methods has been popular these days. The smoothed particle hydrodynamics (SPH) proposed by Monaghan (1992) was based on this coupling, where it uses the particles and smoothing kernels to define the intensity of interactions between particles, depending on their mutual distance. This method was applied for the simulation of breaking waves by Fontaine *et al.* (2000). More recently, another type of meshfree method, Meshless Local Petrov Galerkin method (MLPG) has been successfully adopted in the field of structural mechanics by Atluri and Zhu (1998). This method was based on the local weak form over local sub-domain (circles for 2-D and spheres for 3-D), which is a modified form of Finite Element method (FEM). Recently, this method has been applied to the nonlinear free surface waves by Ma (2005) to study the interaction of steep waves with a floating body. This strategy has been adopted to overcome the difficulty in the generation of mesh while using FEM.

Moving mesh and adaptive mesh method: In these methods, the free surface grid is allowed to move during the simulation. The fluid domain is solved in an Eulerian framework and the structure boundary/free surface movements are carried out in the

Lagrangian framework. When the movement of the grid nodes is taken care by the solution itself then it is called as Arbitrary Lagrangian and Eulerian Method (ALE) first introduced by Hirt *et al.* (1974). The detailed formulation and its application to simulation of nonlinear waves is given by Nitikitpaiboon and Bathe (1993). Ramaswamy and Kawahara (1985) proposed a Lagrangian FEM for the simulation of nonlinear viscous waves. When the movement of the mesh is not implemented in the Lagrangian framework but only the new free surface grid position is evaluated, then, the formulation is called Mixed Eulerian and Lagrangian scheme (MEL) as proposed by Longuet-Higgins and Cokelet (1976). Later, several investigators have been following this procedure for the simulation of nonlinear waves. It has been used to study a wide variety of problems, like forces due to breaking and extreme waves on submerged and surface piercing bodies (Vinje and Brevig, 1981) and interaction of steep waves with floating bodies (Sen, 1993; Maiti, 1999; Contento, 2000; Wu and Hu, 2004; Koo, 2005).

The methods based on meshfree and moving mesh methods are called as surface tracking method. In this thesis, focus is based on the surface tracking method with the inviscid flow. The reason being the principle interest is on the calculation of particle velocity and the free surface movement of only non breaking waves. Hence, literature based on the MEL approach considering the flow as inviscid is reviewed.

2.2.2. Mixed Eulerian and Lagrangian Method

The methodology introduced by Longuet-Higgins and Cokelet (1976) has been widely used by several researchers for the simulation of nonlinear waves, implementing various tools such as, BEM (Ohyama, 1991; Sen and Maiti, 1996) higher order BEM (Grilli *et al.* 1989; Boo, 2002), FEM (Cai *et al.* 1997; Clauss and Steinhagen, 1999; Ma *et al.* 2001a;

Bai and Kim, 2005; Washizu, 1982) and hp spectral FEM (Robertson and Sherwin, 1999). In order to minimize the need for smoothing/regridding on the free surface and remeshing on the domain, the transformation from physical to computational domain (mapping to rectangular grid) has been investigated. In FEM, this has been implemented by Turnbull *et al.* (2003a) and Chern *et al.* (1999), whereas, in Finite difference method notable works are that of Yeung and Vaidhyanathan (1992) and Frandsen (2004). Steinhagen (2001) adopted FEM for evaluating velocity potential and mapping approach for estimating velocity. But the disadvantages in the mapping methods is that overturning waves (breaking) and run-up on the slopes were not possible, where the solution becomes unique to this condition. Most of the methods (other than transformation) needs smoothing or regridding even for steepness (H/λ , where H is the wave height and λ is the wave length) of about 0.05 except the Spline-Boundary Integral Element method (BIEM) proposed by Maiti (1999).

2.2.3. Finite Element based MEL

In BEM, the potential and the derivatives on the boundary are approximated independently, usually by the same set of shape functions. Since no differentiation of the shape function is required for the representation of derivatives, the approximation of the derivatives and velocity potential is of the same order. However, in FEM, the derivatives are usually found from differentiating the shape function, which is the direct differentiation of the velocity potential. This induces further approximation in the velocity field than the approximation of potential. In time-dependent problems, this plays an important role. To overcome the induced discrepancy, Wu and Eatock Taylor (1994) solved a fully nonlinear wave problem based on the potential flow formulation by

considering either the velocity potential as an unknown (FEM) or both velocity potential and velocity as unknowns [Mixed Finite element method (MFEM)]. The advantages and accuracy of both the methods were compared and it was suggested that the MFEM was less accurate and takes larger computational time. A five point smoothing technique (as introduced by Longuet-Higgins and Cokelet, 1976) was applied at every time step for the simulation of the waves, in order to rectify the mesh instabilities. Westhuis (2001) adopted a polynomial function for the calculation of the velocity in which, a correction vector to the final velocity was adopted in order to minimise the drawback in the calculations using the global projection method (Wu and Eatock Taylor, 1994). The global projection (GP) method corresponds to re-sampling the velocity at the Gauss – Lagrange integration points, from which, a more accurate approximation to the velocity field can be obtained compared to the direct differentiation of velocity potential representations. Westhuis (2001) showed the inaccuracy of the GP by a linear stability analysis. A number of techniques (Steinhagen, 2001, Ma *et al.* 2001a, Turnbull *et al.* 2003b) address the main drawback for handling the simulation of nonlinear waves using FEM which is due to inaccurate calculation of velocity. In the case of unstructured mesh, Wang and Wu (2006) used the global projection method for tackling non-wall-sided boundaries but the unstructured mesh was regenerated at every time step requiring a higher computational cost. Other possible approach is the mesh movement strategy which is being widely used in the field of aerodynamics. In free surface simulation, this strategy has been adopted by Sudarsen *et al.* (2004) and Ma and Yan (2006). Though, the approach remains the same, the later named it as Quasi-ALE. Wu and Eatock Taylor (1995) showed that the FEM is advantageous over the BEM in the generation of fully nonlinear waves in terms of its computational efficiency and in its accuracy in the

simulation. Kim *et al.* (1999) reviewed the research and development in the simulation of nonlinear waves in regard to numerical implementations, methods of wave generation and absorption. The review paper focused mainly on BEM and no review paper on the progress of FEM in simulating nonlinear free surface waves is available. The progress of the FEM based potential flow formulation suggested by Wu and Eatock Taylor (1994) has been extended dramatically till date. The flow chart of the chronological progress in nonlinear wave simulation is given in Fig. 2.1. In the above chart, only research work with significant contribution to the wave simulation is quoted.

In the case of the 3-D simulation, the literature available is limited due to the computational intensive simulation (all available methods) and complexity of meshing (FEM). In BEM, the valuable contributions were made by Ferrant (1996), Grilli *et al.* (2008) and Romate (1992). Ma *et al.* (2001a) used FEM with a simple mesh generation routine to study the interaction of steep waves with the single and twin cylinders. Wu and Hu (2004) extended the above work by adopting hybrid mesh to study the wave interaction with a floating body. Recently, Wang and Wu (2007) used an unstructured mesh on the free surface and structured configuration across the depth to study the second order wave effects on the array of cylinders. Ma and Yan (2006) implemented unstructured mesh wherein, the mesh was moved at every time step based on spring analogy for floating body applications respectively.

2.3. WAVE PROPAGATION

The nonlinearity plays a major role when the extreme wave interact with the offshore structures in the deeper waters, whereas, in the near shore, the nonlinearity is due to the changes in the bathymetry, and hence, in the design of coastal structures. The wave

decomposition over a submerged reef or bar has been a topic of great interest over the past few decades ever since, the field investigation of Johnson *et al.* (1951). The waves in shallow waters are found to be cnoidal in nature and two to eight cnoidal waves among six wave packets were observed by Osborne (1994). Researchers carried out these steep wave interactions with the coastal structures through experimental investigation (Dattatri *et al.* 1978; Rey *et al.* 1992; Beji and Battjes, 1993; Ohyama and Nadaoka, 1994) and through field observations by Byrne (1969) and Young (1989). It is of great importance for prediction of coastal wave fields and beach profile formation (Hulsbergen, 1974). Three different approaches are adopted for the above said problem on wave propagation over a submerged bar. The first approach is the inclusion of non-conservative wave fields composed of multiple-frequency components both in shallow and deep water by modelling the wave dispersion accurately. This has been done by using Boussinesq-type equations (Peregrine, 1967), which has been commonly used in the analyses of nonlinear wave propagation in shallow waters. Notable contributions to this problem are that due to Abbott *et al.* (1978), Freilich and Guza (1984), Liu *et al.* (1985) and Seabra- Santos *et al.* (1987). However, since the conventional Boussinesq equation relies on assumptions of weak nonlinearity and weak dispersive of wave fields, this approach have the limitation in deep and shallow waters. In the case of deep waters, it is not applicable for the predictions of free higher harmonics, whereas, in shallow water waves its applicability to highly nonlinear interaction between bound and free waves are questionable. Attempts have been made to improve the dispersion characteristics of the Boussinesq- type equation (Madsen *et al.* 1991; Madsen and Sorensen, 1992; Nwogu, 1993, Beji and Battjes, 1994, Madsen *et al.* 2002, Lynett and Liu, 2004). Recently, Madsen *et al.* (2006) presented the most accurate Boussinesq type formulations capable of treating highly

nonlinear waves characterized by $kh = 25$ and kinematic velocity for $kh = 12$ (where k is the wavenumber and h is the water depth) to model a rapidly varying bottom.

The second approach is to incorporate the strong effects of wave nonlinearity that result from the increased ratio of wave height to water depth over the shelf or a bar. For this, Stokes type expansions of the velocity potential and free surface displacement are considered. The second order approximations for this wave decomposition by considering the phenomenon of incident periodic wave trains are given by Massel (1983) and Kojima *et al.* (1990). The limitations of this model arise from the applicability of the second order Stokes wave theory, to submergence of shelf in deep water and the evolution of random waves composed of multiple-frequency components.

The third approach is to reproduce the experimental facility numerically by considering the fully nonlinear waves along with the arbitrary nature of the bottom topography. Ohyama *et al.* (1995) compared the capability of Boussinesq- type equation, Stokes theory and fully nonlinear model based on BEM for the wave propagation over a submerged bar for different Ursell parameter ($U_r = H\lambda^2/h^3$). The fully nonlinear model was found to be in good agreement with the experimental measurements than the other two types of modeling.

2.4. SHALLOW WATER WAVES

Simulation of the nonlinear shallow water waves is essential for studying the interaction of waves with marine structures. In theoretical wave mechanics, the solitary and cnoidal waves are called as shallow water waves, which are nonlinear to the first degree of approximation. Goring (1979) carried out study on the long wave propagation over the

continental shelf, in which pioneering works on the efficient experimental generation mechanism of solitary and cnoidal waves were put forth, which overcomes the difficulties in the generation of highly nonlinear waves in the flume. Solitary waves or a combination of negative and positive solitons have a single crest/ trough and of infinite wave length. When compared to typical ocean waves, the solitary waves are highly nonlinear and exhibit translatory motion, it also posses a unique relationship between the wave nonlinearity and wave steepness. The wave steepness is usually represented as H/h . and hence in solitary wave-structure interaction problem, the influential parameter can be reduced to one, namely wave steepness. It is important for the coastal engineers to study the propagation of the solitary wave when it travels from deep water to shallow water in order to understand its behavior. The understanding of solitary wave run-up and breaking has received attention in numerous analytical, numerical and experimental studies. The experimental studies on the solitary or cnoidal waves are limited due to the requirement of large paddle stroke in generating these waves. Grilli *et al.* (1994) studied the solitary wave breaking through experimental simulation as well as using 2-D NWT based on BEM. Sen and Maiti (1996) reproduced the same simulation with improved BIEM based on splines. The solitary wave interaction with the vertical wall has been studied in the laboratory by Maxworthy (1976). The analytical modelling (Byatt-Smith, 1971 and Su and Mirie, 1980) and numerical simulation (Chan and Street, 1970; Fenton and Rienecker, 1982 and Maiti, 1999) have added to the understanding on solitary wave interaction with a vertical wall. Studies have been carried out on the interaction of solitary wave with submerged rectangular obstacles (Tang and Cheng, 1998; Cheng *et al.* 2001; Lin, 2004). Lin (2004) quoted that the wave breaking and vortex evolution should

be incorporated in the numerical model for proper understanding of wave transformation over a submerged obstacle.

The solitary wave propagation over an uneven topography has been dealt numerically and analytically by Grimshaw (1970) and Johnson (1973) and its disintegration into two or more solitons over varying depth has been studied using Korteweg-de Vries (KdV) type equation (Pudjaprasetya *et al.* 1999) and fully nonlinear models based on BEM (Van Daalen *et al.* 1997). The analytical studies for the transformation of a solitary wave over a shelf was also dealt by Miles (1979), Germain (1984), Kabbaj (1985) and Sugimoto *et al.* (1987), in which the only characterizing parameter is the relative obstacle height (b/h , where b is the obstacle height). Seabra-Santos *et al.* (1987) conducted the experiments to investigate the wave transformation over a shelf and a submerged triangular obstacle. In wave transformation, both nonlinearity and dispersion play an important role as pointed out by Goring and Raichlen (1992) for solitary waves as well as by Bejji and Battjes (1994) for regular waves.

Recently, Raichlen (2008) in his technical note on dealing with nonlinear waves, showed analytically that the linear waves can be scaled down to model scale and one can easily establish the obtained results to the field condition, whereas, linear establishment is not possible when one deals with nonlinear waves. This has been explained for the solitary wave propagation over continental shelf by making use of the results reported by Goring (1979). Hence, a suggestion has been put forth to study the effect of the nonlinear waves in two different model scale and by establishing the transfer function, one can relate it to the field condition.

Tsunamis that are basically shallow water waves undergo deformation due to the nearshore topography by reducing its speed resulting in an increase in wave height during their propagation. These waves travel inland over a large distance with considerable amount of energy that leads to property damage and loss of life. Therefore, an important aspect of any mitigation effort is to predict the entire scenario. Murty (1979) has shown that the energy released by the moving land mass by an earthquake can be modeled as a solitary wave.

2.5. SIMULATION OF SLOSHING WAVES

The phenomenon of sloshing still needs considerable exploration in the application of various engineering problems. These are highly nonlinear waves that may lead to structural damage of the sidewalls of the tank and/or destabilize the ship. Numerous studies have been carried out in understanding sloshing waves using analytical, experimental and numerical approaches. These include studies in 2-D and 3-D. In the case of 2-D, Faltinsen (1974,1978) derived the analytical solution of sloshing waves for sway and roll/pitch excitations using the perturbation approach; Okamoto and Kawahara (1990) and Armenio and La Rocca (1996) compared the results of numerical and experimental data; Nakayama and Washizu (1980) adopted a numerical approach for the forced pitching oscillation of the liquid tank; and Frandsen (2004) analyzed the sloshing oscillation in the vertical, horizontal and combined motions of the tank using analytical and numerical approaches. For the case of 3-D, Wu *et al.* (1998) numerically simulated the sloshing waves and Huang and Hsiung (1996) used the shallow water equation for the flow on the ship deck. Recently, Faltinsen *et al.* (2005) performed the experimental investigation in a 3-D tank.

The waves generated by the vertical excitation are called as Faraday waves. These waves were originally explored in an experimental study by Faraday (1831). Faraday waves are the resonant waves that are generated when the vertical excitation frequency is twice that of the natural frequency in the presence of initial perturbation in the container. This resonance condition is called as parametric resonance. Because of the requirement of initial perturbation in the free surface, it is difficult to carry out experiments only with the vertical excitation. To have an initial perturbation in the free surface inside the container, horizontal motion needs to be excited before the vertical excitation. A detailed review on sloshing of Faraday waves has been reported by Miles and Henderson (1990). Experiments have been carried out with the Faraday waves by Jaing *et al.* (1996) and Bredmose *et al.* (2003). There has been considerable amount of work carried out based on the horizontal excitation. The focus of many of the studies was on the earthquake induced sloshing. Ibrahim *et al.* (2001) presented a comprehensive review of more than one-thousand articles in the prediction of sloshing oscillation.

Most of the studies related to sloshing waves are based on the regular excitation of the container. This is quite useful in understanding the physical phenomenon of sloshing waves. However, in real field situation, the excitation is not regular but random in nature. Wang and Khoo (2005) analyzed for horizontal random excitation. Nasar *et al.* (2008) studied the sloshing harmonics present in the nonlinear system subjected to coupled dynamics of floating body and liquid on board. The study revealed the interesting phenomena such as inter-modal resonances, bore phenomena, nonlinear response of the floating body with the liquid tank, modal sacrifice of second mode and impact of liquid on tank panels.

2.6. OBJECTIVE AND SCOPE OF THE WORK

The objective of the present work is to simulate the nonlinear free surface waves in 2-D and 3-D Numerical Wave Tank (NWT) based on potential flow using FEM.

The scope of the present work based on the review of literature are given below,

1. To study the various velocity calculation techniques and its effect on smoothing/regridding strategies on the free surface.
2. Comparison of the simulated nonlinear free surface waves with the experimental measurements.
3. Quantitative comparison between numerical and experimental measurements based on Wavelet analysis.
4. To implement unstructured mesh in 2D tank and to study the effect of different mesh moving strategies.
5. Extension to 3D numerical simulation and to implement beach in the numerical model to carry out long time simulation.

The above developed model has been successfully applied to investigate the problems listed below.

1. Solitary wave interaction with vertical wall.
2. Solitary wave propagation over uneven water depth.
3. Nonlinear wave interaction with a submerged bar, a classical test for wave propagation model.
4. Sloshing waves due to regular and random excitation in the horizontal and vertical directions.

2.7. SUMMARY

In this chapter, detailed reviews of literature for the available methods in the simulation of nonlinear free surface waves are reported. The literature pertaining to the Finite Element based simulations are reported in the chronological order ever since the work of Wu and Eatock Taylor (1994). Further, the velocity calculation methods used by different authors in the context of FEM are highlighted. The chapter also shows a brief overview of the literature for the wave propagation over a bar, shallow water wave simulations and its interactions with structure and finally for the simulation of sloshing waves in a tank due to the excitation of the ship motions are reviewed, to show the applicability of the numerical model in these areas. Based on the review of literature, objective and scope of the work are drawn for the present study both in numerical aspects as well as in applications of the developed model.

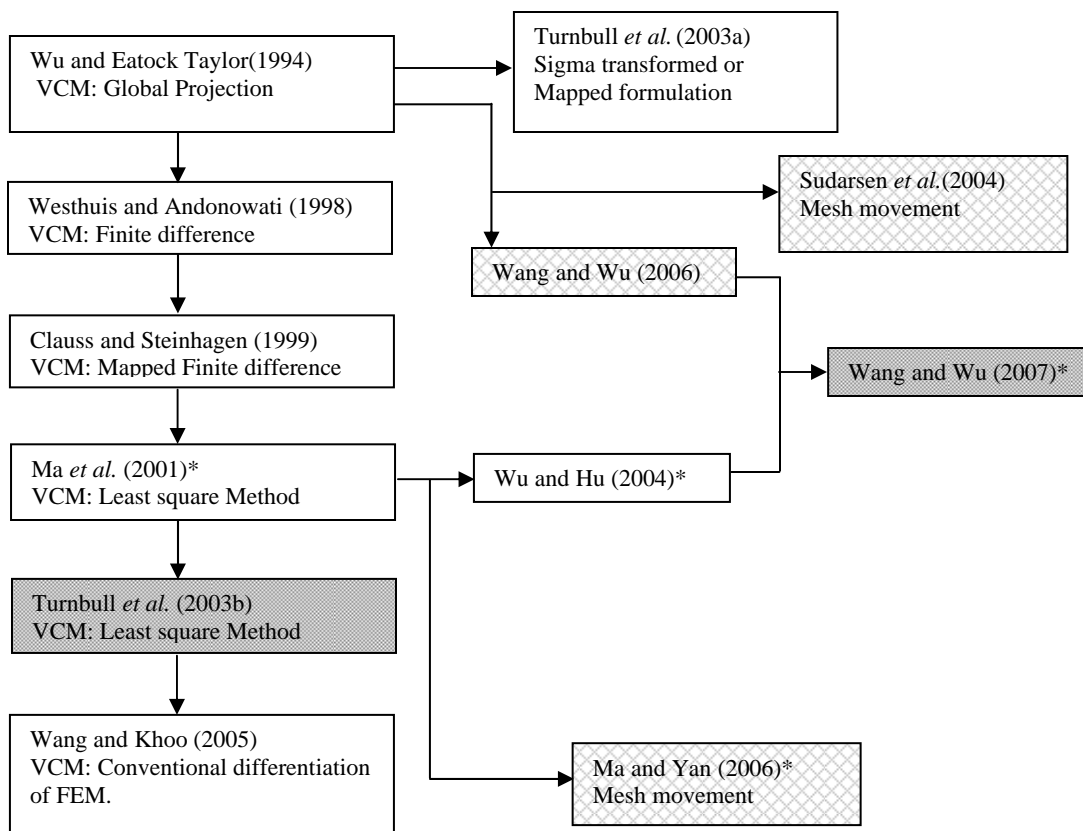
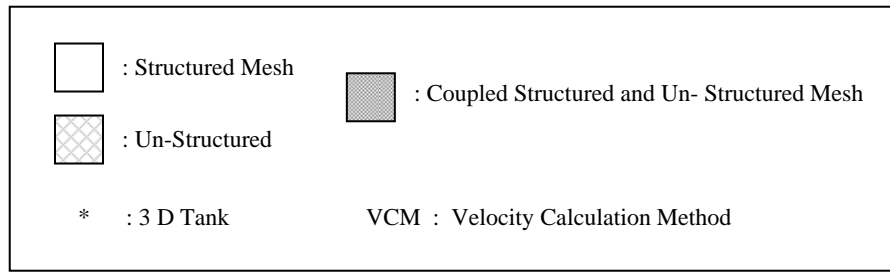


Fig. 2.1 Flow Chart Showing the Progress of the Finite Element Method

CHAPTER 3

NUMERICAL MODELLING

3.1. GENERAL

This chapter deals with the basic assumptions for the simulation of nonlinear free surface flow. The boundary value problem with the mixed Dirichlet and Neumann boundary conditions is solved based on the Mixed Eulerian and Lagrangian (MEL) formulation using Finite Element Method. The finite element formulation along with the proposed technique for the estimation of velocity and its advantages are explained in detail. Further, different velocity calculation techniques are implemented and discussed. The unstructured mesh implementation issues are reported in detail.

3.2. GOVERNING EQUATION

Two-dimensional fluid motion is defined with respect to the fixed Cartesian coordinate system, Oxz , with the z axis positive upwards. The water depth h is assumed to be constant. The fluid is assumed to be incompressible and the flow as irrotational. Viscous forces are neglected. This simplifies the flow problem to be defined with the Laplace's equation involving velocity potential $\Phi(x, z, t)$ given by

$$\nabla^2\Phi=0 \tag{3.1}$$

A potential flow in a rectangular flume with a wavemaker at one end and the nonlinear free surface boundary condition at the top boundary is considered. The schematic representation of the computational domain and the prescribed Neumann and Dirichlet

boundary conditions on the three boundaries (bottom, left and right) and at the free surface is shown in Fig. 3.1.

3.3. BOUNDARY CONDITIONS

Flume bottom is assumed to be flat, rigid and impermeable.

$$\frac{\partial \Phi}{\partial n} = 0 @ z = -h, \text{ on } \Gamma_B \quad (3.2)$$

Far field is modelled as a fully reflecting wall.

$$\frac{\partial \Phi}{\partial n} = 0 @ x = l, \text{ on } \Gamma_\infty \quad (3.3)$$

Wave paddle motion on the left end is prescribed as,

$$\frac{\partial \Phi}{\partial n} = \dot{x}_p(t) @ x = x_p(t), \text{ on } \Gamma_p \quad (3.4)$$

where, $x_p(t)$ is the time history of wave paddle motion.

Dirichlet boundary conditions are specified at the free surface with respect to the instantaneous velocity potential $\Phi(x, z)$ which is obtained from the nonlinear kinematic and dynamic free surface boundary conditions.

The nonlinear dynamic free-surface condition to be satisfied at the air-water interface at $z = \eta$ can be written as,

$$\frac{\partial \Phi}{\partial t} + \frac{1}{2} \nabla \Phi \nabla \Phi + g\eta = 0 @ z = \eta(x, t) \text{ on } \Gamma_f \quad (3.5a)$$

The kinematic boundary condition considering no flow through the free surface can be written as,

$$\frac{\partial \Phi}{\partial z} = \frac{\partial \eta}{\partial t} + \frac{\partial \Phi \partial \eta}{\partial x \partial x} @ z = \eta(x, t) \text{ on } \Gamma_f \quad (3.5b)$$

The difficulty with the above free surface boundary conditions is that the location of the free surface is not known in prior and it makes implicit form of solution. It can be overcome by rewriting in terms of Lagrangian or Eulerian form and marched in time to get the new position. In the simulation of nonlinear free surface waves, the second term in Eqn. (3.5a) usually called as convective term (i.e., the variation of the field variable in space) plays a major role.

Lagrangian form

The Lagrangian form of nonlinear free surface boundary condition is given by Longuet – Higgins and Cokelet (1976).

$$\begin{aligned} \frac{Dx}{Dt} &= \frac{\partial \Phi}{\partial x} \\ \frac{Dz}{Dt} &= \frac{\partial \Phi}{\partial z} \\ \frac{D\Phi}{Dt} &= \frac{1}{2} \nabla \Phi \nabla \Phi - g \eta \end{aligned} \quad (3.6a)$$

The above equations are obtained by substituting the substantial or material derivative

$$\frac{D}{Dt} = \frac{\partial}{\partial t} + \nabla \Phi \cdot \nabla \text{ in the Eqn. (3.5a) and Eqn. (3.5b).}$$

The above dynamic and kinematic free surface conditions can be modified as follows to include the wave absorbing beach on the other end of the flume,

$$\begin{aligned} \frac{Dx}{Dt} &= \frac{\partial \Phi}{\partial x} \\ \frac{Dz}{Dt} &= \frac{\partial \Phi}{\partial z} - v(x)z \end{aligned} \quad (3.6b)$$

$$\frac{D\Phi}{Dt} = \frac{1}{2} \nabla \Phi \nabla \Phi - g\eta - v(x)\Phi$$

where, $v(x)$ is a damping coefficient defined by (Cointe *et al.* 1990)

$$v(x) = \begin{cases} 0 & , x < L - L_{beach} \\ \sigma_b \left(\frac{x - (L - L_{beach})}{L_{beach}} \right)^2 & , L - L_{beach} \leq x \leq L \end{cases} \quad (3.6c)$$

where, L is the length of the wave flume. The damping frequency (σ_b) is used to control the strength of the damping zone, while the parameter L_{beach} (beach length) is used to control the length of the damping zone. For an effective wave absorption, the choice of damping coefficient is crucial.

Semi-Lagrangian form

This form of the free surface boundary condition restricts the movement of the nodes in the horizontal direction but allows only in the vertical direction and is given by,

$$\frac{\delta\Phi}{\delta t} + \frac{1}{2} \nabla \Phi \nabla \Phi + g\eta + \frac{\partial\Phi}{\partial z} \frac{\partial\eta}{\partial t} = 0 \quad (3.7a)$$

$$\frac{\partial\eta}{\partial t} = \frac{\partial\Phi}{\partial z} - \nabla \Phi \nabla \eta. \quad (3.7b)$$

Upon expansion, these can be written as

$$\frac{\partial\eta}{\partial t} = \frac{\partial\Phi}{\partial z} - \frac{\partial\eta}{\partial x} \frac{\partial\Phi}{\partial x}, \quad (3.7c)$$

$$\frac{\delta\Phi}{\delta t} = -\frac{1}{2} \left[\left(\frac{\partial\Phi}{\partial x} \right)^2 - \left(\frac{\partial\Phi}{\partial z} \right)^2 \right] - g\eta - \frac{\partial\Phi}{\partial z} \frac{\partial\eta}{\partial x} \frac{\partial\Phi}{\partial x}. \quad (3.7d)$$

In the above equations, the kinematic free surface boundary condition is still in the Eulerian form, where as, the dynamic boundary condition is strictly not in the Eulerian form. The derivative $\delta/\delta t$ is different from $\partial/\partial t$ (local derivative) and D/Dt (substantial derivative) in the sense that the node is allowed to move only in the vertical direction

over the time rate of change. Thus, this form is known as the Semi-Lagrangian approach, due to the restriction of nodal movement in the horizontal direction. One of the difficulties with this approach is the calculation of the free surface elevation with respect to time [Eqn.(3.7d)], due to which the error accumulates over the period of time. The advantage of this method compared to Lagrangian form, is that the process of regridding is not required.

Depending on the problem considered, one can choose a suitable method. In the literature, it is quoted that for floating bodies or breaking waves, the Lagrangian approach is more suitable. For fixed structure, such as submerged obstacles or multiple cylinder under non-breaking waves, semi-Lagrangian approach suits well compared to Lagrangian approach. In the present study, both forms are adopted depending upon the problem considered.

3.4. MIXED EULERIAN - LAGRANGIAN (MEL) SCHEME

The Mixed Eulerian-Lagrangian scheme was originally proposed by Longuet- Higgins and Cokelet (1976), according to which the boundary value problem associated with the Laplace Equation is split into two steps,

- 1) Eulerian Framework: For the given domain, the instantaneous velocity potential inside the domain is obtained based on the prescribed forcing or rigid boundaries.
- 2) Lagrangian Framework: Based on the solution sought in the above step, the velocity potential and the free surface wave elevation are updated by integrating the free surface boundary condition [Eqns.(3.6a),(3.6b) and (3.6c)].

This scheme plays a major role in the free surface simulation due to the discrete representation of the free surface elevation. In the present study, the solution in the

Eulerian Framework has been sought using FEM, due to the advantages of handling the complex domains and also free from any singularity compared to BEM/BIEM. The second step, *i.e.*, updating of velocity potential and free surface elevation needs more attention, because the integration has to be carried out with respect to time, during which the numerical error accumulates. For the time integration, many different schemes have been addressed in the past studies to eliminate this type of error.

There are two notable approaches: One is based on the truncated Taylor's series expansion as originally implemented by Dold and Peregrene (1986) for the free surface evaluation and later used by many authors in space periodic wave modelling (Grilli *et al.* 1989; Skourup and Jonsson, 1992). The difficulty with this approach is that it is not suitable for wave-structure interaction considering moving surface due to the difficulty in arriving second derivatives. The second approach is based on the direct integration, as proposed in MEL approach by Longuet-Higgins and Cokelet (1976). The direct time integration of the equation can be done, based on the numerical approach such as ABPC, RK method or open trapezoidal rule. This direct time integration of the equation is implemented in the present study and is explained in section 3.8.

3.5. FINITE ELEMENT FORMULATION

The Finite Element method adopted herein follows the formulation of Wu and Eatock Taylor (1994). The boundary value problem, defined by Laplace equation is solved at every time step for the prescribed Neumann and Dirichlet boundary conditions in a closed domain. The fluid domain (Ω) is divided into finite elements connected with ' n ' number of total nodes. The velocity potential inside an element $\Phi(x, z)$ can be expressed

in terms of its nodal potentials, ϕ_j ($j = 1, 2, \dots, m$, where, m is the number of nodes in the element)

$$\Phi(x, z) = \sum_{j=1}^m \phi_j N_j(x, z) \quad (3.8)$$

Herein, N_j is the shape function of the element. Applying the weighted residual statement to the Laplace equation leads to,

$$\int_{\Omega} w_i \nabla^2 \Phi d\Omega = 0, i = 1, 2, \dots, n. \quad (3.9)$$

Galerkin method states that weight function is equal to shape function.

$$\int_{\Omega} N_i \nabla^2 \Phi d\Omega = 0 \quad (3.10)$$

Following the spatial derivative form,

$$\nabla(N_i \nabla \phi) = N_i \nabla^2 \phi + \nabla N_i \nabla \phi \quad (3.11)$$

The integral formulation, Eqn. (3.10) leads to,

$$\int_{\Omega} (\nabla(N_i \nabla \phi) - \nabla N_i \nabla \phi) d\Omega = 0 \quad (3.12)$$

Substitution from Eqn. (3.8) and Gauss theorem yields the above domain formulation into discrete nodal potentials in the entire domain and the boundary (Γ) constraints.

$$\int_{\Gamma} N_i \frac{\partial \Phi}{\partial n} d\Gamma - \int_{\Omega} \nabla N_i \sum_{j=1}^m \phi_j \nabla N_j d\Omega = 0 \quad (3.13)$$

After substituting the boundary conditions, the final FEM formulation without the Dirichlet condition is given by,

$$\int_{\Omega} \nabla N_i \sum_{j=1}^m \phi_j \nabla N_j d\Omega = - \int_{\Gamma_p} N_i \dot{x}_p(t) d\Gamma \quad (3.14)$$

The above equation can be rewritten in the matrix form and the Dirichlet condition on the free surface can be implemented after forming the matrix equations as given below,

$$\mathbf{A}_{ij} \Phi = \mathbf{B}_i \quad (3.15)$$

Where,

$$\mathbf{A}_{ij} = \begin{cases} \int_{\Omega} \nabla N_i \nabla N_j d\Omega, & i, j \notin \Gamma_s \\ 1 & , i = j \& j \in \Gamma_s \\ 0 & ,(i \in \Gamma_s \text{ or } j \in \Gamma_s) \& i \neq j \end{cases} \quad (3.16)$$

$$\mathbf{B}_i = \begin{cases} - \int_{\Gamma_p} N_i \dot{x}_p(t) d\Gamma \\ \phi_i & , i \in \Gamma_s \end{cases} \quad (3.17)$$

In the above, the velocity potential is known at the free surface before the commencement of simulation inside the fluid domain. Due to symmetry, the storage is done on the half-banded assembly and Gauss elimination is used to solve the above matrix to seek the solution, Φ .

3.6. VELOCITY CALCULATION METHODS

3.6.1. General

To satisfy the nonlinear kinematic and dynamic free surface conditions in the potential flow formulation, the horizontal water particle velocity at the free surface needs to be evaluated in order to extract the free surface elevation at each time step. Once the velocity potential is obtained by solving the matrix Eqn. (3.15), the free surface horizontal and vertical velocities can be evaluated. However, the need for smoothing or regriding arises due to the inaccurate evaluation of the velocity from the velocity potential. The direct differentiation of the velocity potential results in the approximation of the velocity field in an order lower than the approximation of potential as,

$$\nabla \Phi = \sum_{j=1}^m \phi_j \nabla N_j \quad (3.18)$$

The above approximation has been used by Wang and Khoo (2005), considering 8 noded iso-parametric element. But, in the case of linear element, it is not that accurate enough. The reason for choosing linear element (3-noded triangular) by most of the authors is that it is easier to implement for complex geometries. Further, all the integration can be performed explicitly, which not only saves considerable computation time but also eliminates a possible source of error in time dependent problem. Hence, to achieve a greater accuracy in the velocity calculation, several approaches were proposed such as the global projection method (Wu and Eatock Taylor, 1994) and local finite differences (Cai *et al.* 1998; Westhuis, 2001; Ma *et al.* 2001; Steinhagen, 2001). The application of the global projection method (considering structured mesh) for the nonlinear free surface problem leads to unstable high frequency waves that will be discussed in section 3.12. The local finite difference technique is more accurate compared to the global projection method, but it requires local smoothing or local regridding. After obtaining the horizontal and vertical velocities, the new positions of the free surface and the velocity potential are evaluated by integrating the dynamic and kinematic equations. The integration is carried out using the standard fourth order methods like Runge-Kutta method/Adam Bashforth method. Both methods are found to be stable based on our investigation, which will be discussed in the subsequent section. The general procedure for the simulation is shown in Fig. 3.2. The smoothing or regridding at each time step has to be minimized for the long term simulation of nonlinear waves to avoid possible energy diffusion. Four methods of velocity calculations are discussed below.

3.6.2. Global Projection (GP) Method

The velocity vector, $\mathbf{u} = u\mathbf{i} + w\mathbf{j}$ is written in terms of shape function similar to Eqn.

(3.8). The Galerkin method is used to approximate the velocity ($\nabla \Phi = \mathbf{u}$) in the form of

$$\int_{\Omega} N_i (\nabla \Phi - u) d\Omega = 0 \quad (3.19a)$$

This leads to the following equation in matrix form,

$$[C]\{u\} = [D1]\{\phi\} \text{ and } [C]\{w\} = [D2]\{\phi\} \quad (3.19b)$$

where,

$$C_{ij} = \int_{\Omega} N_i N_j d\Omega \quad (3.19c)$$

$$D1_{ij} = \int_{\Omega} N_i \frac{\partial N_j}{\partial x} d\Omega \text{ and } D2_{ij} = \int_{\Omega} N_i \frac{\partial N_j}{\partial z} d\Omega$$

u and w correspond to horizontal and vertical velocities at each node. The above method was proposed by Wu and Eatock Taylor (1994). The disadvantage of this method is that it requires a quality mesh at every time step and more computational time which are further discussed in the next Chapter.

3.6.3. Least Squares (LS) Method

The least squares method to estimate the horizontal velocity proposed by Turnbull *et al.* (2003b) is briefly explained as follows. Consider an arbitrary free surface node, i connected to k neighbouring nodes in the Finite Element mesh. Let \mathbf{I}^k denotes the position vector connected to the free surface nodes (i) to the n^{th} ($n=1, \dots, k$) node under consideration. Then, the velocities are estimated by using the following least square approximation in the matrix form.

$$\left(\begin{array}{cc} \sum_{n=1}^k x_{,l}^n x_{,l}^n & \sum_{n=1}^k x_{,l}^n z_{,l}^n \\ \sum_{n=1}^k x_{,l}^n z_{,l}^n & \sum_{n=1}^k z_{,l}^n z_{,l}^n \end{array} \right) \begin{Bmatrix} u \\ w \end{Bmatrix} = \begin{Bmatrix} \sum_{n=1}^k x_{,l}^n \phi_{,l}^n \\ \sum_{n=1}^k z_{,l}^n \phi_{,l}^n \end{Bmatrix} \quad (3.20a)$$

where,

$$x_{,l}^n = \frac{(x_i - x_n)}{\sqrt{(x_i - x_n)^2 + (z_i - z_n)^2}}, \quad z_{,l}^n = \frac{(z_i - z_n)}{\sqrt{(x_i - x_n)^2 + (z_i - z_n)^2}}$$

$$\phi_{,l}^n = \frac{(\phi_i - \phi_n)}{\sqrt{(x_i - x_n)^2 + (z_i - z_n)^2}}$$

The above equation reduces to the following, if one knows the vertical velocity (w) at i^{th} node.

$$u_i = \frac{\sum_{n=1}^k x_{,l}^n \phi_{,l}^n - \sum_{n=1}^k x_{,l}^n z_{,l}^n w_i}{\sum_{n=1}^k x_{,l}^n x_{,l}^n} \quad (3.20b)$$

Similar kind of equations but without normalising by the distance has been implemented in a three - dimensional tank by Ma *et al.* (2001). On the other hand, the vertical velocity can be estimated with the backward finite difference scheme taking the advantage of distributing the nodes in a vertical line during mesh generation. Consider ϕ_j as the velocity potential at the nodes corresponding to z_j , where $j = 1, 2, 3$ as shown in Fig. 3.3.

The vertical velocity at the free surface node can then be obtained as

$$\frac{\partial \Phi}{\partial z} = \frac{(\alpha^2 - 1)\phi_1 - \alpha^2 \phi_2 + \phi_3}{\alpha(\alpha - 1)(z_1 - z_2)}, \quad (3.21)$$

where,

$$\alpha = \frac{z_1 - z_3}{z_1 - z_2}.$$

When the nodes are equidistant (i.e., $\alpha = 2$), the above equation reduces to the standard Backward Finite Difference (BFD) scheme. The procedure for estimating horizontal velocity holds good irrespective of the mesh structure, when one knows the vertical velocity. The estimation of vertical velocity using BFD is also successfully implemented by Ma and Yan (2006) with unstructured mesh discretization; the details are given in the unstructured mesh implementation of this chapter.

3.6.4. Mapped Finite Difference (MFD)

The estimation of vertical and horizontal velocities is evaluated based on mapped finite difference scheme. The wavy surface domain is transformed to a rectangular domain, i.e., the mesh is transformed from the physical coordinate system (x, z) to a mapped coordinate system (ξ, ζ) as follows,

$$\begin{aligned}\xi &= x \\ \zeta &= \frac{h+z}{h+\eta(x)}\end{aligned}\tag{3.22a}$$

Then, the velocities are estimated based on the second - order FD scheme which are based on the velocity potentials with respect to the new coordinate system (ξ, ζ) . After estimation of velocity, it is again transformed to the physical coordinate system using the following equations which are obtained using the chain rule of differentiation.

$$\frac{\partial}{\partial x} = \frac{\partial}{\partial \xi} - \frac{\partial}{\partial \zeta} \frac{h+z}{(h+\eta(x))^2} \frac{\partial \eta(x)}{\partial x}\tag{3.22b}$$

$$\frac{\partial}{\partial z} = \frac{\partial}{\partial \zeta} \frac{1}{h+\eta(x)}\tag{3.22c}$$

This methodology is adopted by Steinhagen (2001). From the procedure, it is clear that it leads to accurate velocity estimation but the mapping has to be done at each time step.

Limitations that arise by using this procedure are the simulation of overturning waves and the implementation for unstructured mesh.

3.6.5. Cubic Spline (CS)

In order to minimize the need for smoothing or regridding, splines are used as a velocity calculation method. Splines provide a better approximation for the behaviour of functions that have abrupt local changes. Further, splines perform better than higher order polynomial approximations. The efficient implementation of cubic splines as numerical differentiation for the evaluation of the tangential velocity in the simulation of waves using the lower order BEM has been adopted by Sen *et al.* (1989). In the present study, the cubic spline has been tried as a first attempt to evaluate the velocities in the context of FEM. The horizontal velocity is evaluated by fitting a cubic spline to the 'x'-coordinates and potentials, $\phi(x, z)$. The end conditions are considered as the natural spline condition. To evaluate the smooth first derivative at the i^{th} node, five nodes are considered (two nodes on either side of the i^{th} node) in order to minimize the effect of boundary constraints (natural spline condition).

Let us consider that f_i, f'_i, f''_i , are continuous over a given interval. Based on the continuity condition, we have

$$\frac{\delta x_i}{6} f''_{i-1} + \frac{\delta x_i + \delta x_{i+1}}{3} f''_i + \frac{\delta x_{i+1}}{6} f''_{i+1} = \frac{1}{\delta x_{i+1}} (f_{i+1} - f_i) - \frac{1}{\delta x_i} (f_i - f_{i-1})$$

$$i = 2, 3, \dots, k-1. \quad (3.23a)$$

The above equation leads to a set of $(k-2)$ linear equations for k unknown functional values, f_i . The horizontal spacing (δx) between the two nodes is a known parameter. The

above stated equation is solved by using the tridiagonal system of matrix assuming the second derivatives at the ends are zero i.e., the natural spline condition.

In the present simulation, assuming $f_i = \phi_i$, the derivatives at a particular node (ϕ_i) are found out by considering two nodes on either side ($k = 5$) as can be seen in Fig. 3.4, with the second derivatives (ϕ''_{i-2} , ϕ''_{i+2}) at the end nodes being set to zero. Following the evaluation of the second derivatives, the first derivative can be estimated using Eqn.(3.23a) at the required node (ϕ'_3), which are derived in the intermediate steps of the cubic spline interpolation (Jain *et al.* 2003).

$$2f''_i + f''_{i+1} = \frac{6}{\delta x_i} \left(\frac{f_{i+1} - f_i}{\delta x_i} - f'_i \right). \quad (3.23b)$$

It should be noted that the above formula is valid only for calculating velocities at the intermediate nodes and not at the end nodes. At the wave board, the velocity is assumed to be the input velocity and the velocity at the second node is evaluated by interpolation between the wave board and the third node (which is estimated from the above method). Similarly, at the end of tank, the velocity is assumed to be zero. For the evaluation of velocity in the vertical direction, second order FD scheme is used as described in section 3.6.3.

One of the main advantages of the cubic spline approach is its capability of estimating smooth first derivatives, that minimizes the requirement of smoothing/ regridding when adopting the Lagrangian approach and smoothing in the case of Semi- Lagrangian approach, which are discussed in the following section. On the other hand, this method does not hold good for the very steep wave fronts. When the nearby nodes fall on a vertical line, Eqn. (3.23a) becomes singular. Moreover, the procedure holds good for

two-dimensional tank only. A modification is certainly required for an extension into simulation in the three-dimensional tank.

3.7. MESH GENERATION

The generation of structured mesh is made simple in the present study. The required mesh structure should follow the velocity potential phenomenon (i.e., exponential decay across the depth) to minimize the number of nodes in the simulation. The new nodal coordinates have to be generated at every time step using the formula. Hence, the nodal numbers and the element connectivity remain the same throughout the simulations. To explain the mesh generation routine, consider a known free surface elevation,

$$\eta_i = \frac{H}{2} \cos\left(\frac{2\pi}{\lambda} x_i\right) \quad (3.24)$$

where, λ is the wave length and H is the wave height. i is the index number on the free surface. The known free surface is then divided into equal distance using,

$$x_i = \frac{((i-1)*\lambda)}{NX} \quad (3.25)$$

where, NX is the number of elements in the x - direction (at the free surface).

Having divided the x - coordinates and evaluated the free surface elevation through Eqn. (3.24), the z - coordinates are evaluated using,

$$z_{i,j} = -(h + \eta_i) \frac{1 - \exp(\alpha_z (h + \eta_i)(NZ + 1 - j) / NZ)}{1 - \exp(\alpha_z (h + \eta_i))} + \eta_i \quad (3.26)$$

$$\text{for } i = 1, 2, \dots, NX+1 \text{ and } j = 1, 2, \dots, NZ+1$$

where, α_z is the parameter controlling the mesh size along the vertical direction, taken as 2.0 (Wu and Eatock Taylor, 1994). $NX+1$ and $NZ+1$ are the number of nodes along the

horizontal and vertical directions, whereas, $Z_{i,j}$ are the vertical coordinates. Typical nodal coordinates for the above said problem, assuming λ as 2 is depicted in Fig. 3.5.

Once, the nodal coordinates and node numbering are established, the element connectivity is done using the following subroutine. The column to the right explains the physical interpretation.

<pre> N = 1 Q = 1 IE = 2 * NX * NZ DO M = 1,IE,2 ELENOD(M,1) = N ELENOD(M,2) = N+NZ+1 ELENOD(M,3) = N+NZ+2 ELENOD(M+1,1) = N ELENOD(M+1,2) = N+NZ+2 ELENOD(M+1,3) = N+1 N = N+1 IF(N.EQ.Q*(NZ+1)) THEN N = (Q*(NZ+1))+1 Q = Q+1 END IF END DO </pre>	
--	--

Typical generated mesh configuration is shown in Fig. 3.6. In the context of FEM, the mesh orientation plays a major role in the evaluation of velocity potential when one deals with structured mesh. The above mesh structure has been taken based on the mesh orientation study carried out by Westhuis (2001) using the Eigen values.

3.8. NUMERICAL TIME INTEGRATION

The numerical time integration plays a major role in any time marching problem. For the present nonlinear wave simulation study, the numerical integration has to be carried out for the dynamic and kinematic free surface boundary conditions given in Eqn. (3.6) or Eqn. (3.7). To explain this, consider Fig. 3.7, if one knows (x, z, ϕ) values at time t , the

new coordinates at the next time step ($t+\Delta t$) can be evaluated using Taylor's series (forward difference).

$$\begin{aligned} x|_{t+\Delta t} &= x|_t + \left(\frac{Dx}{Dt}\right)_t \Delta t \\ z|_{t+\Delta t} &= z|_t + \left(\frac{Dz}{Dt}\right)_t \Delta t \\ \phi|_{t+\Delta t} &= \phi|_t + \left(\frac{D\phi}{Dt}\right)_t \Delta t \end{aligned} \quad (3.27)$$

where, the second term in the above equations has been evaluated as described above using either of Eqn. (3.6) or Eqn. (3.7). The direct application of the above equations lead to spurious free surface oscillations even if small time steps are adopted. Hence, a fourth-order method based on Runge-Kutta (RK) or Adam–Bashforth predictor corrector (ABPC) method is adopted in the present study.

The fourth-order method based on RK using explicit time integration is carried out as described below. If the free surface nodes and the associated velocity potential at current time step i , are known then,

$$S_i = (\mathbf{x}_i, \mathbf{z}_i, \boldsymbol{\phi}_i) \quad (3.28)$$

where,

$$\begin{aligned} \mathbf{x}_i &= \{x_1, x_2, \dots, x_{NX+1}\}_i, \quad \mathbf{z}_i = \{z_1, z_2, \dots, z_{NX+1}\}_i, \\ \boldsymbol{\phi}_i &= \{\phi_1, \phi_2, \dots, \phi_{NX+1}\}_i \end{aligned}$$

Similarly, the time derivatives can be written as,

$$\frac{DS_i}{Dt} = F(t_i, S_i) = F_i \quad (3.29)$$

The above equation corresponds to the dynamic and kinematic free surface boundary conditions either in Lagrangian or semi-Lagrangian form.

In order to know the updated free surface location and the corresponding velocity potential for the next time step, the explicit RK requires the evaluation of velocity at intermittent time steps as given below.

$$\begin{aligned}
S_1 &= \Delta t F(t_i, S_i) \\
S_2 &= \Delta t F(t_i + \Delta t / 2, S_i + S_1 / 2) \\
S_3 &= \Delta t F(t_i + \Delta t / 2, S_i + S_2 / 2) \\
S_4 &= \Delta t F(t_i + \Delta t, S_i + S_3)
\end{aligned} \tag{3.30a}$$

$$S_{i+1} = S_i + \frac{S_1}{6} + \frac{S_2}{3} + \frac{S_3}{3} + \frac{S_4}{6} \tag{3.30b}$$

Thus, it requires the evaluation of the Laplace equation for four times [at the intermediate time steps Eqn. (3.30a)] for the boundary movement to evaluate the new free surface location and the corresponding velocity potential for the time step, Δt . The advantage of using the above classical RK method is that it is numerically stable for a large class of problems and it can be used as a self starter for other time integration methods.

In the case of ABPC, this multi step method consists of an explicit predictor and an implicit corrector for each time step Δt . It is given by,

$$\begin{aligned}
S_{i+1}^p &= S_i + \frac{\Delta t}{24} (55F_i - 59F_{i-1} + 37F_{i-2} - 9F_{i-3}) \\
S_{i+1}^c &= S_i + \frac{\Delta t}{24} (9F_{i+1}^p + 19F_i - 5F_{i-1} + F_{i-2})
\end{aligned} \tag{3.31}$$

In free surface problem using MEL procedure, one-time evaluation of corrector step is found to be adequate. Thus, ABPC requires the evaluation of Laplace equation two times with the new boundary conditions to obtain the updated free surface coordinates and the associated velocity potential for a time step of Δt . Hence, the computation time for this method is half that of RK method.

3.9. SMOOTHING/REGRIDDING TECHNIQUES

In a time stepping simulation, numerical instability and the high frequency oscillation are common phenomena due to inaccurate evaluation in any part of the numerical algorithms (for example, in the process of velocity estimation in case of FEM, during numerical integration). In order to overcome these difficulties, the usual practice is to apply smoothing or regridding at the new free surface and the associated velocity potential. There is major difference between smoothing and regridding techniques. Smoothing is a process by which data points are averaged with their neighbours in a series. It filters the high frequency component and enhances the low frequency component. Thus, too much smoothing leads to energy loss in the system. Regridding is nothing but redistributing the nodes and the associated values at an equal or variable spacing. In the present thesis, the smoothing is carried out based on five point smoothing technique proposed by Longuet-Higgins and Cokelet (1976) and the regridding technique based on constant arc length by fitting a cubic spline as proposed by Dommermuth *et al.* (1988). They applied it periodically and postulated that regridding results in relatively lesser loss of energy from the system. Thus, it can easily be applied at intersection points, not like smoothing techniques that are difficult to implement. The main disadvantage of regridding is the loss of resolution in the zone of higher gradients.

3.10. ALGORITHM

The algorithm for the numerical procedure is briefly reported herein. Assume the initial velocity potential and surface elevation. Digitize the entire domain using the required number of nodes and establish the element connectivity. Apply FEM and obtain the velocity potential inside the fluid domain. The challenging task in the simulation is then

the velocity estimation. Recover the horizontal velocity using the suitable methodology on the free surface. Based on the velocities, update the free surface nodes using the dynamic and kinematic boundary conditions based on Lagrangian / Semi-Lagrangian approach. The integration can be carried out using the fourth order Runge-Kutta method that requires repeated evaluation of velocity potential and velocity at the intermediate time steps to obtain the new position at next time step. The integration using Adam-Bashforth method is half expensive than the Runge-kutta method. Depending upon the problem in hand, choose the respective one. After the computation of the new free surface position and velocity potential, repeat the calculation as many times required based on the termination time. The flow chart of the numerical simulation is depicted in Fig. 3.8.

3.11. UNSTRUCTURED MESH IMPLEMENTATION

For modeling complex geometry or for the simulation in the presence of floating bodies, one needs to resort to an unstructured mesh simulation. In this section, the implementation issues related to the simulation of nonlinear free surface waves in the context of unstructured FEM has been briefly described. For successful implementation, suitable velocity calculation methodology should be adopted. The MFD method is difficult to implement when the mesh is generated using unstructured mesh, where, the node numbers are not in regular orientation, whereas, LS, CS and GP methods can be implemented.

3.11.1. Dynamic Mesh Moving

In the case of structured mesh, the element connectivity remains the same, whereas, the node positions at every time step are evaluated based on the new free surface nodes with

the vertical elevation calculated using a simple formula [Eqn.(3.26)]. The computation is inexpensive and thus regeneration of mesh nodes can be done with ease. In the case of unstructured mesh, one has to resort to the external mesh generation code (First approach) or commercial CFD mesh generators (second approach). While using the first approach, regeneration of mesh is possible at every time step by simply calling the external code from the source code, whereas, in the second approach, it is not possible to update at every time step automatically. Wang and Wu (2006) used the first approach of regenerating the mesh at every time step using the public domain code called BAMG. In the second approach, one can use the commercial CFD mesh generators like GAMBIT, ICEM-CFD to create the initial mesh. Then at every time step, a mesh moving technique like Laplacian smoothing/ Torsional spring/spring analogy method can be invoked to find the new nodal position. The second approach is more popular in the field of aerodynamics and is similar to Arbitrary Lagrangian and Eulerian (ALE) method. Hence, in the present study, it has been named as Semi-ALE (SALE) but the basic principle remains the same.

Sudharsan *et al.* (2004) compared three different mesh movement schemes namely Laplacian smoothing, Torsional spring and Spring analogy for the nonlinear free surface problem. It has been concluded that the spring analogy is a good choice for handling complex geometries. There are two different methods usually used in spring analogy: one is vertex method and the other is segment method. The vertex spring analogy was originally used for smoothing a mesh after mesh generation or refinement. The segment spring analogy was developed for the deformation of the mesh in a moving boundary problem. Blom (2000) gave a detailed considerations on both segment and vertex methods. Both the normal vertex and spring methodologies led to mesh skewness near

the boundary. So, the method has been improved by using modified stiffness and hence, the name ‘improved vertex/segment spring methodologies’. Blom (2000) has suggested that the stiffness should be increased for the boundary layers compared to the interior layers. Considering the applicability in the field of simulation of nonlinear waves, Sudharsan *et al.* (2004) assumed the stiffness in the boundary layer alone and concluded that vertex method is superior to all the available methods to treat wave-structure interaction problems. However, Ma and Yan (2006) used segment method and showed promising results, by adopting the stiffness in such a way that the adjacent layers (*i.e.*, along the entire water depth) were also stiffened. Hence, in the present study both the segment and vertex methods of spring analogy have been considered to test its suitability. In the following sections, an overview of both vertex and segment methods is given in detail to understand the physics behind these methods before applying them to nonlinear free surface waves.

3.11.2. Vertex Method

When the segments are considered as springs, it has to possess equilibrium length which is the initial length of the segment at rest. For vertex method, this equilibrium length is zero. The springs are taken as linear and therefore Hooke’s law determines the force (\vec{F}_i) at every node i exerted by the nodes j , which are connected to node i ,

$$\vec{F}_i = \sum_{j=1}^m \kappa_{ij} (\vec{x}_j - \vec{x}_i) \quad (3.32)$$

Where, κ_{ij} is the stiffness of the spring between node i and j , m is the number of neighbours for node i . X is the coordinate vector (x, z are the coordinates of the node). The physical interpretation is shown in Fig. 3.9. For the system to be in equilibrium, the

force at every node i has to be zero. After simplifying, the Jacobi iterative equation can be written as,

$$x_i^{n+1} = \frac{\sum_{j=1}^m \kappa_{ij} x_j^n}{\sum_{j=1}^m \kappa_{ij}} \quad (3.33)$$

Equilibrium is not imperative for the mesh deformation since the spring model is only used as a tool to retain mesh quality. Therefore, a convergence limit of 1×10^{-5} has been adopted. When the boundary is moved or deformed, the position of the boundary nodes is strongly imposed by Dirichlet boundary conditions after moving all the interior nodes.

Since the equilibrium position of the springs is zero, every spring is under tension. That is, the new nodal positions are prescribed on the boundaries of the old nodal coordinates and the interior nodes are moved. Hence, the mesh can be deformed or moved by this spring analogy method even when the boundaries are not moved. Here, the spring stiffness is taken as one, a constant value.

3.11.3. Segment Method

Segment spring analogy was proposed by Batina (1990) in order to deform a mesh around a pitching airfoil. In this method, the equilibrium length of the spring is assumed to be equal to the initial length of the segments. According to Hooke's law, the force is written similar to Eqn. (3.32) for the displacement of nodes as,

$$\vec{F}_i = \sum_{j=1}^m \kappa_{ij} (\vec{\delta}_j - \vec{\delta}_i) \quad (3.34)$$

where, $\vec{\delta}_i$ is the displacement vector of the node i . For static equilibrium, the force at every node i has to be zero. Then the Jacobi iterative equation is,

$$\vec{\delta}_i^{n+1} = \frac{\sum_{j=1}^m \kappa_{ij} \vec{\delta}_j^n}{\sum_{j=1}^m \kappa_{ij}} \quad (3.35)$$

The above equation has to be solved separately for δ_{xi} (displacement along x direction) and δ_{zi} (displacement along z - direction). The Dirichlet boundary conditions are strictly imposed like in vertex method. Batina (1990) proposed the spring stiffness to be inversely proportional to the length of the segment.

$$\kappa_{ij} = 1 / \sqrt{(x_i - x_j)^2 + (z_i - z_j)^2} \quad (3.36)$$

After the iteration of Eqn. (3.35), the new nodal coordinates are found out by adding the final displacement to the old nodal coordinates.

$$\vec{x}_i^{new} = \vec{x}_i + \vec{\delta}_i^{final} \quad (3.37)$$

Thus in the above algorithm the displacement vector has to be kept in memory and hence the segment spring method requires more memory than the vertex method. The convergence limit for the iterative Eqn. (3.35) is 1×10^{-6} . The convergence limit has been set to be higher compared to vertex method, since this is basically a deforming algorithm unlike a smoothing scheme. For efficient implementation and to reduce the number of iterations, the final displacement of the previous solution is taken as the initial known displacement for the interior nodes.

3.11.4. Improved Vertex/Segment Method

The concept of spring analogy is shown to be similar to the elliptic grid generation by Bloom (2000). Then, the principle of Saint Venant for elliptic equations holds for the deformation of the mesh by the spring analogy. This principle states that local perturbations of the solution only have local impact. As shown in the previous sections,

the spring analogy regularizes the mesh only near the moving or deformed boundaries at every time step. Thus, it could handle only small deformations. If the deformation is large then the overlapping of the nodes could take place. Hence, the improvement of the above methods (Bloom, 2000) has been suggested by modifying the stiffness as,

$$\kappa_{ij} = \chi((x_i - x_j)^2 + (z_i - z_j)^2)^\psi \quad (3.38)$$

The above equation shows the inclusion of the principle of Saint Venant, *i.e.*, the stiffness near the boundary is increased so that the deformation is spread out to the interior regions of the mesh. In order to achieve this, the factor χ is incorporated in the above said equation to increase the stiffness for a number of elements adjacent to the deformed boundaries. The stiffness in Eqn. (3.38) is applicable to both segment and vertex methods by suitably taking the spring stiffness, which depends upon the problem in hand and also in understanding the physics behind the methods (as described earlier). While using vertex method, basically a smoothing algorithm, a constant value of χ for the boundary and interior elements is used. While using segment method, basically a mesh deformation algorithm, a group of layers adjacent to the boundary has to be taken into consideration depending upon the problem. For the present nonlinear free surface problem, it is well known fact that the behaviour of wave kinematics is an exponential decay across the depth. Thus, an exponential decay factor of χ should be a good approximation. The power coefficient ψ defines the strength of the stiffness with respect to the distance between the nodes.

3.11.5. Node Table Connectivity (NODETAB)

The important part of the unstructured mesh implementation, when one deals with mesh moving algorithms, is the establishment of nodal connectivity table. In the present

application, this table serves for two purposes: one as described above for mesh moving strategies and the other for the interpolation of velocity potential when one uses Moving Least Square method which is explained later. After, the mesh is generated by using any of the commercial softwares, the node renumbering has been done to optimize the bandwidth of the matrix to reduce the computational time. The node renumbering has been done using Reverse- Cuthil Mckee reordering scheme for triangular mesh. The next step is to establish the node table connectivity. This will give the information of the neighbouring nodes connected to the node under consideration. Thus, the node connectivity table remains same for the mesh under consideration throughout the simulation time. The physical interpretation of node table is explained below in reference to Fig. 3.10. If one considers the given node number, then the neighbouring nodes can be easily identified by searching all neighbouring element. The final table will be generated as shown in Table 3.1 after omitting all the duplicate nodes. The column values in J indicate the number of nodes that are connected to the given node (but it has been stored in terms of array dimension, i.e., J-1 gives the number of neighbours).

3.11.6. Vertical Velocity Estimation

The implementation of the above formulation based on FEM to evaluate velocity potential and global projection method (to calculate velocity) to extract the velocity is straight forward irrespective of the mesh whether it is structured or unstructured. The estimation of the horizontal velocity using LS method also still holds good. The investigators in the past have taken advantage of the vertical distribution of mesh and evaluated the vertical velocity accurately using BFD scheme. However, in the case of unstructured mesh, BFD scheme does not hold good. Ma and Yan (2006) proposed a

sensible technique of effectively using this strategy by drawing the normal line with respect to free surface and used an effective Moving Least Squares (MLS) method for the interpolation of the two points over the normal line. But computationally, it is expensive since it deals with the group of old nodes. After the estimation of normal velocity, the LS method is used to evaluate the tangential velocity. This is used in the calculation of the LS [Eqn.(3.20b)]. Thus, CS can also hold good for 2D unstructured mesh. Hence, in order to use the above strategies, the vertical velocity has been calculated by using the following algorithm.

A vertical line to the free surface node is constructed and two points in that line have been used to evaluate the vertical velocity using backward finite difference method. The first point should lie in the triangle (say 'A') which has the given point under consideration, criteria is $d_1 = 0.7d$ where, d is the perpendicular distance from the given point to the intersection of the virtual vertical line to triangle segments (opposite edge) as depicted in Fig. 3.11. The second point should lie in the adjacent triangle below 'A' , criteria is $d_{12} = 1.4d$ and it should not be too far away. The important tasks are locating the triangle and interpolating the velocity potential to the new point since the values are not known inside the triangles in FEM. These two algorithms are described below.

Finding a triangle (TRIFIND)

In order to find a triangle, for the known x, z coordinates inside the triangulation domain, the following algorithm can be used. Consider, 'J' a point under consideration assumed to be inside a triangle then corresponding element can be found out by calculating the following vectors.

$$\begin{aligned} \mathbf{V}_{J1} &= \{x_J - x_a, z_J - z_a\}, \mathbf{V}_{J2} = \{x_J - x_b, z_J - z_b\}, \mathbf{V}_{J3} = \{x_J - x_c, z_J - z_c\} \\ \mathbf{V}_{ab} &= \{x_a - x_b, z_a - z_b\}, \mathbf{V}_{bc} = \{x_b - x_c, z_b - z_c\}, \mathbf{V}_{ca} = \{x_c - x_a, z_c - z_a\} \end{aligned} \quad (3.39)$$

where, a, b, c are the element vertices under consideration.

In order that the nodal point J should lie under the element, then, the following inequality should satisfy,

$$\begin{aligned} \mathbf{V}_{J1} \times \mathbf{V}_{ab} &\geq 0, \\ \mathbf{V}_{J2} \times \mathbf{V}_{bc} &\geq 0, \\ \mathbf{V}_{J3} \times \mathbf{V}_{ca} &\geq 0 \end{aligned} \quad (3.40)$$

If the above cross-product equality satisfies for a given point and element under considerations, then the point lies inside the element. Once, the triangle is known, the point 'J' has the corresponding 3 vertices as the neighbouring node.

Interpolation

One can adopt shape function of the element using TRIFIND algorithm in order to evaluate the velocity potential at point 'J' within the element. This is reasonably accurate enough for small steep waves. But when the waves are steep enough, it leads to an over estimation of the values, a general drawback of the interpolation technique. In order to overcome this drawback, MLS technique has been adopted. This is a popular interpolation algorithm emerged in the context of Meshfree technique. The details regarding the MLS method is reported in Appendix A. This method basically does the interpolation using a group of nodes. The computational efficiency to minimize the time consumption to find the group of nodes at every time step is still a topic of research in meshfree methods (Liu, 2002). Various stand alone algorithms are available to find the group of nodes like bucket algorithm, cell based algorithm, trapezoidal map and sweep algorithm. These algorithms, in general, consume more time. Hence, in the present study,

a new methodology has been developed by making use of the existing available data in the context of simulation of nonlinear free surface waves. The present algorithm is based on the nodal connectivity table (NODETAB) which has been explained in the previous section. The methodology starts from the previous section after one finds three nodes (TRIFIND algorithm). The methodology has been explained below in connection with the physical interpretation depicted in Fig. 3.12. The dark circles in Fig. 3.12a represent the point 'J', by using the algorithm of TRIFIND one can find the neighboring three points (as depicted by black dots, corresponds to node number 1989, 2084, 1985). Then use the NODETAB algorithm to find the neighbouring points for 1989, 2084, 1985 by neglecting the duplicate node numbers as shown in Fig. 3.12b. The NODETAB algorithm is repeated for 5 times to find the group of nodes surrounding the point J and eliminate the duplicate node numbers in the array that contains group of neighboring nodes for point J. From this group, one can select the required number of nodes (sub domain) which are required for MLS method.

3.12. VALIDATION

3.12.1. General

In this chapter, a basic validation exercise has been presented to test various aspects of 2-D structured mesh simulation algorithm. The subsequent chapters explore various aspects of modelling and application of nonlinear wave simulation.

3.12.2. Steep Standing Waves in a Container

Initially, the efficacy of the velocity calculation methods such as GP and CS for the simulation of 2-D nonlinear waves is studied by considering structured mesh. The generation of standing waves in a container, for which analytical and numerical solutions

are available from Wu and Eatock Taylor (1994), has been considered. Let $L= 2h$, where L is the length of the tank and h is the water depth. The initial water surface elevation is assumed as

$$\eta_i = \frac{H}{2} \cos\left(\frac{2\pi}{\lambda} x_i\right) \quad (3.41)$$

where, H is the wave height, λ is the wave length and i is the free surface node index. From the given free surface profile, the wave propagation is initiated by no flow boundary conditions on the sidewalls of an impervious container and the propagation is governed by Eqn. (3.41). A comparison of the simulated free surface profile with results based on CS, GP and the second-order analytical solution for $H/\lambda = 0.05$ and 0.1 are shown in Fig. 3.13 and Fig. 3.14, respectively. The number of nodes used for both (CS and GP) simulations in the horizontal and vertical directions are 65 and 17, respectively. The time step of 0.06s is adopted which leads to a Courant number of 0.44. In these simulation, no smoothing was found necessary for applying the CS approximation on the free surface. However, Wu and Eatock Taylor (1994) stated the need for smoothing in the GP method. The CPU time required for the CS simulation by evaluating only the free surface velocity is 0.8750s per time step, whereas, for evaluating velocity at all the grid nodes, it is 1.2188s per time step, and in the case of GP method this was 1.8438s per time step. These simulations were carried out on a Pentium IV with 2.8GHz processor. Thus, the CS methodology is computationally inexpensive compared to GP method of velocity calculation.

3.12.2 Error Analysis

An approximation in a modeling system can be assessed by examining the energy loss. To quantitatively examine the energy conservation, a relative error analysis has been

carried out. A comparison has been made between the CS method, the results of Westhuis (2001) , the GP method and the analytical approach.

The simulation was performed using the initial condition defined by Eqn. (3.41) for a steepness of 0.033 with the number of nodes in the x and z directions being 31 and 11, respectively.

The total energy in the system is estimated from,

$$E(t) = \int_0^L \int_{-h}^{\eta} \frac{1}{2} \|\nabla \Phi\|^2 dz dx + \int_0^L \frac{1}{2} (h + \eta)^2 dx \quad (3.42)$$

The relative energy error (δE_t) for this simulation has been calculated using

$$\delta E_t = \frac{E(t) - E(0)}{E(0) - e_0} \quad (3.43)$$

where, $E(t)$ is the total discrete energy at any time t , $E(0)$ is the initial discrete energy in the container. The first term in Eqn. (3.42) is the absolute of convective inertia term and e_0 is the total potential energy in the system when $\eta_i = 0$.

The second-order analytical solution of wave time history for the standing wave problem has been derived for the more general case that leads to the first and second order potential and the surface elevation at each time step in the entire domain. The derivation is given in Appendix B. The total energy is evaluated using Eqn. (3.42) and the integration is carried out numerically. A comparison between the CS simulation and the analytical solution for the wave profile at the center of the container is shown in Fig. 3.15.

The relative energy error (δE_t) for the simulation using the GP method is presented in Fig. 3.16. The average relative energy error is of the order of 2.8×10^{-3} . The comparison of relative energy error using the CS simulation with the results of Westhuis (2001) and

second order analytical solution is depicted in Fig. 3.17. It is clearly seen that the relative error is of the same order as that of analytical results. Thus, it can be inferred that the GP method leads to relatively higher energy loss due to relatively inaccurate calculation of velocity (leading to some high frequency waves) and mesh instability. The CS method has an average relative energy error of an order of 1×10^{-3} .

Subsequently, the relative energy loss $[\nabla E_t]$ with respect to the energy calculated from the second order analytical solution has been derived using

$$\nabla E_t = \frac{E(t) - E_2(t)}{E_2(t)} \quad (3.44)$$

where, $E_2(t)$ is the second order energy at any time t ,

Typical comparison of the relative energy loss obtained from Westhuis (2001) and GP method with the CS method are shown in Figs. 3.18a and 3.18b. It should be mentioned that the digitized result of Westhuis (2001) shown in the Fig. 3.17 has been used for evaluating $E(t)$ to estimate the relative energy loss ∇E_t . From the results, the energy loss in the CS method is found to be of an order less than the other methods. The error is found to accumulate with an increase in simulation time in all the methods. It should be mentioned here that in all the simulations, mesh is regenerated at every time step based on the simple mesh generation technique suggested by Wu and Eatock Taylor (1994), without checking the mesh properties like skewness, aspect ratio. The results given by Sudharsen *et al.* (2004) based on GP method using mesh moving method is only for the short simulation time. The behavior of the GP method when one takes care of the mesh structure is discussed in the next chapter.

3.13. SUMMARY

In this chapter, an in-depth explanation of the numerical modeling developed under the present study has been presented. The basic assumptions and boundary conditions for the simulation of nonlinear free surface waves are presented. The finite element formulation and the different velocity calculation techniques along with the proposed cubic spline approach are discussed in detail. The implementation issues for the unstructured mesh have been dealt with the different mesh moving algorithms. Different algorithms that are implemented in the present context for handling unstructured mesh have been explained in detail. Finally, the developed numerical model is validated for the free sloshing problem and an error analysis has been carried out.

Table 3.1 Node Connectivity Table.

Node	J	Neighbouring Nodes					
1989	7	1940	1942	1901	2008	2004	1985
1985	5	1940	1989	2004	1986	0	0

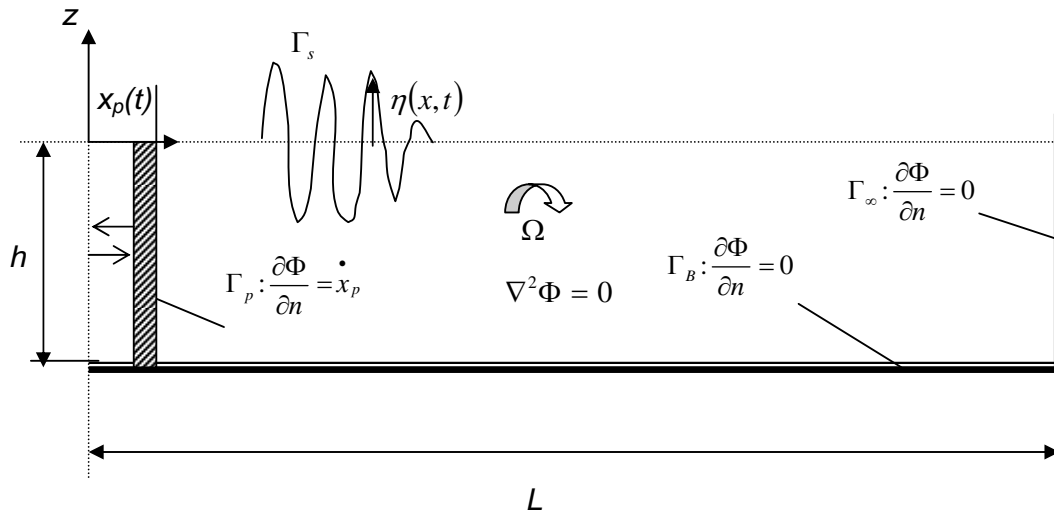


Fig. 3.1 Computational Domain with Specified Boundaries

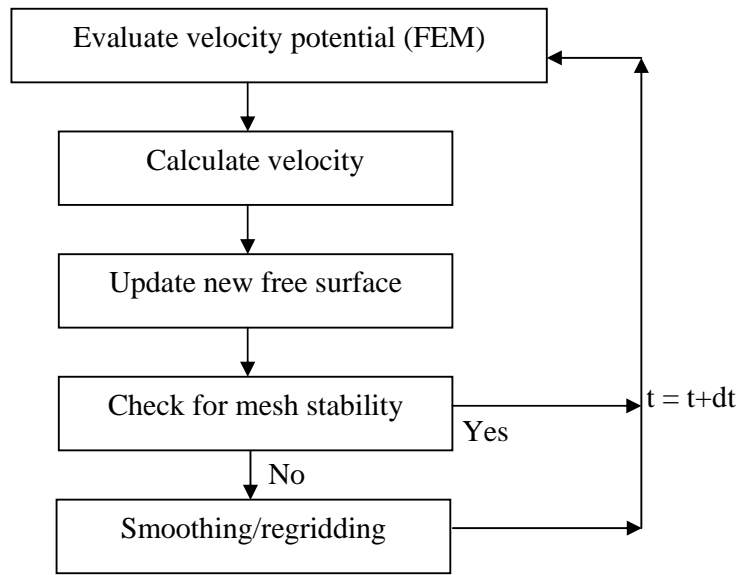


Fig. 3.2 General Procedure for the Wave Simulation

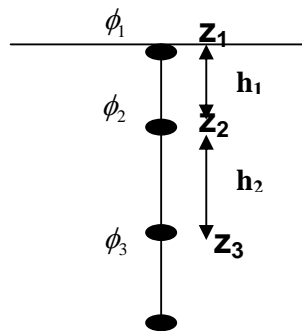


Fig. 3.3 Node Configuration for Calculating Vertical Velocity

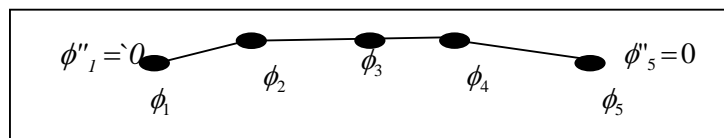


Fig. 3.4 Cubic Spline Approximation using Five Nodes

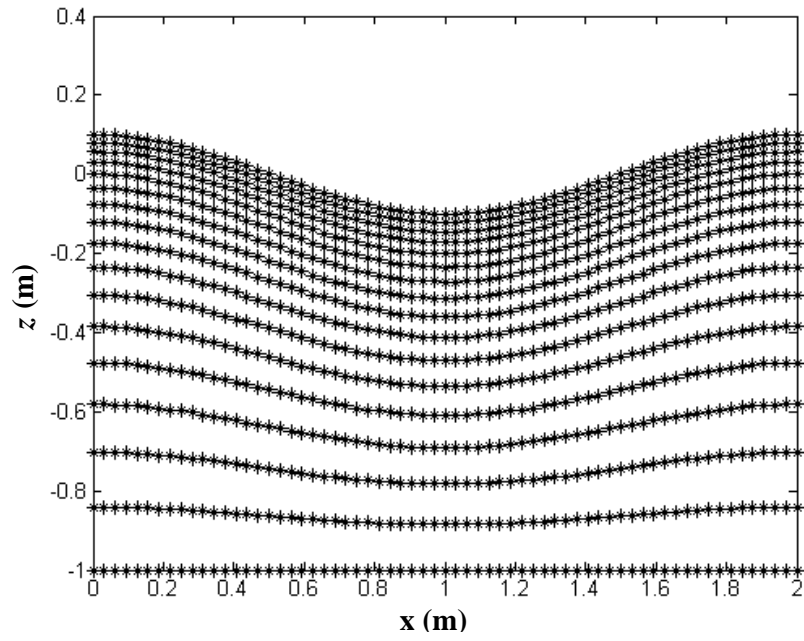


Fig. 3.5 Typical Nodal Variation for a Cosine Free Surface Elevation

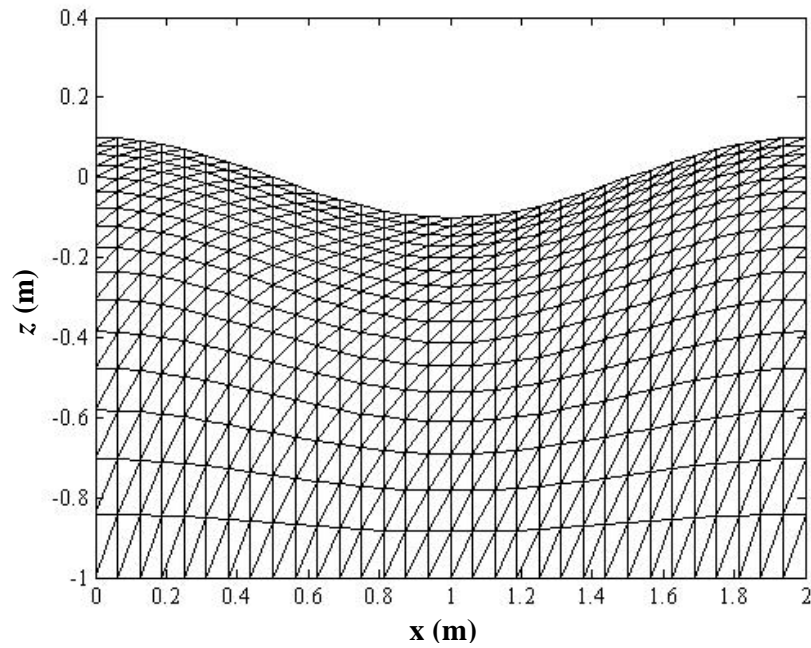


Fig. 3.6 Typical Mesh Structure using Linear 3-Noded Triangular Element

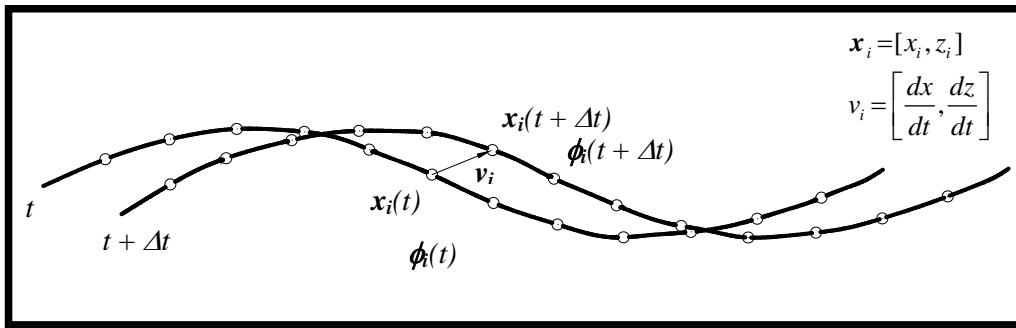


Fig. 3.7 Time Updating Procedure

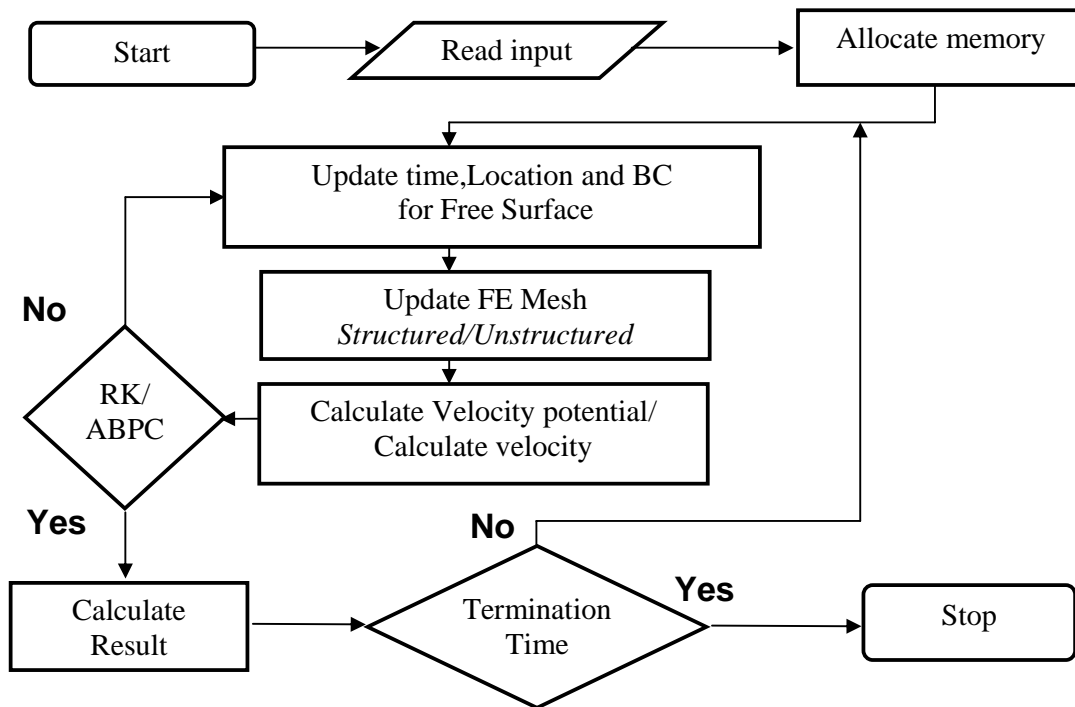


Fig. 3.8 Flow Chart of the Simulation

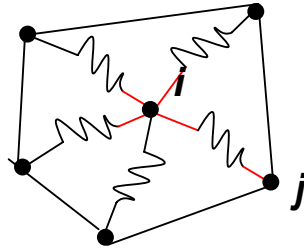


Fig. 3.9 Physical Interpretation of Springs Connected to 'i'th node to its neighbours such as 'j'

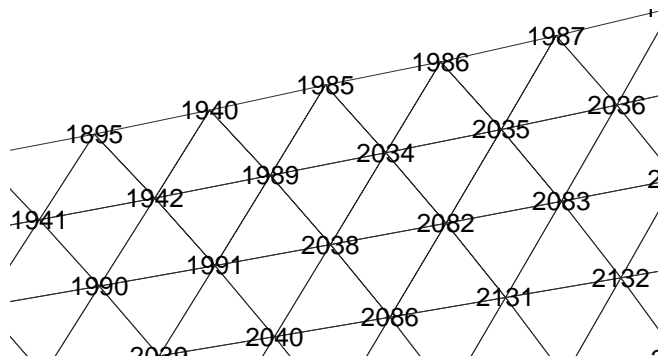


Fig. 3.10 Mesh with Node Numbering

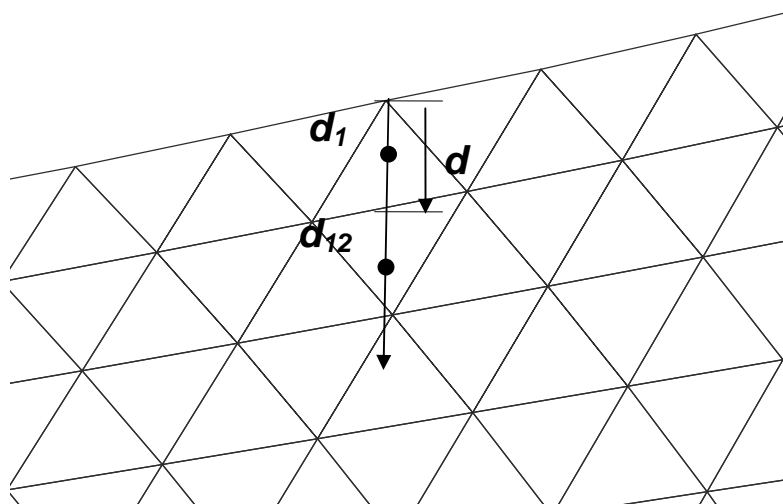


Fig. 3.11 Physical Interpretation to Calculate Vertical Velocity

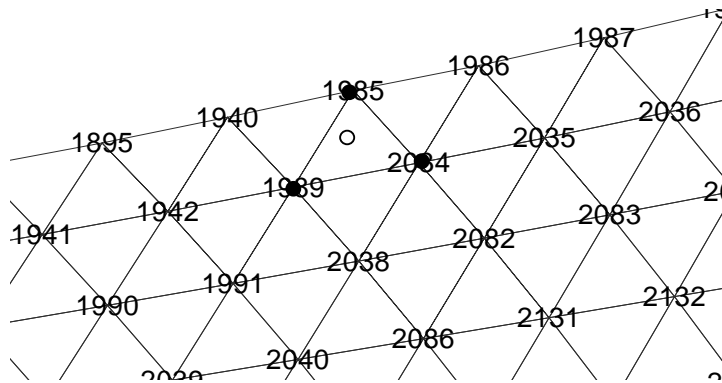


Fig. 3.12a TRIFIND

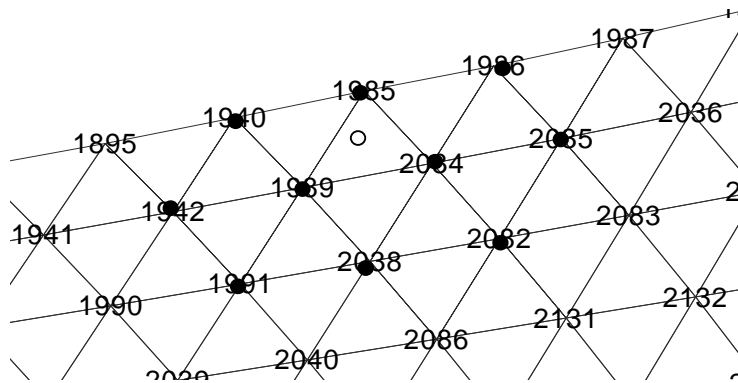


Fig. 3.12b Using NODETAB (1st Loop)

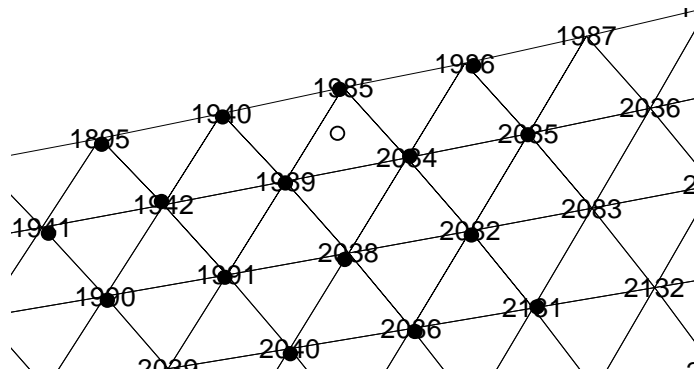


Fig. 3.12c NODETAB (2nd Loop)

Fig. 3.12 Physical Representation to Find the Group of Nodes

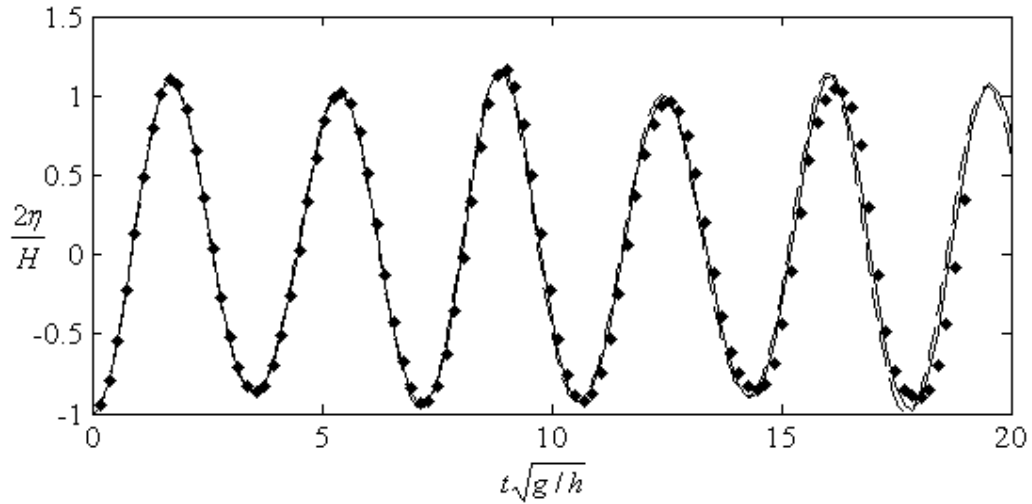


Fig. 3.13 Time History of the Free Surface Profile at the Center of the Container for a Wave Steepness, $H/\lambda = 0.05$ [----Analytical (upto 2nd order); ♦♦♦ GP; — CS]

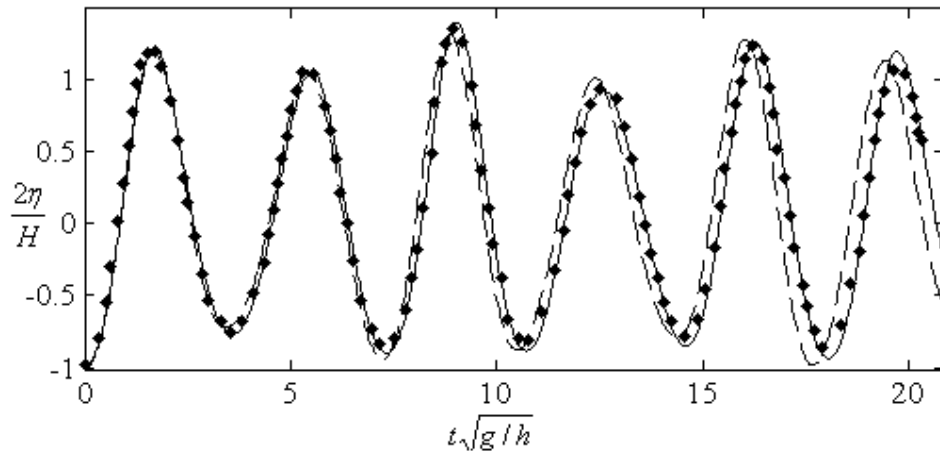


Fig. 3.14 Time History of the Free Surface Profile at the Center of the Container for a Wave Steepness, $H/\lambda = 0.1$ [----- Analytical (upto 2nd order) ; ♦♦♦ GP; — CS]

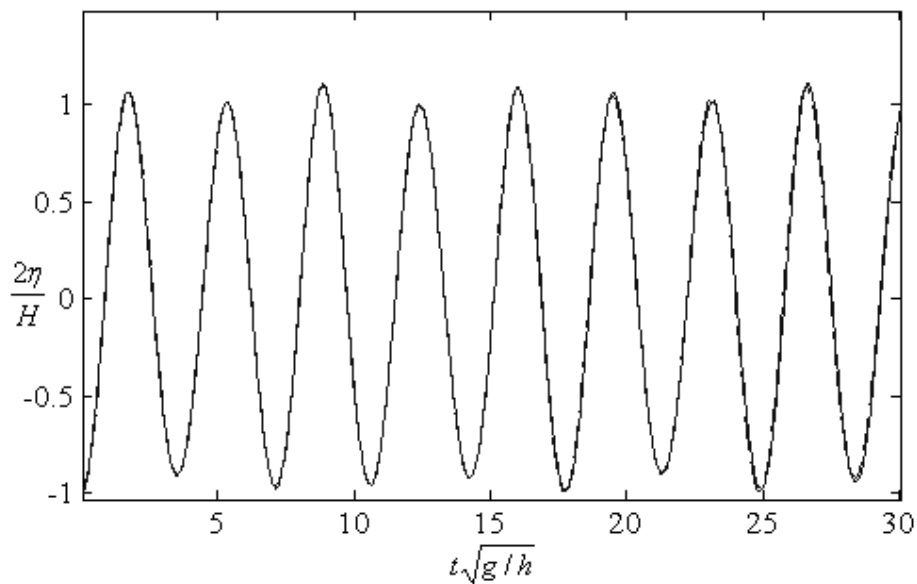


Fig. 3.15 Time History of the Free Surface Profile at the Center of the Container for a Wave Steepness $H/\lambda = 0.033$ [---- Analytical (upto 2nd order); — CS]

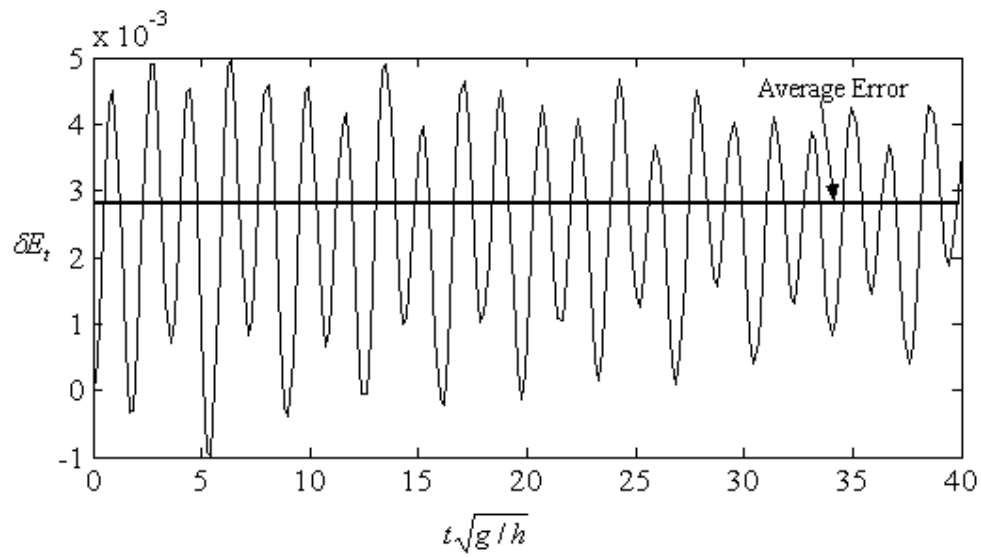


Fig. 3.16 Relative Energy Error (δE_t) while using GP Method

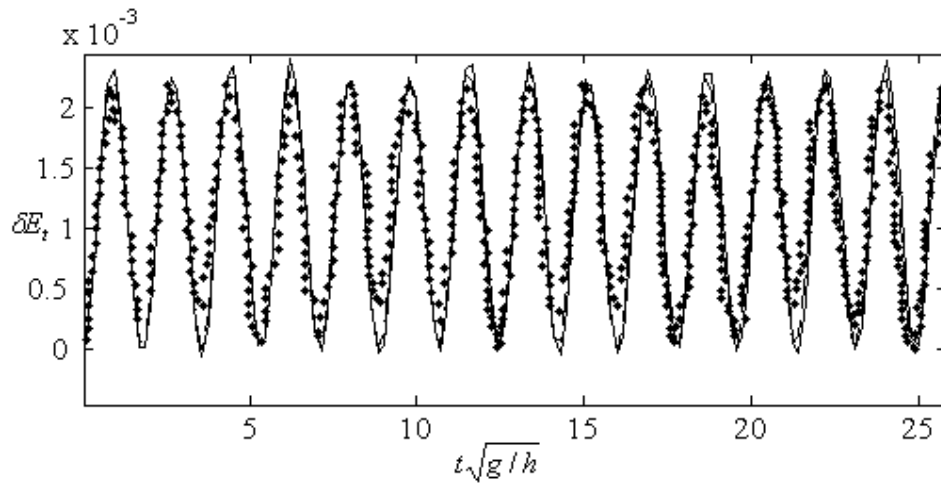


Fig. 3.17 Comparison of Relative Energy Error (δE_t) [----- Analytical Solution (upto 2nd order); ♦♦♦ Westhuis (2001); — CS]

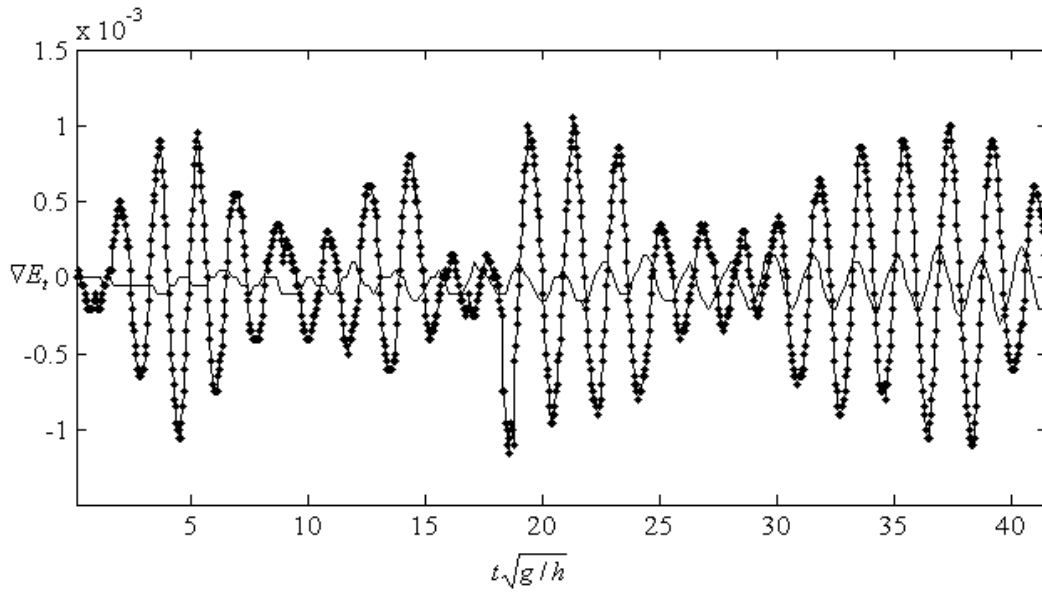


Fig. 3.18a Relative Energy Loss (∇E_t) with respect to Second order Analytical Solution [\blacklozenge - \blacklozenge - \blacklozenge Westhuis (2001); — CS]

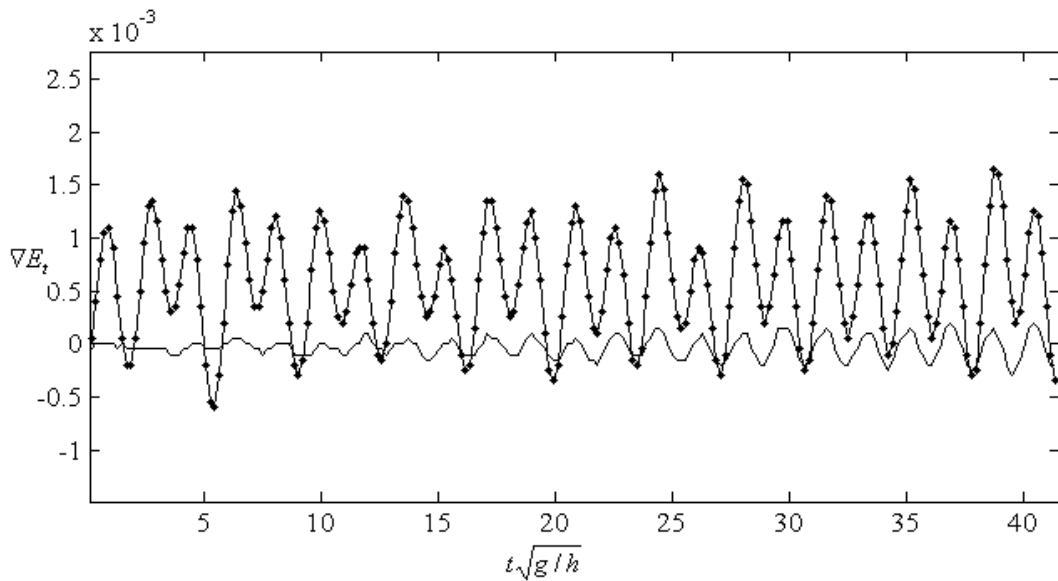


Fig. 3.18b Relative Energy Loss (∇E_t) with respect to Second order Analytical Solution [\blacklozenge - \blacklozenge - \blacklozenge GP; — CS]

CHAPTER 4

NUMERICAL WAVE TANK SIMULATION

4.1. GENERAL

The simulation based on FEM has the advantages of extending the code easily to viscous flow and to three-dimensional (3D) tank with complex geometry. While adopting FEM, the derivatives are usually found from differentiating the shape function, which is the direct differentiation of the velocity potential. The approximation of velocity field thus obtained is inferior to the approximation of the velocity potential. In time-dependent problems, this plays an important role. Thus, researchers have been focusing on obtaining the derivatives through different methods such as GP, MFD and LS method. The proposed method based on CS is also studied. The present chapter shows a detailed review of these methods for calculating the derivatives including the advantages and disadvantages in the context of simulation of nonlinear free surface waves using structured/unstructured FEM.

4.2. SIMULATION USING WAVE PADDLE: STRUCTURED MESH

4.2.1 General

The advantage of using the Finite Element method compared to the Boundary Element method is that even sudden startup of the wave paddle is possible. For simulation of regular waves, one end of the tank is considered to be a ‘piston’ type wave paddle. The paddle displacement, $x_p(t)$ is given by,

$$x_p(t) = -\frac{S}{2} \cos(\sigma t) \quad (4.1)$$

and the velocity of the paddle is,

$$\dot{x}_p(t) = \sigma \frac{S}{2} \sin(\sigma t) \quad (4.2)$$

where, ‘ S ’ is the maximum stroke of the wave paddle and σ is the angular wave frequency. It is well known that when the wave steepness is very small, the waves follow linear wave theory. Hence, a comparison between the nonlinear and linear wave simulation has been carried out. For simulating the linear waves, the free surface boundary condition [Eqn. (3.6) and Eqn. (3.7)] has been linearised. A comparison between linear and nonlinear wave simulation for very small steepness of 0.0036, considering the stroke length, $S = 0.002h$ and $\sigma = \sqrt{g/h}$, is shown in Fig. 4.1. It can be seen that the influence of the nonlinear terms is negligible. Considering, $S = 0.2h$ and $\sigma = \sqrt{g/h}$, a wave with a steepness of 0.046 can be generated. A comparison of simulation with and without the nonlinear free surface terms is shown in Fig. 4.2. The nonlinear characteristics of the wave, i.e., steep crest and shallow trough, are clearly visible. A comparison of the simulation using the present methodology with that of Wu and Eatock Taylor (1995) is shown in Fig. 4.3. The number of nodes used in the present simulation is 236 and 13 along the x and y directions, respectively. Wu and Eatock Taylor (1995) adopted 1320 nodes along the x direction and 32 nodes along the y direction for their study.

4.2.2. Mesh Independent Study

Mesh convergence criteria can be deduced for fully nonlinear waves by superimposing the wave time history at a fixed location for different meshes with an increase in the

number of nodes on the free surface. Such a convergence study has been carried out for the wave generation problem with a steepness of 0.046. The mesh convergence is examined with the number of free surface nodes taken as 117, 194, 235 and 309, which correspond to 15, 25, 30 and 40 nodes per wavelength. The free surface elevation is presented in Fig. 4.4a. It can be observed that the profiles obtained using 25 and 30 nodes per wavelength tends to converge. Hence, it may be said that a mesh independent solution could be obtained for mesh with above 25 nodes per wavelength. Similarly for the temporal resolution, a mesh independent solution has been carried out for time steps of $T/15$, $T/30$, $T/40$ and $T/50$. It is observed from Fig. 4.4b that the mesh tends to converge for time steps greater than $T/40$. The maximum and minimum Courant numbers adopted for the above simulation are 0.4 and 0.007 respectively.

4.2.3. Simulation of Medium Steep Waves

Four different velocity calculation methods, discussed in the previous chapter were used to simulate a regular wave of steepness (H/λ) 0.03 in a tank of length 40m. The water depth is 1m. The number of nodes used in the horizontal and vertical directions is 416 (corresponding to 30 nodes per wavelength) and 13, respectively. The stroke of the wave paddle is 0.025m and the circular wave frequency is $1.45\sqrt{g/h}$. No smoothing/regridding strategy has been adopted for the simulation while using the CS, LS and MFD methodologies. The need for smoothing/regridding in the context of the simulation of nonlinear waves is discussed in the next section. The free surface profile at 20s along the length of the tank using the three different methodologies (CS, LS, MFD) are shown in Fig. 4.5. It is observed that the simulation breaks down at 3.16s while adopting GP method. Hence, the smoothing and regridding were done after 10 time steps by increasing

the number of nodes in horizontal direction to 1101 and in vertical direction to 21. Even after adopting smoothing and regridding, the simulation is observed to break down at 10.4s. Due to frequent smoothing and regridding, a small damping in amplitude has been noticed. The time series at 12m from the wave paddle is depicted in Fig. 4.6. The dark black line shows the break down of the simulation using GP method. In the same figure, an excellent agreement between the other three methods namely, CS, LS and MFD schemes can be noticed. The time taken to run the entire computation using CS was 4.939 min, whereas, LS method took 5.0859 min and MFD took 5.0760 min. The simulation was carried out in Pentium(R) CPU 3 GHz. with 1 GB of RAM.

4.2.4. Simulation of Steep Waves

In this section, simulation of steep waves is discussed. The stroke of the wave paddle was increased to 0.0415m, so as to produce a steepness of 0.05 keeping the remaining parameters same as mentioned in the previous section. The free surface elevation near the wave paddle is shown in Fig. 4.7. It is clearly seen that the simulation carried out using LS and MFD methods shows higher amplitude than the given input near 17 to 20s, whereas, CS method does not exhibit this property. The reason is that the x -coordinate of the first node at the free surface is set to the position of wave paddle and the horizontal gap to the near by node increases with an increase in time due to the Lagrangian motion characteristics. Hence, in the case of nonlinear waves, as the steepness increases, due to mass transport, the node movement quickly leads to instability of the mesh. This phenomenon is shown by considering a snap shot of the node locations near the wave paddle during initial period (Fig. 4.8a) and after certain time steps (Fig. 4.8b). The figure shows an increase in nodal spacing near the wave paddle. This is a common phenomenon

encountered near the paddle during the generation of highly nonlinear waves. Hence, the calculation of velocity (by LS or MFD) leads to inaccurate free surface estimation, whereas, the CS method fits a curve through these nodes to estimate the velocity which overcomes the difficulties that are faced by the other methods. To avoid the instability posed by other methods, the number of nodes has to be increased in the entire domain. Another possibility, as suggested by Steinhagen (2001), is the dynamic inclusion of the new nodes whenever the spacing is greater than twice the initial grid spacing. The new node values such as velocity potential and velocities are evaluated using linear interpolation based on the neighbouring node details. Physically, this is correct in the linear approximation but it again leads to instability near the wave paddle. Hence, a local smoothing scheme is suggested. Instead of this technique, in the present study, the initial number of nodes is increased. If the number of nodes is more, collision of nodes takes place and hence the mesh has to be regridded/ smoothed after certain time steps. Consequently, the energy loss accumulates. This also should be taken care while considering the increase of number of nodes in horizontal direction. Thus, the simulation was repeated considering the number of nodes in the horizontal direction as 825 (corresponding to 60 nodes per wavelength) while using LS and MFD methods. In usual practice, the regridding is not highly sensitive and depends on the frequency of the waves. However, for the present case, this is not required. In general, for the simulation of steep nonlinear waves, regridding can be adopted at every 20 to 70 time steps depending upon the wave frequency. After increasing the number of nodes, the simulation was successful as depicted in Fig. 4.9. The simulation was later carried out by increasing the stroke of the wave paddle to 0.0572m such that the generated wave has a steepness of about 0.07. For this test case, the mesh was regridded at every 50 time steps

in all the methodologies. The time history at 12m from the wave paddle is shown in Fig. 4.10 for three velocity calculation methods. The LS and MFD methods yielded exactly same results, whereas, CS method shows a phase shift due to the fact that as the wave steepness increases, the CS method based on the neighboring x-coordinates along the free surface predicts a very smoothed first derivatives, leading to loss of information (filtered high frequency components in steep nonlinear waves).

The GP method for the above two cases, breaks down after 10s. Considering the computational aspect of the simulation for this case, the MFD took 26.7318 min., whereas, LS method and CS method took 26.6659 min. and 26.1508 min., respectively. This clearly shows that all the three methods require similar computational performances.

4.2.5. Simulation of Solitary Waves

The comparison of the different velocity calculation techniques for the simulation of solitary waves is carried out. The solitary wave is generated by using the wave paddle motion given by Goring (1979), as detailed in Appendix C, with the suitable modification suggested by Grilli and Svendsen (1990) to truncate the initial motion of the infinitely long solitary waves. First, the simulation is carried out for a small steep wave of 0.1. The steepness in the case of shallow water waves is defined as H/h . The length of the tank is 10m with a water depth of 0.3m. The number of nodes considered is 301 and 13 along the horizontal and vertical directions, respectively. No smoothing/regridding has been applied. The simulation has been carried out over 20s, which means that the wave reflected from the vertical wall and gets re-reflected from the wave paddle. This is clearly depicted in Fig. 4.11 which shows three profiles recorded at the centre of the tank (5m). All the three methodologies are in excellent agreement. The simulation was then carried

out for a solitary wave with steepness of 0.6 maintaining all other parameters same. The simulation was carried out only for 5s. The comparison is shown in Fig. 4.12, which reveals that LS and MFD methods are in excellent agreement, whereas, a phase shift and a reduction in amplitude are clearly visible for CS method.

4.3. COMPARISON WITH EXPERIMENTAL MEASUREMENTS

4.3.1. Wave Focusing

In order to understand the damping mechanism in the velocity calculation methodologies, the simulation has been carried out for a long time. For validation of such simulation, experimental measurements form the basis for comparison. The various methodologies are compared with the experimental results (Clauss and Steinhagen, 1999) for a long time wave simulation. The length of the tank was 200 m and water depth was 4 m in the experimental setup. The wave paddle motion with a sampling interval of 0.05s is given in Fig. 4.13a. The duration of the simulation is 120 s. For the numerical modeling, the number of nodes in the horizontal and vertical directions is taken as 501 and 21, respectively. The time step adopted is 0.05 s. The corresponding free surface elevation at different locations along the tank is shown in Fig. 4.13b. It shows a satisfactory agreement between different methodologies with the experimental measurements. The focusing point of the transient wave at a very long distance (126.21 m) is also well predicted by CS, whereas, LS and MFD methods show a phase delay of 0.2s.

4.3.2. Cnoidal Waves

The long time simulation of shallow water waves such as cnoidal wave has been attempted using different velocity calculation methodologies. The experimental setup of

Jeong (2003) has been considered for validating the numerical simulation. The length of the tank was 300 m and water depth was 4 m in the experimental setup. The wave paddle motion with a sampling interval of 0.05s is given in Fig. 4.14a. The duration of the simulation is 100 s. For the numerical modeling, the number of nodes in the horizontal and vertical directions is taken as 801 and 21, respectively. The time step adopted is 0.01 s. The corresponding free surface elevation at different locations along the tank is shown in Fig. 4.14b. Since, the three methodologies produced identical results; only simulation from CS approach is plotted. An excellent agreement with the experimental measurements even after a long distance can be seen. The numerical results of Jeong (2003) using the finite volume method are superposed in the above figure which exhibit a phase difference compared with the present numerical results. The velocity vector plot at a particular time step along the length of the tank shown in Fig. 4.15 demonstrates a return flow under the trough. These velocity vector plots are obtained by solving Eqn. (3.19b) from the known velocities at the free surface (CS), side walls and the bottom boundary condition at particular time steps.

To proceed further with the topic of unstructured mesh, the analysis based on time integration using RK and ABPC has been made. The above said simulation has been re-executed using ABPC and the relative error is calculated with respect to the experimental measurements for ABPC, RK and Jeong (2003) numerical results. The relative error is calculated based on the formula similar to the standing wave problem as,

$$\delta E = \frac{\|\eta - \eta_e\|}{\|\eta_e\|},$$

$$\|\eta\| = \int_0^t \eta^2 dt \tag{4.3}$$

where, η_e is the free surface elevation of the experimental measurements. The relative errors are estimated for the simulated free surface profile (Fig. 4.14b) and are depicted in Fig. 4.16. It shows that the relative error for RK and ABM is of the same order, whereas, the results of Jeong (2003) exhibit a higher relative error.

4.3.3. Solitary Waves

The simulation of solitary waves by prescribing the ‘piston’ wave paddle motion is determined from the first order Boussinesq wave theory used by Goring (1979). An excellent agreement between simulated solitary waves using the present method with that of experimental measurements of Yim *et al.* (2004) has been observed as shown in Fig. 4.17. The target wave height is 0.24m in a water depth of 0.8m. This scenario is reproduced in the numerical model with 301 nodes in the horizontal direction and 13 nodes in the vertical direction with a time step of 0.01s assuming the length of the tank as 40m. The comparison of wave simulation at 15.7m from the wave board has been made with the laboratory measurements.

Experimental study

In the present study, an experimental investigation was carried out in a 30m long, 2m wide wave flume in the Department of Ocean Engineering, IIT Madras. The wave flume has a wave paddle at one end and an artificial rubble mound beach is provided at other end of the flume to absorb the generated waves. The piston type wave paddle is capable of generating regular, random, cnoidal and solitary waves. The desired wave characteristic was given to the wave paddle through a personal computer and the same computer was used to acquire the signals from the wave gauges through an amplifier.

Three conductive type wave gauges were used to measure the wave surface elevation at different locations (3m, 8m and 9m from the wave paddle) along the length of the wave flume. The wave probes were pre-calibrated by immersing in the water for a known depth and measuring the corresponding voltage variation. A constant water depth (h) of 0.8m was maintained in the present study. The solitary waves with different height (H) were generated covering the wave steepness (H/h) ranging from 0.025 to 0.1. The adopted wave characteristics are shown in Table 4.1. The surface elevations measured at the three locations were simultaneously acquired at a sampling rate of 0.01s. A typical comparison of the present laboratory simulated solitary wave in the wave flume with the numerical prediction is shown in Fig. 4.18. It is observed that the initial elevation of the solitary wave profile starts below the still water level and the numerical simulation over predicts at the peak. The reasons for the above discrepancies are explained below.

Initial paddle pullback

When the driving signal activates the wave paddle to generate a solitary wave, initially the paddle pulls back from its initial vertical position. This takes about 20 to 50 seconds depending on the target wave characteristics. The above stated pull back of the wave paddle results in the lowering of water depth in its vicinity followed by the generation of the trough portion of the solitary wave in the wave flume. The trough depth is about 0.0038m (for $H/h=0.1$) during the start of wave generation, whereas in the numerical simulation, the paddle motion is only towards the forward direction and, hence there are no negative elevations. To overcome the discrepancies faced in the laboratory tests, the initial water depth is approximated in NWT to match the average depth measured in the flume right after pullback of the wave paddle from its vertical position, which is smaller than the initial depth. The numerical simulation has been carried out by applying the

water depth corrections as measured in the flume and the comparison is found to be in good agreement for the wave steepness (H/h) of 0.1 and 0.075 as can be seen in Fig. 4.19 and Fig. 4.20, respectively.

Other sources of discrepancies

The NWT calculations are based on the assumption of an inviscid fluid and the flow as irrotational and therefore, do not include any internal dissipation or friction losses. A reduction in wave height in the flume, however, could also occur because of side walls and bottom friction. Such effects should be relatively more significant for long waves like solitary waves, for which horizontal particle velocities remain large down to the bottom. Further, the viscous damping plays a dominant role in the interaction of solitary waves with structures (Grilli *et al.* 2004). However, in the present laboratory simulation, there was no structure obstructing the propagation of the solitary waves and hence, the decrease in the wave elevation in the experimental simulation might not be due to the viscous damping effects.

Comparison of solitary wave speed

The theoretical speed (Celerity) of the soliton is given by Boussinesq (1871) as $C_{Bou} = \sqrt{g(h+H)}$. The average wave speed obtained from the experimental and numerical simulations are normalized with the Boussinesq's wave speed and are presented as a function of H/h in Fig. 4.21. It is observed that the experimental wave speed decreases with an increase in H/h . While, the numerically predicted wave speed increases with H/h , the reduction in wave height as observed in experiments is the cause for the reduction in the wave speed.

4.4. QUANTITATIVE COMPARISON

4.4.1. General

It has been found that both the LS and MFD methods produced identical results for a wide range of wave steepness. Hence in this section, the results based on CS and LS approach are compared with the experimental measurements and the phase differences are reported. Clauss and Steinhagen (1999) and Ma *et al.* (2001b) have made qualitative comparison between the laboratory generated and numerical simulated waves, but for the best of author's knowledge none revealed the phase difference quantitatively.

The comparison of the numerical simulation of breaking waves with that from physical measurements carried out by Dommermuth *et al.* (1988) exhibited a slight deviation which was claimed to be due to dissipation of wave energy in the laboratory. The phase difference can exist in numerical simulation due to two main reasons, one being the dissipation of the wave energy which results in the reduction of wave celerity and the other being due to the effect of surface tension that leads to an increase in the wave celerity during the laboratory generation. Jensen and Grue (2002) reported a detailed note on the phase differences between the numerical and experimental measurements of waves with very small slope. The phase difference analysis has been carried out for the measurements of wave packets using Fourier analysis, and a difference of 0.01 ± 0.006 rad per wavelength was reported between the numerical and physical measurements. The numerical simulation of Jensen and Grue (2002) was based on a linear formulation. Apart from this analysis, to the best of the author's knowledge, the comparison between the nonlinear wave simulation and the corresponding physical measurement has not been reported elsewhere. The analysis can be carried out in the frequency domain and the

Fourier analysis only give mean phase angle in the time series. However, the time-frequency evolution of the phase difference would give meaningful quantification. Schlurmann (2004) described the time-frequency methods (namely wavelet transformation and Hilbert transformation) in hydrology and hydraulic engineering. Balaji *et al.* (2007) applied time-frequency methods for the prediction of wave groups and breaking waves from a data buoy heave response time history. One of the most common tools for time- frequency space is the wavelet analysis. By decomposing a time series into the time-frequency space, one can determine the time evolution of the frequency components in the signal. The details of the wavelet analysis with reference to the practical implementation of the algorithms are given in Torrence and Compo (1997). It has been pointed out by Torrence and Compo (1997) in many studies that wavelet analysis have suffered from an apparent lack of quantitative results and highlighted the importance of statistical significance test. In order to examine the comparison between two (numerical and experimental) time series with large common power and to evaluate the phase relationship in time-frequency space, Cross Wavelet transformation (XWT) is adopted, which is constructed from two Continuous Wavelet Transform (CWT). Further, from Wavelet coherence (WTC) between the two CWT, one can find significant coherence even when the common power is low. A brief overview on wavelet transformations is provided in Appendix D. In this section, the analyses are reported both qualitatively and quantitatively for numerically simulated (by adopting CS and LS approach) and laboratory generated wave elevation time series.

4.4.2. Experimental Details

The experiments were also carried out in the wave Flume at Franzius-Institute, University of Hannover, Germany. The flume is 100m long, 2m wide and 4m deep. The water depth was adopted as 0.61m. The existing system of water circulation to cool the wave paddle to avoid friction between the wave paddle and the side walls was not working satisfactorily; thus necessitating the supply of water through an external pipe that leads to an increase in water level. An increase in the water level by about 2cm in the flume was noticed over a day and hence the measurement of water depth was carried out prior to every run. This plays a major role in the numerical simulation. Six numbers of wave probes were deployed in the wave flume at distances, 4.849m (WP1), 20.146m (WP2), 25.136m (WP3), 30.425m (WP4), 40.406m (WP5) and 50.609m (WP6) from the wave paddle. The distances were measured using laser distometer. The input to the numerical model is from the feedback signal of the wave paddle in the flume. The paddle motion, water depth and the location of the measurement of time histories for a particular run are important parameters in the experiments that are essential for comparing the results with numerical simulation. The generation of regular waves and cnoidal waves have been carried out in the flume. A view of the flume is shown in Fig. 4.22. Further, the generation of solitary waves was carried out in a glass flume, 24m long, 0.3m wide and 0.5m deep at University of Wuppertal, Germany. A water depth of 0.2145m for these studies was considered. This flume is equipped with a wave paddle driven by a digital motor to which signals can be provided with high precision. The view of the flume is shown in Fig. 4.23. The wave histories were recorded using Ultrasonic sensors at distances of 1.743m and 6.74m from the wave paddle. The PIV measurements of water particle velocities were carried out at 3.45m from the paddle using the high Speed CCD

camera having the resolution of 256 x256 pixels. The camera is placed at 1.45m (focus) from the center of the flume. The minimum focusing distance of the camera is 1m. The field of View (FOV) is 0.26 x 0.26m. The sampling interval for recording was 0.002s and for the analysis it was 0.004s, such that the mean of the particle in FOV to move at least one cell distance to avoid spurious velocities. The PIV setup is shown in Fig. 4.24.

4.4.3. Regular Waves

The experiments were carried out to generate a regular wave with a period of 1.92s, and two different wave heights, corresponding to wave steepness of 0.01 and 0.047. In the numerical modeling, the number of nodes used in the horizontal and vertical directions are 1101 and 17, respectively. For the case of CS approach, no regridding was applied, whereas, the regridding has been carried out for every 40 time steps while adopting LS approach. The time step used for the calculation is 0.02s. The numerical model setup is kept constant for all the wave simulations reported in this section, unless and otherwise quoted. The comparison of wave surface profile from the experimental measurement and the numerical simulation at various locations along the length of the tank for waves with a steepness of 0.01 (wave height of 0.04m) is shown in Fig. 4.25. The input paddle velocity has been obtained by differentiating the measured paddle displacement, which resulted in spurious noises in the signal as can be seen in Fig. 4.25a. The wave surface elevation at a distance of 4.849m, 25.136m and 50.609m are shown in Figs. 4.25b, c and d, respectively. An excellent comparison between the numerical simulation based on the CS and LS approaches and that from experimental measurements (EXP) can be seen. The wave spectra for the surface elevation near the paddle (WP1) and far away from the paddle (WP6) are depicted in Figs. 4.26a and b. The wavelet power spectra for the

experimental measurements at WP1 and WP6 are shown in Figs. 4.26c and d, respectively. The measured wave period is found to be close to 1.92s. Edge effects that might have influence the analysis is shown as a lighter shade (the values within this region are presumably reduced in magnitude due to zero padding). This edge effect is called as Cone of Influence (COI). The thick black contour designates the 95% confidence contours (energy concentration). In order to reveal the difference between the two time histories near to the paddle, the cross wavelet power and phase difference for EXP with CS and EXP with LS are shown in Figs. 4.27a and b, respectively. The arrows indicate the relative phase difference between the two time series: the arrows pointing to the right indicate the in-phase, whereas, the left arrows indicate out-of-phase. The arrows pointing downward indicate that the numerical simulation exhibits a phase shift of about 90° with respect to the experimental measurements. Within the 95% energy concentration, the simulated time series is in phase with the experimental observation. The quantitative mean phase angle in the XWT for EXP - CS is $-2.28^{\circ} \pm 1.571^{\circ}$ (\pm indicates error estimated using the circular standard deviation), whereas, for EXP - LS, it is $-2.49^{\circ} \pm 1.470^{\circ}$. The cross wavelet shows the existence of high common power between the two time series and, in order to reveal the phase lock behaviour, the wavelet coherent transform (WTC) is used. The squared wavelet coherent transform for EXP - CS and EXP - LS are shown in Figs. 4.27c and d, respectively. The area of the 95% confidence contour is large compared to the cross wavelet power, which shows the intensity of covariance irrespective of high common power. Significant wavelet coherence is found to exist for the wave period less than 1s. In the region of primary frequency, the time series are in-phase as indicated by arrows and scattered elsewhere. The mean phase angle for squared WTC of EXP - CS and EXP - LS are $-1.82^{\circ} \pm 39.73^{\circ}$ and $-1.36^{\circ} \pm 37.08^{\circ}$,

respectively. Similar kind of wavelet analysis has been carried out for all the time series of this simulation and only the quantitative results are depicted in Table 4.2.

The numerical and experimental measurements for a wave of height 0.2m along the various locations of the tank are shown in Fig. 4.28. This simulation corresponds to a steepness of 0.047. When the distance from the wave paddle increases, the CS approach shows a slight phase shift even though, the wave height is maintained constant. Qualitative wavelet analysis has been reported for the two time series for this case, one near to the paddle and the other far away from the paddle. The power spectra from Fourier analysis for the wave surface elevation time histories at 4.895m shows the concentration of energy at 0.52Hz and 1.05Hz, due to the existence of nonlinearity (Fig. 4.29a). The wavelet power spectrum for the experimental measurement is also shown in Fig. 4.29b. The XWT for EXP - CS and EXP - LS are shown in Figs. 4.29c and d, respectively. For a medium steep wave, the time series of EXP - CS is in-phase at the primary period of 1.92s, whereas, a positive phase difference at the secondary mode is observed. In the case of EXP - LS, the waves are found to be in-phase within the 95% confidence contours. The squared WTC also reveals a similar behavior as shown in Figs. 4.29e and f. The XWT mean phase angle is $-4.95^{\circ} \pm 15.24^{\circ}$ and $-4.79^{\circ} \pm 2.678^{\circ}$ for EXP - CS and EXP - LS, respectively. A larger error for the CS approach has been noted compared to LS approach. The power spectra from Fourier analysis, CWT for experimental data, XWT and squared WTC for the time histories far away from the paddle are reported in Fig. 4.30. The wave surface elevation simulated with CS approach is found to advance compared to the measured wave surface elevation towards the direction of propagation. For the CS approach, this is noticed in the wavelet results both for primary as well as for secondary mode, whereas, such a difference is noticed only in

secondary mode while adopting the LS approach. The quantitative results of this case for all the time series are presented in Table 4.3. The phase shift is found to be increased for CS approach compared to that for LS approach. This shows that CS approach is unable to capture the low period waves due to smooth fitting for the velocity estimation. Moreover, the phase angle is not a constant over the length of the tank which may be due to the uncertainty in the location of wave probes along the flume for the measurement of the wave time history. Probable reason for the small deviation in the lower period may be due to the fact that the input signal (paddle displacement) obtained from the paddle for the low period must have been polluted by the noisy signal when one differentiate to obtain the paddle velocity.

4.4.4. Cnoidal Waves

The nonlinearity in a shallow water wave is relatively difficult to model and is of practical relevance compared to the regular waves of higher order propagating near the coast. Hence, an attempt has been made to understand the performance of the present numerical code for the simulation of shallow water waves such as cnoidal and solitary waves. In this section, cnoidal wave simulation is discussed and in the next section, the aspects of simulation of solitary waves are deliberated. cnoidal waves of different characteristics were generated in the laboratory with Ursell parameter of 30, 307 and 41 referred to as CN1 ($H = 0.03\text{m}$, $T = 6.4\text{s}$), CN2 ($H = 0.3\text{m}$, $T = 6.4\text{s}$) and CN3 ($H = 0.2\text{m}$, $T = 3.2\text{s}$), respectively. The wave paddle signal is generated from the cnoidal wave theory and obviously the generated profile could not be stable during its propagation due to the dispersion of many of the frequency components. A more stable cnoidal wave form could be achieved by using the formulation of Goring (1979). Since the main objective of this

study is to investigate the physical and numerical aspects of nonlinear wave simulation, a simple approach of wave generation using cnoidal wave theory is sought. The input wave paddle velocity and the generated wave elevation at a distance of 4.84m, 25.136m and 50.609m from the wave paddle are depicted in Fig. 4.31. The simulated wave profile using the approaches of CS and LS is superposed on the same plots. An excellent agreement between both the numerical approaches with the measurements can be seen. The frequency spectrum of wave elevation at 50m (Fig. 4.32a) shows the peak period as 6.4s, however, the spectrum is found to be broad. The corresponding wavelet power spectrum for the measurement (Fig. 4.32b) shows that the 95% of energy is concentrated within the range of 1.5s to 8.5s, having a peak around 6.4s. The phase angle estimated using XWT (Figs. 4.32c and d) shows that in both the cases of CS and LS, the secondary mode (near 3s) shows a positive phase shift, whereas, the wave near the primary period is in-phase. The squared WTC is also shown in Figs. 4.31e and f and, the quantitative phase angle information inside the 95% energy levels is presented in Table 4.4 for all the simulated cnoidal profiles.

The measured wave elevation history for CN2 and the numerical simulation at various distances from the paddle are shown in Fig. 4.33. The comparison is found to be excellent. The measured and simulated frequency spectra for the wave elevation at 50.609m are superposed in Fig. 4.34a. The experimental CWT (Fig. 4.34b) shows a peak wave period of 6s and the energy spreads over a period varying between 0.5s and 8s. The XWT shown in Figs. 4.34c and d, reveal that the simulation with CS approach exhibits a phase lag except near the primary period, while, simulation using LS shows a lesser phase lag. However, the squared WTC (Figs. 4.34e and f) shows a larger significant

coherence for both the approaches of numerical simulation. The quantitative phase lag inside the 95% energy level is given in Table 4.5.

The measured wave elevation and its comparison with the simulation from the two numerical approaches for a wave period of 3.2s (CN3) are shown in Fig. 4.35. The Fourier spectrum and CWT for the measured wave elevation near the paddle are shown in Figs. 4.36a and b. The energy concentration occurs over a period ranging between 0.5s and 4s, with a peak at 3.2s. The analyses on XWT and WTC reveal similar observation as that for CN2. The mean phase angles in the 95% energy level for all the wave probes used in the laboratory investigation are reported in Table 4.6. For small wave steepness, the phase difference is found to be small, while for the medium wave steepness, the phase difference is larger for CS compared to that for LS approach.

4.4.5. Solitary Waves and PIV Measurements

The generation of solitary waves has been carried out at University of Wuppertal, Germany. The generation of solitary waves by prescribing the piston type wave paddle motion follows from the first order Boussinesq wave theory used by Goring (1979). The solitary waves were generated in the wave flume and the surface profile has been measured using ultrasonic probe at two locations. The experiments were carried out for wave steepness (H/h) between 0.1 and 0.4. The comparison of measured wave elevation with the numerical simulation (LS) is shown in Figs. 4.37 (a-d). A slightly broader wave profile can be seen in the numerical simulation compared to the measured wave surface elevation for waves with smaller steepness. The simulated peak magnitude is also found to be higher. For steeper waves, though the wave height remains the same, the width of the simulated solitons is wider. This is due to the difference in the displaced mass of the

water even though the paddle signal is same. The loss of volume of water is accounted for the water flowing backward to the paddle through the gap between the wave paddle and the side walls when the paddle is set into motion. As the width of the flume is small, this effect is more pronounced. The reason for the wave height remaining unchanged for the steeper waves is due to the fact that the paddle stroke is quite fast compared to smaller steepness. This feature has been captured using a high speed camera and the various snap shots of the water flowing through the gaps are shown in Fig. 4.38. One can minimize this effect by adjusting the input signal to generate the target wave height and profile using trial and error method. The input signal for the numerical model (i.e., the generated signal) and the signal given to the paddle (i.e., tuned signal) to generate a wave with specified characteristics are shown in Fig. 4.39 for $H/h = 0.1$. Since, the incident wave profile matches near the paddle and also a good comparison has been achieved at the second location, the wavelet analysis is not carried out. The comparison between the numerical simulation (CS and LS) and experimental measurements for waves with steepness ranging from 0.1 to 0.5 is shown in Fig. 4.40. The number of nodes in the horizontal and vertical direction used in the numerical modeling is 601 and 17, respectively. An interesting feature noted is discussed below.

After the propagation of the soliton, the oscillation is below the mean water surface (zero level), which once again proves that the water is flowing back through the side of the wave paddle after reaching the extreme position of the wave paddle. This eventually reduces the trailing waves that should be presented in the solitary wave generation. But, attempts are being made by several researchers for the minimization of trailing waves. For higher wave steepness, the numerically simulated trailing waves are different from the measurement. CS shows a phase difference for steepness above 0.4. In order to reveal

the water particle motion, due to which the phase difference exists, PIV measurements were carried out.

MATPIV developed by Sveen (2003) has been used for analysis. The comparison between the numerical simulation (LS and CS) and the experimental measurement for particle velocity at the crest is shown in Fig. 4.41. The CS simulated particle velocity is taken at the crest irrespective of the phase difference. It shows a good comparison for velocity magnitudes using LS with that of EXP. The CS shows lower velocity magnitude for H/h greater than 0.4. A snapshot of images from the CCD high speed camera at various stages before analysis is shown in Fig. 4.42. The spatial velocity information using PIV and numerical simulation (LS) for $H/h = 0.5$ is depicted in Fig. 4.43.

4.5. UNSTRUCTURED MESH

4.5.1. General

The analysis has been carried out to know the possibilities of the spring analogy methods in the context of highly nonlinear free surface waves. Two analogies, as discussed in the section 3.11, namely vertex and segment methods are used to simulate the nonlinear waves.

To use in segment spring method (Ma and Yan, 2006), $\chi = e^{\mu[2+(z_i+z_j)/2h]}$ is adopted, where, $\mu = 1.7$ and $\psi = -1.0$. Whereas, for vertex spring method (Sudarsen *et al.* 2001), $\chi = 2$ (boundary node), 1 (interior node) with $\psi = 0.1$ have been used in the Eqn. (3.38). The reason for not stiffening at the adjacent layers like in the segment method is that the basic principle of vertex method is a smoothing algorithm, so stiffening one layer is sufficient. If one needs to stiffen the adjacent layers too, the numerical coefficient used in segment

method needs to be changed. For the time integration in the case of unstructured mesh, ABPC is used in-order to reduce the computational time.

4.5.2. Comparison with Structured Mesh: Interpolation Techniques

The initial validation of the proposed methodologies is carried out by comparing with the structured code. The initial mesh is generated using GAMBIT commercial software. The simulation using shape function and moving least square (MLS) method when calculating vertical velocity has been first analysed for steep waves. The length of the numerical wave tank is 40m having a water depth of 1m and simulated steepness corresponds to 0.082. The wave profile at 15s along the length of the tank is shown in Fig. 4.44 for MLS and shape function estimation. Fig. 4.45a shows the wave surface elevation at 5m from the wave paddle. There is an over prediction of wave height by using the shape function interpolation. This is interpreted qualitatively from the zoomed in view of Fig. 4.45a as depicted in Fig. 4.45b. Hence for all the cases considered herein, the MLS method is being adopted.

4.5.3. Comparison with Structured Mesh: Mesh Moving Strategies

As pointed out in Chapter 2, the mesh moving strategies shows a conflicting report in the context of nonlinear free surface simulation. A comparison between the two different spring analogies, namely, vertex and segment spring are carried out in this section. To carry out this investigation, the input to the wave paddle is kept same as mentioned in above sub-section. The simulation using segment and vertex methods are compared with the structured mesh. The free surface profile along the length of the tank at 15s after the initiation of the motion of the wave paddle is shown in Fig. 4.46a. The time history at 5m from the wave paddle is shown in Fig. 4.46b. It shows an excellent agreement. The

snapshot of the moved mesh structure is shown in Fig. 4.47. Similar behaviour has been noted for different numerical simulation of different wave frequency components. Thus, it has been proved that both these methods can be used for the simulation of nonlinear free surface waves but one has to test the assumed stiffness before adopting it. The spring stiffness given above may be used for wide variety of problems, if one deals with the simulation of nonlinear free surface waves interacting with the fixed objects.

4.5.4. GP Method and its Improvement

From the forgoing sections, it is revealed that the GP method exhibits poor results for the simulation of nonlinear waves, unless the mesh structure is taken care, the details of which are discussed below.

The mesh moving strategy of vertex method has been adopted. The length of the tank (L) is 9m and water depth (h) is 0.6m. The stroke of the wave paddle (S) is $0.05h$ and the wave frequency (ω) is $1.5539\sqrt{g/h}$. The number of elements in the structured mesh was chosen as 16000, while, in the unstructured mesh, it was 13598. The initial mesh was generated using GAMBIT commercial software. A total number of 200 time steps per wave period that corresponds to a sampling interval of 0.005s was adopted for both the structured and unstructured mesh simulation. The beach length (L_{beach}) and the damping frequency of the beach (σ_b) are assumed to be equal to wavelength and the frequency of the incoming wave. Smoothing and regridding have been adopted after every 20 time steps. The simulation was carried out over a long time. The time histories near the wave paddle and at a distance of 5m from the wave paddle are shown in Figs. 4.48a and b. The free surface profile over the entire length of the tank at 25s after the initiation of the motion of the wave paddle is shown in Fig. 4.48c. The comparison between the two

methods is found to be good. Thus, it is clear that GP method can also be used as a velocity calculation technique as used by Wang and Wu (2006) but the quality of the mesh has to be considered with utmost care.

4.5.5. Comparison between Different Velocity Calculation Methods

In this section, a comparison is made between different velocity calculation techniques namely, CS, LS and GP methods. The simulation was carried out for the transient wave packets. The length of the tank is 50m with a water depth of 1m. The comparison is reported in the Figs. 4.49a and b at two different locations, one near to the paddle (12.513m) and the other at the focusing point (31.552m). This is the model scale of the experiments reported in section 4.3.1. The comparison shows that CS method is in reasonable agreement with the experimental measurements (Clauss and Steinhagen, 1999), whereas, LS method shows a lag of 0.2s at the focussing point. Further, the GP method is found to break down even after smoothing at 40s. For this case, both vertex and segment spring methods have yielded identical results and hence, segment spring method only reported in the above said simulation. The moved mesh at the focusing point is depicted in Fig. 4.50.

4.6. SUMMARY

The chapter also provides an in-depth analysis on different velocity calculation methods and its comparisons with the existing experimental measurements are reported. Further, a series of experiments are conducted for regular, cnoidal and solitary waves and compared with the numerical model. The quantitative results are reported for the two different methods of velocity calculations with that of experimental measurements by using Wavelet analysis. PIV measurements on solitary waves are also reported in detail with

the difficulties faced in generating these kinds of extreme waves. The unstructured mesh simulations are compared with the structured mesh results and the two different mesh moving strategies are analyzed for the simulation of wave-structure interaction problems. The improvement in GP method is highlighted in this chapter that has high frequency oscillations during simulation.

Table 4.1 Tested Solitary Wave Characteristics.

No.	Wave Height(H)	Wave Steepness(H/h)
1.	0.02	0.025
2.	0.03	0.0375
3.	0.04	0.05
4.	0.05	0.0625
5.	0.06	0.075
6.	0.08	0.1

Table 4.2 Wavelet Phase Angle for the Test Case T = 1.92s, H = 0.04m, D = 0.613m (R1). [XWT1 and WTC1: EXP-CS , XWT2 and WTC2: EXP-LS , WP1 @ 4.8495m; WP2 @ 20.146m; WP3 @ 25.136m; WP4 @ 30.425m; WP5 @ 40.406m; WP6 @ 50.609m]

Wavelet	WP 1 (in Deg)	WP2 (in Deg)	WP3 (in Deg)	WP4 (in Deg)	WP5 (in Deg)	WP6 (in Deg)
XWT1	0.49±12.20	-2.24±14.22	-2.74±29.03	-1.42±23.44	-1.22±13.58	-4.38±6.33
WTC1	-0.52±20.6	-2.62±22.42	-5.25±35.60	-1.56±22.03	-2.14±37.51	-0.96±23.05
XWT2	0.51±12.26	-2.30±13.95	-2.74±28.99	-1.46±23.37	-1.28±13.52	-4.41±6.32
WTC2	-0.51±19.19	-2.55±24.01	-5.68±37.03	-1.55±22.40	-1.85±38.45	-1.41±24.48

Table 4.3 Wavelet Phase Angle for the Test Case T = 1.92s, H = 0.2m, D = 0.621m (R2).[XWT1 and WTC1: EXP-CS , XWT2 and WTC2: EXP-LS , WP1 @ 4.8495m; WP2 @ 20.146m; WP3 @ 25.136m;WP4 @ 30.425m;WP5 @ 40.406m; WP6 @ 50.609m]

Wavelet	WP 1 (in Deg)	WP2 (in Deg)	WP3 (in Deg)	WP4 (in Deg)	WP5 (in Deg)	WP6 (in Deg)
XWT1	-4.95±15.24	37.12±18.07	47.85±26.45	62.65±30.56	80.34±42.86	89.98±55.87
WTC1	1.38±26.51	14.81±35.98	30.20±42.56	30.09±51.88	29.96±72.41	37.1±77.24
XWT2	-4.79±2.678	-3.76±8.10	-1.50±5.21	3.32±7.00	8.91±4.760	9.74±5.51
WTC2	-2.11±24.05	-0.61±24.12	0.07±22.84	5.85±25.25	5.28±35.32	6.51±38.95

Table 4.4 Wavelet Phase Angle for the Test Case T = 6.4s, H = 0.03m, D = 0.619m (CN1). [XWT1 and WTC1: EXP-CS , XWT2 and WTC2: EXP-LS , WP1 @ 4.8495m; WP2 @ 20.146m; WP3 @ 25.136m;WP4 @ 30.425m;WP5 @ 40.406m; WP6 @ 50.609m]

Wavelet	WP 1 (in Deg)	WP2 (in Deg)	WP3 (in Deg)	WP4 (in Deg)	WP5 (in Deg)	WP6 (in Deg)
XWT1	-2.28±1.571	2.18±4.21	1.71±6.057	3.59±1.84	4.40±2.4762	1.05±2.15
WTC1	-1.82±39.73	5.11±34.09	0.00±28.427	6.25±34.61	-2.68±39.10	3.01±36.58
XWT2	-2.49±1.470	0.62±2.81	0.28±4.9812	2.05±1.56	2.44±1.8406	-1.40±1.94
WTC2	-1.36±37.08	4.66±35.38	-1.06±29.00	5.36±32.11	-3.91±39.14	0.96±36.16

Table 4.5 Wavelet Phase Angle for the Test Case T = 6.4s, H = 0.3m, D = 0.62m (CN2). [XWT1 and WTC1: EXP-CS , XWT2 and WTC2: EXP-LS , WP1 @ 4.8495m; WP2 @ 20.146m; WP3 @ 25.136m;WP4 @ 30.425m;WP5 @ 40.406m; WP6 @ 50.609m]

Wavelet	WP 1 (in Deg)	WP2 (in Deg)	WP3 (in Deg)	WP4 (in Deg)	WP5 (in Deg)	WP6 (in Deg)
XWT1	6.4±5.62	12.11 ±21.84	13.70 ±17.50	19.43±17.30	19.86±19.04	19.72 ±17.91
WTC1	8.04±25.6	8.88 ±26.83	10.91 ±30.77	13.30±32.74	14.44±33.44	12.87±33.19
XWT2	1.59±3.37	2.16±11.68	2.14±9.26	3.59±7.56	2.95±4.72	0.57±4.08
WTC2	4.29±21.4	2.07±22.60	3.36±26.22	3.59±27.06	2.60±25.94	1.06±25.95

Table 4.6 Wavelet Phase Angle for the Test Case T = 3.2s, H = 0.2m, D = 0.621m (CN3). [XWT1 and WTC1: EXP-CS , XWT2 and WTC2: EXP-LS , WP1 @ 4.8495m;WP2 @ 20.146m; WP3 @ 25.136m;WP4 @ 30.425m;WP5 @ 40.406m; WP6 @ 50.609m]

Wavelet	WP 1 (in Deg)	WP2 (in Deg)	WP3 (in Deg)	WP4 (in Deg)	WP5 (in Deg)	WP6 (in Deg)
XWT1	3.19±4.42	11.67±7.87	12.00±6.52	15.95±9.9	20.43±12.30	16.39±9.32
WTC1	1.09±20.94	7.97±21.95	9.65±23.36	10.67±24.69	14.3±34.87	8.61±28.09
XWT2	0.12±3.14	1.49±2.85	0.76±1.57	5.71±4.68	2.60±3.12	-0.54±2.85
WTC2	0.21±20.35	0.43±18.84	0.79±20.93	3.68±21.50	1.93±29.66	-1.00±26.03

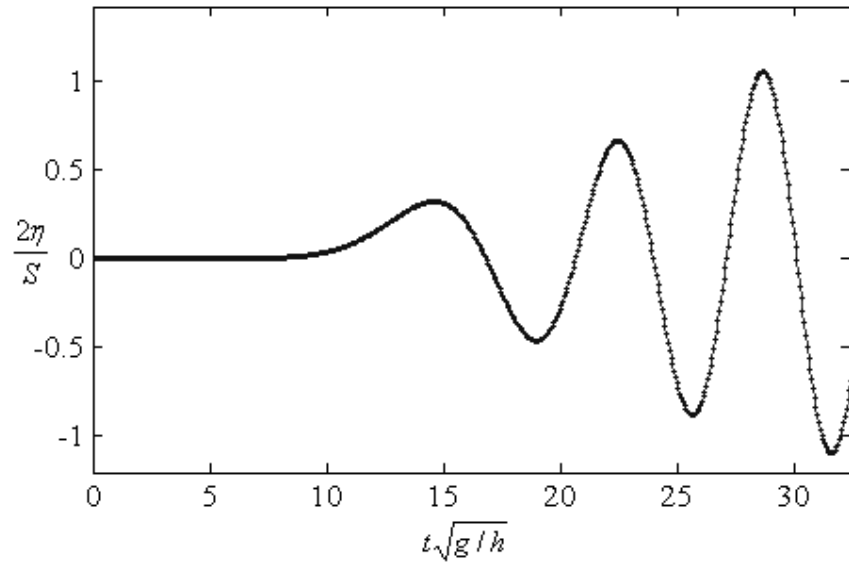


Fig. 4.1 Comparison between Nonlinear and Linear Wave Simulation at 12m from the Wave Paddle for a Wave Steepness, $H/\lambda = 0.0036$
 [— Nonlinear Wave; ◆◆ Linear Wave]

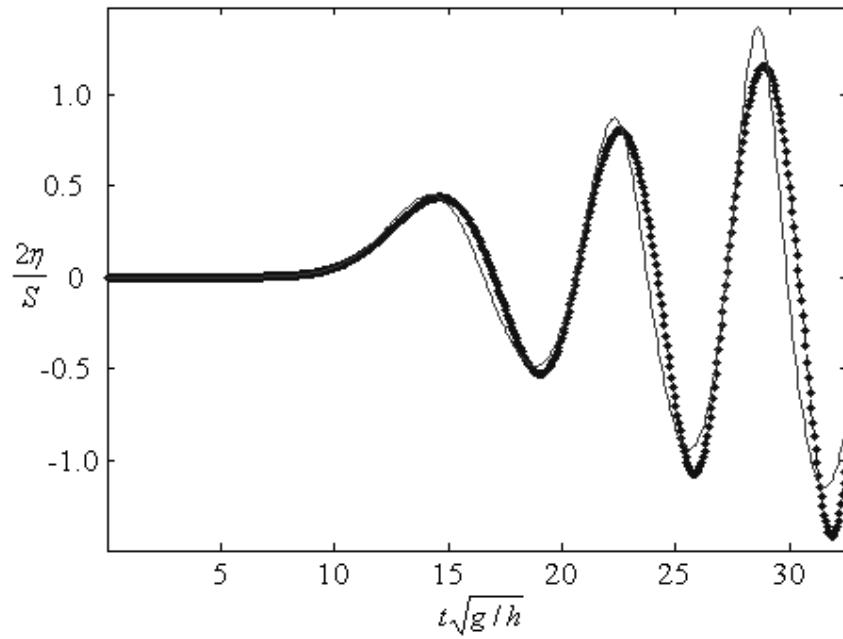


Fig. 4.2 Comparison between Nonlinear and Linear Wave Simulation at 12m from the Wave Paddle for a Wave Steepness, $H/\lambda = 0.046$
 [— Nonlinear Wave; ◆◆ Linear Wave]

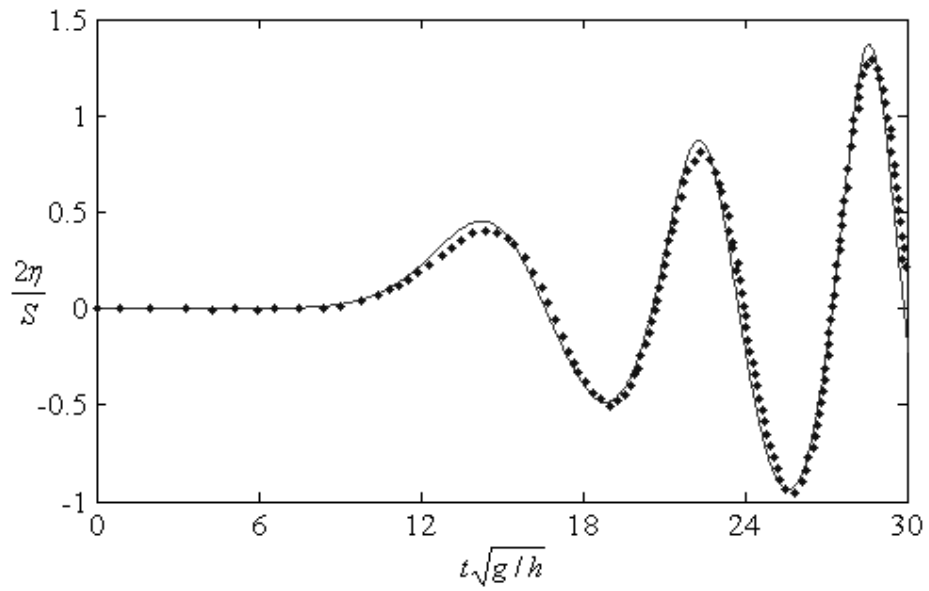


Fig. 4.3 Free Surface Elevation at 12m from the Wave Paddle for a Wave Steepness, $H/\lambda = 0.046$
[◆◆◆ Wu and Eatock Taylor (1995); — Present Simulation]

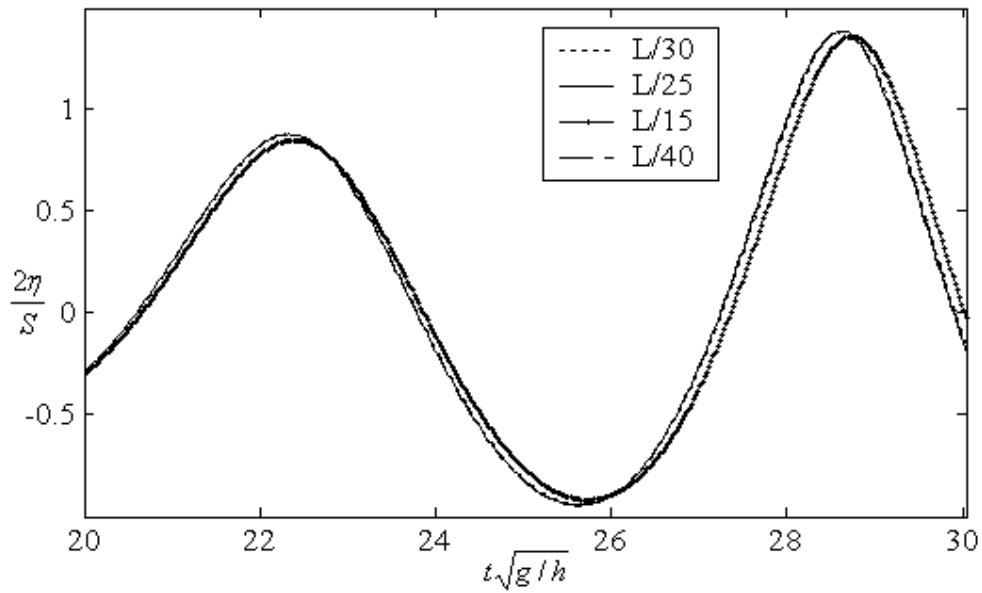


Fig. 4.4a Mesh Convergence for the Spatial Resolution for 15, 25, 30 and 40 Nodes per Wavelength

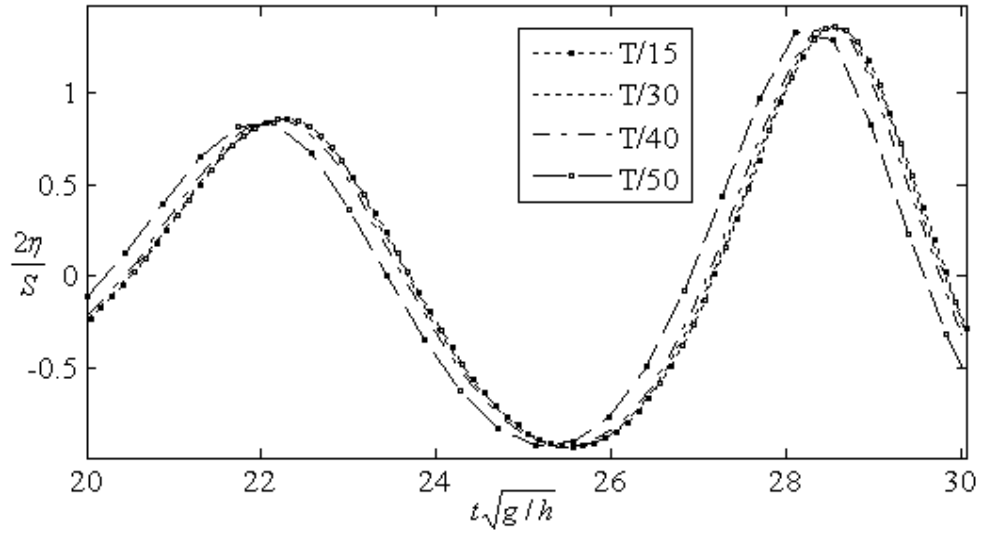


Fig. 4.4b Mesh Convergence for the Temporal Resolution of 15, 30, 40 and 50 Time Steps per Wave Period

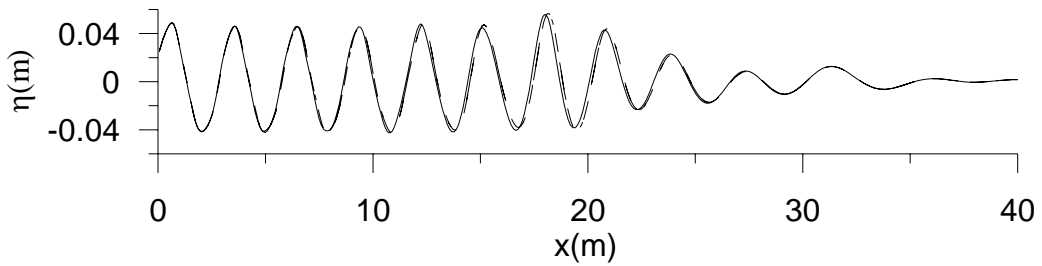


Fig. 4.5 Free Surface Profile at 20s along the Length of the Tank [----- LS; — CS; -·-·- MFD]

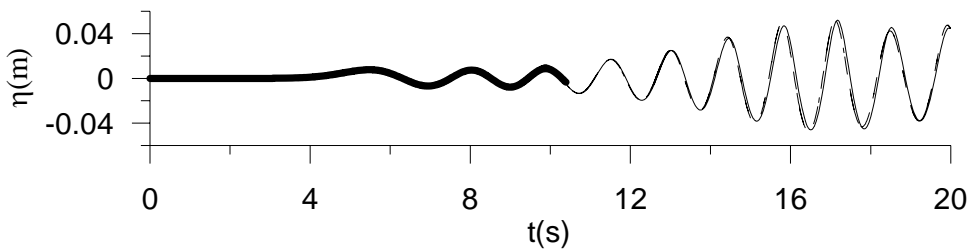


Fig. 4.6 Time History at 12m from the Wave Paddle [----- LS; — CS; -·-·- MFD; — GP]

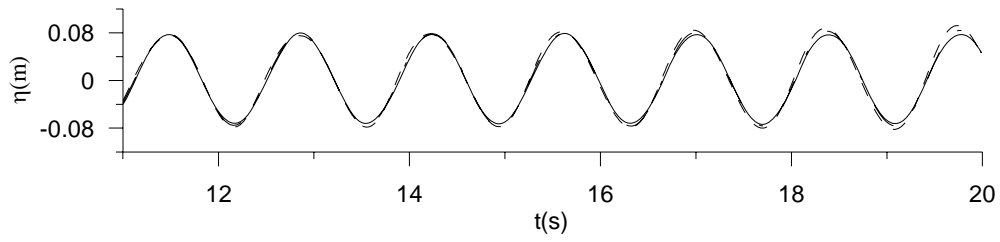


Fig. 4.7 Free Surface Elevation near the Wave Paddle showing Instability after 17s [----- LS; — CS; -·-·-· MFD]

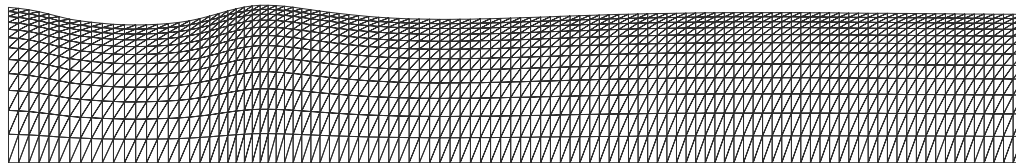


Fig. 4.8a Mesh Structure near the Wave Paddle at 2s

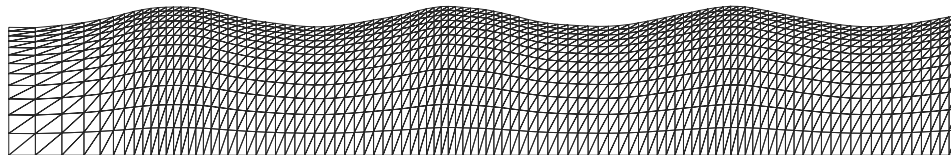


Fig. 4.8b Mesh Structure near the Wave Paddle showing Node Movement around 18s

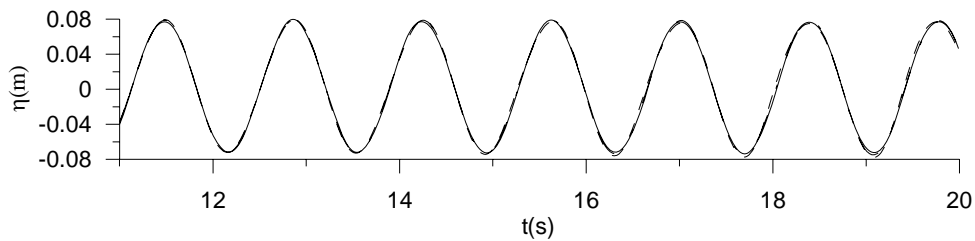


Fig. 4.9 Free Surface Elevation near the Wave Paddle after Increasing the Number of Nodes to 825 [----- LS; — CS; -·-·-· MFD]

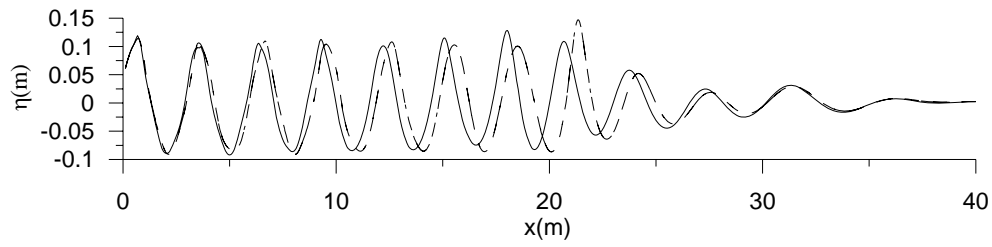


Fig. 4.10 Free Surface Elevation along the Length of the Tank for a Wave Steepness of 0.7 [----- LS; — CS; -·-·-·- MFD]

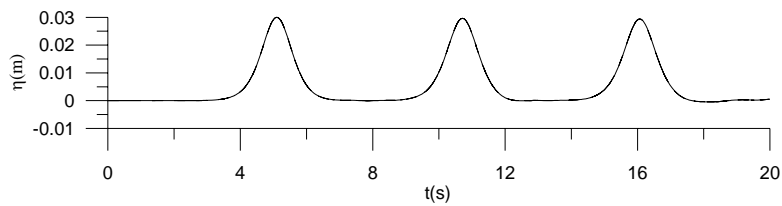


Fig. 4.11 Time History at the Center of the Tank [----- LS; — CS; -·-·-·- MFD]

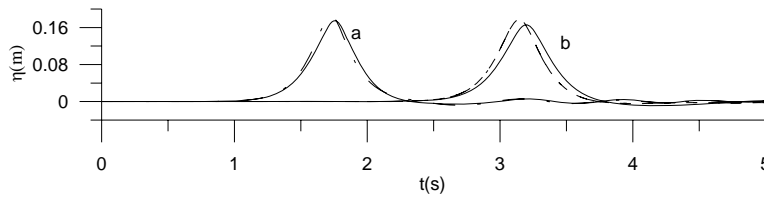


Fig. 4.12 Time History at a) 2m and b) 5m from the Wave Paddle [----- LS; — CS; -·-·-·- MFD]

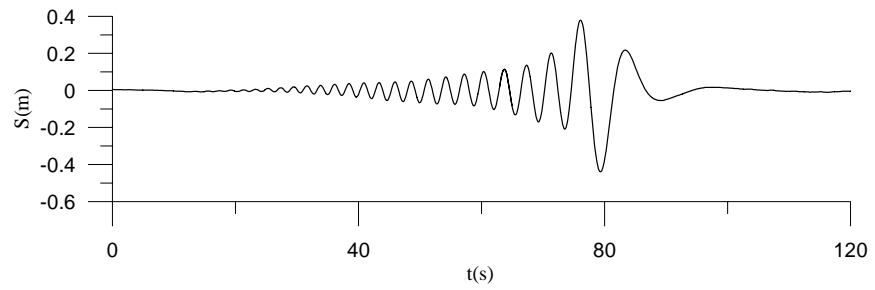


Fig. 4.13a Paddle Displacement for the Simulation of Transient Wave Packet

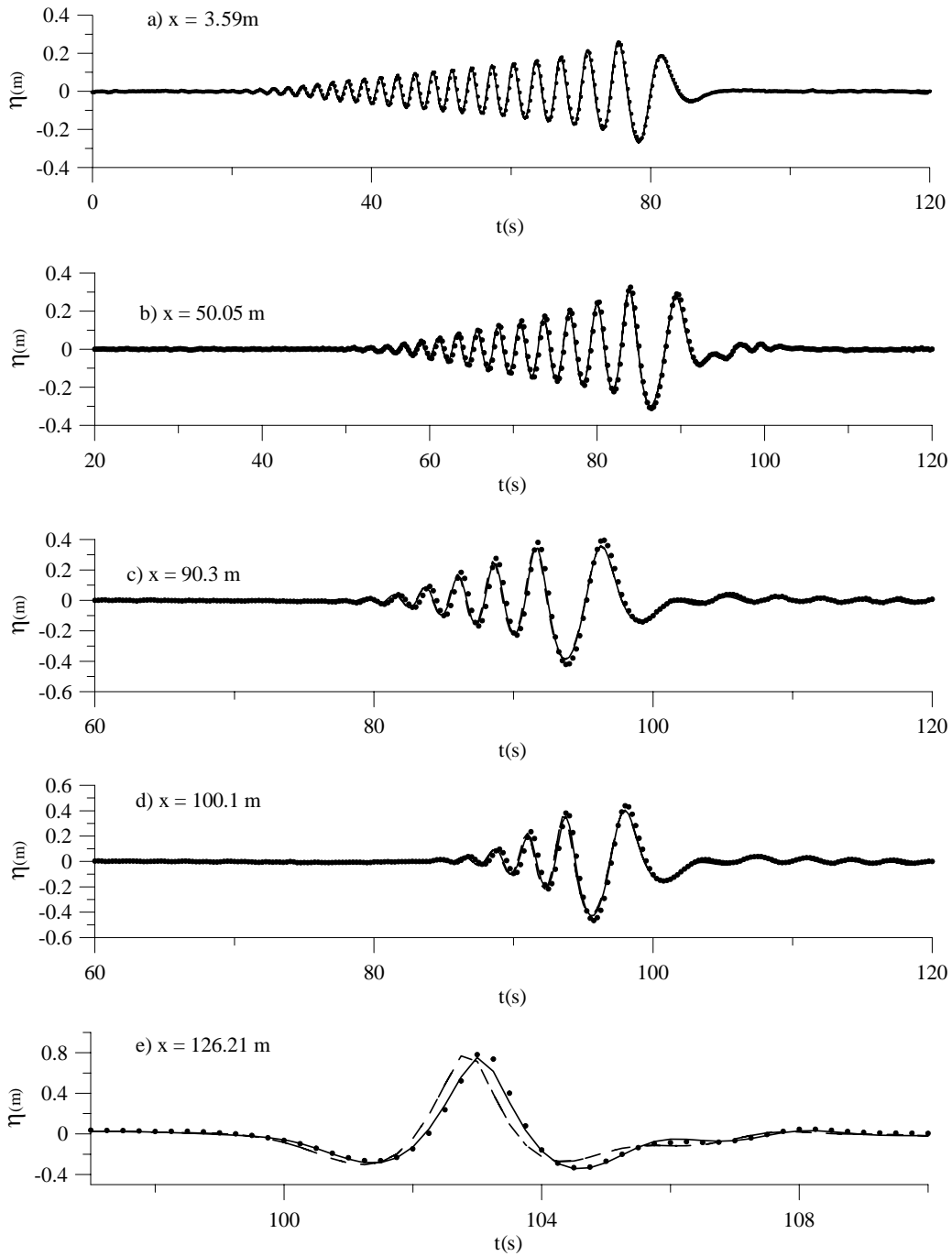


Fig. 4.13b Time History Comparison at Various Locations [••••Experiments (Claus and Steinhagen, 1999); - - - - LS; — CS; - · - · - MFD]

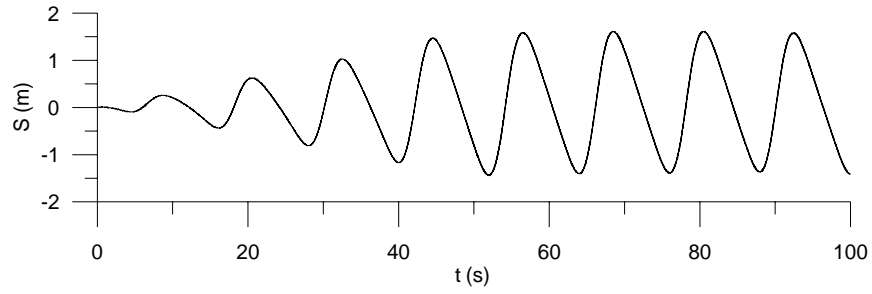


Fig. 4.14a Paddle Displacement for the Simulation of Cnoidal Waves

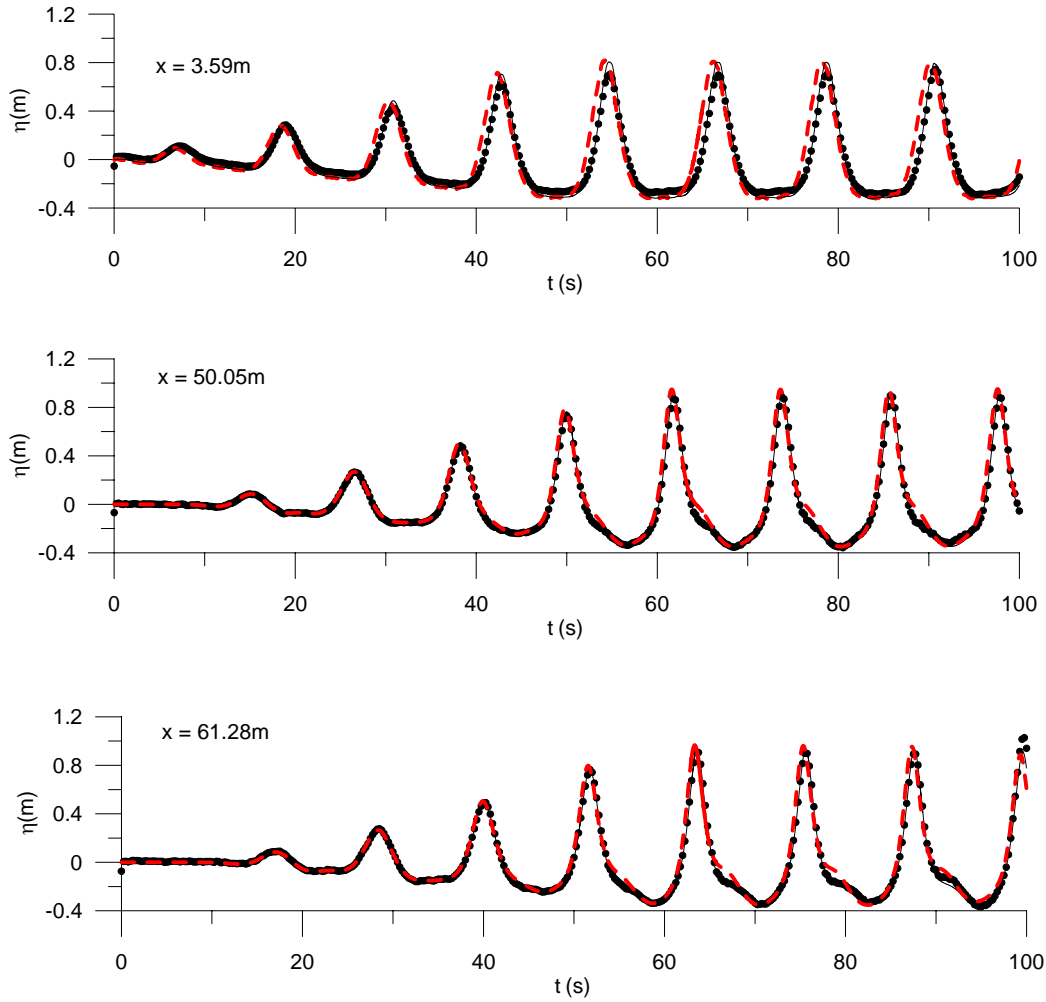


Fig. 4.14b Time History Comparison at Various Locations [•••• Experiments (Jeong, 2003); - - - - Numerical (Jeong, 2003); — CS]

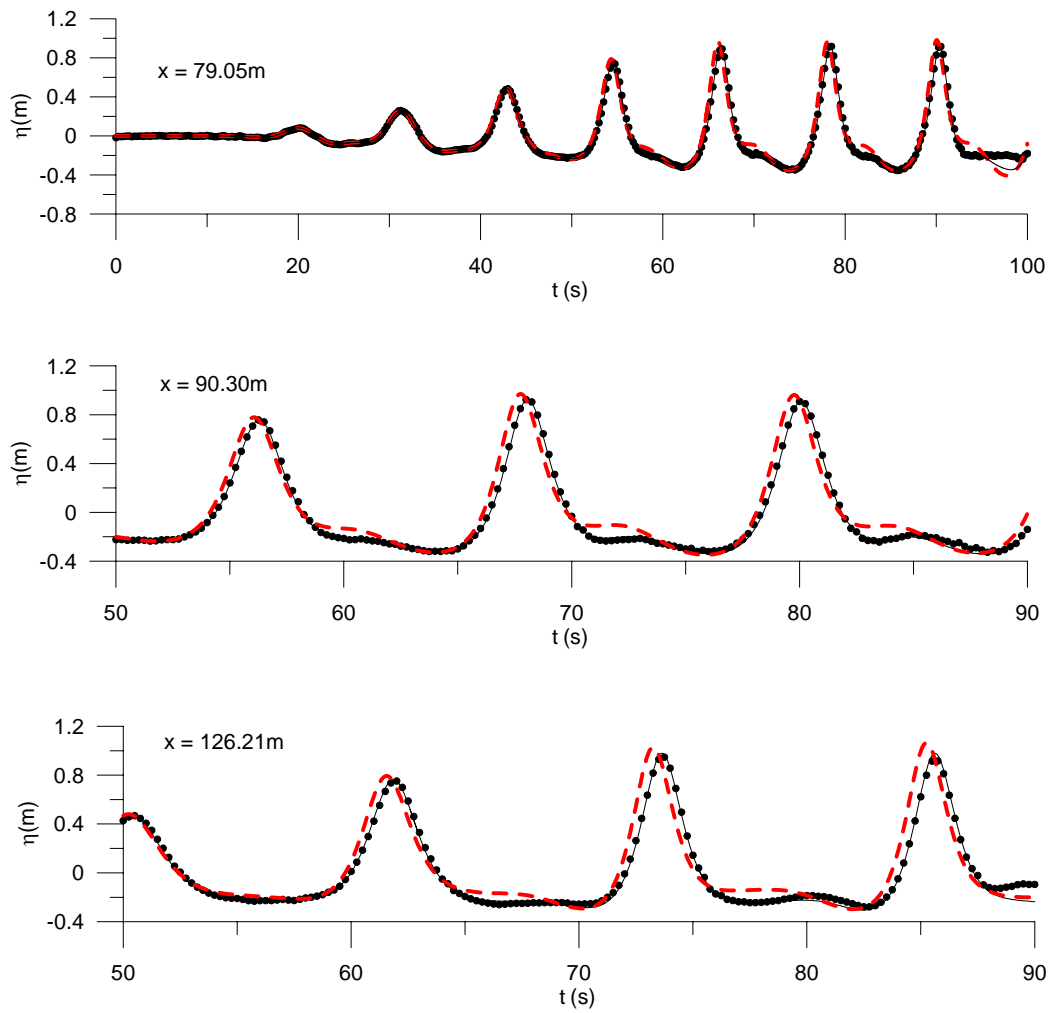


Fig. 4.14b Contd.

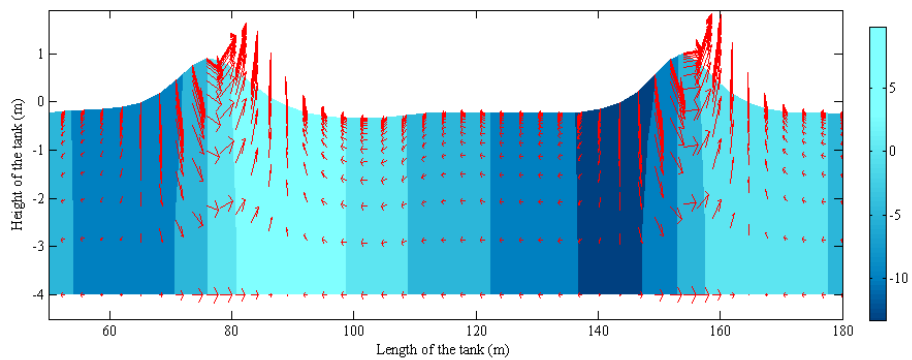


Fig. 4.15 Velocity Vector Plot along the Length of the Tank at 80s

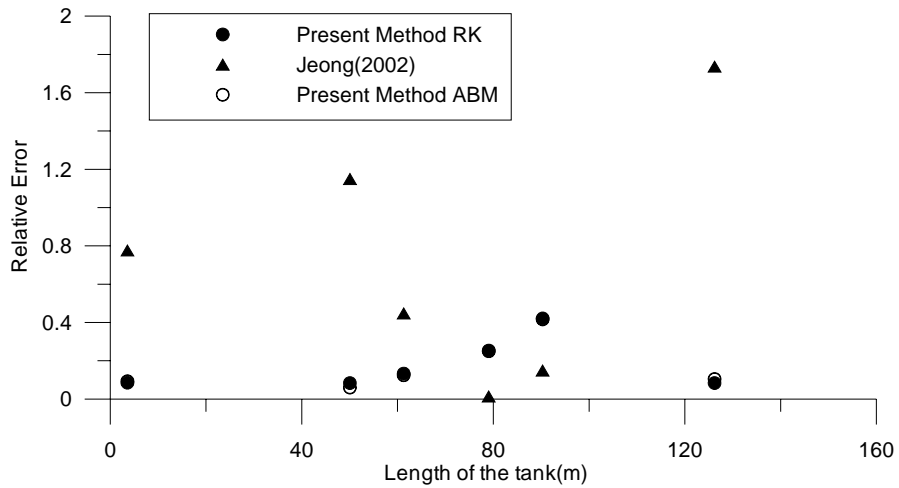


Fig. 4.16 Relative Error along the Length of the Tank

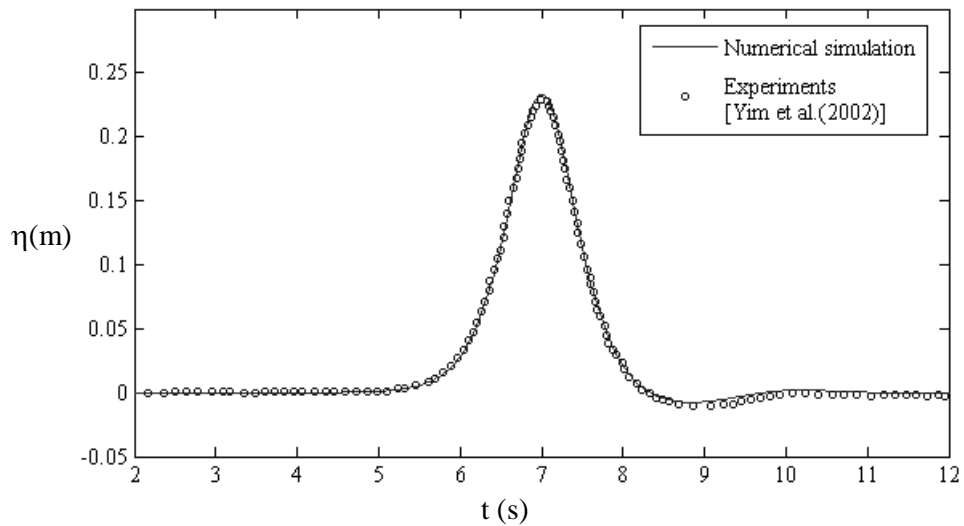


Fig. 4.17 Comparison of the Numerical Simulation of Free Surface Profile at 15.7m from the Wave Paddle with the Experimental Measurements (Yim *et al.* 2004) for a Wave Height of 0.24m in a 0.8m Water Depth

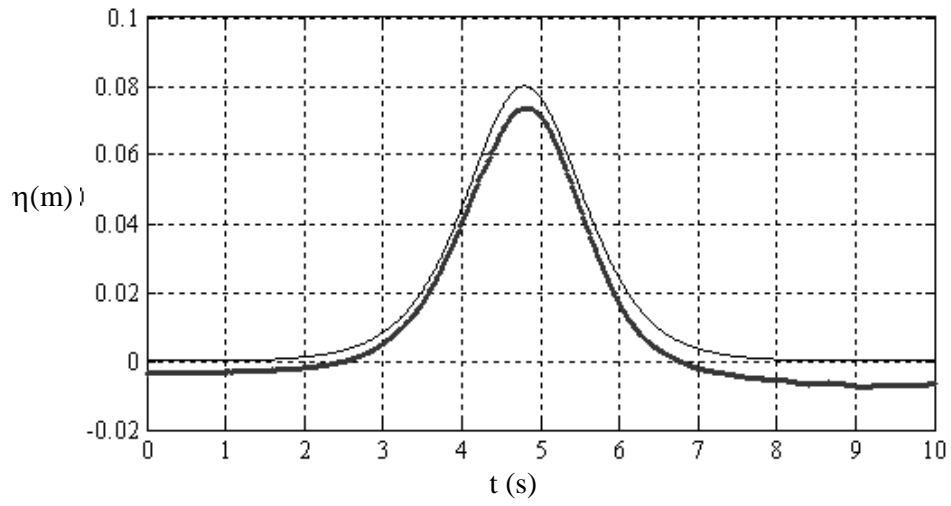


Fig. 4.18 Comparison of Numerical Simulation with Present Experimental Measurements at 3m for $H/h=0.1$ [••••• Experiments; — Numerical]

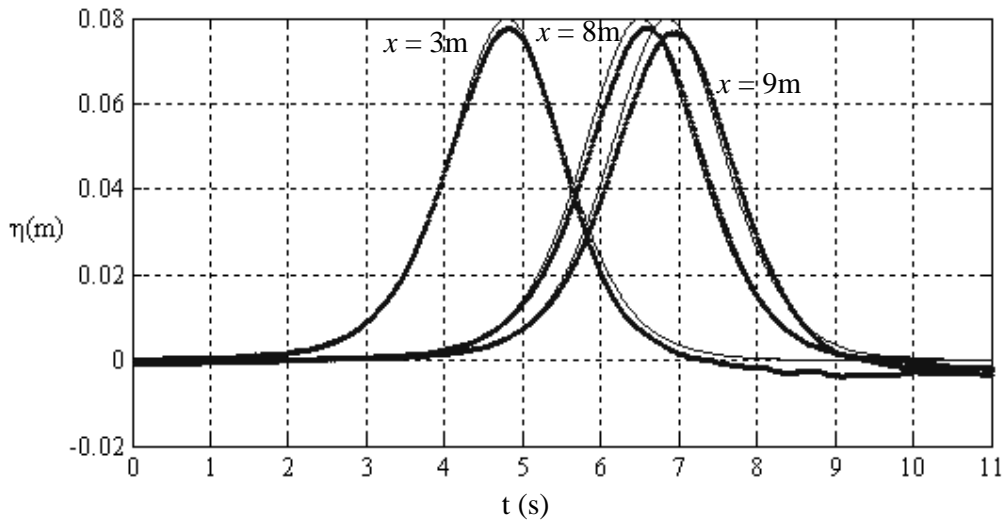


Fig. 4.19 Comparison of Numerical Simulation with Experimental Measurements with Corrected Water Depth at Various Distances of 3m, 8m and 9m from the Wave Paddle for $H/h = 0.1$ [••••• Experiments; — Numerical]

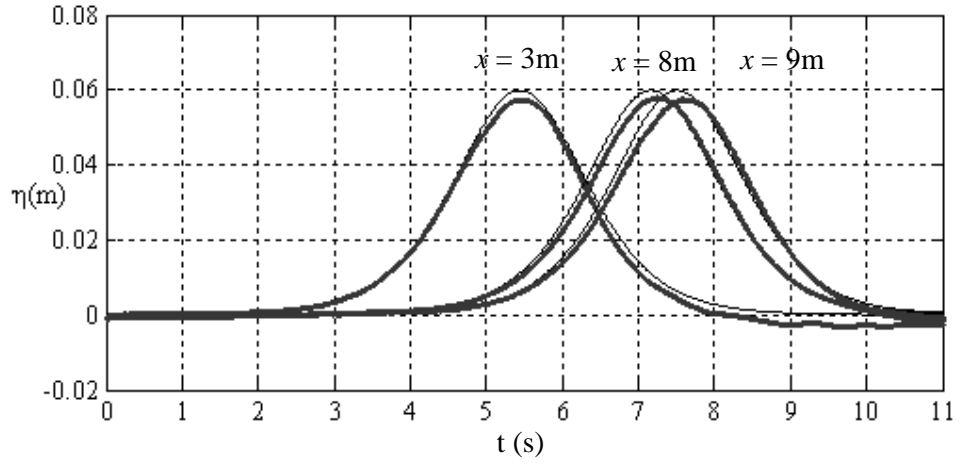


Fig. 4.20 Comparison of Numerical Simulation with Experimental Measurements with Corrected Water Depth at Various Distances of 3m, 8m and 9m from the Wave Paddle for $H/h = 0.075$ [.....-Experiments; — Numerical]

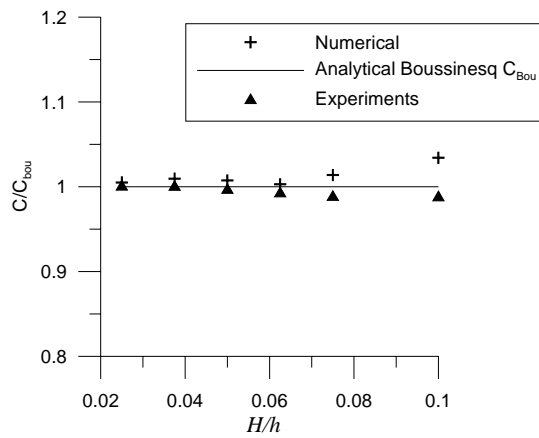


Fig. 4.21 Variation of Wave Speed with respect to Wave Steepness



Fig. 4.22 View of the Flume at University of Hannover, Germany



Fig. 4.23 View Showing the Glass Flume at University of Wuppertal, Germany

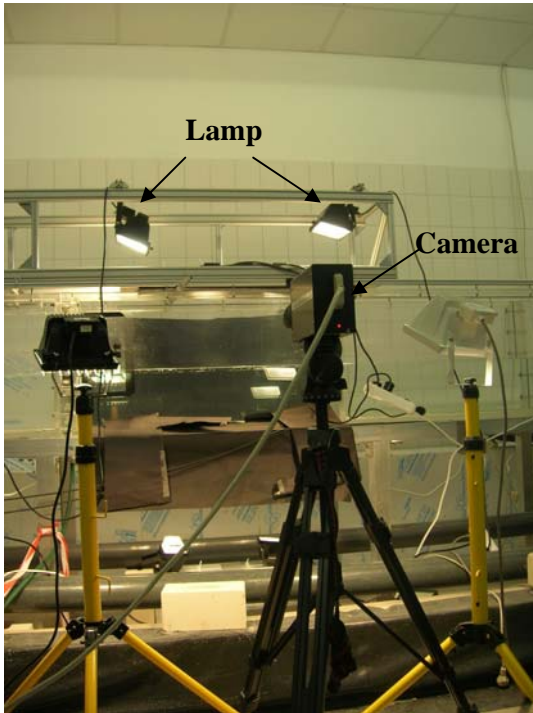
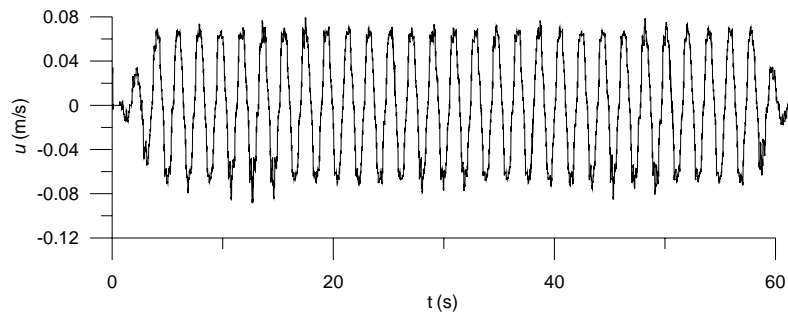
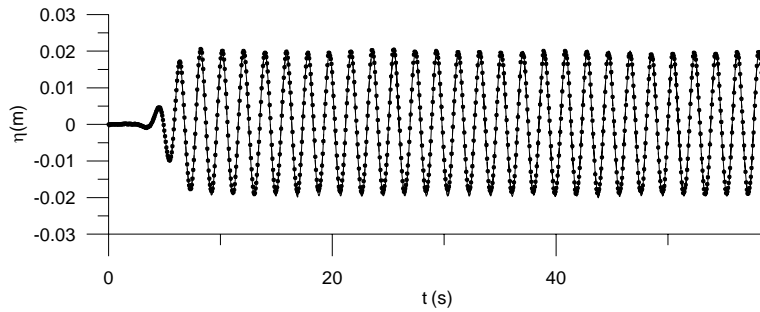


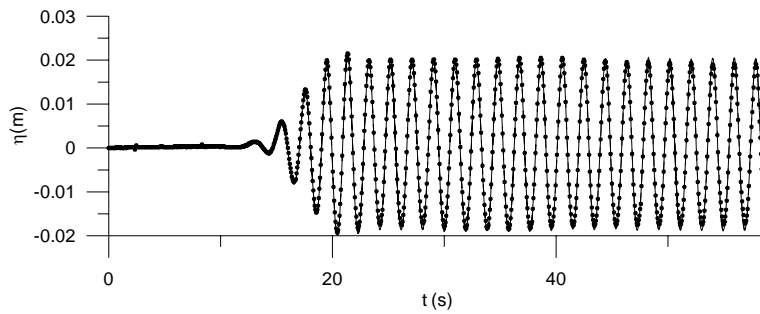
Fig. 4.24 PIV Set-up and Light Settings



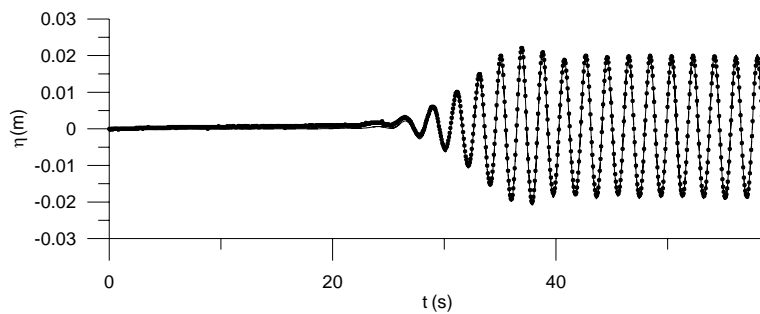
(a) Input Velocity obtained from the Paddle Displacement



(b) Wave Surface Elevation at 4.849m

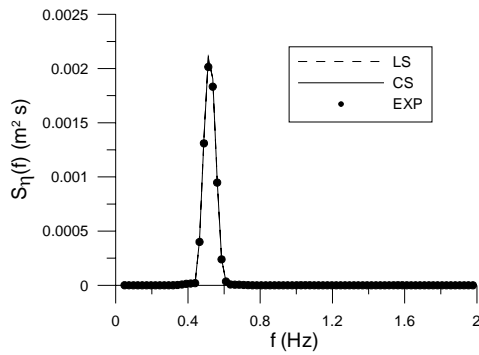


(c) Wave Surface Elevation at 25.136m

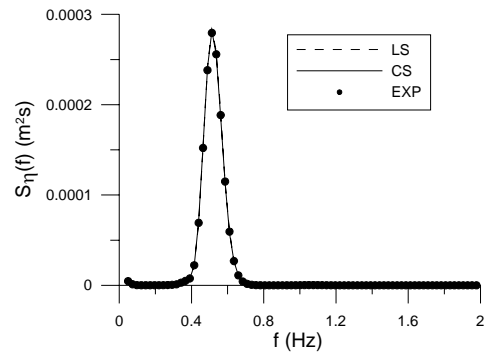


(d) Wave Surface Elevation at 50.609m

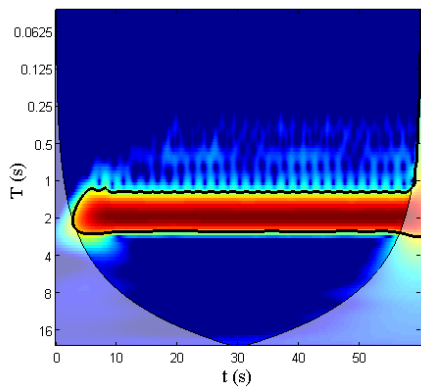
Fig. 4.25 Input Velocity and Time History Comparisons to Simulate a Regular Wave with a Steepness of 0.01 [R1: ●●●●● EXP; ---- LS; — CS]



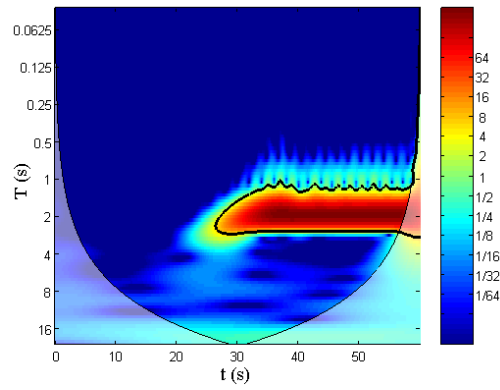
(a) Wave Power Spectrum for WP1



(b) Wave Power Spectrum for WP6



(c) Wavelet Power for EXP at WP1



(d) Wavelet Power for EXP at WP6

Fig. 4.26 Fourier and Wavelet Spectrum for R1 [WP1 @ 4.895m; WP6 @ 50.609m]

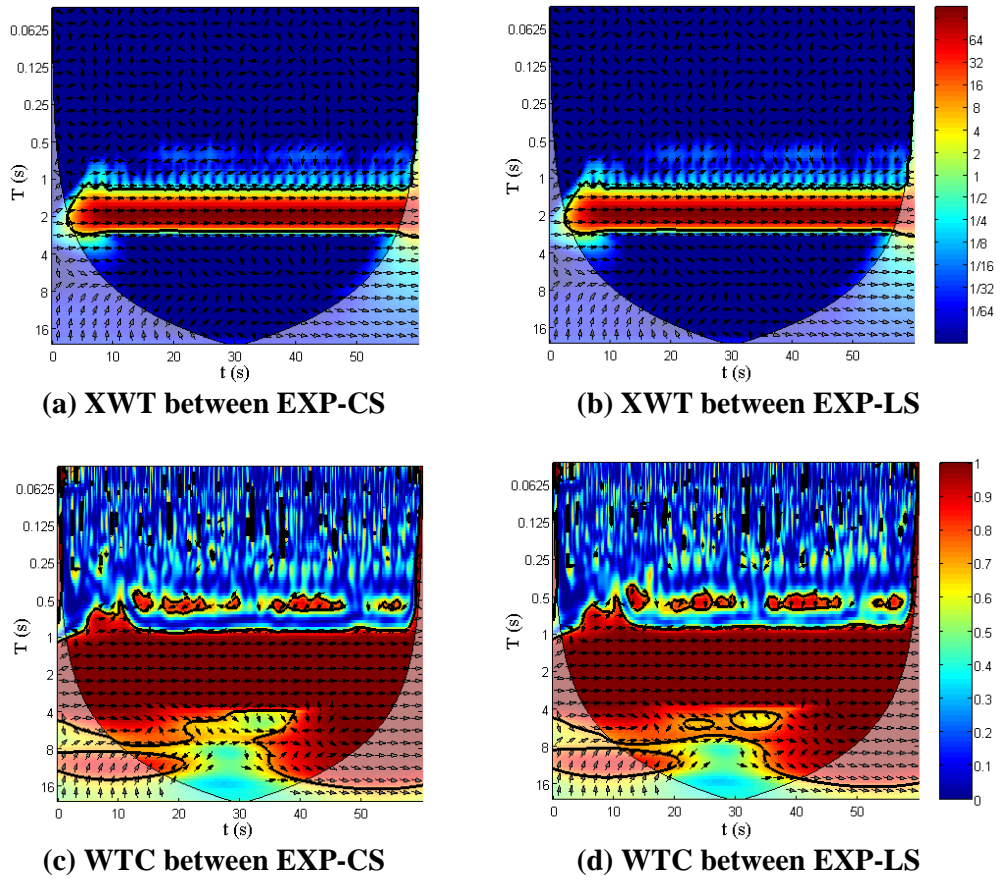
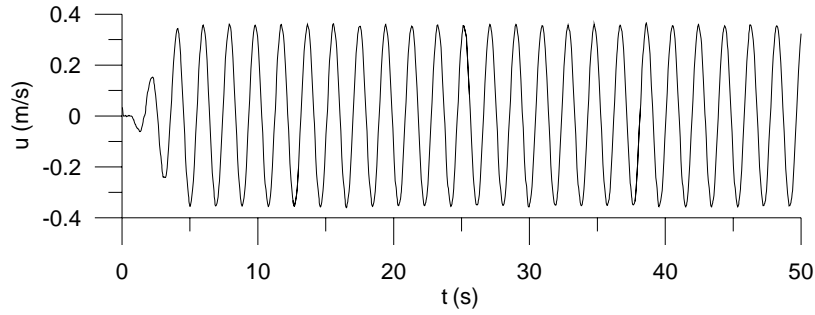
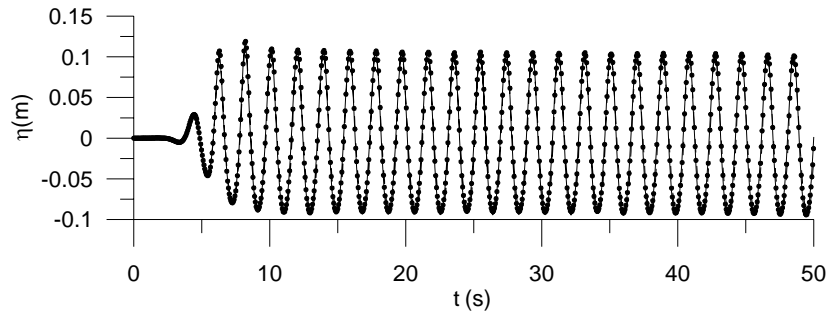


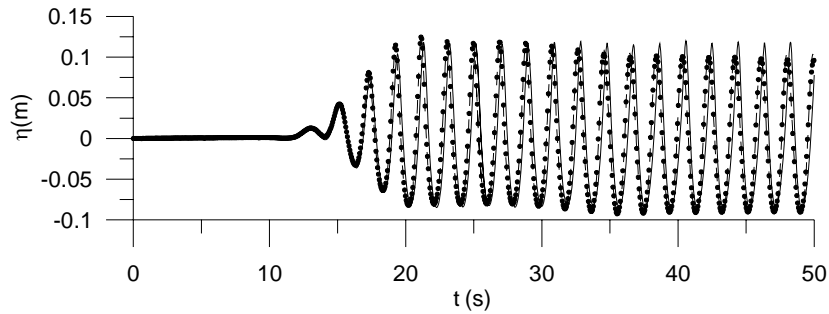
Fig. 4.27 Cross Wavelet Transform and Wavelet Coherence between Numerical Approaches and Experiment for the Time History near to the Wave Paddle [R1]



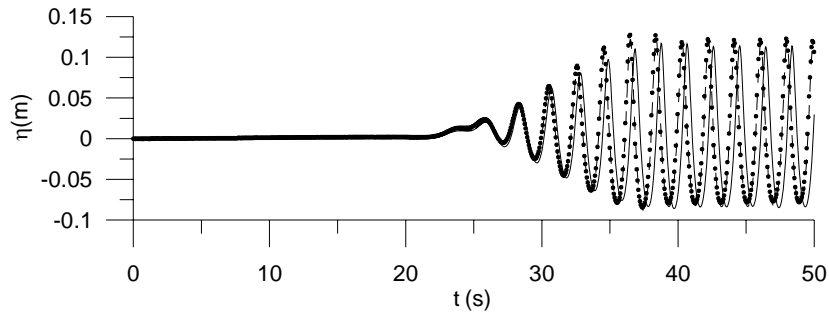
(a) Input Velocity obtained from the Paddle Displacement



(b) Wave Surface Elevation at 4.849m

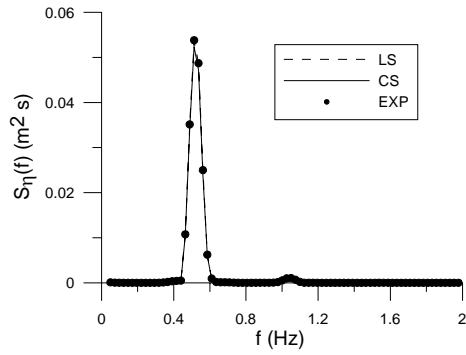


(c) Wave Surface Elevation at 25.136m

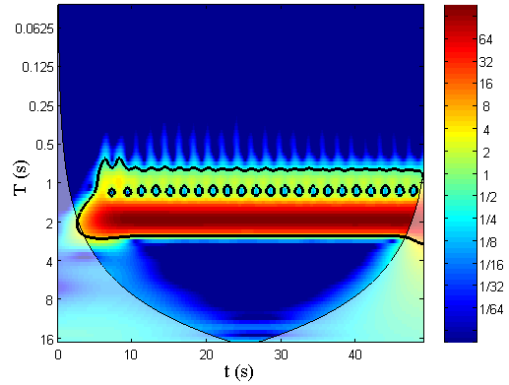


(d) Wave Surface Elevation at 50.609m

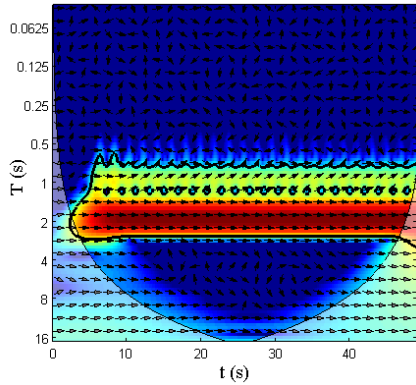
Fig. 4.28 Input Velocity and Time History Comparisons to Simulate a Regular Wave with a Steepness of 0.047 [R2: ●●●●● EXP; - - - - LS; — CS]



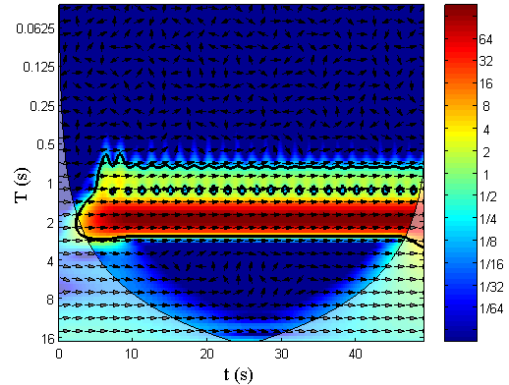
(a) Wave Power Spectra



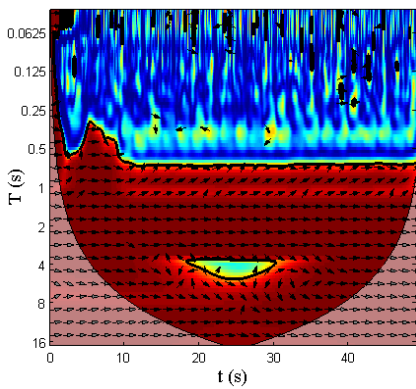
(b) Wavelet Power for EXP



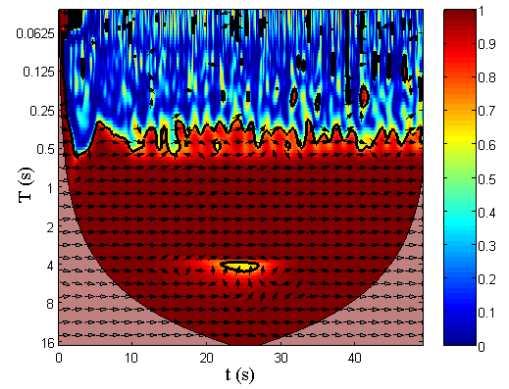
(c) XWT between EXP-CS



(d) XWT between EXP-LS

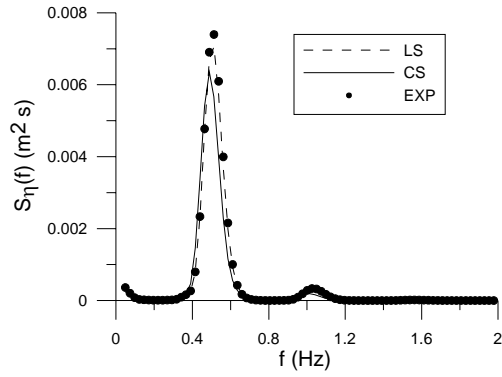


(e) WTC between EXP-CS

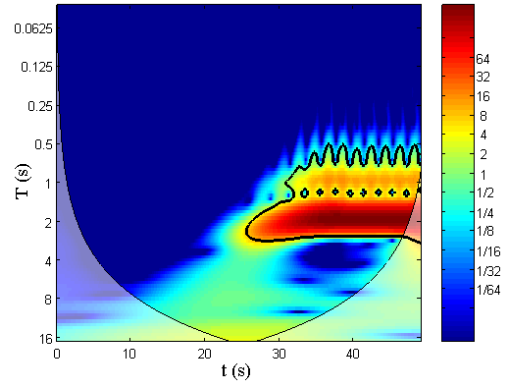


(f) WTC between EXP-LS

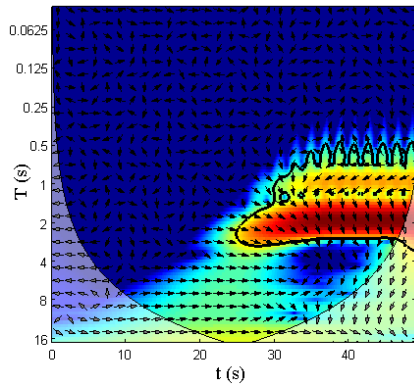
Fig.4.29 Fourier and Wavelet Analysis for Time History near the Wave Paddle [R2]



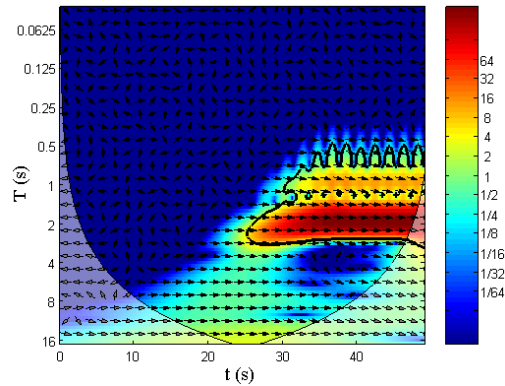
(a) Wave Power Spectra



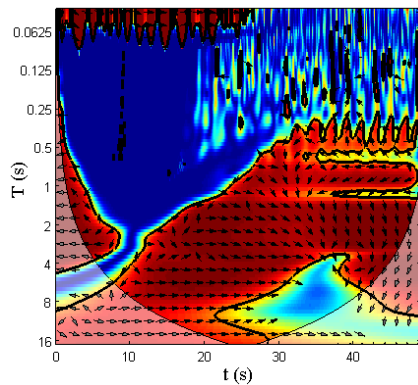
(b) Wavelet Power for EXP



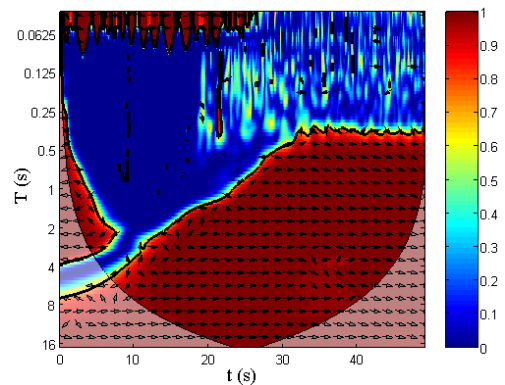
(c) XWT between EXP-CS



(d) XWT between EXP-LS

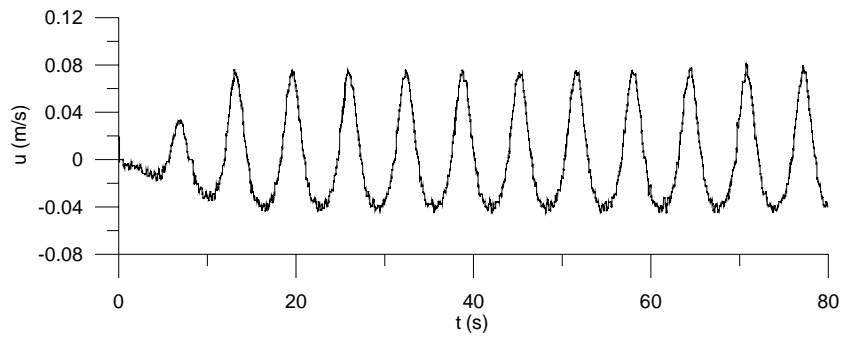


(e) WTC between EXP-CS

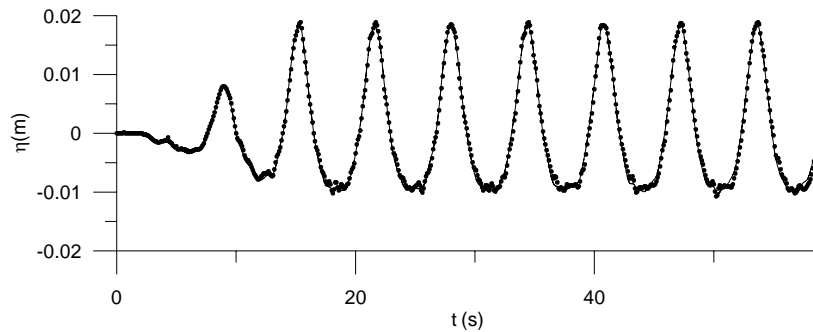


(f) WTC between EXP-LS

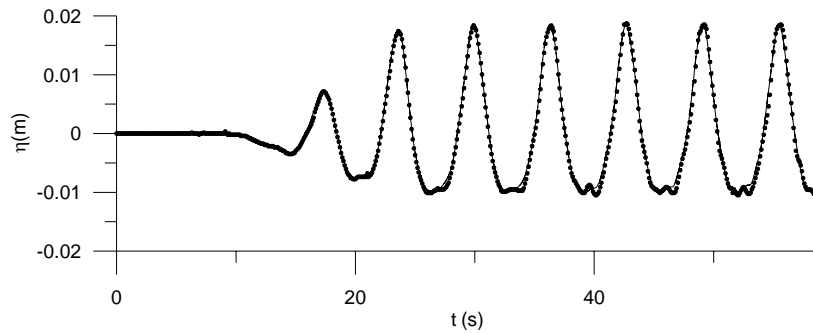
Fig. 4.30 Fourier and Wavelet Analysis for the Time History far away from the Paddle [R2]



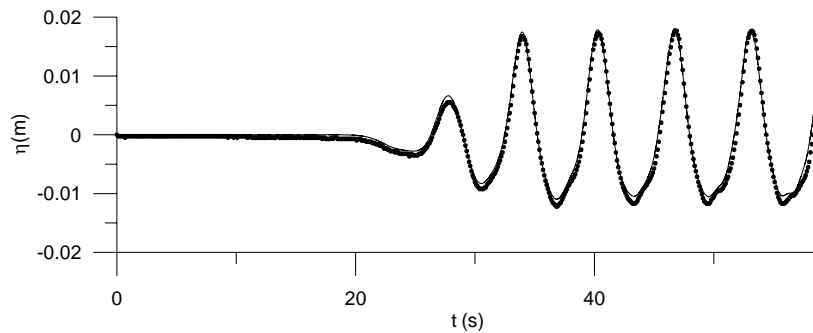
(a) Input Velocity obtained from the Paddle Displacement



(b) Wave Surface Elevation at 4.849m

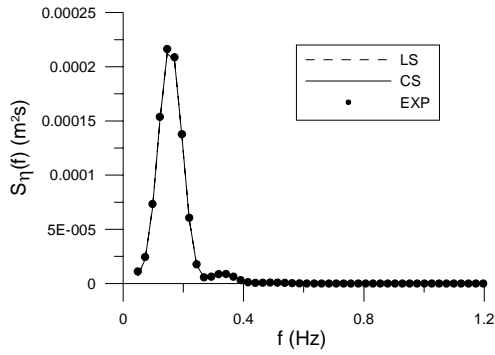


(c) Wave Surface Elevation at 25.136m

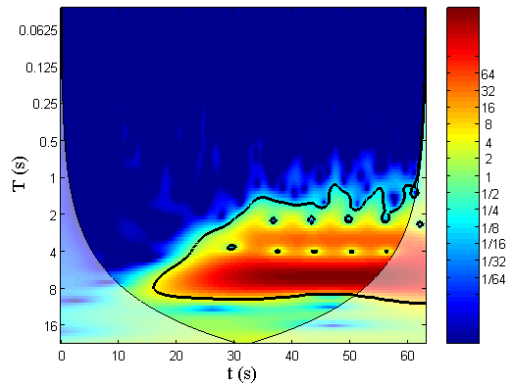


(d) Wave Surface Elevation at 50.609m

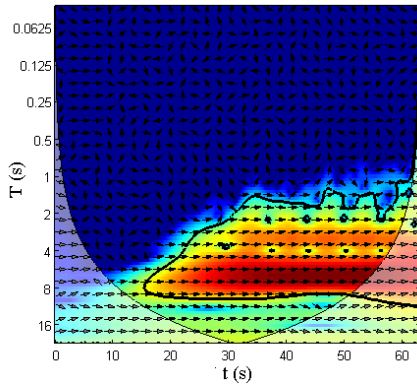
Fig. 4.31 Input Velocity and Time Histories Comparison to Simulate a Cnoidal Wave of Ursell Parameter 30 [CN1: ●●●●● EXP; - - - - LS; — CS]



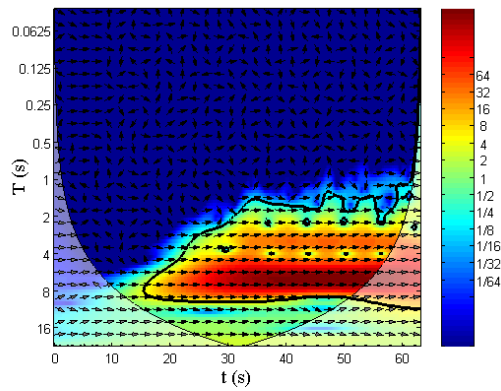
(a) Wave Power Spectra



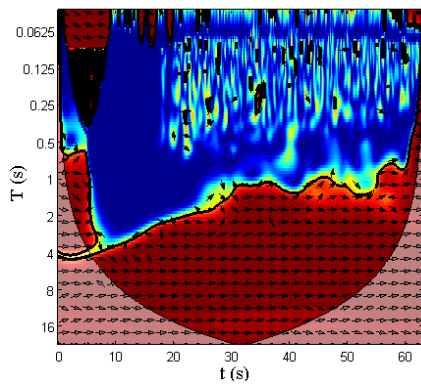
(b) Wavelet Power for EXP



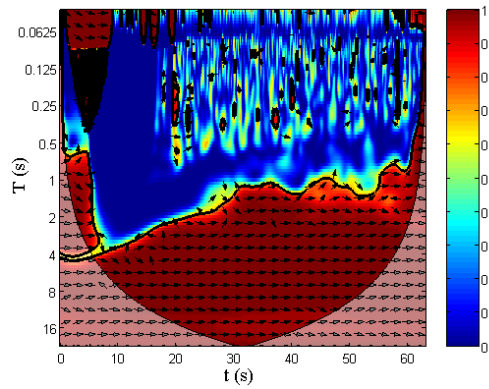
(c) XWT between EXP-CS.



(d) XWT between EXP-LS.

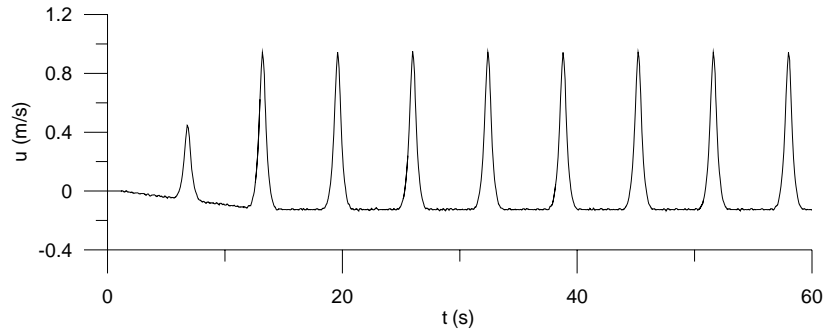


(e) WTC between EXP-CS

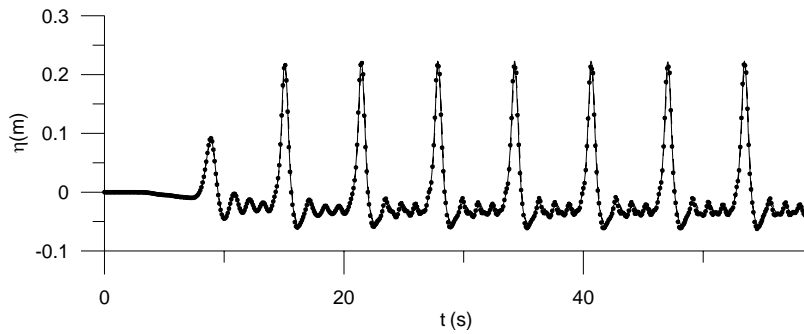


(f) WTC between EXP-LS

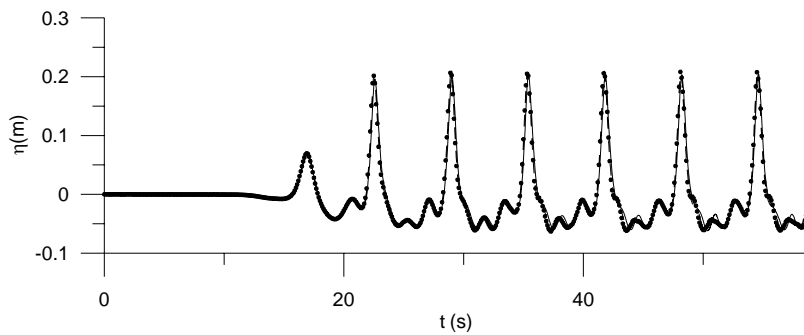
Fig. 4.32 Fourier and Wavelet Analysis for Time History far away from the Paddle [CN1]



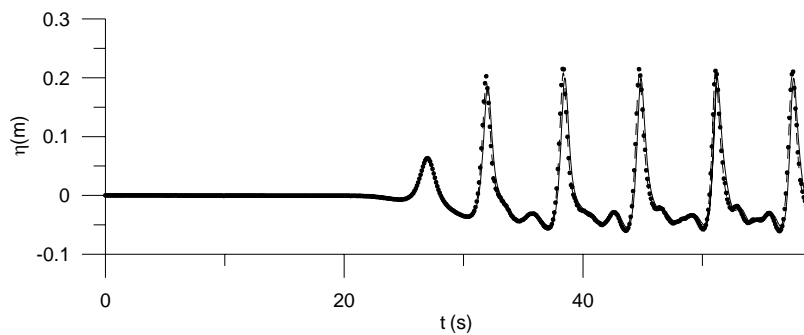
(a) Input Velocity obtained from the Paddle Displacement



(b) Wave Surface Elevation at 4.849m

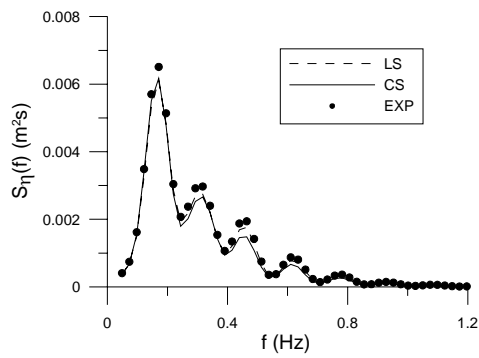


(c) Wave Surface Elevation at 25.136m

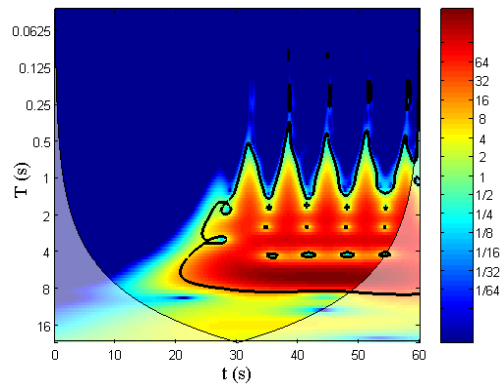


(d) Wave Surface Elevation 50.609m

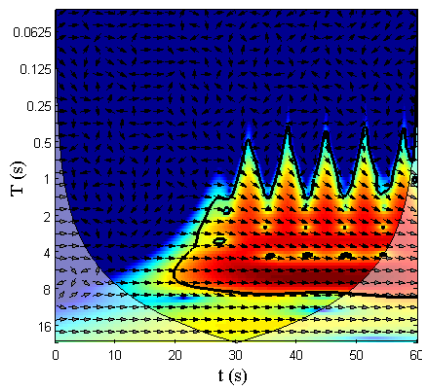
Fig. 4.33 Input Velocity and Time History Comparison to Simulate a Cnoidal Wave of Ursell Number 307 [CN2: ●●●●● EXP; - - - - LS; — CS]



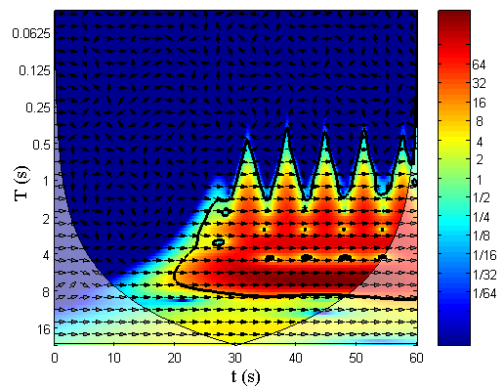
(a) Wave Power Spectra



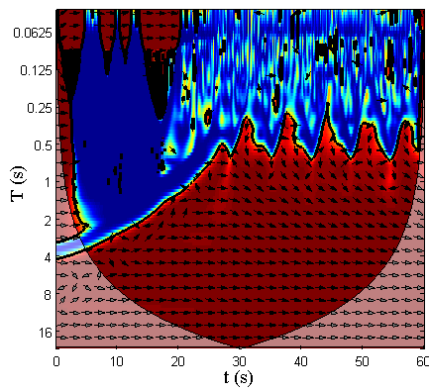
(b) Wavelet Power for EXP



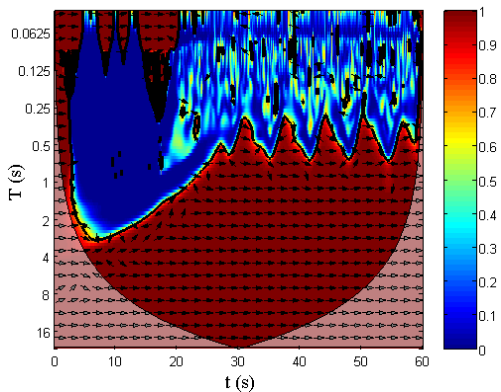
(c) XWT between EXP-CS



(d) XWT between EXP-LS

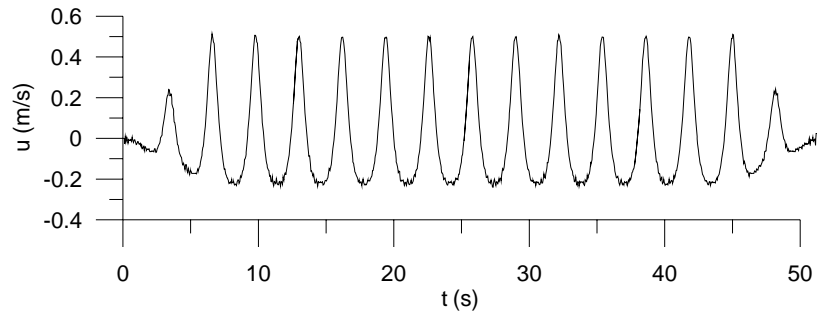


(e) WTC between EXP-CS

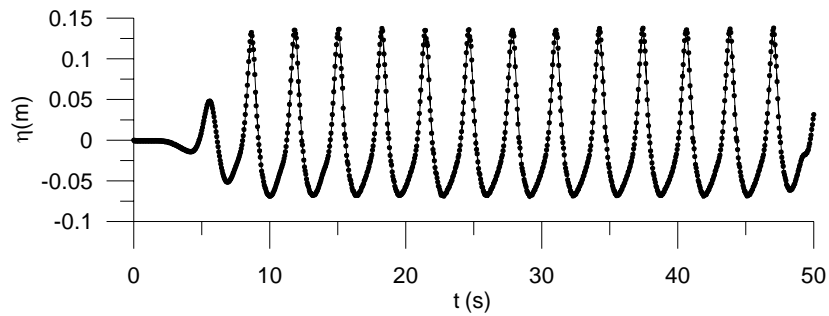


(f) WTC between EXP-LS

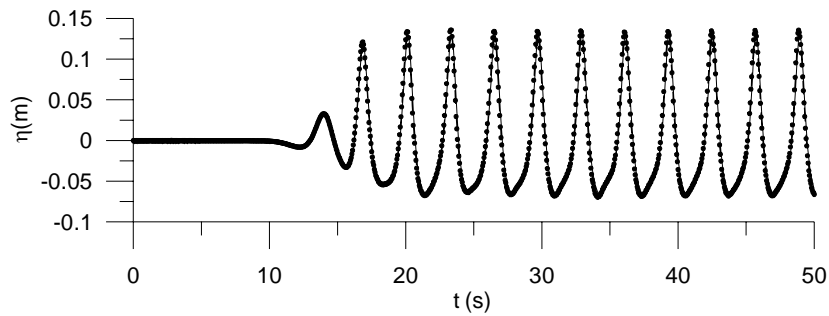
Fig. 4.34 Fourier and Wavelet Analysis for the Time History far away from the Paddle [CN2]



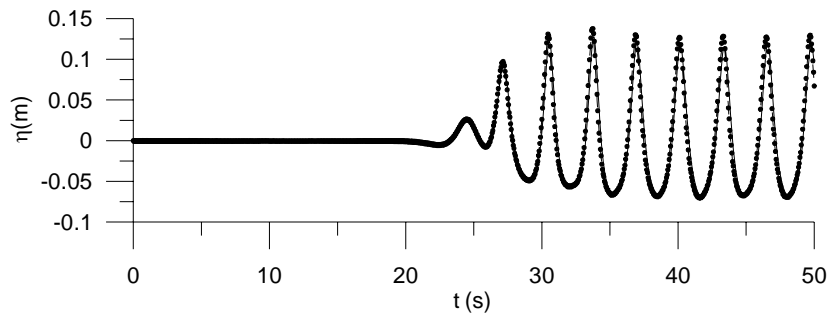
(a) Input Velocity obtained from the Paddle Displacement



(b) Wave Surface Elevation at 4.849m

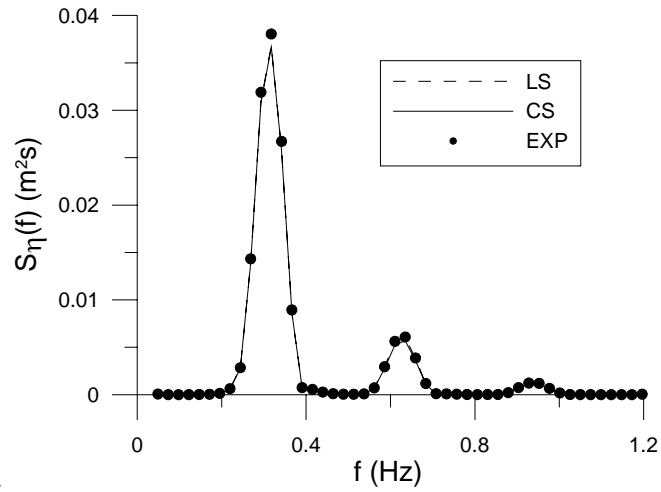


(c) Wave Surface Elevation at 25.136m

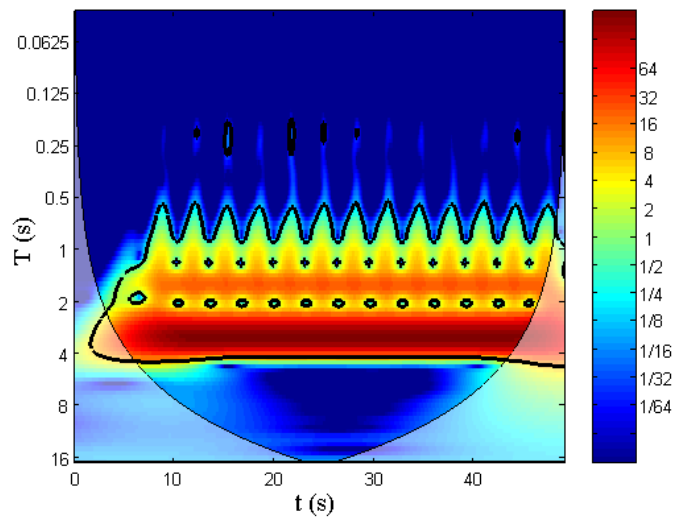


(d) Wave Surface Elevation at 50.609m

Fig. 4.35 Input Velocity and Time Histories Comparison to Simulate a Cnoidal Wave of Ursell Number 41 [CN3: ●●●●● EXP; - - - - LS; — CS]

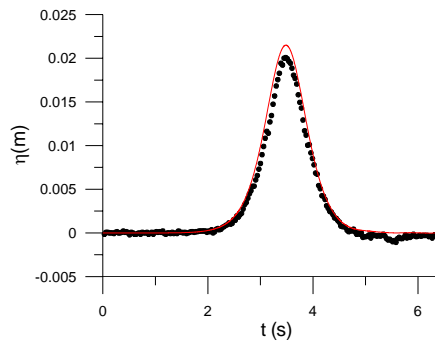


(a) Fourier Power Spectra

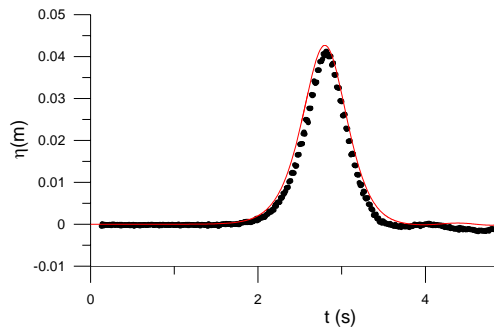


(b) Wavelet Power for EXP

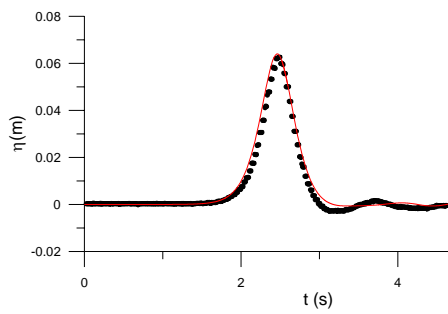
Fig. 4.36 Fourier and Wavelet Spectrum for Time History near to the Paddle [CN3]



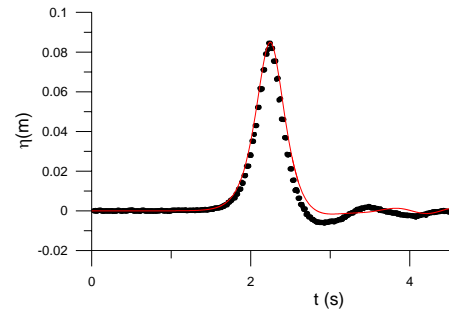
(a) $H/h = 0.1$



(b) $H/h = 0.2$



(c) $H/h = 0.3$



(d) $H/h = 0.4$

Fig. 4.37 Comparison of Time Histories for Solitary Waves [••••• EXP; — Numerical]

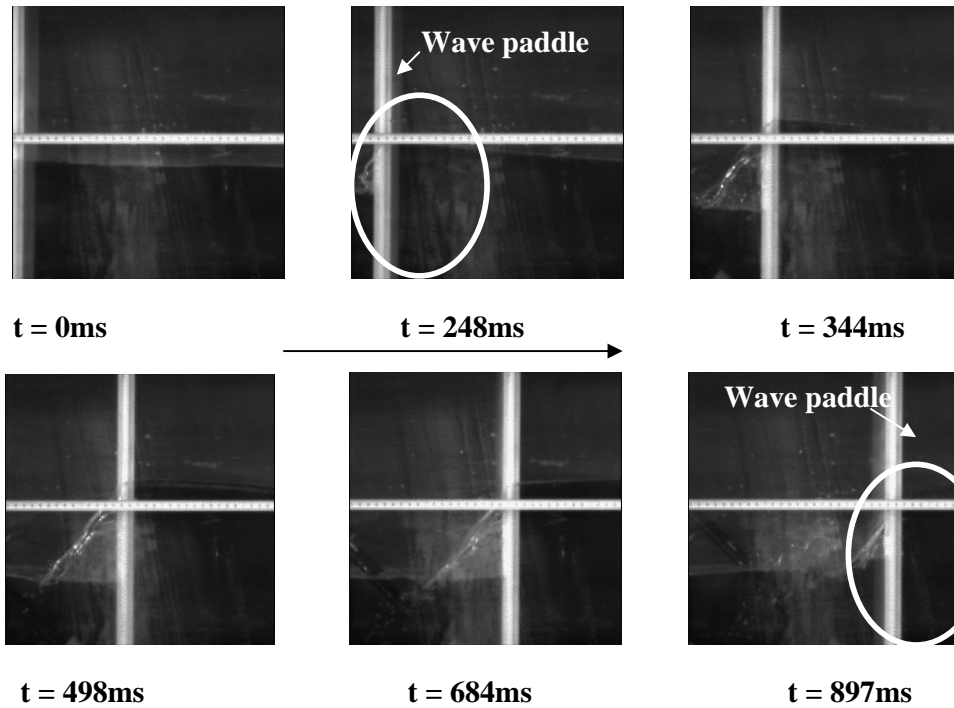


Fig. 4.38 Snap Shots of the Water Flowing through the Side Walls

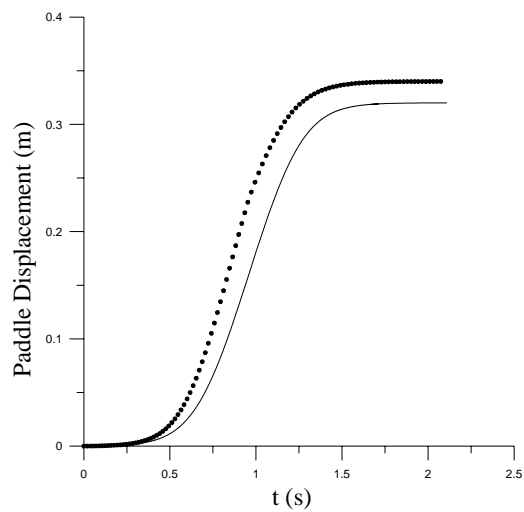


Fig. 4.39 Generated Signal [—] and the Tuned Signal [•••••] to the Wave Paddle to Generate the same Wave Height [$H/h = 0.1$]

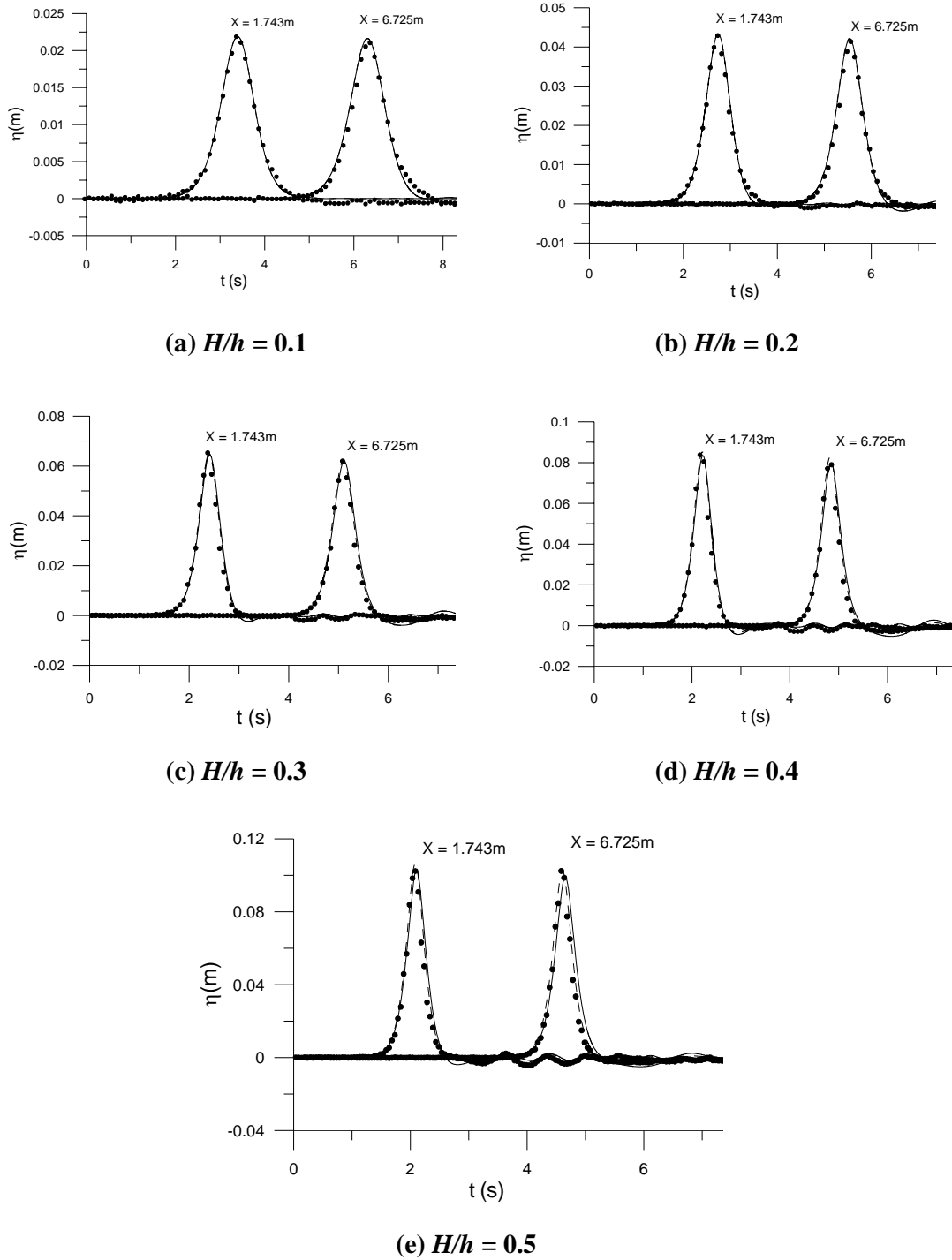
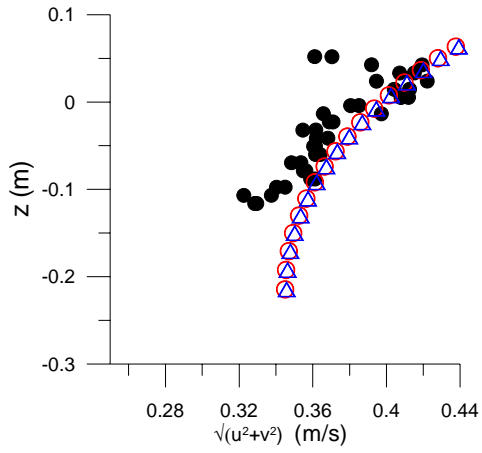
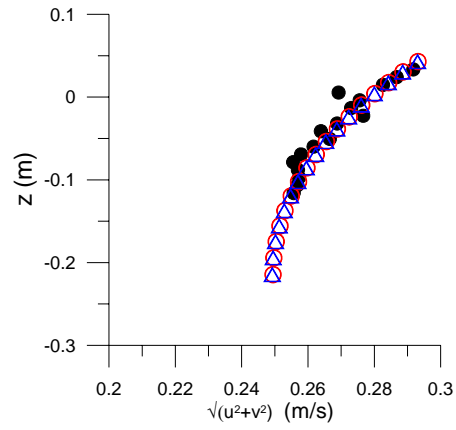


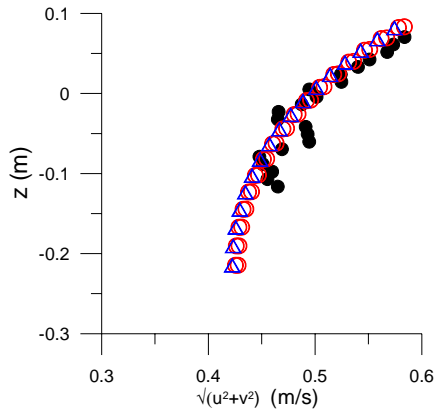
Fig. 4.40 Comparison of Time Histories for Solitary Waves with Modified Input Signal [••••• EXP; - - - - LS; — CS]



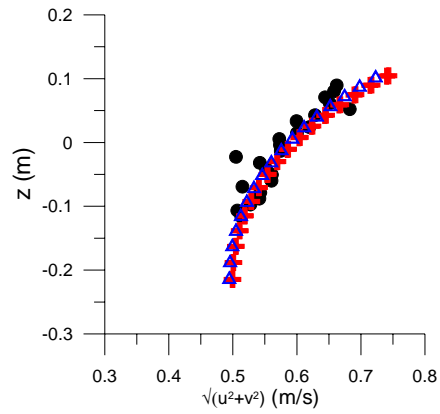
(a) $H/h = 0.2$



(b) $H/h = 0.3$

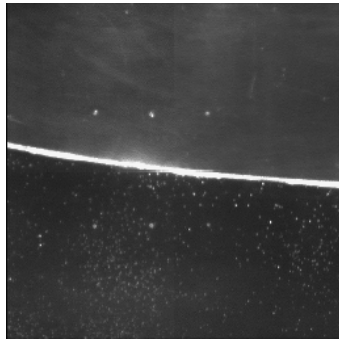


(c) $H/h = 0.4$

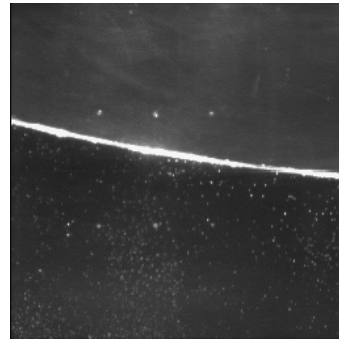


(d) $H/h = 0.5$

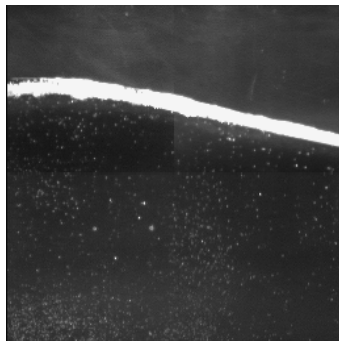
Fig. 4.41 Velocity Comparison at the Crest of the Solitary Waves for Various H/h Ratio [●●● Experiments; ○○○ LS; ▲▲▲ CS]



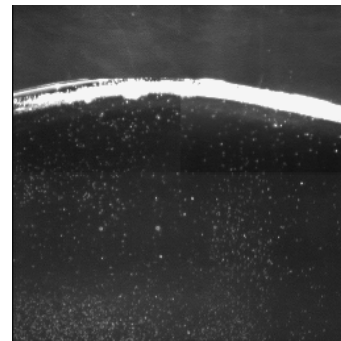
(a) Frame No. 170



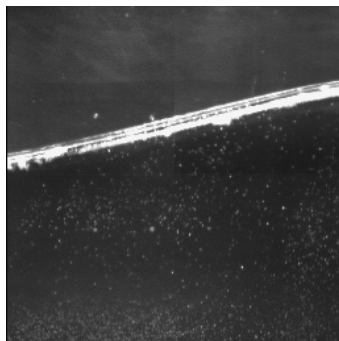
(b) Frame No. 200



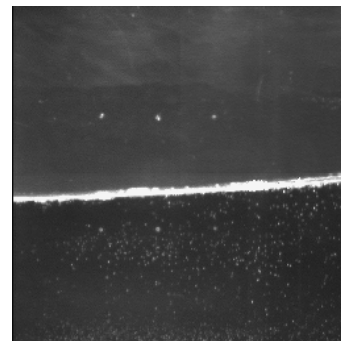
(c) Frame No. 270



(d) Frame No. 300



(d) Frame No. 370



(e) Frame No. 500

Fig. 4.42 Snapshots of the Image from CCD High Speed Camera before Processing [Sampling Interval is 2ms]

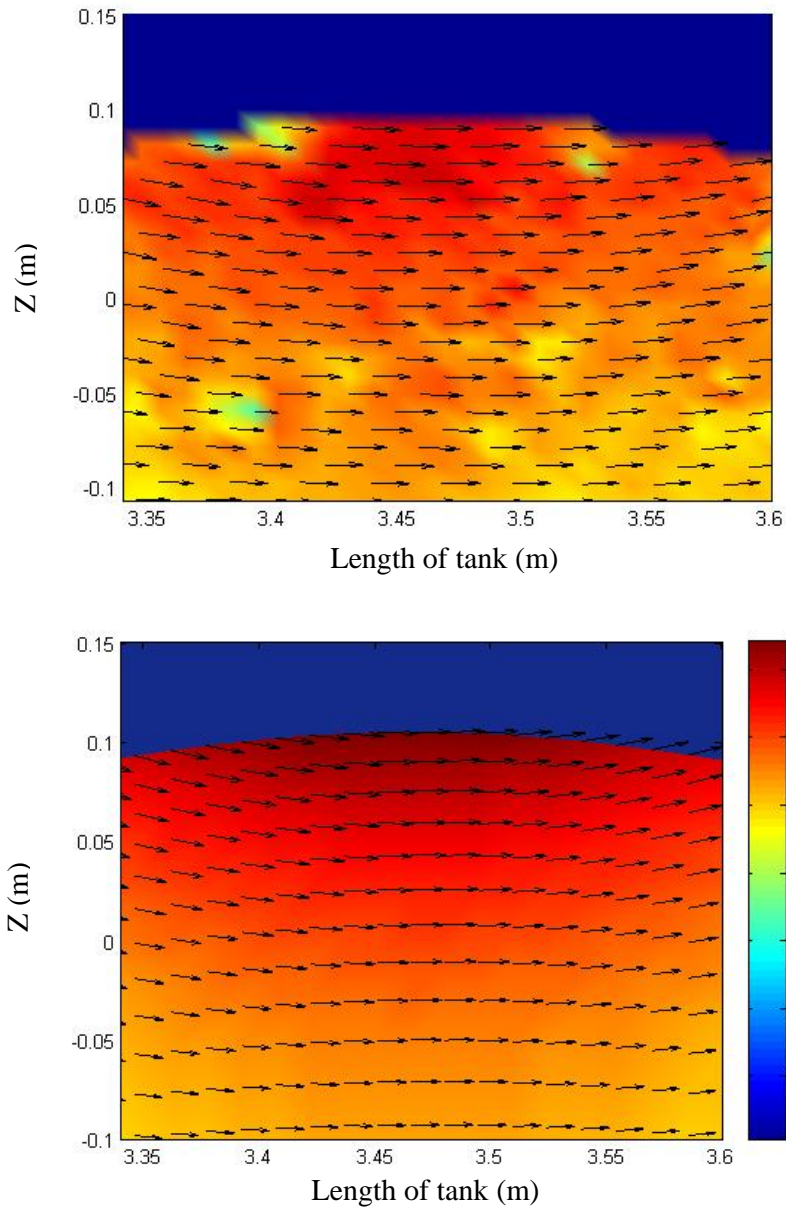


Fig. 4.43 Spatial Velocity Information of Solitary Waves obtained from PIV Measurement (Top) and Numerical Simulation (Bottom) for $H/h = 0.5$

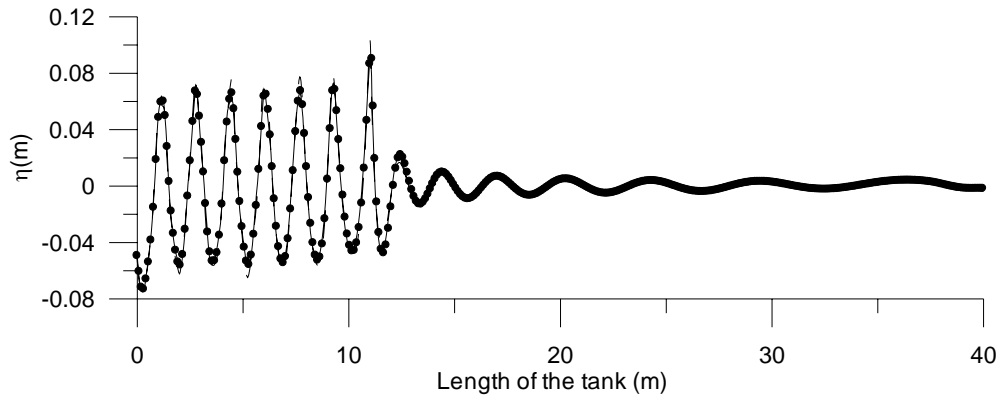


Fig. 4.44 Wave Profile at 15s along the Length of the Tank [••••• Structured Mesh; — MLS; - - - Shape Function]

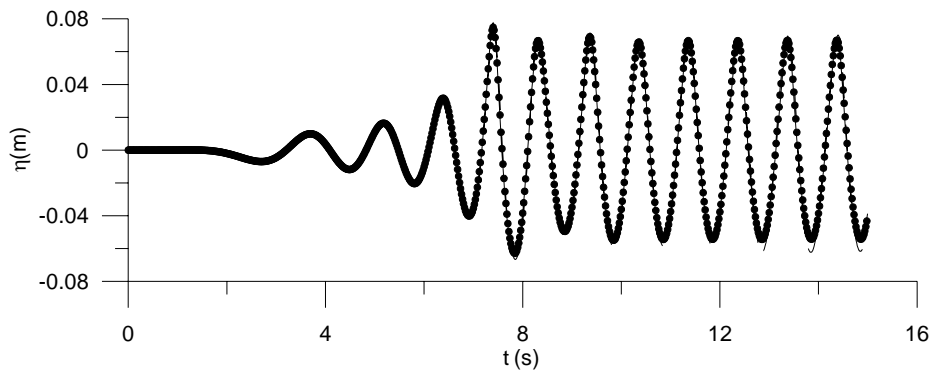


Fig. 4.45a Wave Time History at 5m [••••• Structured Mesh; — MLS; - - - Shape Function]

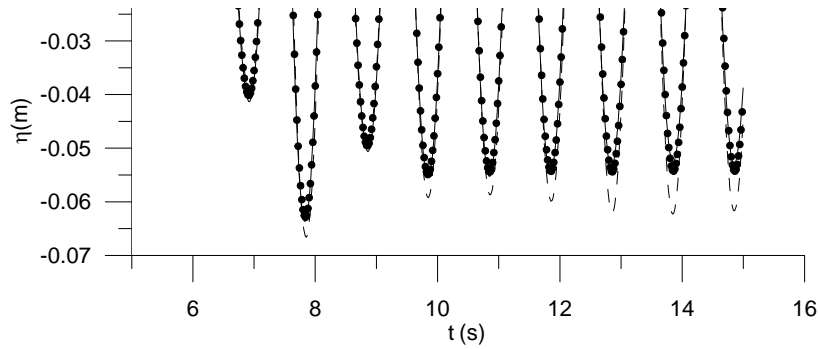


Fig. 4.45b Zoomed in View of Fig. 4. 45a

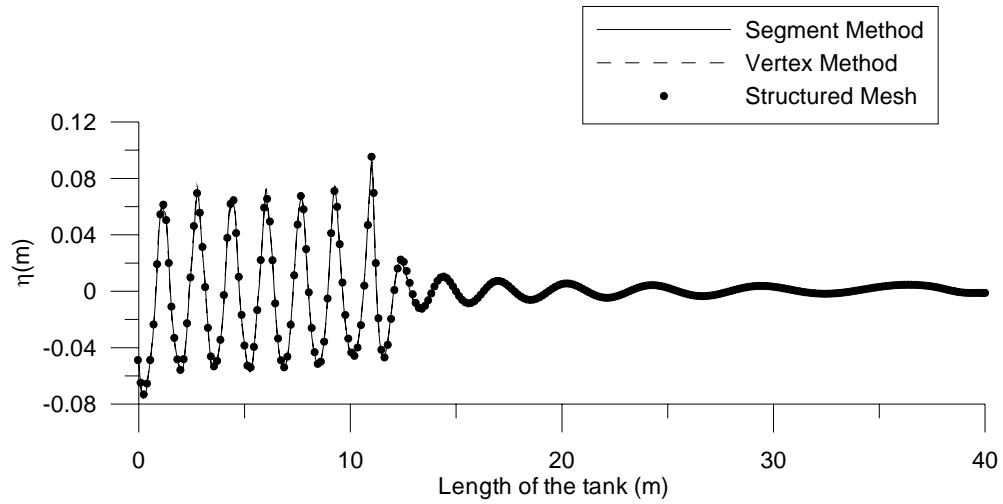


Fig. 4.46a Free Surface Profile along the Length of the Tank at 15s for Different Mesh Moving Strategies

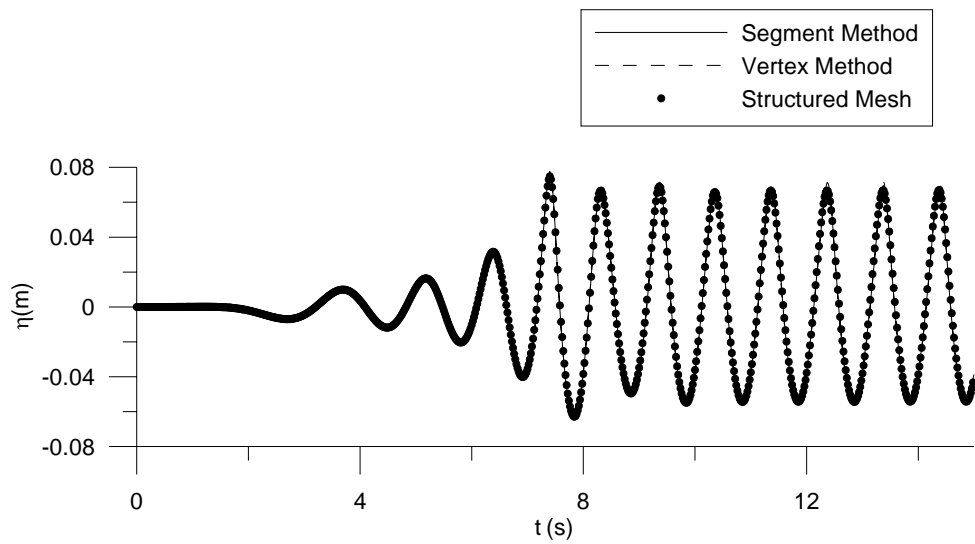


Fig. 4.46b Time Histories at 5m from the Wave Paddle for Different Mesh Moving Strategies

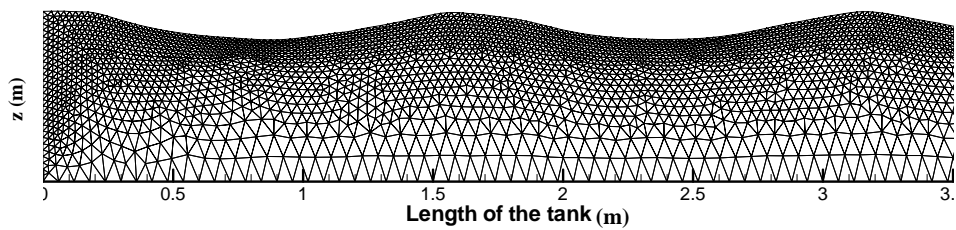
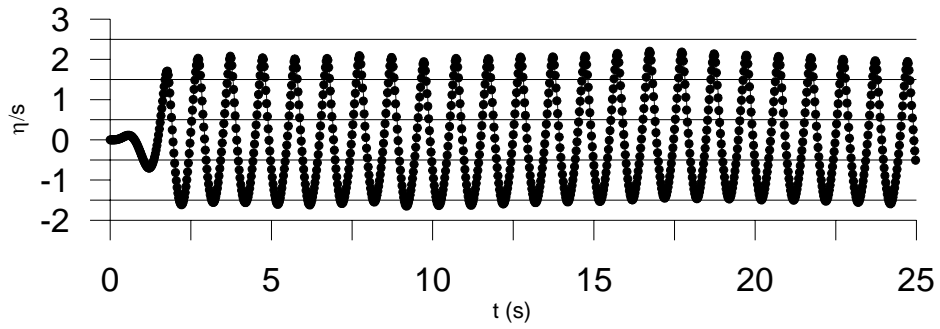
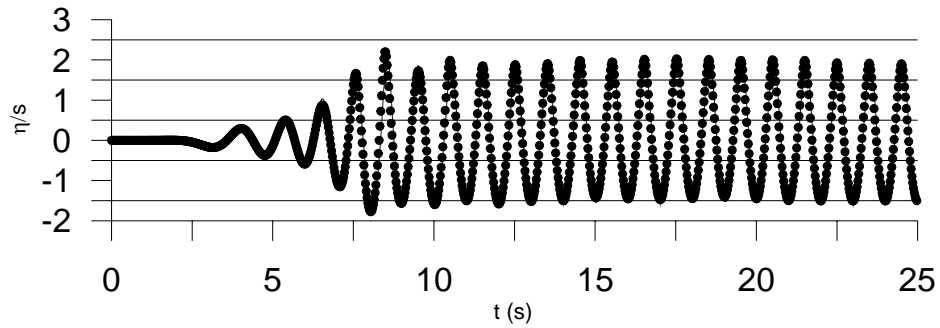


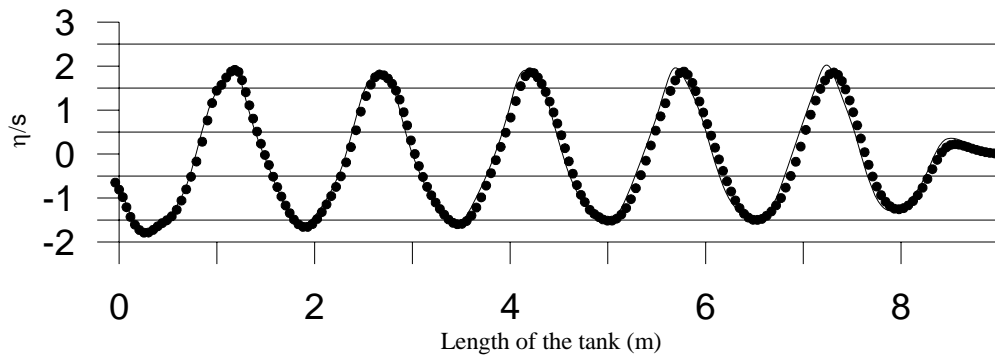
Fig. 4.47 Snapshot of the Mesh Movement using Vertex Method at 10s



(a) Time History of Free Surface Profile near the Wave Paddle

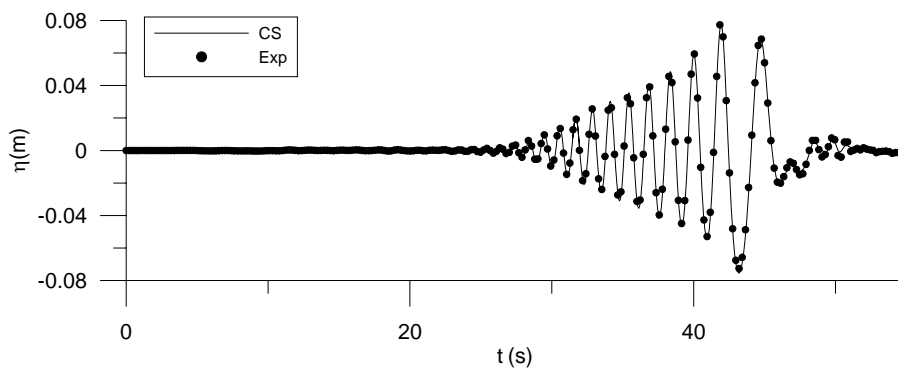
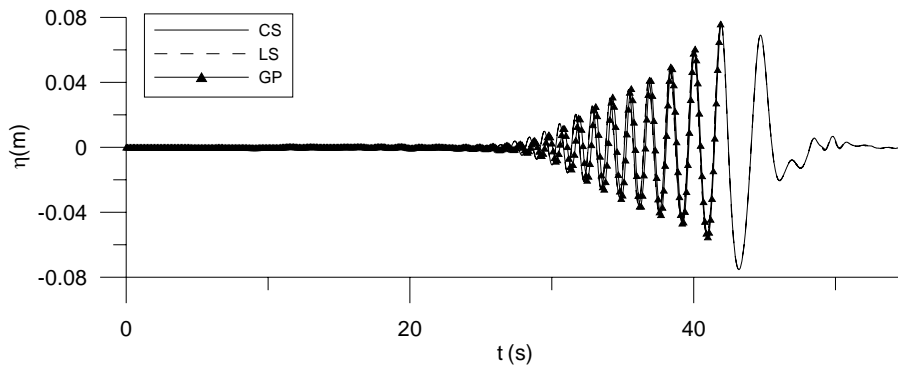


(b) Time History of Free Surface Profile a 5m from the Wave Paddle

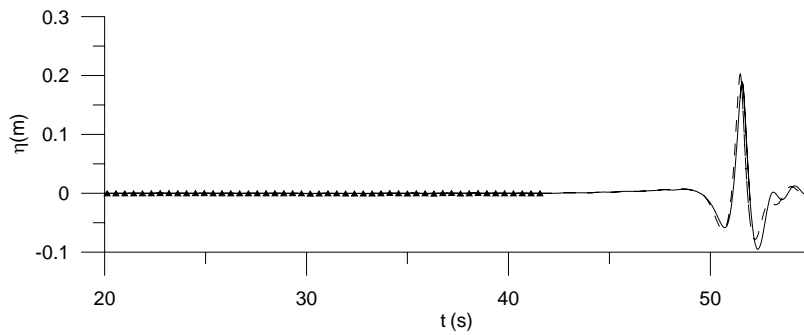


(c) Free Surface Profile along the Length of the Tank at 25s

Fig. 4.48 Comparison between Structured and Unstructured Code for a Stroke of the Wave Paddle, $0.05h$ [•••••Unstructured; — Structured]



(a) Comparison at 12.513m from the Wave Paddle



(b) Comparison at the Focusing Point (without experimental measurements)

Fig. 4.49 Time History Comparison using Different Velocity Calculation Methods for Transient Wave Packet Simulation

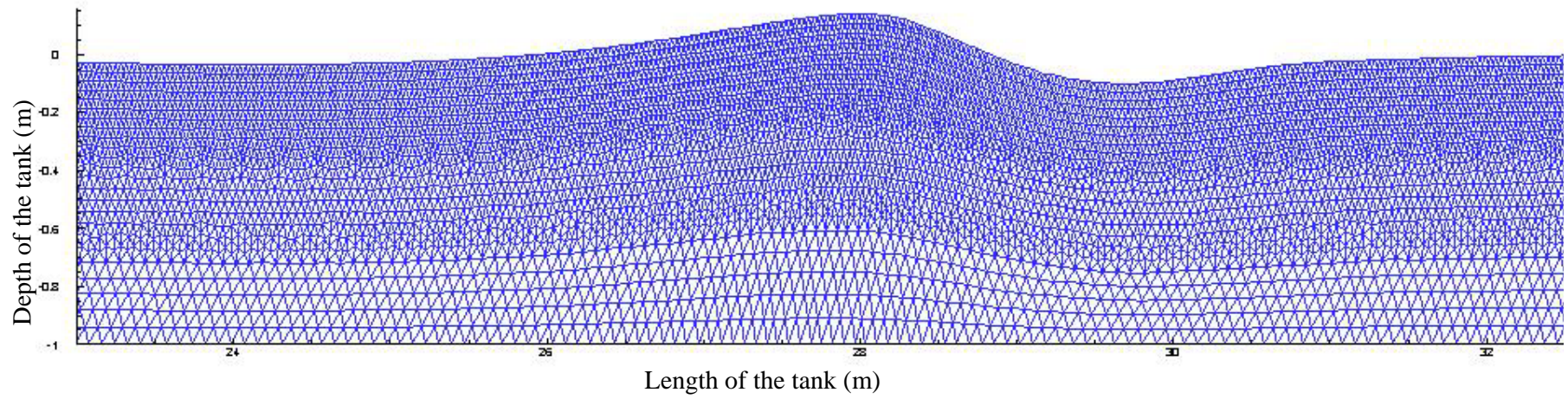


Fig. 4.50 Moved Mesh at the Focusing Point [Segment Method]

CHAPTER 5

APPLICATIONS OF NONLINEAR WAVE SIMULATION

5.1. GENERAL

In this chapter, the applications of the developed model for various wave-structure interaction problems are investigated. Two typical experimental results available in the literature are used to test the applicability of the present model [based on CS and LS as the velocity calculation methods] to the wave propagation problem. The model is further extended to the propagation of the solitary waves over the continental shelf and its interaction with a vertical wall. A typical test for the unstructured mesh implementation to a surface piercing structure and a submerged cylinder near the free surface are investigated. The nonlinear wave interaction with structure itself is a topic of intense research and, hence, a detailed investigation on a particular topic is beyond the scope of the present research work. The last section of this chapter shows an in-depth analysis on the sloshing waves generated by two types of excitatory motion, viz., horizontal and vertical excitations corresponding to the sway and heave motion of a ship.

5.2 WAVE PROPAGATION MODELLING

5.2.1 General

The accurate description of wave nonlinearity and wave dispersive characteristics are essential since, the dispersive character of free higher harmonics is a major factor i.e, the amount of energy transferred between the harmonics. When the wave form propagates over submerged obstacle, the leeside of the obstacle is in relatively deep water region. Hence, nonlinearity tends to become weak leading to the non-existence

of bound waves (nonlinear distortion of the long waves). Drastic changes in the wave form takes place due to the higher harmonics that travel with different phases. Thus, predicting the above said phenomena proves to be a classical case study to test the applicability of the numerical model for wave–propagation models.

5.6.2. Interaction with Submerged Bar I

The interaction of small steep waves with a submerged bar was dealt by Beji and Battjes (1993, 1994) both numerically and experimentally. It was concluded that when the dispersion terms in the Boussinesq equation were not properly modelled, the waveform was poorly predicted. The experimental setup is shown in Fig. 5.1. The same domain is numerically modeled in the present study with 1101 nodes in the horizontal direction and 12 nodes in the vertical direction. A regular progressive wave of period 2 s and height of 0.02 m is generated by the wave paddle. The time step adopted is 0.02 s. The comparison of the free surface elevation with the experimental data at different locations over the up-slope as well as over the downward slope ($x = 10.5\text{m}$ to 17.3m , where x is measured from the wave board) are shown in Fig. 5.2. It shows a reasonable agreement between the numerical simulation and the experimental results. On the upstream side when the wave runs over, the waves become steeper due to shoaling, the behaviour of which is simulated well. At the end of the downward slope, a comparison between numerical simulation and experimental results exhibit slight deviations. The reason for this deviation is that over the downward slope, the transfer of wave energy between different frequency components is greater, which eventually results in turbulence. The overestimation of trough level (Fig. 5.2 f) was also noticed by the numerical model of Casulli (1999), which includes viscous and non hydrostatic pressure but neglects the effect of turbulence. The snapshot of the

mesh configuration at a particular time step near the trapezoidal section is shown in Fig. 5.3.

5.6.3. Interaction with Submerged Bar II

The experimental setup consisting of a tank of length 65m and water depth of 0.5m with a submerged bar of Ohyama *et al.* (1995) is shown in Fig. 5.4. The bar is placed at 28.3m from the wave board. The locations of the wave gauges are also shown. The same setup is reproduced in the numerical model by using the structured FEM mesh with the number of nodes in the horizontal and vertical direction as 1700 and 15 respectively. This numerical setup is used to carry out for all the test cases. The characteristics of the regular waves adopted for the study are shown in Table. 5.1.

The free surface profile over the length of the tank near the submerged bar along with the moving mesh configuration is shown in Fig. 5.5. The spatial evolution showing drastic change in the wave form is clearly visible compared to the long wave profile before the bar. Cases A and B correspond to the short and smaller waves and case C and D represent the higher wave heights. The comparison between the experimental measurement and numerical computation is shown in Fig. 5.6. The left side of the figure shows the comparison at station 3 and the right side of the figure shows the comparison at station 5. Considering cases A and B at station 3, the comparison is in good agreement with the experimental measurements. Behind the submerged bar, in the region of dispersive wave field, the agreement is quite satisfactory, however, a slight phase shift is noticed. Considering the steep wave cases i.e., cases C and D, at station 3, a wiggling tail is seen both in experiments and numerical simulation. This is similar to the splitting of solitary waves as studied in detail using the present model in

the next section. The numerical simulation is in good agreement but there is a slight reduction in wave heights over the bar. However, behind the bar, slight discrepancy between the numerical results and that of the experimental results of Ohyama *et al.* (1995) is observed, which may be due to the disadvantage in using CS as a velocity calculation method. Hence, the LS method was applied for the present problem. The same mesh density as used earlier was applied. No smoothing/ regriding of nodes on the free surface are carried out even after adopting the LS method. The computed results are incorporated in the same figure. The results show a good agreement with the measured results and furthermore, slight phase shift that was encountered behind the bar using the CS approach is absent using this method of simulation. However, still in the simulation, some minor changes in the wave form is noticed that may be due to the viscous effect being predominant during the wave interaction with the bar in the experiments. The results given by Shen *et al.* (2004) using the VOF method with the inclusion of turbulence effect reveals that their model has not predicted well at station 5 and hence had claimed room for further improvement in their viscous code. This also justifies the well known fact that the potential flow assumption is a better approximation in numerical modelling which proves to be good in dealing with wave-structure interaction problems.

5.3 SOLITARY WAVES AND ITS INTERACTION

5.3.1 Split-up of Solitary Waves

The propagation of a solitary wave over an uneven topography has been numerically simulated in a flume of length 300m with a water depth of 0.5m. An initial condition

of the solitary wave profile is assumed using the relationship of Westhuis (2001) given as below,

$$\eta(x,0) = 0.215 \operatorname{sech}(1.18x) \quad (5.1)$$

The above equation generates a wave height of 0.1m corresponding to a wave steepness (H/h) of 0.2. Initially, the water surface elevation was simulated over a constant water depth in order to validate the results of the Boussinesq theory. The comparison is shown in Fig. 5.7. The wave profile captured at different time steps during propagation is also shown in Fig. 5.8. The test was followed by allowing the same wave profile to propagate over a slope that starts at 30m and ends at 40m from the source point. In order to study the splitting phenomena of solitary waves over slopes, the simulation was carried out in a water depth, h of 0.5m and allowed to propagate into a water depth, h_0 of 0.45m. The tests were repeated for different h_0 of 0.4m, 0.35m, 0.3m and 0.25m. As the wave propagates over a lesser depth beyond the slope, the height of the solitary wave increases and then disintegrates into two or more solitons depending on the water depth on the shoreward side of the slope. During this process, the wave transmission is predominant than the reflection from the bottom topography. The split-up into three solitons is visible when the wave propagates over the water depth of 0.25m considered in the study (Fig. 5.9). The solitary wave reduces its speed due to the decrease in water depth leading to the splitting up into solitons at a particular time step, $t = 119s$ as can be seen in Fig. 5.10. Further, it is seen that although the initiation of the splitting of the solitons takes place, it gets amplified as the shoreward depth (h_0) decreases. In order to verify whether the split solitons also behave as solitary waves, the wave height and the speed of the solitons was compared with that of the analytical solution of the Boussinesq model. The comparison shows a

good agreement as inferred from Table 5.2. This particular application shows the robustness of the present model, through which the possibility of the splitting of a single solitary into three solitons is demonstrated, while in BEM it is able to split only upto two solitons for the test cases shown above as reported by Van Daalen *et al.* (1997).

5.3.2 Propagation of Solitary Wave over Step

The wave flume considered herein is 50m long and the water depth is 0.2m. The simulation of solitary wave for the present problem is governed by the theory of Goring (1979) as described in Chapter 3. The vertical step leading to a sudden decrease in water depth starts at 12m from the wave paddle. The locations of the numerical wave gauges for the present setup are shown in Fig. 5.11. The initial mesh discretisation for a typical case is shown in Fig. 5.12. The simulation is carried out for three different relative obstacle height ($b/h = 0.33, 0.4$ and 0.5 , where, b is the obstacle height), thus ensuring that b/h is less than 0.5 , the conditions for which the present model holds good. In the event b/h exceeds 0.5 , vortices play a major role and the wave steepness would become high closer to its critical value. It should be noted that in this study, regridding or smoothing has not been adopted. The number of nodes in the horizontal direction is 601, whereas, in the vertical direction, it is 11. The time step adopted is 0.01s. The transmission and reflection coefficients have been estimated and compared with the experimental measurements (Seabra-Santos *et al.* 1987) and first order shallow water theory based on Germain (1984) and Kabbaj (1985). Lin (2004) quoted that the transmission and reflection coefficients (K_t and K_r) based on the energy flux are more appropriate than using the conventional method for solitary wave reported by Seabra-Santos *et al.* (1987). However, in this work, in order

to compare with the experimental measurements, conventional method of finding K_r ($= H_r/H_i$) and K_t ($= H_t/H_i$) is followed. The transmission coefficient for the three different obstacles of different heights is shown in Fig. 5.13. The dashed vertical line shows the breaking limit. It can be seen that K_t based on the present method is in good agreement with the experimental measurements, while the first order shallow water theory over predicts K_r . The dependence of K_t on wave steepness (H_i/h) in the experimental measurements is due to the presence of viscous damping as quoted by Seabra-Santos *et al.* (1987). The reflection coefficient for different obstacles is shown in Fig. 5.14. The experimental data is provided only for $b/h \geq 0.5$. The comparison with the experimental measurements for $b/h = 0.5$ is found to be good as can be seen in Fig. 5.14c. The reflection coefficient is found to depend on the incident wave steepness (H_i/h). The first order shallow water theory under predicts K_r . It was claimed by Seabra-Santos *et al.* (1987) that the above said variation was due to the formation of vortices near the step being dominant as wave steepness increases. It is felt that this may not be true as the present model which is based on inviscid flow theory also exhibit a similar trend in its variation. Hence, the probable reason may be due to the fact that the transmitted energy is predominant than the reflected energy as the steepness increases.

5.3.3 Propagation of Solitary Wave over Smooth Slope

The solitary wave over a water depth of 0.2m was then allowed to propagate over different slopes over an obstacle of height 0.1m into a water depth, h_0 of 0.1m. Instead of having sharp corners over the slope, it is approximated as a half sinusoidal profile i.e., $b\sin(0.5\pi x/l)$, where l is the horizontal length of the slope. It can also be noted that in real field situation, presence of sharp corners over the slope is rare. If there are

sharp corners, vortices would exist, while, the present model is based on inviscid theory. Hence, the result produced by the numerical model is practically valid. The tested slopes are 1:10, 1:20, 1:40 and 1:50 that would correspond to l of 1m, 2m, 4m and 5m, respectively. The simulation is carried out for different incident wave steepness and for different slopes. In order to show the reflection and transmission characteristics with respect to slope at two different locations, the wave profile, one near to the slope and the other at the reduced water depth for the incident wave steepness (H/h) of 0.215, are shown in Fig. 5.15a and Fig. 5.15b, respectively. It can be noted that the first transmitted wave is in phase with the incident wave and shows an increase in amplitude as the slope becomes flatter, while, there is a phase shift and decrease in amplitude of the second transmitted profile as the slope becomes flatter. This is due to the fact that for the steeper slope, the split up or fission process occurs faster than that for the flat slope which can be seen in Fig. 5.15d. The reflected wave decreases as the slope becomes flatter as can be seen in Fig. 5.15c. Thus, when the solitary wave enters the flatter continental slope, the reflection become less, whereas, the transmission is large compared to when it propagates over a steep slope.

5.3.4 Solitary Wave Interaction with Vertical Wall

In order to understand the interaction of solitary wave with vertical wall, the tests were carried out with a wall positioned at 10m from the wave board in a constant water depth of 0.3m. The run up and the forces on the vertical wall are analysed. The simulation was carried out for relative wave steepness, (H/h) varying between 0.1 and 0.6. The number of grid nodes in horizontal and vertical directions are considered as 301 and 13, respectively. The time step adopted is 0.01s. The comparison of the results for run up (R) from the present simulation with that of Fenton and Rienecker

(1982) which is based on Fourier method is shown in Fig. 5.16a. The comparison is found to be good for the waves with steepness ranging between 0.1 and 0.4. For waves with higher steepness, the run-up prediction is found to be higher than that of Fourier method. In the present computation for high steepness, the waves are not truly solitary type due to an increase in the trailing waves. In the Fourier method, this may not be replicated in the absence of higher order terms. The comparison between the maximum horizontal forces using the present method with that of second order empirical results (Fig. 5.17) is found to be good.

There have been conflicting reports concerning the shape of the wave profile after reflection. The numerical model from Chan and Street (1970) and second order analytical results from Byatt-Smith (1971) claimed that the wave remains unchanged. Similar conclusion has been drawn from the third-order results of Su and Mirie (1980) but it has been reported that a third order asymmetric about the crest, part of which appeared as dispersive trailing waves. While, Maxworthy (1976) found experimentally that the reflected wave assumes a shape that is clearly steeper than that of the incoming wave, and moves faster. Fenton and Rienecker (1982) noticed a reduction in wave height and the formation of trough on the reflected wave, with a marked increase in its celerity. In the present simulation, for small steepness, the reflected wave shows a reduction in its height (Fig. 5.18a), but for steep waves, the reduction in the crest height as well as the formation of trough (Fig. 5.18 (b-e)) is noticed following the observation of Fenton and Rienecker (1982). The reason for an increase in celerity as quoted by Fenton and Rienecker (1982) is due to the formation of trough, thus, the effective wave height increases. But, it has been unable to explain the above said phenomenon for the low steepness when trough is absent. This reason

is explained based on the continuity of flow condition written in terms of the horizontal water particle velocity (u) of the wave multiplied by the water depth (h),

$$(uh)_i = (uh)_r \quad (5.2)$$

where, i and r represent incident wave and reflected wave, respectively. Based on long wave theory,

$$u = \frac{\eta C}{h} \quad (5.3)$$

where, C is Celerity. Substituting Eqn. (5.3) in Eqn. (5.2) leads to,

$$(\eta C)_i = (\eta C)_r \quad (5.4)$$

where, $C = \sqrt{gh}$ Thus, as per continuity condition, when the wave elevation decreases, the celerity should increase, which explains the reason for an increase in the wave celerity with a lesser steepness as well as this holds good even for the high steep waves. The increase in celerity (ΔC) and difference in wave elevation of the incident and reflected wave ($\Delta \eta$) with respect to wave steepness is depicted in Figs. 5.19a and b, respectively. The comparison with the cubic fit as suggested by Fenton and Rienecker (1982) shows a good agreement.

The pressure time history at the free surface and at the bottom of the vertical wall for different steepness is shown in Figs. 5.20a and b, respectively. The nonlinearity in terms of double peak is predominant for both the location under consideration. This shows the existence of nonlinearity across the entire depth, as it should be for the shallow water waves. Moreover, for higher steepness ($H/h = 0.55$), it shows that the simulation breaks down, which is due to the crossing of the nodal points. This particular effect can be explained by the fact that the pressure becomes zero and

eventually the water falls from the free surface suddenly, i.e, the wave breaking takes place. The present formulation is based on inviscid fluid and moreover the mesh is structured. So, overturning of waves could not be modelled. The forces on the vertical wall for different wave steepness are shown in Fig. 5.21. The trend in the variation of total force on the wall is similar to the free surface pressure variation.

5.4 WAVE INTERACTION WITH A RECTANGULAR OBJECT

A rectangular object with $D/B = 0.5$ (where, D and B are the depth and breadth of the object) is considered at the center of the tank. The tank size considered for this case is 10m. The frequency (σ) is taken as $1.25 \sqrt{2g/B}$ that corresponds to the wavelength of $2B$. The water depth is 0.5 times the wavelength. Diffraction effects are considered to be large at this frequency. The mesh configuration at a particular time step with the object is shown in Fig. 5.22. This study has been carried out to prove the capability of the unstructured model in handling complex problems. Waves of two different steepness were considered in the study. The free surface profile on the upstream of the body ($x = 3.5\text{m}$) is shown in Fig. 5.23a. It is clearly seen that the steeper wave travels faster. Standing wave of amplitude twice that of the incident wave is observed on the upstream side of the body as can be seen in Fig. 5.23b. The transmission of waves is observed to be negligible on both the cases as shown in Fig. 5.23c. Based on the linear theory, the incident waves are fully developed on the upstream of the body at $t/T > 8$. Thus, at this frequency, the body acts as a vertical wall reflecting most of the incident wave energy and transmitting only a small part of energy onto the downstream side.

5.5 WAVE INTERACTION WITH A SUBMERGED CYLINDER

A submerged horizontal cylinder of diameter 0.12m is placed at a distance of 10m from the paddle. The centre of the cylinder is 0.12m below the still water level. The mesh structure near the cylinder is shown in Fig. 5.24. In order to compare with the experimental measurements, a regular wave of height, 0.002m and frequency, $1.8485\sqrt{g/h}$ is generated in a water depth of 1m. This case corresponds to Case E of Chaplin (1984). The simulated wave profile with and without the cylinder at 5m, 10m and 12m from the wave board are shown in Fig. 5.25. It is clearly evident that there is no difference in the wave profile before the wave encounters the cylinder, whereas, a phase shift has been developed while the wave propagates over the cylinder and continued to propagate with a phase shift ($x = 12\text{m}$). This is in agreement with the observation made by Chaplin (1984) that after the wave passing over the cylinder, a phase lag of 15° is noticed. Moreover, Dean (1948) showed an interesting result that the reflection coefficient for a submerged cylinder is zero to first-order. This is shown in Fig. 5.25d, proving that there is no reflection from the cylinder. Even though, there is a phase shift after the wave passing over the cylinder, the wave height remains the same in the presence of the cylinder. The force on the submerged cylinder is also calculated by integrating the pressures over the surface, the force component is split into \mathbf{F}_a and \mathbf{F}_b to clearly depict the mean vertical force.

$$F_a = -\rho \int_{\Gamma_d} \frac{\partial \phi}{\partial t} \begin{pmatrix} n_x \\ n_z \end{pmatrix} d\Gamma_d \quad (5.5a)$$

$$F_b = -\frac{\rho}{2} \int_{\Gamma_d} \left(\left(\frac{\partial \phi}{\partial x} \right)^2 + \left(\frac{\partial \phi}{\partial z} \right)^2 \right) \begin{pmatrix} n_x \\ n_z \end{pmatrix} d\Gamma_d \quad (5.5b)$$

The x - and z - components of force, \mathbf{F}_a and \mathbf{F}_b are shown in Fig. 5.26 and Fig. 5.27, respectively. The amplitude of the force component builds up and reaches a steady state after 20s, since for the input profile the *tanh* tapering is used to remove the transient waves. The phase shift in the x and z component of the force time histories is clearly visible for \mathbf{F}_a , whereas, for \mathbf{F}_b , a mean vertical force component is observed. The non dimensional mean vertical force component for the present method is 0.191 which is in excellent agreement with the results from analytical model (Ogilvie, 1963) of 0.190 and with the experimental results of (Chaplin, 1984) of 0.187.

5.6 SIMULATION OF SLOSHING WAVES

5.6.1. General

The need for numerical modeling of sloshing waves arises due to the significant importance of the higher order effects for the sloshing waves which are nonlinear. Neither the linear nor the second order potential considerations are sufficient enough to describe steep waves (Frandsen, 2004). The advantage of the numerical modelling is the flexibility in the simulation of the real sea state situation that has been carried out herein. The viscous effects play an important role after a critical depth (Faltinsen *et al.* 2000). Based on the dimensions of the tank, in the case of horizontal excitation, Wu *et al.* (1998) reported the transition from standing wave form to progressive waves in the form of a bore. Hence, the dimensions of the tank are the influential parameters in the study of sloshing waves. As this section, mainly deals with the effect of random horizontal and vertical excitations, the dimension of the tank is assumed to be of constant length (L) of 2m and depth (h) of 1m, such that the depth aspect ratio (h/L) is 0.5. The present numerical model is initially validated with the

numerical work of Frandsen (2004) for regular motions and then applied for the computation of the sloshing due to random excitation, which is elaborated in detail. It is worthwhile to note that the results presented herein, give rise to more questions than answers.

5.6.2. Mathematical Formulation

Let $O_0 x_0 z_0$ be the fixed coordinate system and $O x z$ be the moving coordinate system fixed with the tank. These two coordinate systems coincide with each other when the tank is at rest. The origins of this system are at the left end of the tank wall at the free surface and pointing upwards in z - direction. These two coordinates along with the prescribed boundary conditions in each coordinate system is represented in Figs. 5.28a and b.

The displacements of the tank are governed by the directions of axes as,

$$X_t = [x_t(t), z_t(t)] \quad (5.6)$$

On the assumption that the fluid is governed by potential flow theory, the velocity potential ϕ satisfies the Laplace equation.

$$\nabla^2 \phi = 0 \text{ in the fluid domain, } \Omega \quad (5.7)$$

The component of the water particle velocity normal to the walls of the tank is equal to the tank velocity.

$$\frac{\partial \phi}{\partial n} = U \cdot n \text{ in the side walls, } \Gamma_B \quad (5.8)$$

where, $U = \frac{dX_t}{dt}$ is the velocity of the tank and n is outward normal to the tank walls.

The dynamic and kinematic free surface boundary condition in the fixed coordinate system can be written as,

$$\frac{\partial \phi}{\partial t} + \frac{1}{2} \nabla \phi \cdot \nabla \phi + g \eta_0 = 0 \quad (5.9)$$

$$\frac{\partial \eta_0}{\partial t} + \frac{\partial \phi}{\partial x_0} \cdot \frac{\partial \eta_0}{\partial x_0} - \frac{\partial \phi}{\partial z_0} = 0 \quad (5.10)$$

The free surface motion can be described in the moving coordinate system as,

$$\frac{\partial \phi}{\partial t} - \nabla \phi \cdot \frac{dX_t}{dt} + \frac{1}{2} \nabla \phi \cdot \nabla \phi + g(\eta + z_t) = 0 \quad (5.11)$$

$$\frac{\partial \eta}{\partial t} + \left(\frac{\partial \phi}{\partial x} - \frac{dx_t}{dt} \right) \cdot \frac{\partial \eta}{\partial x} - \left(\frac{\partial \phi}{\partial z} - \frac{dz_t}{dt} \right) = 0 \quad (5.12)$$

which is obtained by substituting the following Eqns.(5.13) and (5.14) in Eqns.(5.9) and (5.10),

$$\nabla_{x_0 z_0} = \nabla_{xz} \quad (5.13)$$

$$\left(\frac{\partial}{\partial t} \right)_{x_0 z_0} = \left(\frac{\partial}{\partial t} - \frac{dX_t}{dt} \cdot \nabla \right)_{xz} \quad (5.14)$$

on $z=\eta$, where $\eta=\eta_0 - z_t$ is the free surface elevation in the moving coordinate system $O x z$.

Now, let the velocity potential be decomposed into,

$$\phi = \varphi + xu + zw \quad (5.15)$$

i.e., the velocity potential in the fixed coordinates system contains the velocity potential in the moving coordinates and the direction of the excitation with the corresponding velocity in that direction, u and w are the velocity components in the x and z directions. Substituting Eqn. (5.15) in Eqns.(5.7),(5.8),(5.11) and (5.12) leads to,

$$\nabla^2 \varphi = 0 \text{ in the fluid domain, } \Omega \quad (5.16)$$

$$\frac{\partial \varphi}{\partial n} = 0 \text{ in the side walls, } \Gamma_B. \quad (5.17)$$

The dynamic and kinematic free surface condition becomes,

$$\frac{\partial \varphi}{\partial t} + \frac{1}{2} \nabla \varphi \cdot \nabla \varphi + g \eta + x x_T'' + \eta z_T'' = 0 \quad (5.18)$$

$$\frac{\partial \eta}{\partial t} + \frac{\partial \varphi}{\partial x} \cdot \frac{\partial \eta}{\partial x} - \frac{\partial \varphi}{\partial z} = 0 \quad (5.19)$$

Rewriting the above equations in Lagrangian form of motion following Longuet-Higgins and Cokelet (1976),

$$\frac{d\varphi}{dt} = \frac{1}{2} \nabla \varphi \cdot \nabla \varphi - (g + z_T''(t)) \eta - x x_T''(t) \quad (5.20)$$

$$\frac{dx}{dt} = \frac{\partial \varphi}{\partial x} \text{ and } \frac{dz}{dt} = \frac{\partial \varphi}{\partial z} \quad (5.21)$$

where, $x_T''(t) = \frac{du}{dt}$ and $z_T''(t) = \frac{dw}{dt}$

The initial condition of the system can be assumed as,

$$\phi(x_0, z_0, t) = 0 \quad (5.22)$$

$$\eta_0(x_0, t) = \zeta_0 \text{ where } t = z_0 = 0 \quad (5.23)$$

In moving coordinates, at $t = 0$ and $z = 0$, the above equations become,

$$\varphi(x, 0, 0) = -xu \quad (5.24)$$

$$\eta(x, t) = 0 \text{ for horizontal excitation.} \quad (5.25a)$$

$$\eta(x, t) = \zeta_0 \text{ for vertical excitation} \quad (5.25b)$$

where, ζ_0 is the non physical condition, specifying the initial elevation.

Based on the initial condition, the boundary value problem is solved and the free surface elevation and potential values are updated at the subsequent time steps. Eqns.(5.17), (5.20) and (5.21) form the boundary conditions. Thus, this form of boundary conditions reduces the computational burden of creating a finer mesh structure along the free surface boundary, since the tank excitation is incorporated in the kinematic and dynamic free surface boundary condition.

Formulating the governing Laplace's equation constrained with the associated boundary conditions (without considering the Dirichlet condition), it leads to the following finite element formulation [as per Eqn.3.14],

$$\int_{\Omega} \nabla N_i \sum_{j=1}^m \phi_j \nabla N_j d\Omega = 0 \quad (5.26a)$$

The above equation can be rewritten in the matrix form and the Dirichlet condition on the free surface can be imposed as,

$$\mathbf{A}_{ij} \Phi = \mathbf{B}_i \quad (5.26b)$$

Where,

$$\mathbf{A}_{ij} = \begin{cases} \int_{\Omega} \nabla N_i \nabla N_j d\Omega, & i, j \notin \Gamma_s \\ 1 & , i = j \& j \in \Gamma_s \\ 0 & , (i \in \Gamma_s \text{ or } j \in \Gamma_s) \& i \neq j \end{cases} \quad (5.26c)$$

$$\mathbf{B}_i = \begin{cases} 0 \\ \phi_i \end{cases}, i \in \Gamma_s \quad (5.26d)$$

5.6.3 Input Generation

Regular wave excitation

The container is assumed to take the following horizontal and vertical oscillations,

$$x_T(t) = a_h H(\omega_h t) \quad (5.27a)$$

$$z_T(t) = a_v V(\omega_v t) \quad (5.27b)$$

where $a_{h,v}$ and $\omega_{h,v}$ are the characteristics excitation amplitude and excitation frequency. The motion of the container is assumed as $V(\chi) = H(\chi) = \cos(\chi)$.

For the rectangular container, the order of the natural frequency is (Faltinsen, 1974)

$$\omega_n = \sqrt{gk_n \tanh(k_n h)}, \quad n = 1, 2, 3, \dots \quad (5.28)$$

where, the wave number is given by $k_n = n\pi/L$.

Random wave excitation

In this study, Bretschneider spectrum is used as the input wave spectrum which is given by,

$$S_\eta(\omega) = \frac{5H_s^2}{16\omega_p} \left(\frac{\omega_p}{\omega}\right)^5 \exp\left[-\frac{5}{4}\left(\frac{\omega_p}{\omega}\right)^4\right] \quad (5.29)$$

The free surface elevation is described by,

$$\eta = \sum_{i=1}^{N_w} a_i \cos(\omega^i t + \psi^i) \quad (5.30)$$

where, a_i is the amplitude that is defined as $a_i = \sqrt{2S_\eta(\omega)\Delta\omega}$.

N_w is the number of sinusoidal wave components, ω^i and ψ^i are the frequency and the phase angle, wherein the frequency ranges from 0 to π/dt and phase angle (random variable based on the fixed seed number is used in this study) ranges from 0 to 2π . Herein, ω_p and H_s are the peak frequency and significant wave height. In this study, the range of frequency has been taken up to the cut off frequency and is assumed to be

five times the natural frequency of the container; since the higher frequency will not have much influence on the generated waves. Based on the spectrum, the random waves are generated which are given as the input to the oscillation of the container, thus, the Eqn.(5.25) is assumed to be

$$x_T(t) = \sum_{i=1}^{N_W} a_i \cos(\omega^i t + \psi^i) \text{ for horizontal random oscillation} \quad (5.31)$$

$$z_T(t) = \sum_{i=1}^{N_W} a_i \cos(\omega^i t + \psi^i) \text{ for vertical random oscillation} \quad (5.32)$$

5.6.4. Regular Wave Excitation

Horizontal excitation

The present numerical model is initially compared with analytical solution from Faltinsen (1974), assuming the excitation velocity as $a_h \omega_h \cos(\omega_h t)$. The comparison between the numerical and the analytical results after every 2s interval is shown in Fig. 5.29. An excellent agreement is found. Further, the numerical simulation of regular waves using the present methodology is compared with the numerical results of Frandsen (2004). The displacement $Z_T(t)$ of the container is given by the Eqn. (5.27a) results in the excitation velocity as $a_h \omega_h \sin(\omega_h t)$. This leads the initial condition for velocity potential [Eqn. (5.24)] to zero and the surface elevation is considered as in Eqn.(5.25a) for this mode of excitation. For only horizontal excitation to exist, the vertical acceleration is assumed to be zero. Comparison has been made for a smaller and a steeper wave with the numerical simulation of Frandsen (2004) [Fig. 5.30]. It can be observed that both the simulation are in close agreement for the forcing frequency (ω_h) equal to seventy percent of the first mode of natural frequency (ω_1). There are 31 nodes in the x direction (free surface) and 13

nodes in the z direction. The time step adopted is 0.01s for both the simulations. An automatic regridding condition is adopted in the present study when the movement of the nodes is 75% more or less than the initial grid spacing. Smoothing is not adopted in the present simulation. It is found that no regridding is required for the simulation of small amplitude waves. In the case of steep waves, the need for regridding arises about 20 times for a simulated duration of 61.44s.

The induced sloshing time series is subjected to frequency domain analysis for a range of excitation frequency with an excitation amplitude of $a_h=0.005h$ from which the occurrence of spectral peaks is identified. The spectral density of free surface elevation in the tank for the excitation frequencies, $\omega_h = 0.35\omega_1$, $\omega_h = 0.75\omega_1$, $\omega_h = \omega_1$, $\omega_h = 1.5\omega_1$, $\omega_h = 2.0\omega_1$ and $\omega_h = \omega_3$, are depicted in Fig. 5.31. The maximum spectral peak occurs at the excitation frequency when the excitation frequency is less than the natural frequency and, a secondary peak occurs at the container natural frequency as can be seen in Figs. 5.31a and b. While, the excitation frequency is more than the container natural frequency and upto the second modal frequency [$\omega_1 < \omega_h < \omega_2 (=1.5\omega_1)$], the primary peak occurs at the first mode followed by a secondary peak at the third natural frequency (Fig. 5.31d). For excitation frequencies equal to or greater than $1.8\omega_1(=\omega_3)$, the third modal frequency dominates the sloshing motion. From Figs. 5.31c and f, the sloshing motion is more violent at the natural frequency of the container when the excitation frequency is equal to the first mode rather than at the third mode, which is a well-known resonance phenomenon. The typical moving mesh generated after every 5s interval is shown in Fig. 5.32 for the above said resonance condition.

In order to have an in-depth knowledge on the occurrence and the magnitude of the spectral peaks with respect to the excitation frequency, the above simulation was executed for different excitation frequencies. The magnitude of the first, third and excitation mode from the spectral analysis is shown in Fig. 5.33 with respect to the ratio of excitation by first mode of the container frequency (excitation frequency ratio). The figure is separated into three zoomed zones for the excitation frequency ratio between 0.2 to 1.1, 1.1 to 1.55 and 1.55 to 2.6 [Fig. 5.33a]. When the excitation frequency is less than first mode ($\omega_h < \omega_1$), the primary spectral peak is observed at the excitation frequency as inferred from the results reported in Fig. 5.33b. The response component at the first modal frequency is observed to increase as the frequency increases. When the excitation frequency is greater than first mode, the sloshing dominates at the first modal frequency upto second mode ($\omega_2=1.5\omega_1$) and till this frequency, the secondary peak is observed at the excitation frequency as can be seen in Fig. 5.33c. When the excitation frequency is greater than ω_1 , the domination of the first mode reduces with an increase in the frequency ratio. With a further increase in the excitation frequency ratio ($\omega_h \geq 1.5\omega_1$), the normalized spectral peak at third mode increases rapidly to 450 and 485 at $\omega_h = 1.72\omega_1$ and $\omega_h = 1.8\omega_1$ respectively. This can also be clearly seen in Fig. 5.33d. Furthermore, for the range of excitation frequency ratio 1.5 to 1.8, the response at the excitation frequency is insignificant. It is also observed that the sloshing is not dominant at the fifth or higher order modal frequency. Beyond the third modal frequency (ω_3), the contribution at the excitation frequency is influenced apart from oscillation at first and third modal frequency components. But, one should keep in mind that the fifth mode ($2.3\omega_1$) can

also excite. The maximum sloshing amplitude occurs, when the excitation frequency is equal to the first mode and the next largest is 5.65 times lesser occurring at ω_3 .

Vertical excitation

To simulate the condition of vertical excitation for the container, X_T is set to zero in Eqn.(5.20). The tank is assumed to be periodically excited with the displacement given by Eqn (5.27b), which leads to velocity of the form $-a_v\omega_v\sin(\omega_v t)$. Thus, initial velocity potential becomes zero according to Eqn.(5.24). The initial condition for the surface elevation is an important parameter as there should be some initial perturbation in the system for the generation of waves due to vertical excitation. The linear solution and the stability criteria of Faraday waves are given by Benjamin and Ursell (1954). In the numerical simulation, it is quite often to adopt an initial free surface perturbation of $\eta = \zeta_0 = a \cos(k_n x)$. It should be noted that this condition does not necessarily arise in the real situation because both horizontal and vertical motions co-exist. For experimental purposes, the initial perturbation is introduced in the system, by exciting tank horizontally for the prescribed time. Two typical sloshing simulations are carried out, following small amplitude motion and steep wave excitation as shown in Fig. 5.34. The steepness parameter depends on the adopted initial condition, $\varepsilon = a \omega_n^2/g$. The present simulation shows a close agreement with the numerical simulation of Frandsen (2004). The grid size and the time step adopted are the same as that for horizontal motion.

A frequency domain analysis for the sloshing motion due to vertical excitation has been carried out. Even though, it may not clearly depict the exact phenomenon of the waves such as the detonating effects as noticed by Frandsen (2004), it gives the

picture of the critical resonance condition based on the intensity as discussed in sway mode. The spectra of sloshing time series for two different initial steepness conditions of 0.014 and 0.288 and with constant excitation amplitude are presented in Fig. 5.35 and Fig. 5.36, respectively. Such plots have been reported for $\omega_v=0.75\omega_l$, ω_l , $1.5\omega_l$, $2\omega_l$ and $2.5\omega_l$. A comparison of the results presented in the above two figures reveals the following. In the case of lesser initial steepness, a single peak of the dimensionless sloshing energy is observed at frequency ratio of 1, irrespective of the magnitude of the excitation frequency. In the case of the higher initial steepness adopted in the study, the dimensionless sloshing frequency spectrum exhibits secondary peaks at $\omega/\omega_l = 1.5$ and 2 for all the ω_v tested. The magnitude of the secondary peak is insignificant compared to the primary peak at the resonance frequency. Frandsen (2004) noticed similar existence of peaks in the wave spectra.

5.6.1. Random Wave Excitation

General

In order to understand the sloshing phenomenon, the container is subjected to random excitation under the real random sea state, with different peak frequency by keeping the total supplied energy to the system as constant. Typical input excitation spectrum and the corresponding displacement time history are given in Figs 5.37a and b, respectively. The horizontal and vertical container displacements are obtained from this spectrum [Eqn.(5.31) or Eqn. (5.32)]. The surface elevations at the left wall of the container due to horizontal $(\eta/h)_h$ and vertical $(\eta/h)_v$ excitation are shown in Figs. 5.37c and d, respectively. The time step adopted is 0.06s and the duration of the

simulation is 61.44s that corresponds to 1024 data points. These are used to analyse the spectrum herein.

Horizontal excitation

For a significant wave height of $0.006h$, the tank is excited with random waves of different peak frequency ($\omega_p = 0.35\omega_1, \omega_p = 0.75\omega_1, \omega_p = \omega_1, \omega_p = 1.5\omega_1, \omega_p = \omega_3$). The power spectra of free surface sloshing elevation at the left corner of the tank wall for various excitation peak frequencies are shown in Fig. 5.38. It can be seen that while the excitation peak frequency is less than the natural frequency, the sloshing spectral peaks appear only at natural frequencies (first, third and fifth mode) of the tank and no peak is visible at the excitation peak frequency as noticed in the case of regular excitation. The primary spectral peak lies at the first mode. When the excitation peak frequency is greater than the first mode of the tank system, there were some high frequency waves in the container [Figs. 5.38 d, e and f]. Thus, in horizontal excitation, the spectral peaks appear only at the first or higher mode natural frequency, irrespective of the excitation peak frequency. Similar trend in the occurrence of spectral peaks is also noticed by Wang and Khoo (2005). The spectrum for forces and surface elevation of the tank wall were examined using FEM adopting iso-parametric elements. It has been shown that the energy mainly concentrates at the natural frequency of the container and found to dominate at the i^{th} mode of the container when the peak frequency is close to the i^{th} mode.

Vertical excitation

The sloshing behavior of the tank when subjected to random vertical excitation is studied. The container was subjected to vertical excitation with the same input

characteristics as that for horizontal motion for two different initial conditions. The initial conditions correspond to small amplitude with a steepness of 0.014 and large amplitude with a steepness of 0.288. The power spectra of waves at the left corner of the tank wall with the above initial conditions having steepness of 0.014 and 0.288 are shown in Fig. 5.39 and Fig. 5.40, respectively. It can be seen that in spite of the excitation frequency, the spectral peaks appear at the first modal frequency only while the initial perturbed waves of small steepness. The spectral peaks appear at first, second and two times the first mode (parametric) frequency, if the initial perturbed waves are of large steepness. This is similar to that of the regular wave excitation as discussed earlier for the heave mode. The dominating frequency appears at the first mode. However, the spectral peak magnitudes at the first modal frequency are of same order, irrespective of excitation peak frequency. This phenomenon is observed irrespective of the different initial perturbation in the tank. It should be noted that no regridding is necessary for small steepness case, and hence the numerical damping does not play any role for the above results. However, in the case of regular wave excitation, the magnitude of peak is higher at $\omega_v = 2\omega_l$ for small and high initial steepness.

5.7. SUMMARY

The present chapter shows the applicability of the developed model to steep wave propagation over a submerged bar, interaction of solitary waves over continental shelf and vertical wall, wave interaction with surface piercing object and submerged cylinder. In particular, a detailed investigation is carried out for the interaction of solitary waves over continental shelf and the reflection characteristics of the solitary wave profile, in order to understand the physics behind the solitary waves, owing to

the increase in research demands after Indian Ocean Tsunami 2004. The last part of this chapter gave an in-depth analysis for the sloshing waves under two different excitatory motions in regular and random sea states, which is one of the complex nonlinear phenomena for the LNG ship carrying tank.

Table 5.1 Simulated Input Wave Parameters in a Water Depth of 0.5m.

Case	Wave Period (T in sec)	Wave Height (H in m)	Ursell parameter over the shelf
A	1.34	0.025	21.6
B	1.34	0.05	43.3
C	2.01	0.05	108.7
D	2.68	0.05	201.5

Table 5.2 Comparison with the Boussinesq Model for Wave Speed in Split-up Waves. C_{nwt} – Numerical Celerity, C_{bou} – Boussinesq Celerity [$C_{Bou} = \sqrt{g(h + H)}$].

No	Wave Height(H in m)	C_{nwt}	C_{Bou}
1	0.0130	1.6	1.6064
2	0.0547	1.71	1.7289
3	0.1578	2.0	2.0001

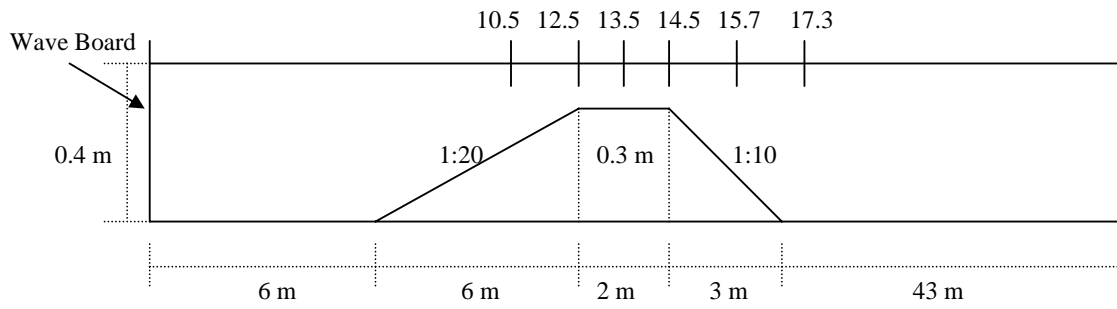


Fig. 5.1 Experimental Setup of Beji and Battjes (1993)

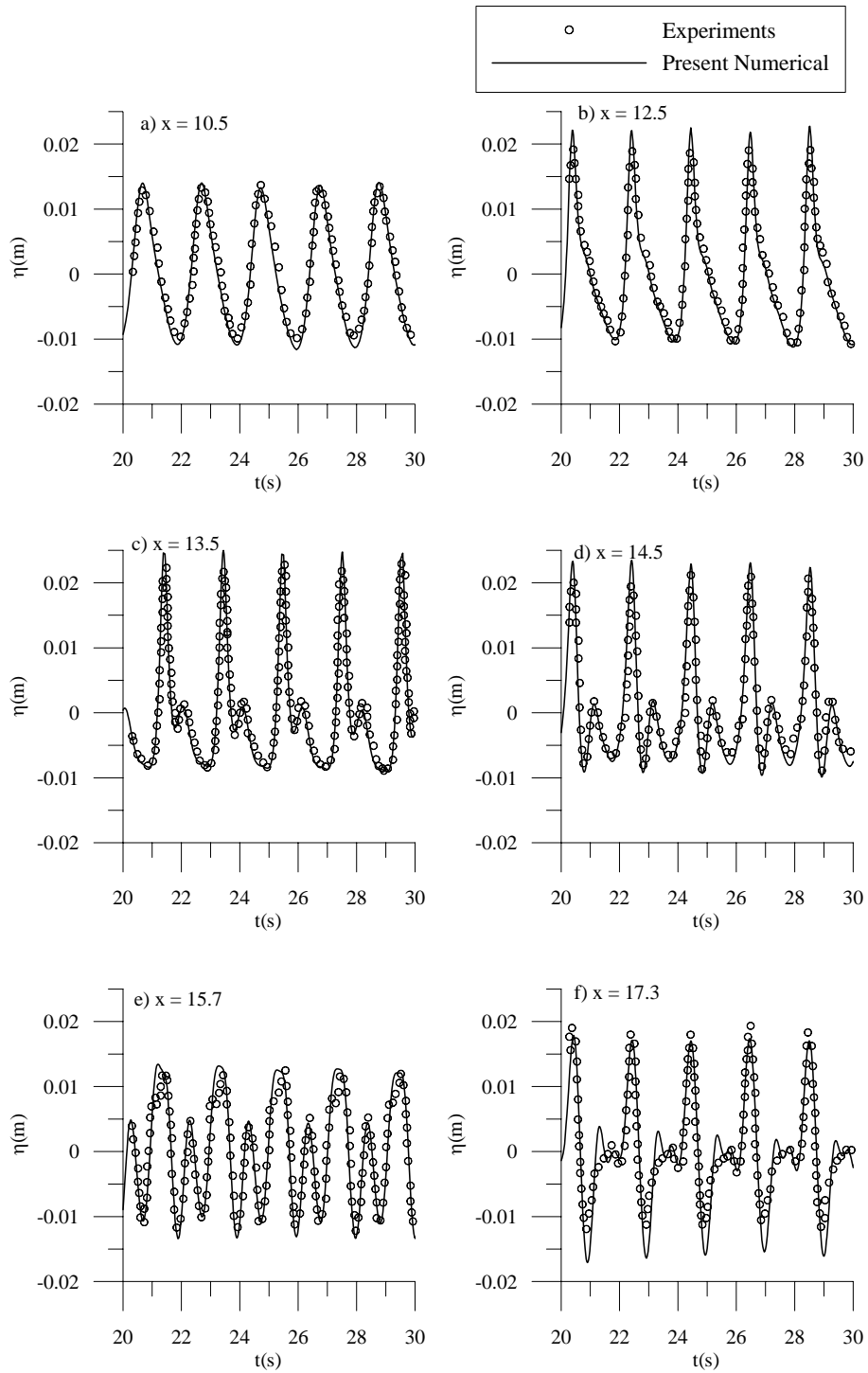


Fig. 5.2 Comparison of the Free Surface Elevation with the Experimental Measurements of Bejji and Battjes (1994) at Seven Different Position in the presence of a Submerged Bar

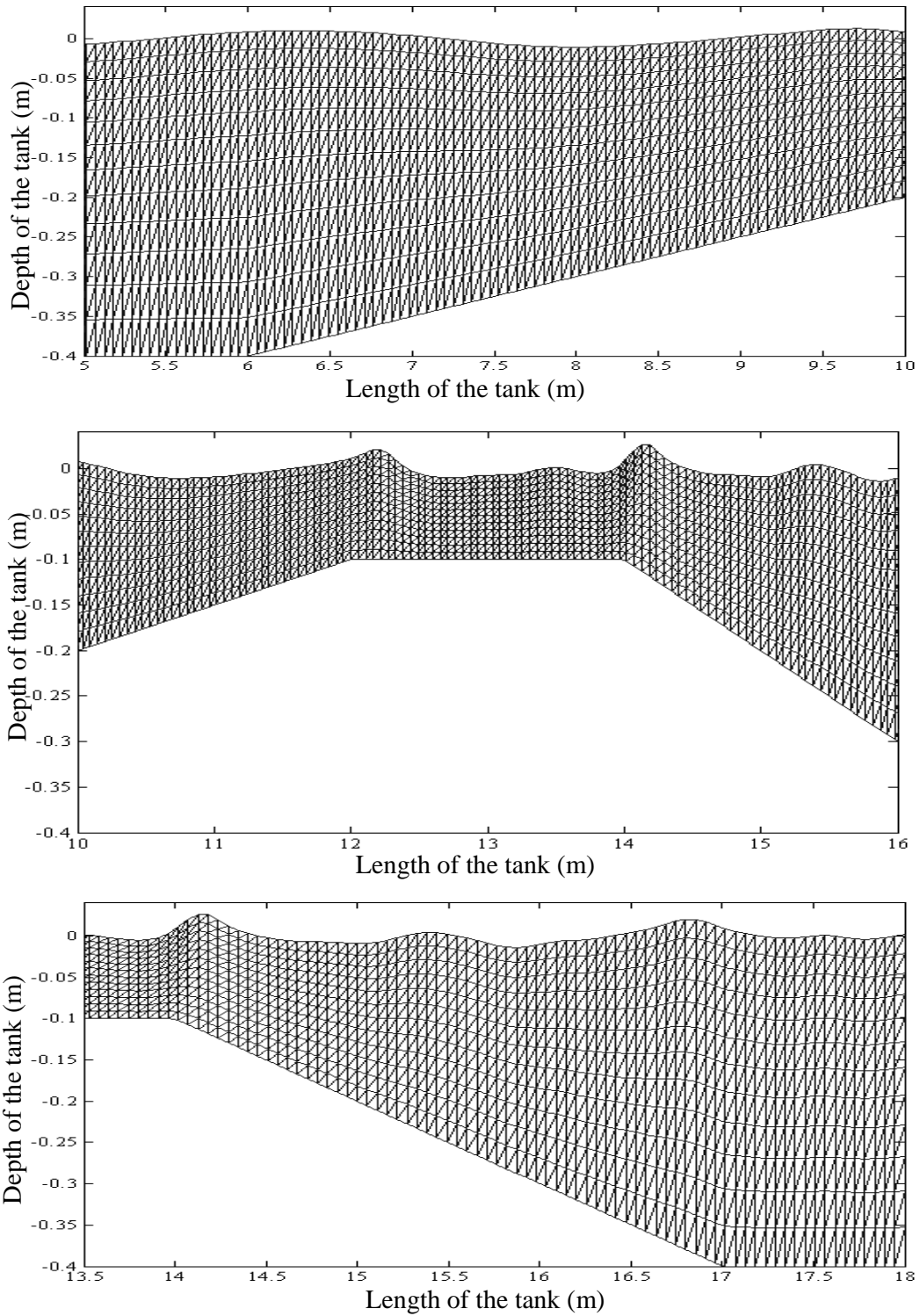


Fig. 5.3 Mesh Configuration at a particular Time Step near the Trapezoidal Obstacle along the Length of the Tank (5m to 18m)

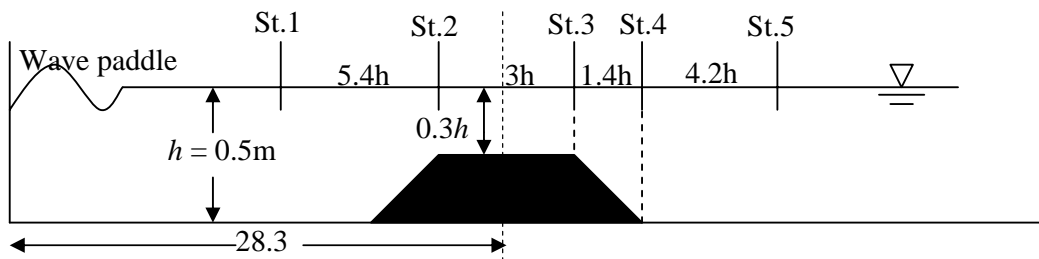


Fig. 5.4 Experimental Setup of Ohyama *et al.* (1995)

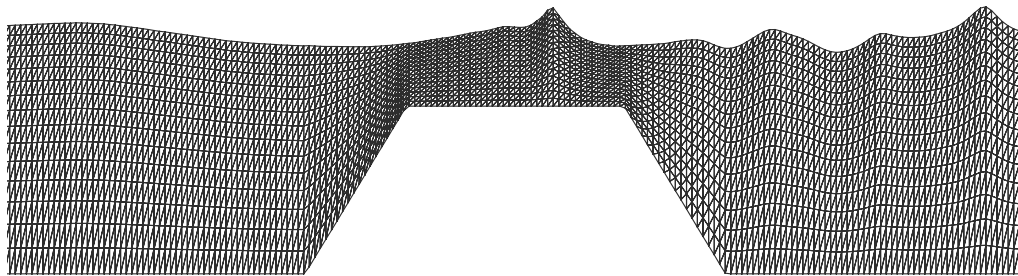


Fig. 5.5 Free Surface Profile and the Mesh Configuration when the Wave Reaches the Deeper Water Region from the Shallow Water Region

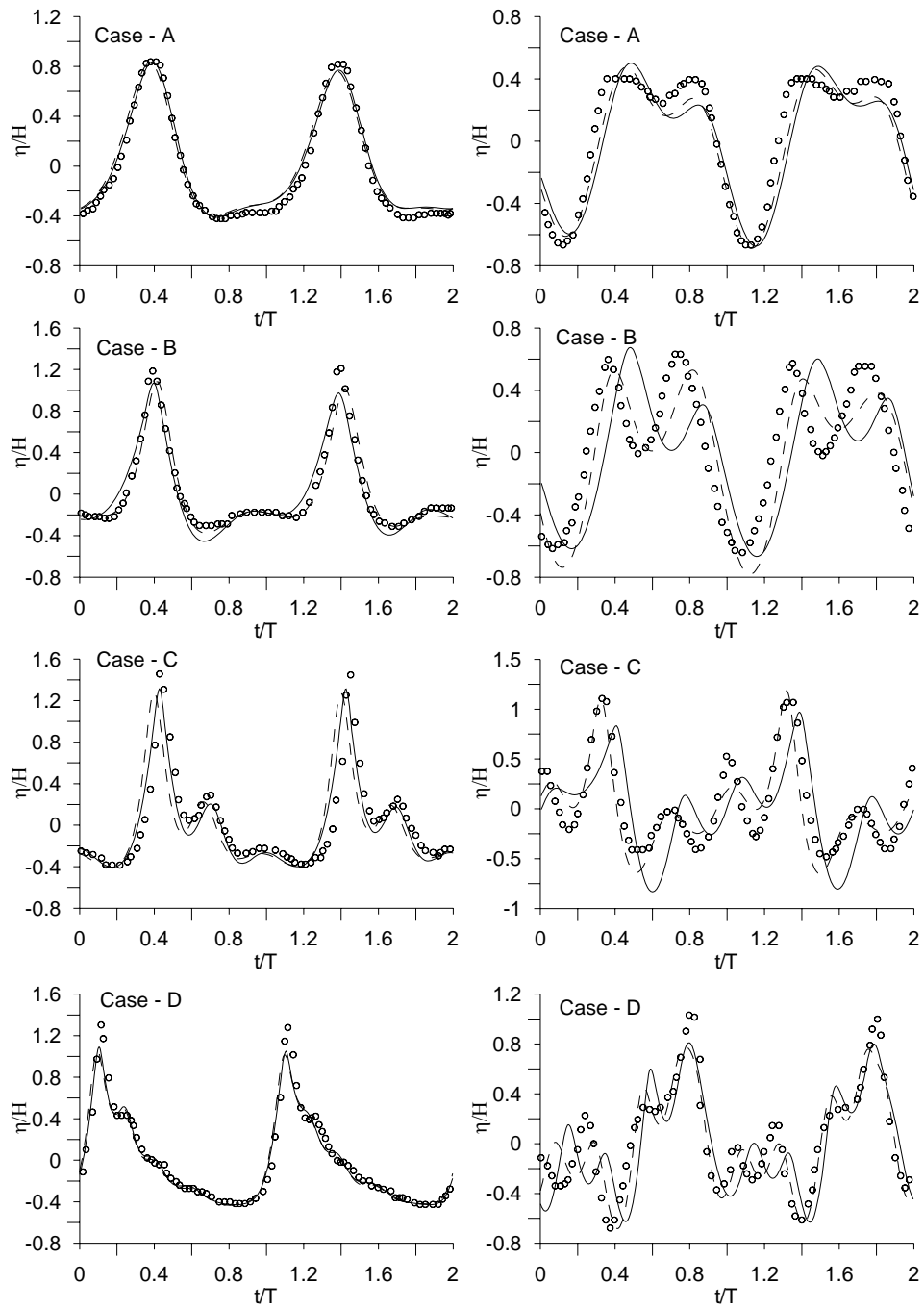


Fig. 5.6 Comparison of Numerical Simulation with Experimental Measurements. Left Side Figures are at Station 3 and Right Side Figures are at Station 5 [ooooExperiments (Ohyama *et al.* 1995); — CS; ----- LS]

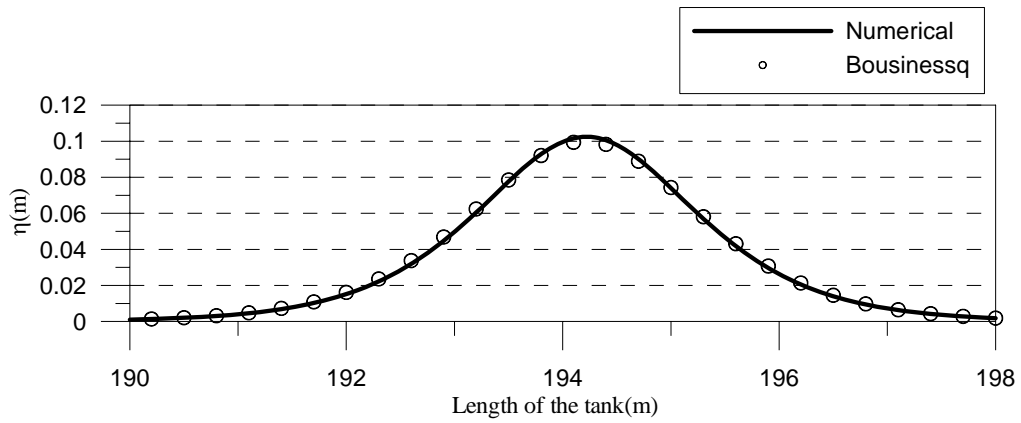


Fig. 5.7 Comparison of the Free Surface Profile with the Bousinesq Theory at $t = 80s$ over a constant Water Depth

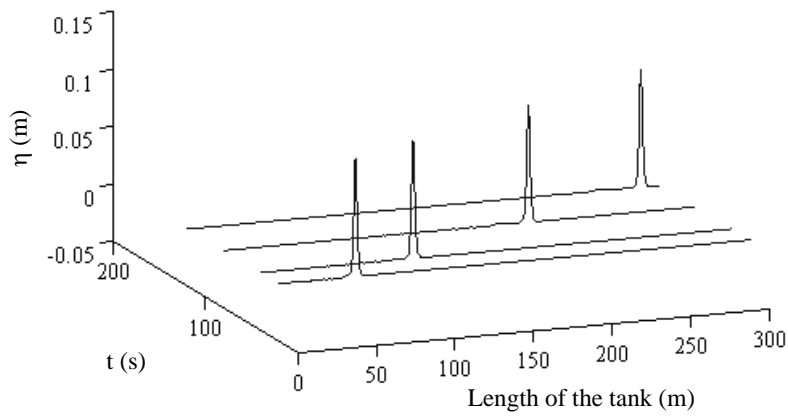


Fig. 5.8 Free Surface Profile at Time 20s, 40s, 80s and 119s along the Length of the Tank

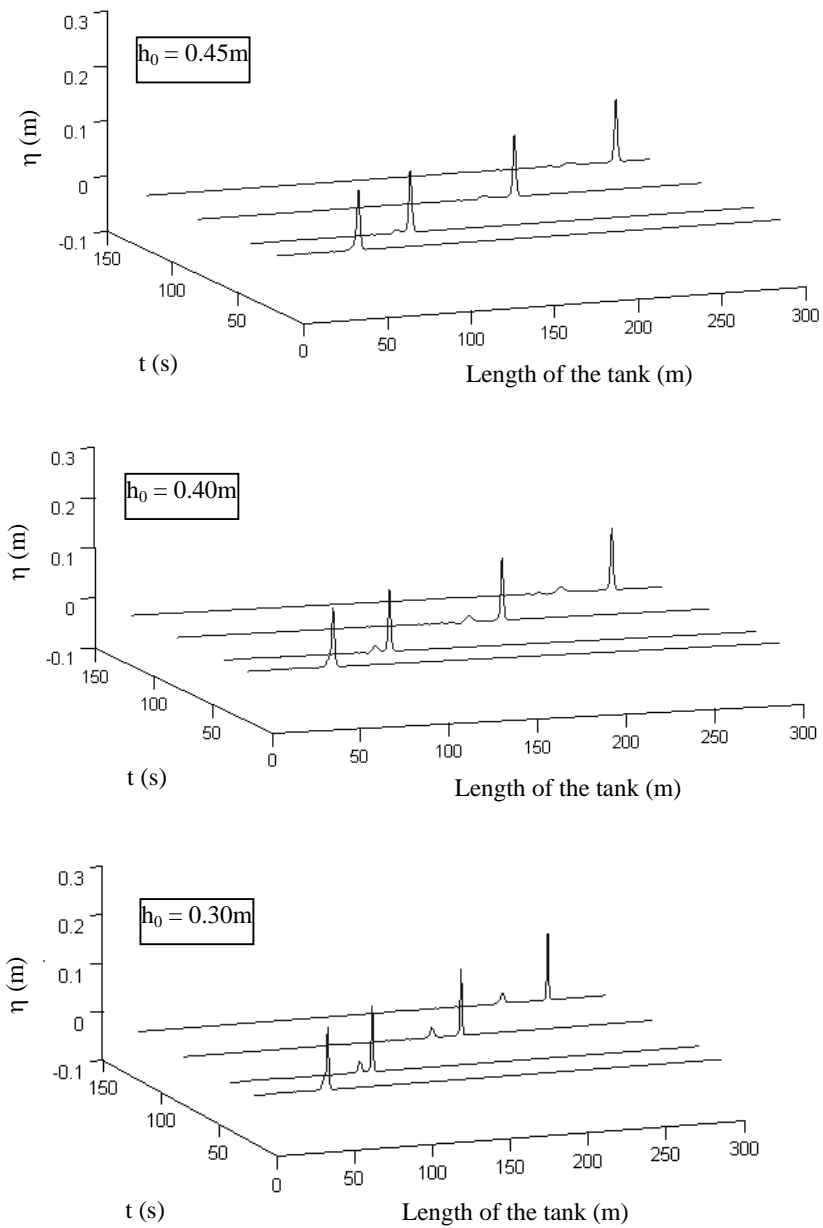


Fig. 5.9 Space – Time Plot showing the Splitting of Solitary Waves while Propagating into Shallower Water Depths (h_0) [$h = 0.5\text{m}$; $H = 0.1\text{m}$]

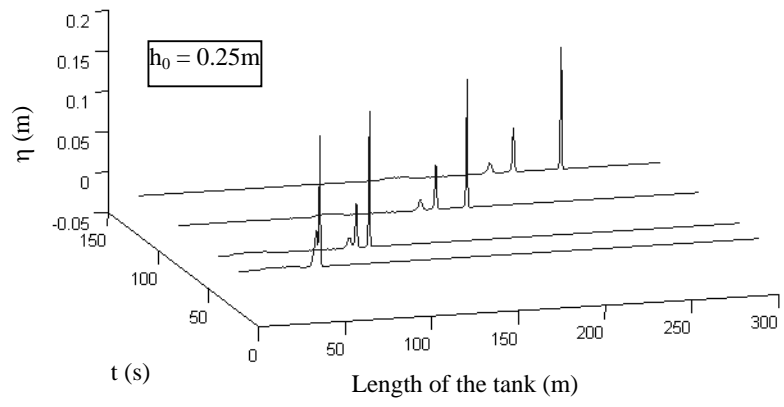


Fig. 5.9 Contd.

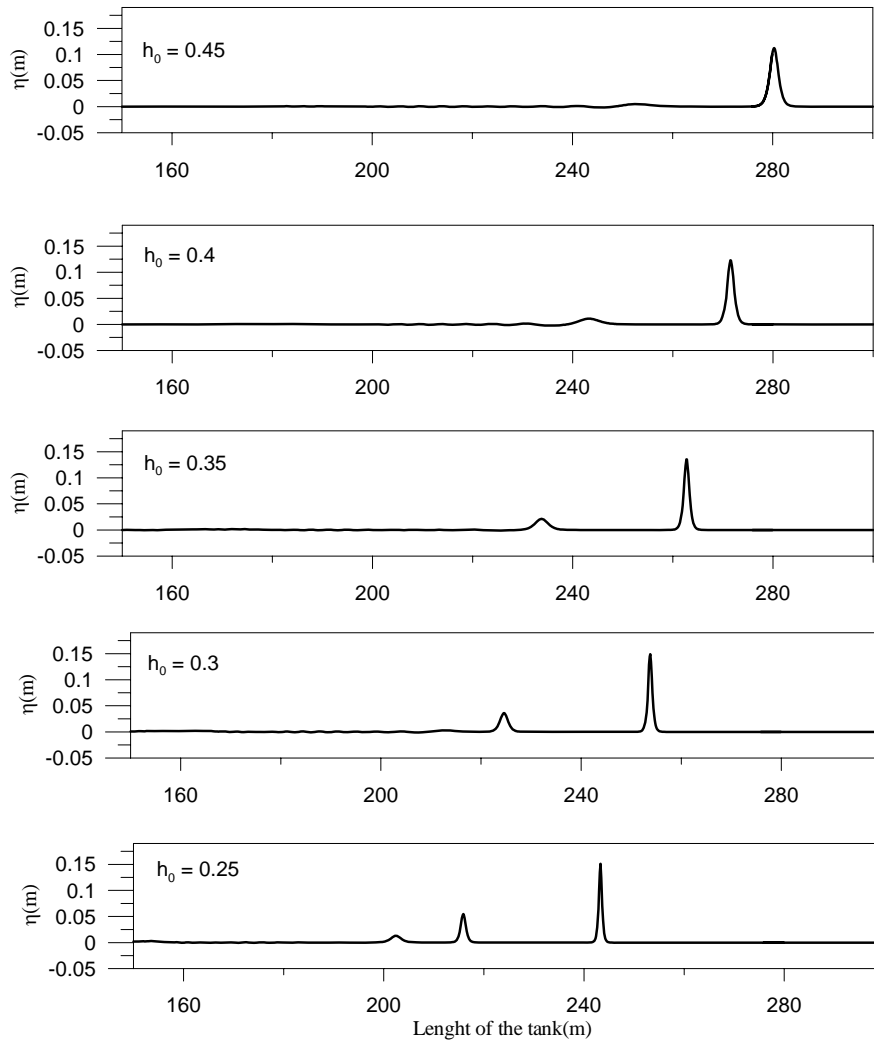


Fig. 5.10 Free Surface Profile at $t = 119$ s While Solitary Wave Propagates into Shallow Water Depths [$h = 0.5$ m; $H = 0.1$ m]

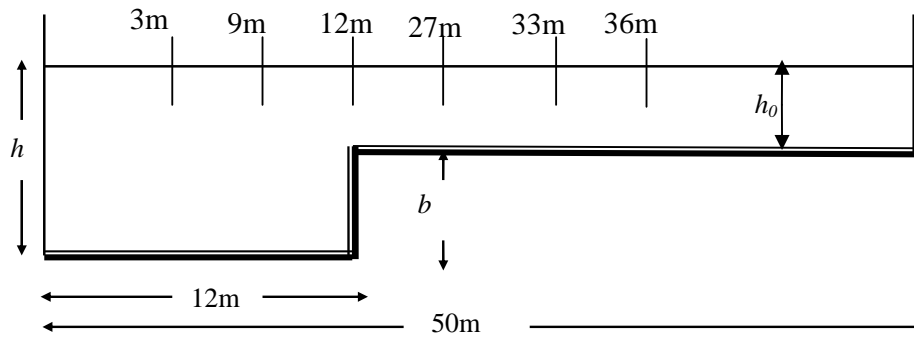


Fig. 5.11 Dimensions of the Wave Tank with the Location of the Numerical Wave Gauges

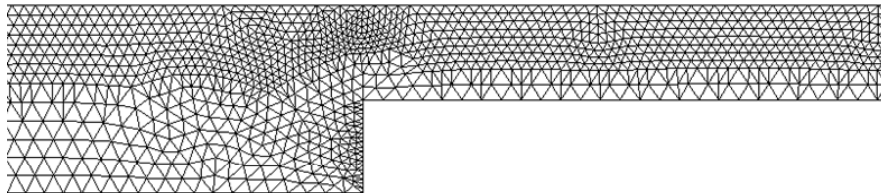


Fig. 5.12 Discretisation of the Step using Triangular Elements

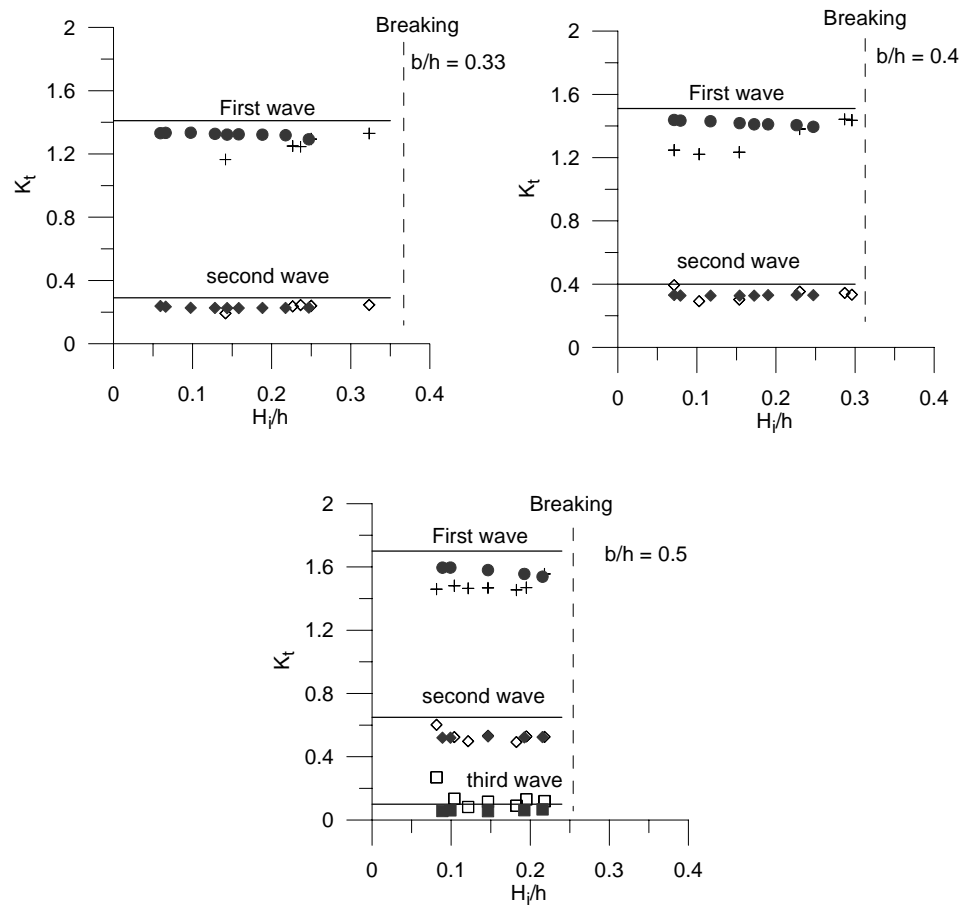


Fig. 5.13 Transmission Coefficient over Obstacles of Different Relative Height [— First Order Shallow Water Wave Theory; (+) First, (\diamond) Second and (\square) Third Transmitted Wave of Experiments (Seabra-Santos *et al.* 1987); (\bullet) First, (\blacklozenge) Second and (\blacksquare) Third Transmitted Wave of Numerical Simulation]

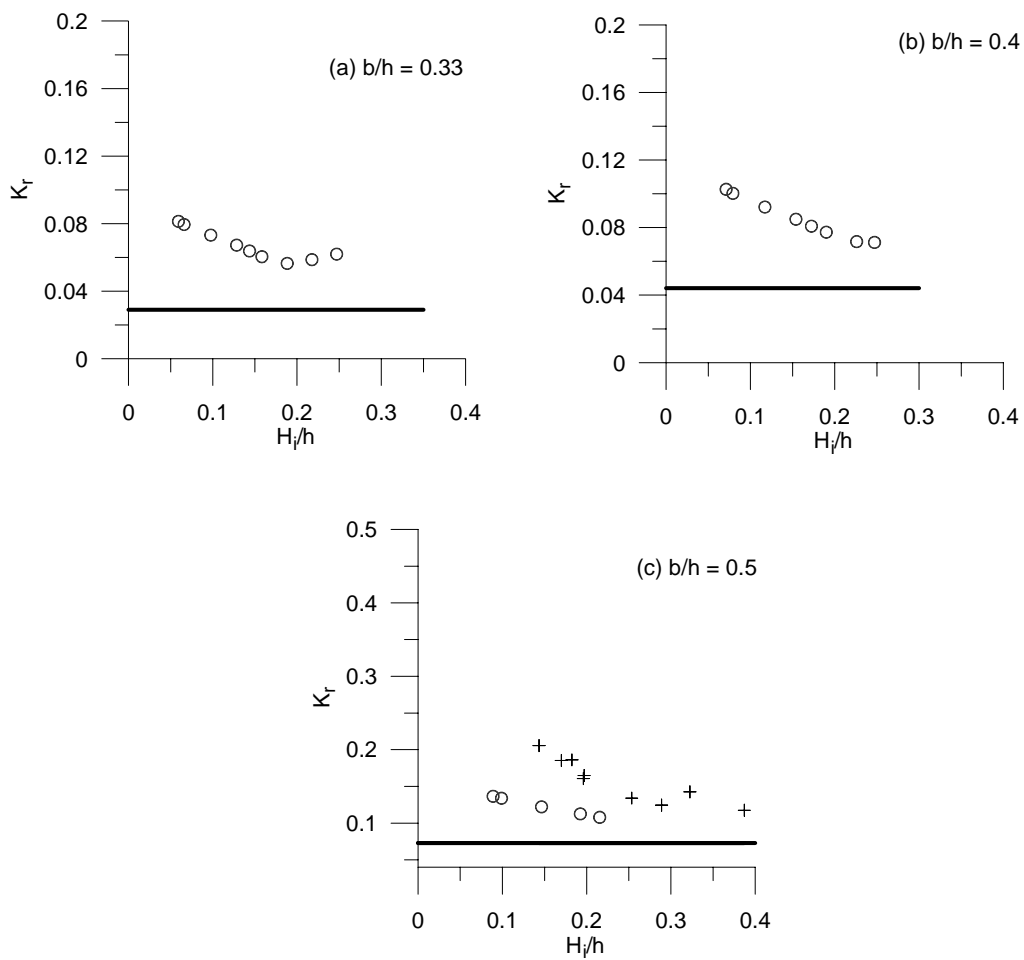


Fig. 5.14 Reflection Coefficient for Different Relative Obstacle Height [—First Order Shallow Water Wave Theory; +++ Experiments (Seabra-Santos *et al.* 1987); ooo Numerical]

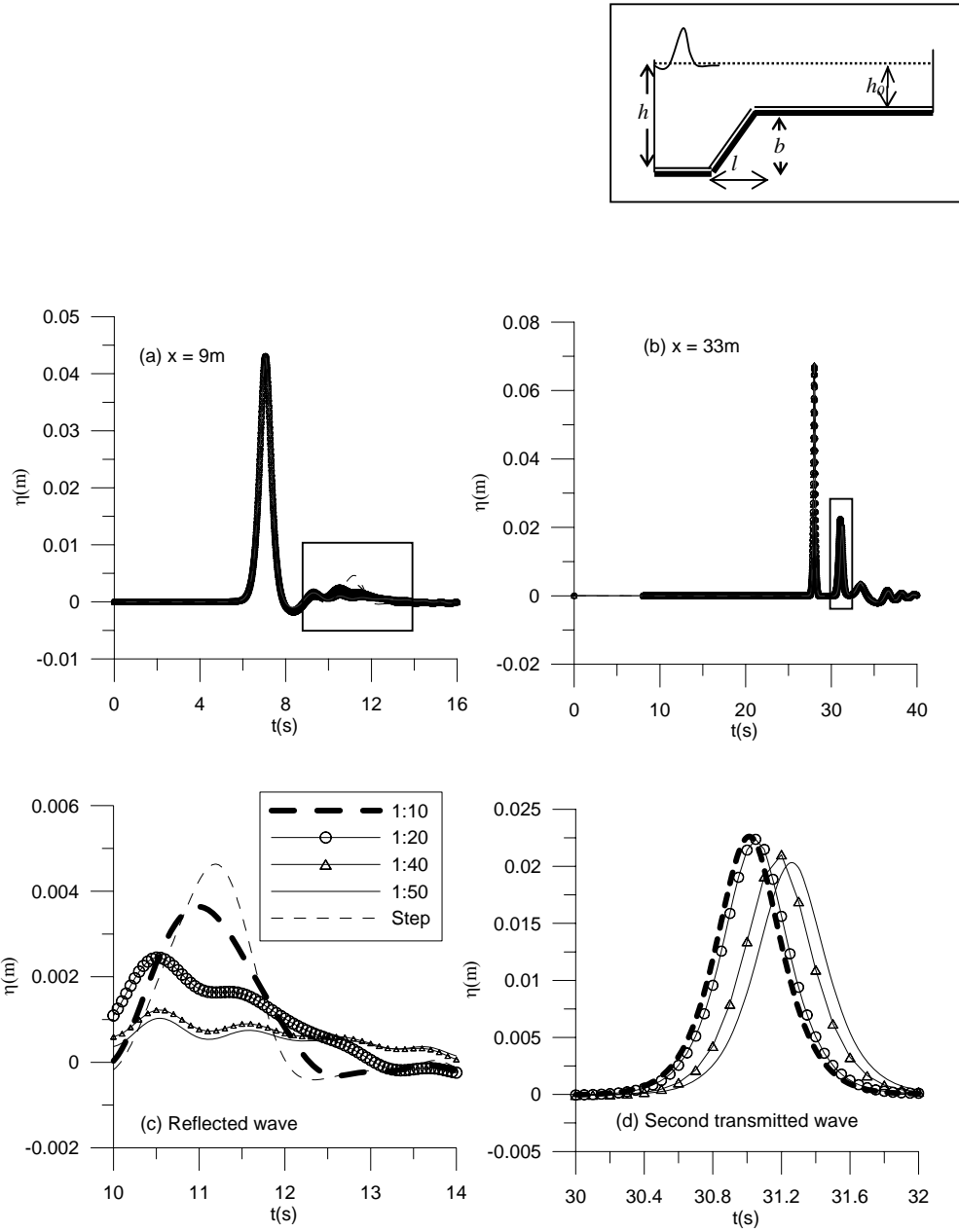


Fig. 5.15 Propagation of the Solitary Wave over a Smooth Slope, (c) and (d) are the zoomed in view of the Rectangle Marked in (a) and (b) respectively

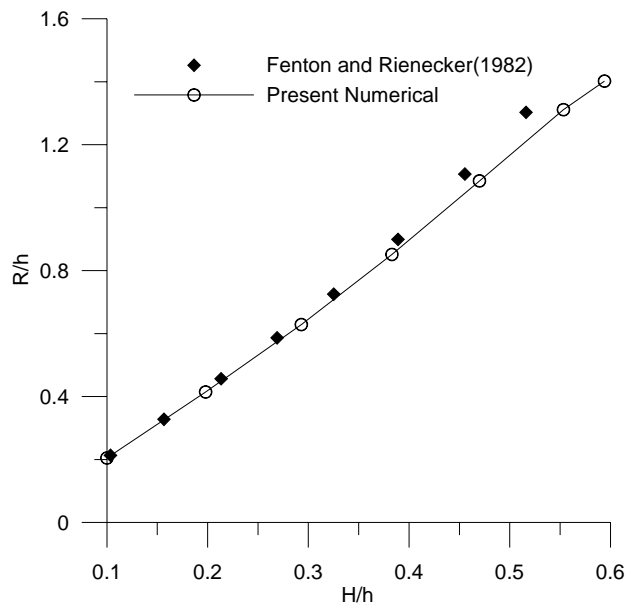


Fig. 5.16 Vertical Wall Run-up due to Different Wave Steepness

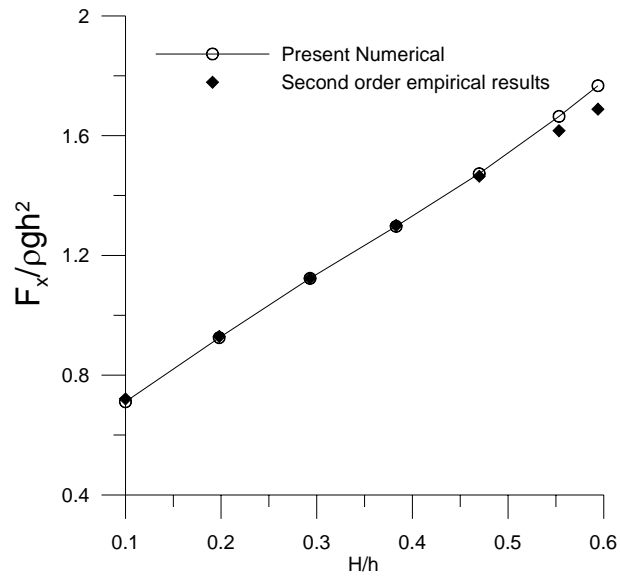


Fig. 5.17 Maximum Horizontal Force on the Vertical Wall due to Different Wave Steepness

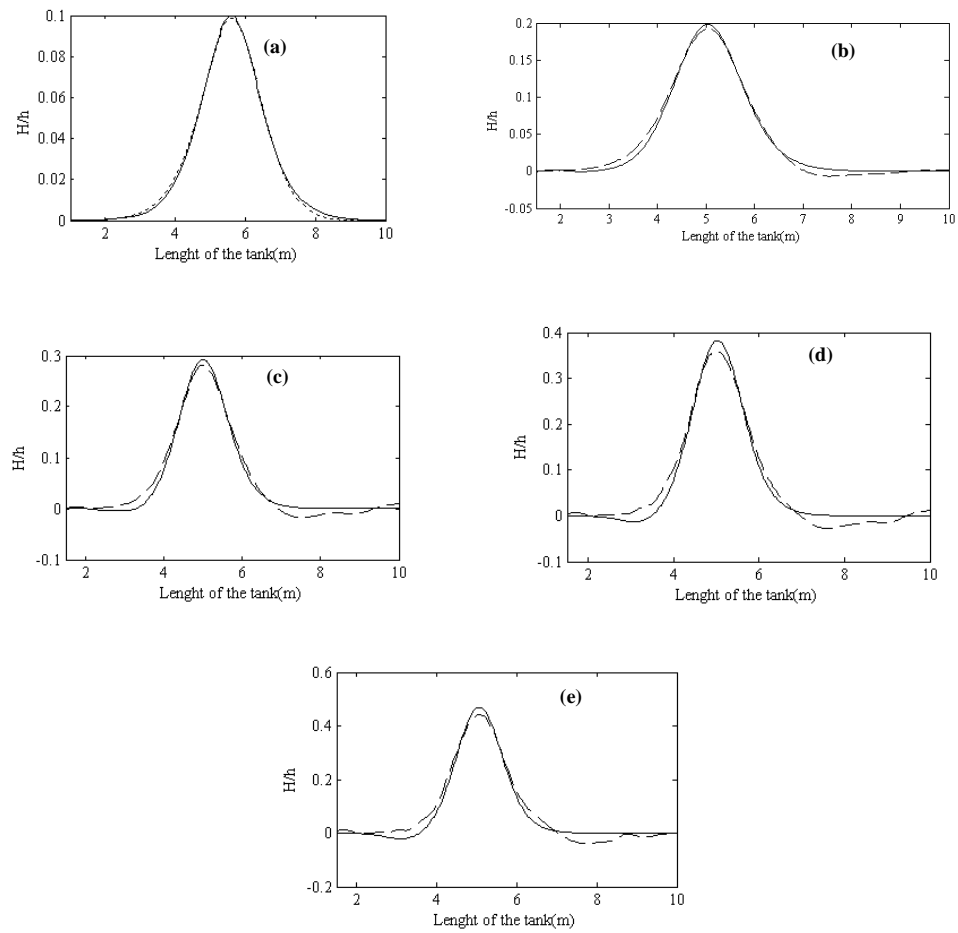


Fig. 5.18 Reflected Shape of the Profile for Different Steepness:(a) $H/h = 0.1$, (b) $H/h = 0.2$, (c) $H/h = 0.3$, (d) $H/h = 0.4$, (e) $H/h = 0.5$, [— Incident Wave;----- Reflected Wave]

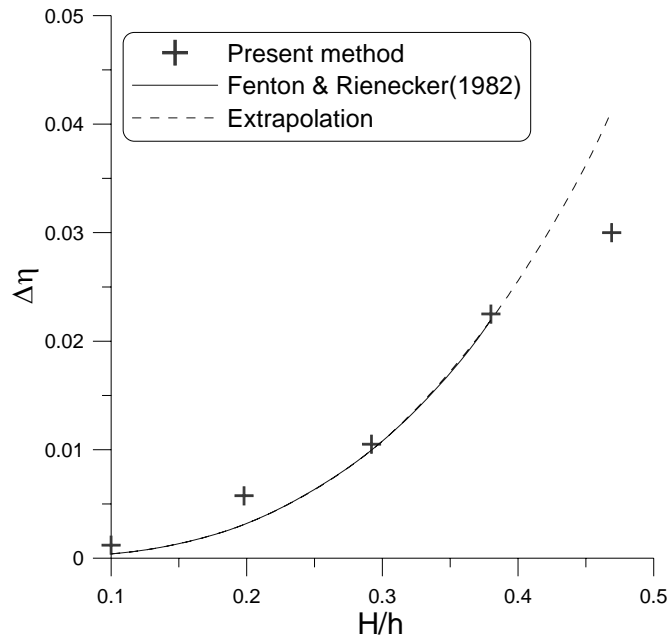


Fig. 5.19a Variation of the change in Wave Elevation ($\Delta\eta$) with respect to Wave Steepness

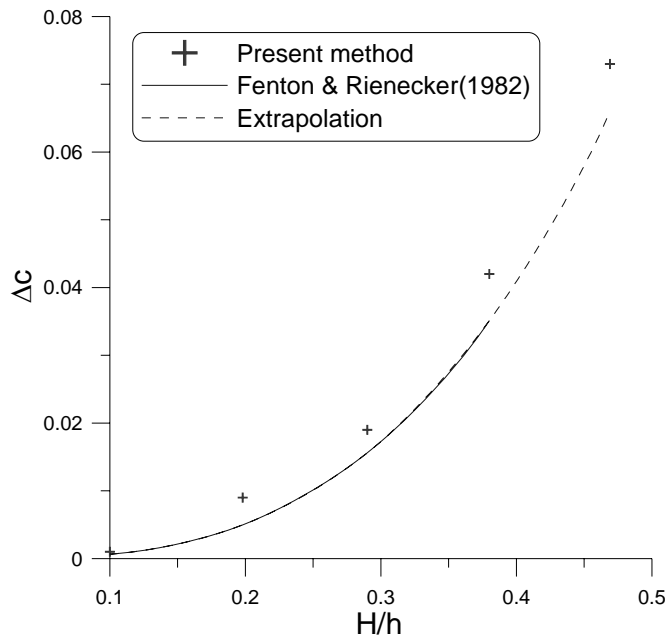


Fig. 5.19b Variation of change in Wave Celerity (ΔC) with respect to Wave Steepness

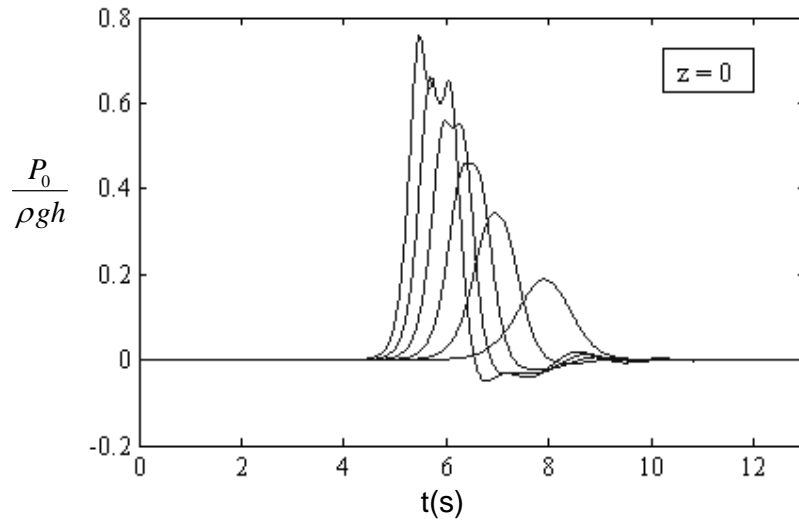


Fig. 5.20a Pressure Time History on the Vertical Wall at the Still Water Level [From Left to Right: $H/h = 0.1$; 0.198 ; 0.293 ; 0.383 ; 0.4699 ; 0.5533]

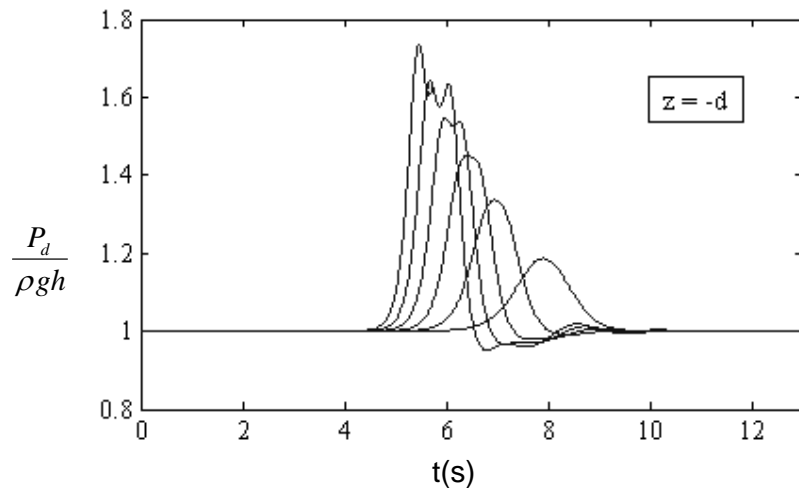


Fig. 5.20b Pressure Time History at the Bottom of the Vertical Wall [From Left to Right: $H/h = 0.1$; 0.198 ; 0.293 ; 0.383 ; 0.4699 ; 0.5533]

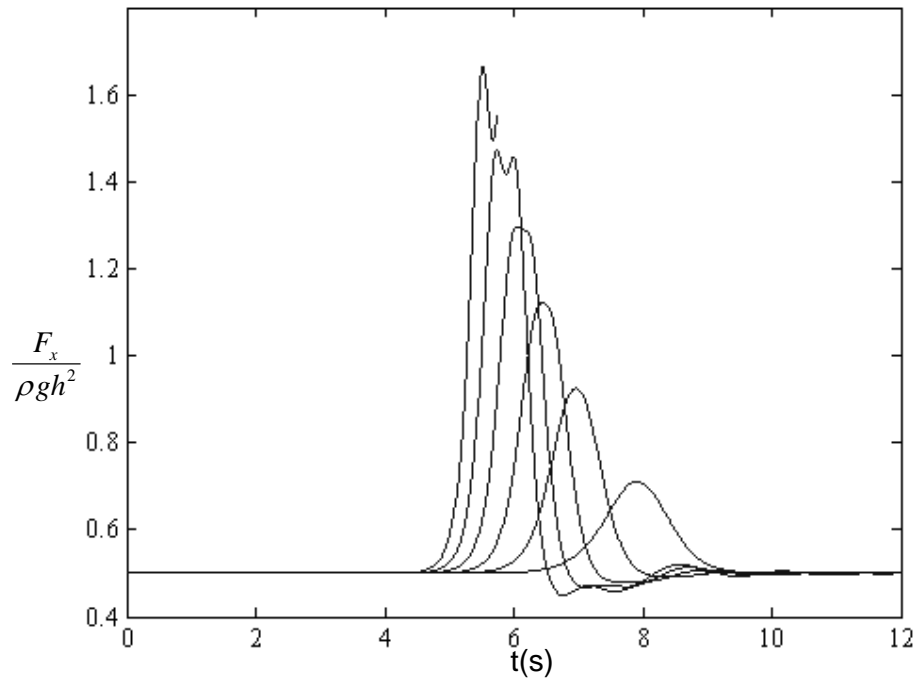
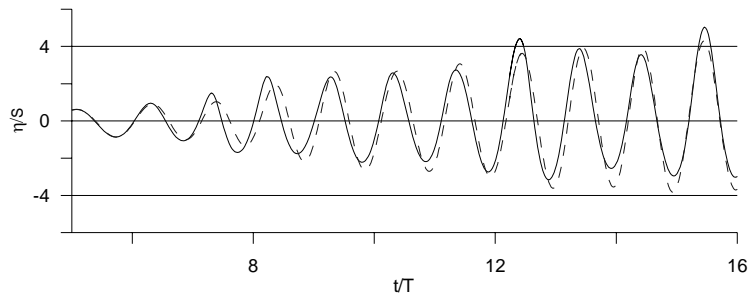


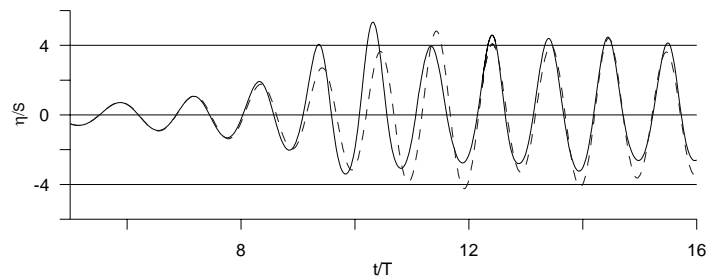
Fig. 5.21 Force Time History on the Vertical Wall [From Left to Right: $H/h = 0.1; 0.198; 0.293; 0.383; 0.4699; 0.5533$]



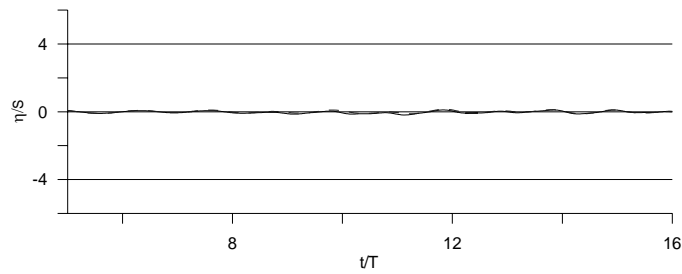
Fig. 5.22 Typical Mesh Configuration in the Presence of a Rectangular Object



a) Time History at 3.5m from the Wave Paddle



b) Time History at Upstream Side of the Body



c) Time History at the Downstream Side of the Body

Fig. 5.23 Comparison of Free Surface Profile between Two Different Wave Heights with a Rectangular Object [----- $H/\lambda = 0.015$; ——— $H/\lambda = 0.075$]

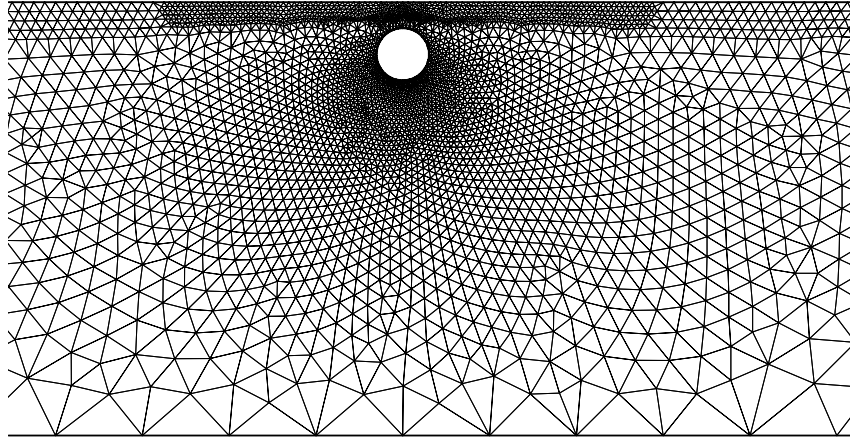


Fig. 5.24 Initial Mesh Structure with Cylinder Generated using GAMBIT and Refined using ICEM-CFD

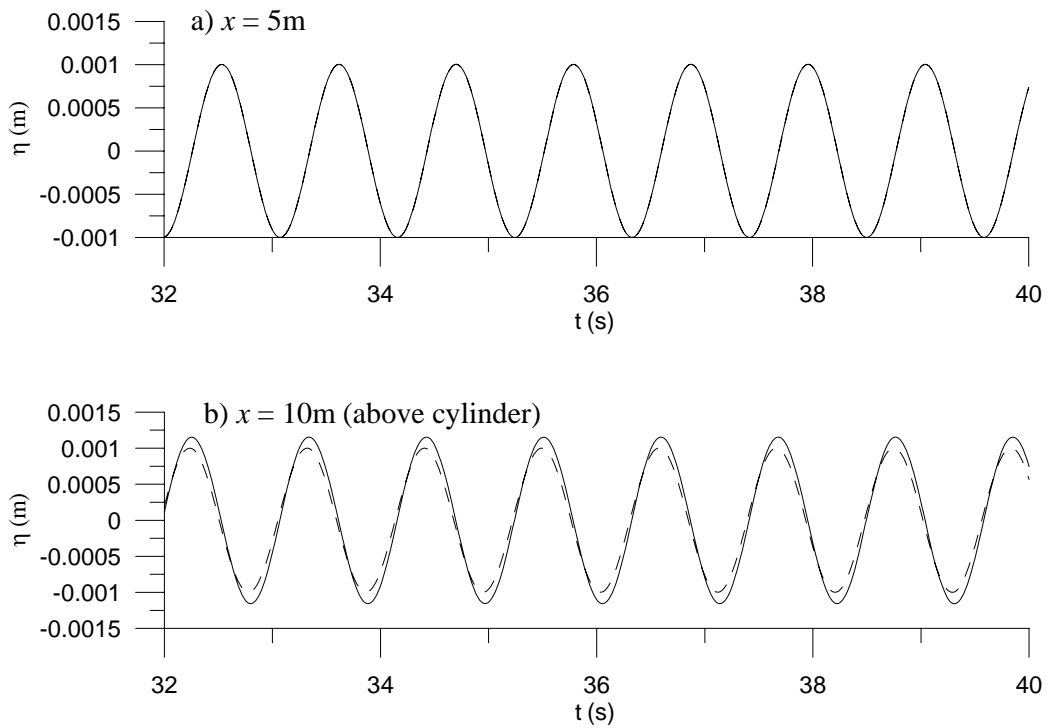


Fig. 5.25 Comparison of the Wave Profiles with and without the Cylinder [----- without Cylinder; — with Cylinder]

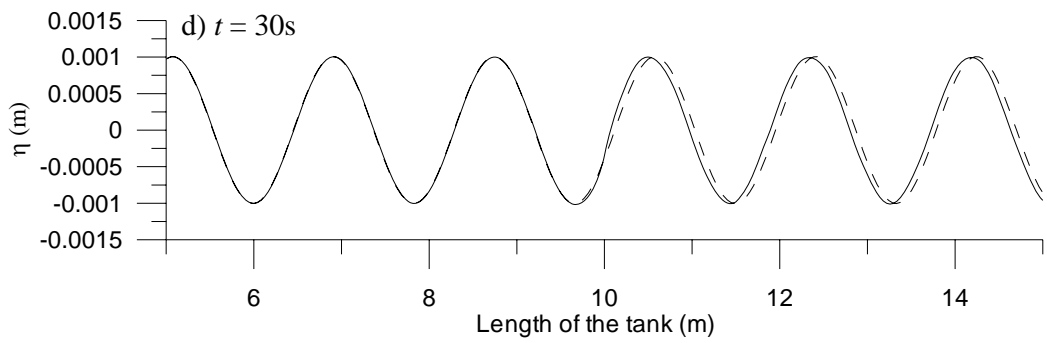
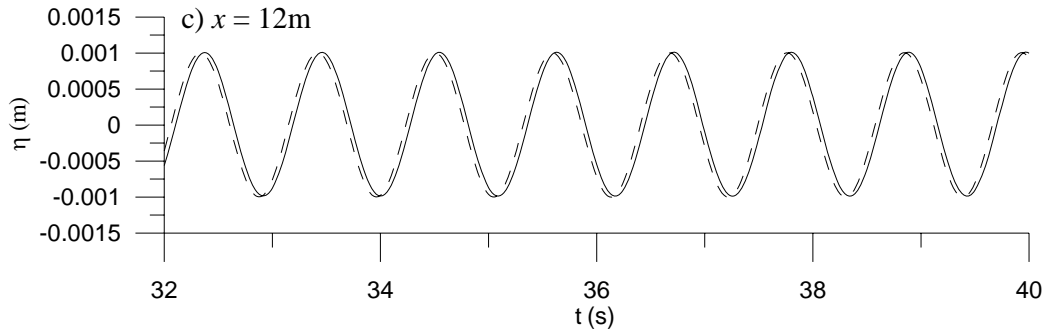


Fig. 5.25 Contd.

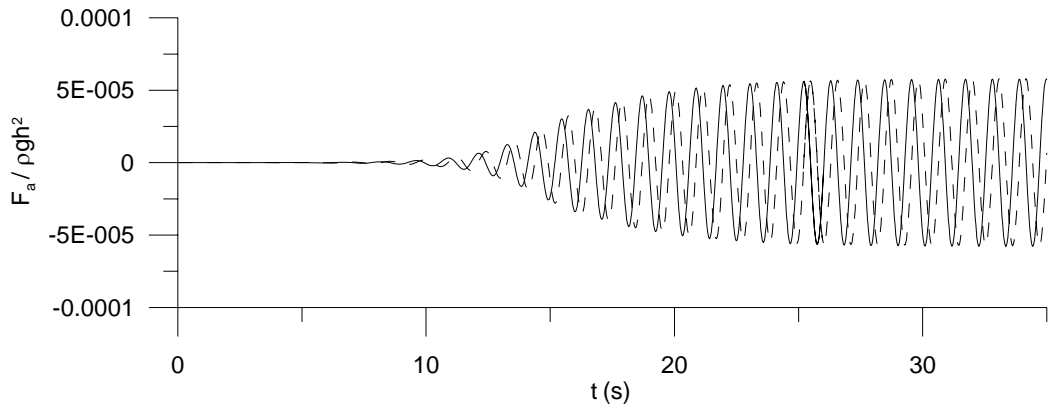


Fig. 5.26 Force Time Histories of Component F_a [----- x Component; ——— z Component]

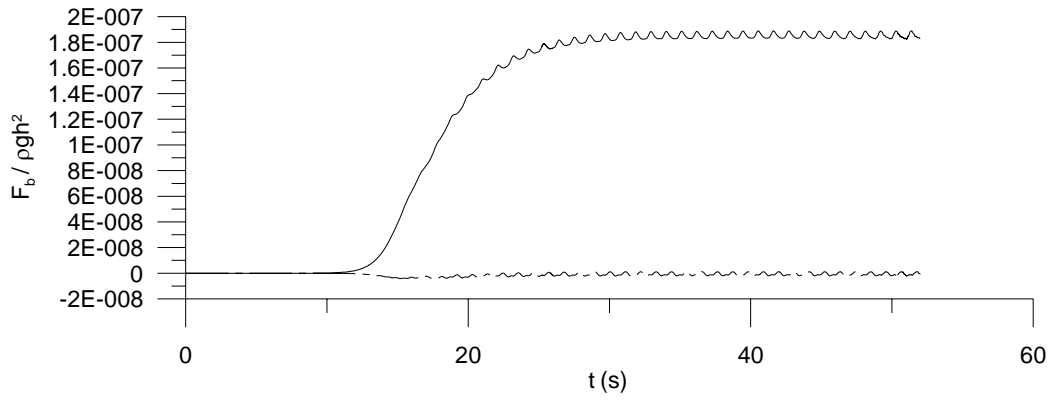
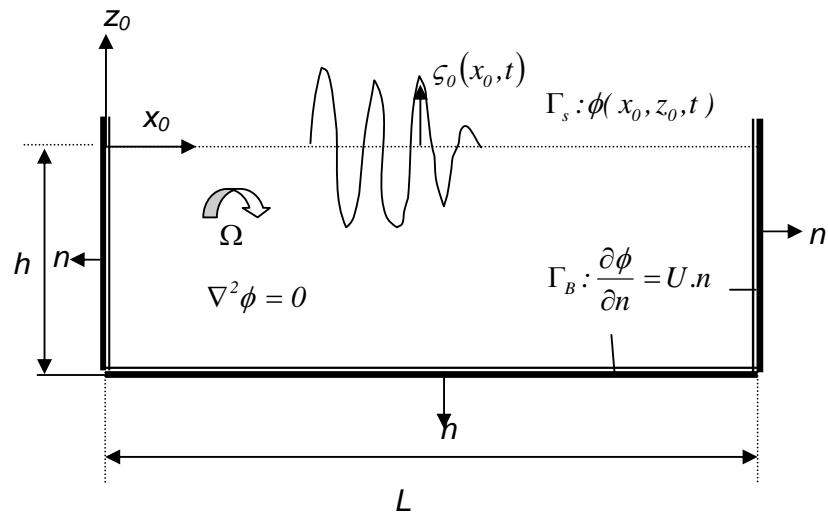
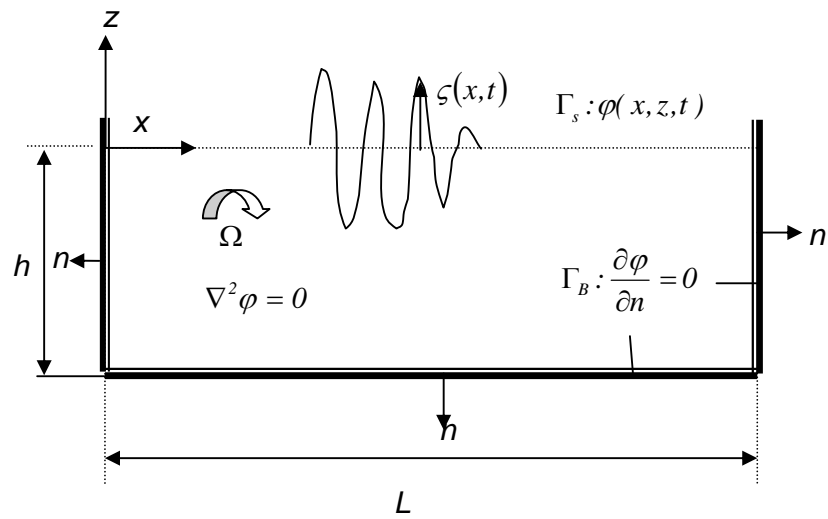


Fig. 5.27 Force Time Histories of Component F_b [----- x Component, — z Component]



(a) Fixed Coordinate System.



(b) Moving Coordinate System.

Fig. 5.28 Sloshing Wave Tank Model Domain

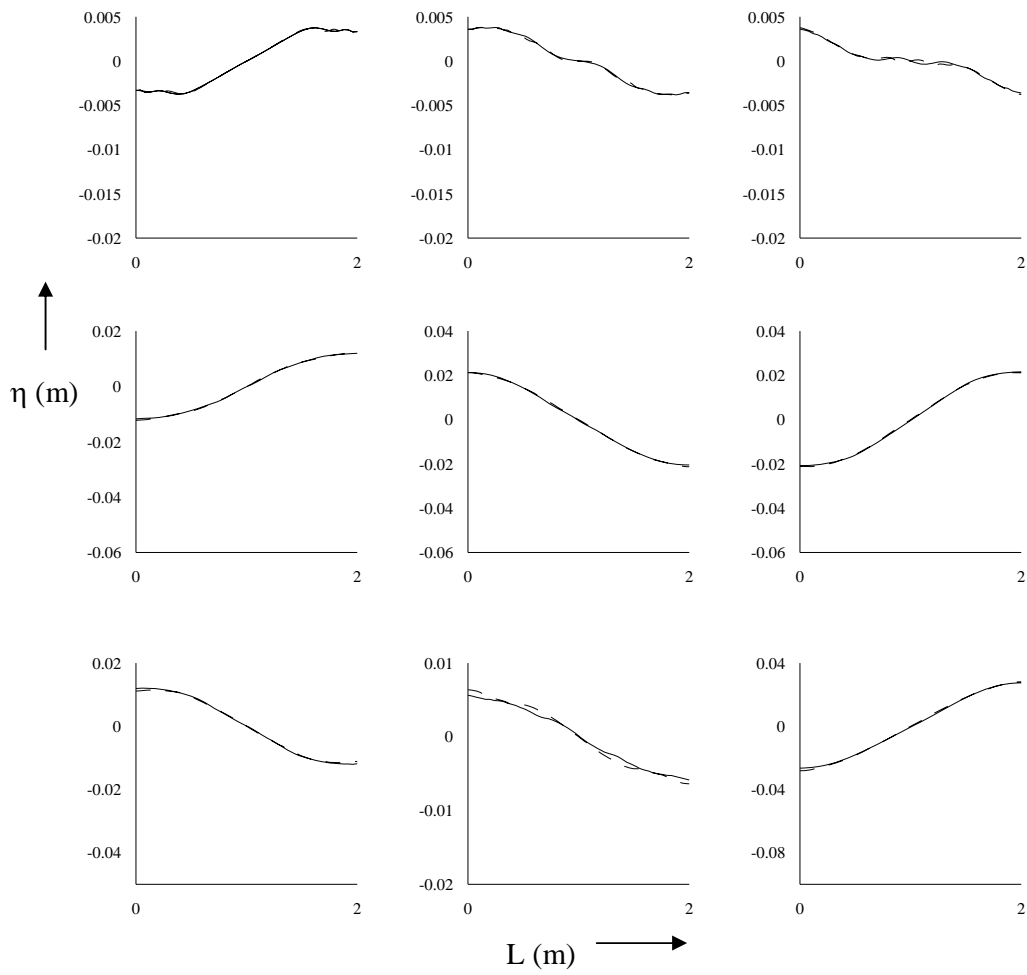
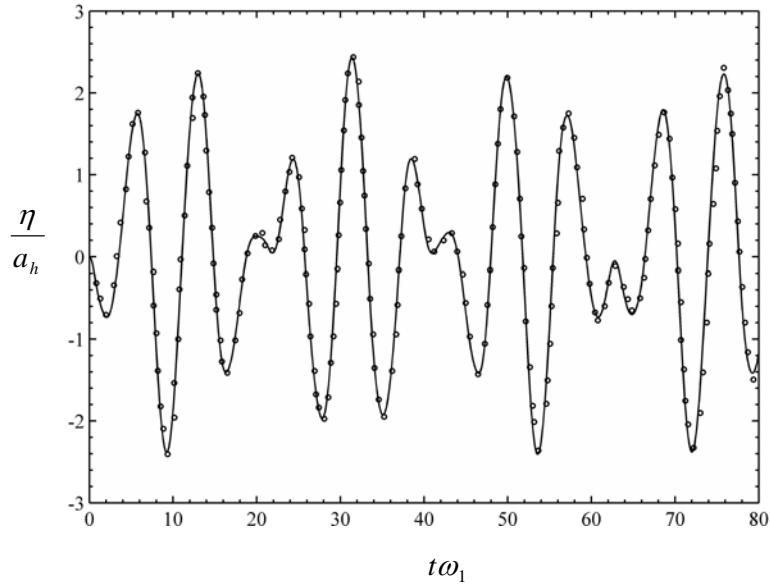


Fig. 5.29 Free Surface Profiles over the Length for $\omega_h=0.999\omega_l$ and $a_h = 0.0018$ after every 2s Interval [— Numerical; - - - Analytical]

(a)



(b)

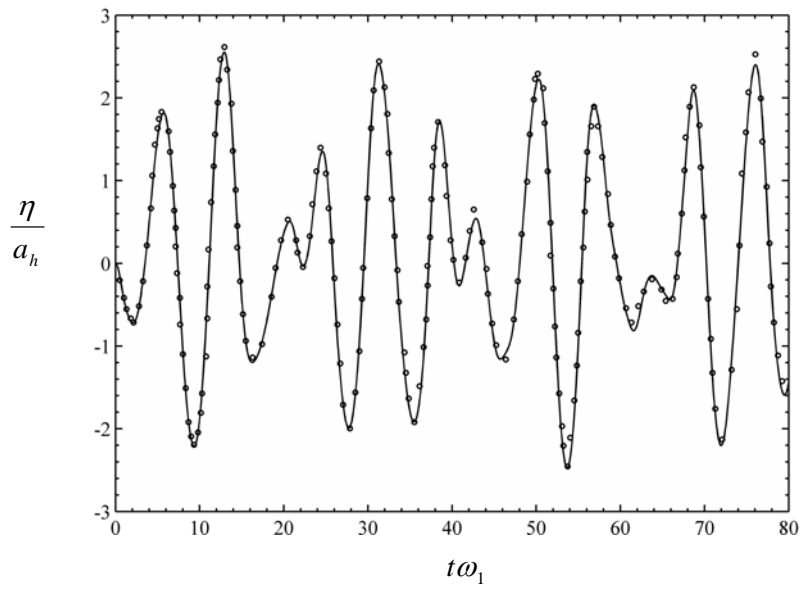


Fig. 5.30 Free Surface Elevation at the Left Wall due to Regular Horizontal Excitation at a Frequency, $\omega_h = 0.7\omega_l$
(a) $a_h\omega_h^2=0.0036g$; (b) $a_h\omega_h^2=0.036g$ [— Present Numerical; ●●● Numerical (Frandsen, 2004)]

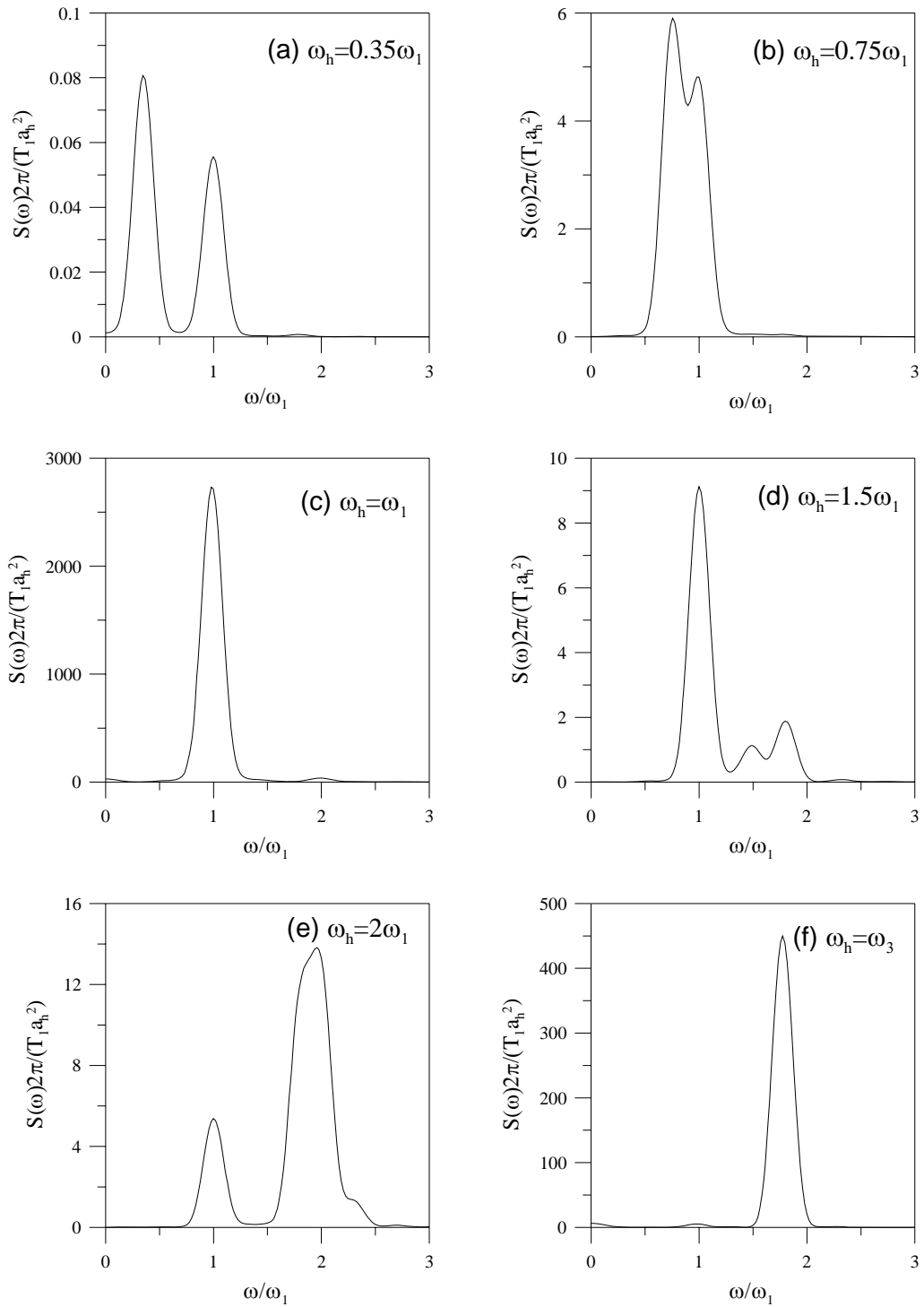


Fig. 5.31 Power Spectra of Waves at the Left Corner of the Wall due to Horizontal Excitation, $a_h = 0.005h$ [$T_1 = 2\pi/\omega_1$]

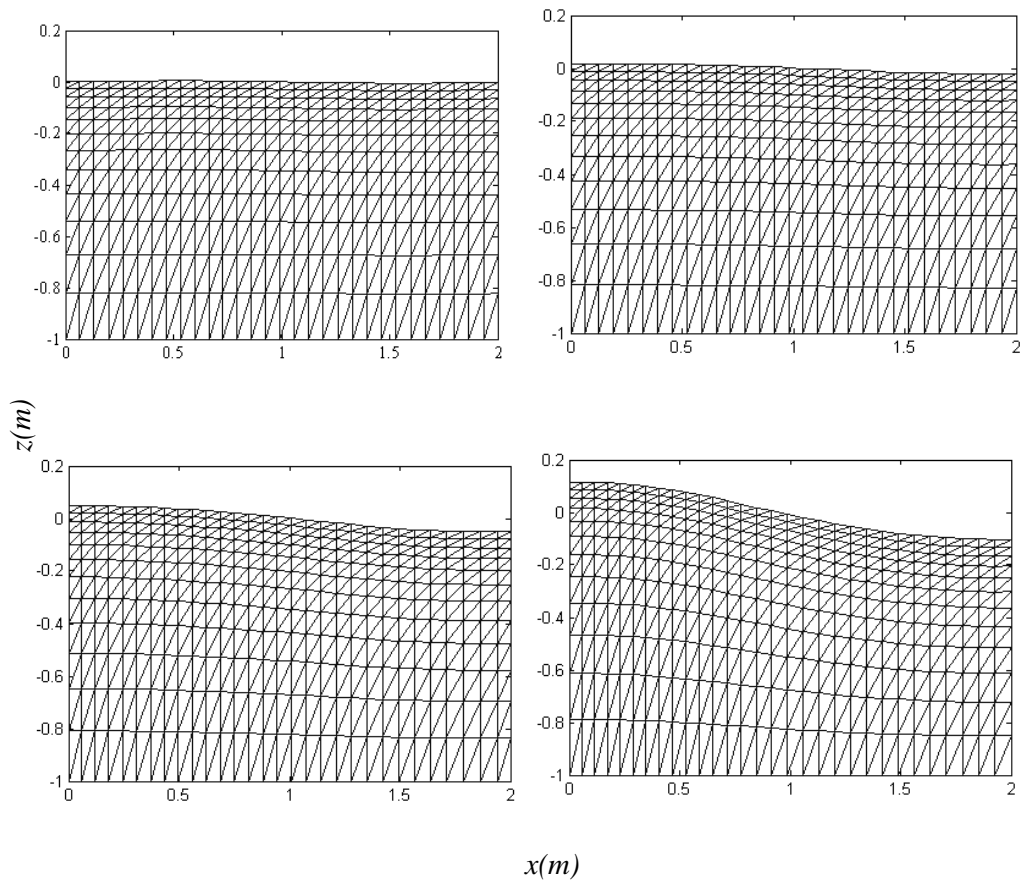


Fig. 5.32 Movement of the Generated Mesh during a Horizontal Excitation after every 5s Interval for $a_h = 0.005h$ and $\omega_h = \omega_1$, Number of Nodes in x Direction is 31 and in z Direction is 13

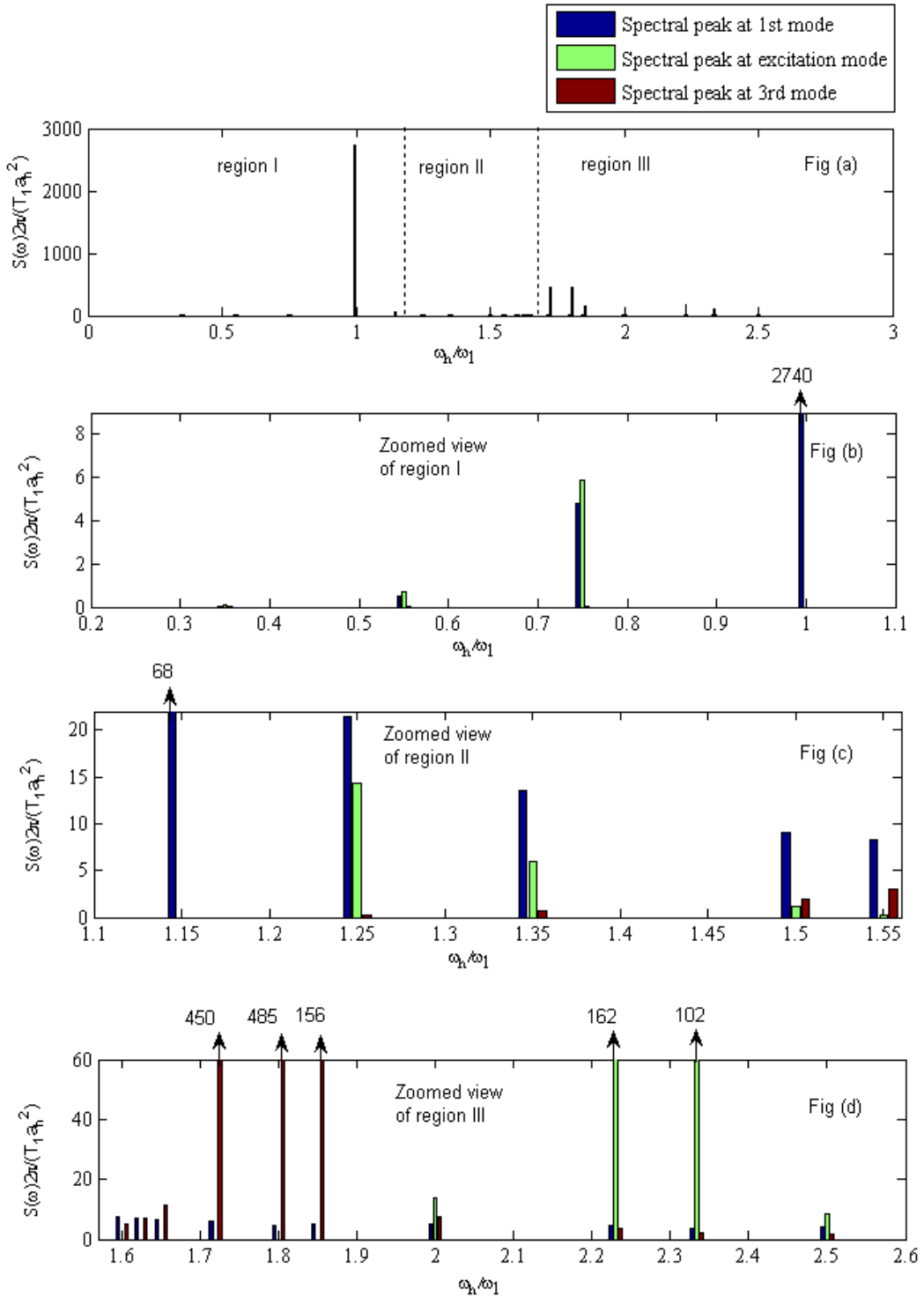


Fig. 5.33 Bar Chart showing the Magnitude of Different Spectral Peaks of Sloshing Waves due to Horizontal Excitation with Frequencies $[\omega_2 = 1.5\omega_1; \omega_3 = 1.8\omega_1; \omega_5 = 2.334\omega_1]$

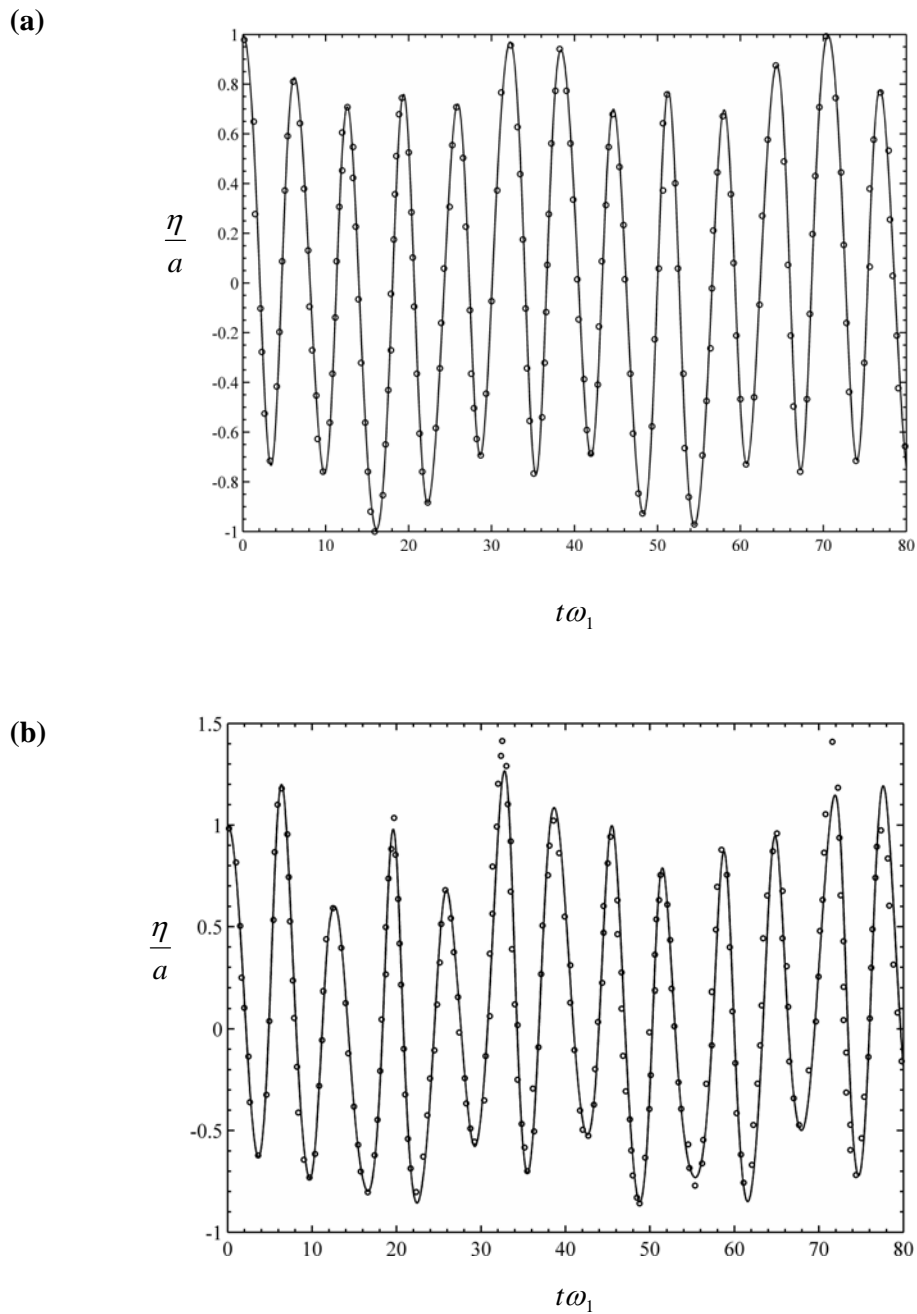


Fig. 5.34 Free Surface Elevation at the Left Wall due to Regular Vertical Excitation of Frequency, $\omega_v = 0.789\omega_l$, $a_v\omega_v^2 = 0.5g$. a) $\epsilon=0.0014$ b) $\epsilon=0.288$ [— Present Numerical; ●●● Numerical (Frandsen, 2004)]

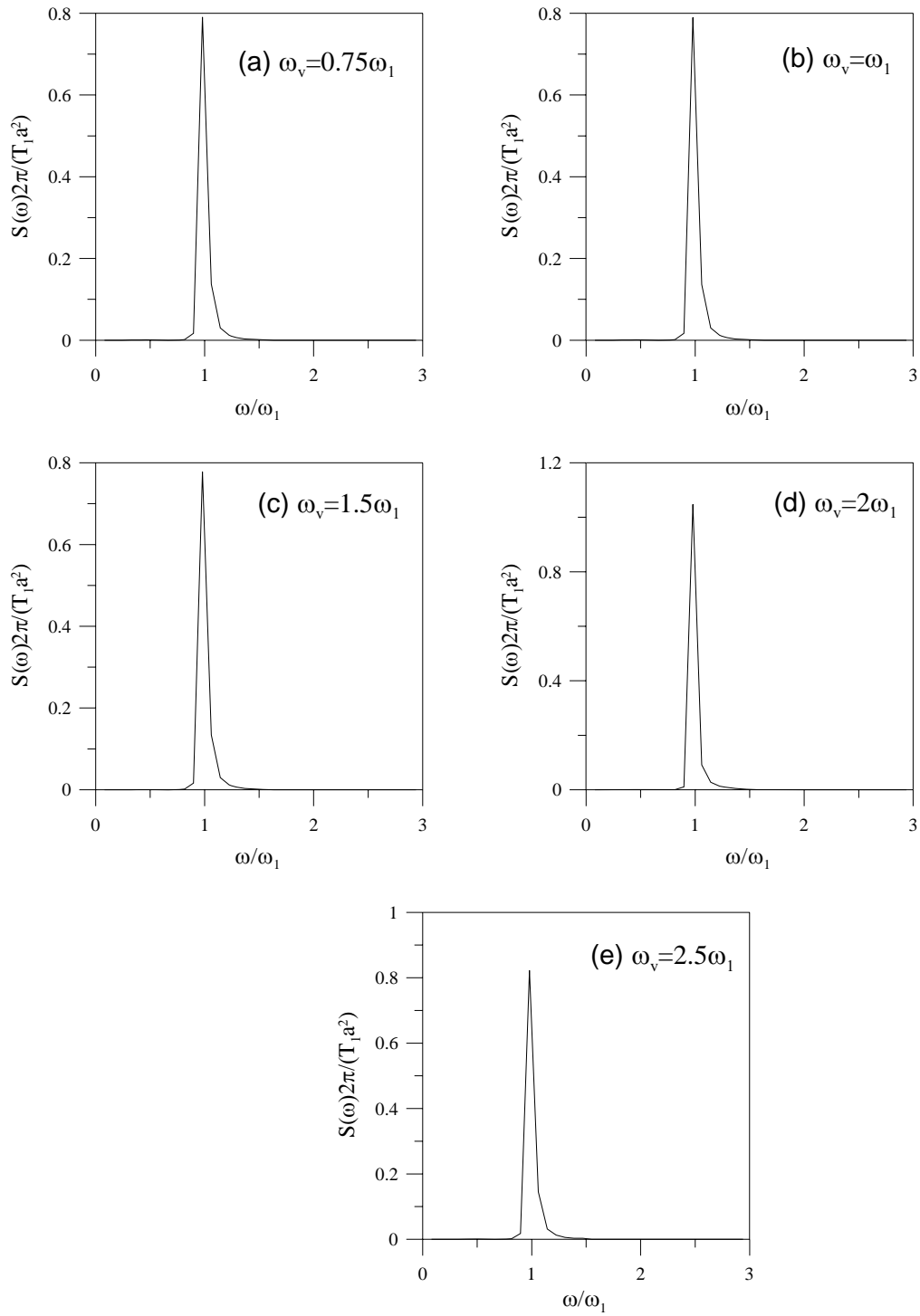


Fig. 5.35 Power Spectra of Free Surface Sloshing Waves at the Left Corner of the Wall due to Regular Vertical Excitation for an Initial Steepness of 0.014, $a_v = 0.005h$ [$T_1 = 2\pi/\omega_1$]

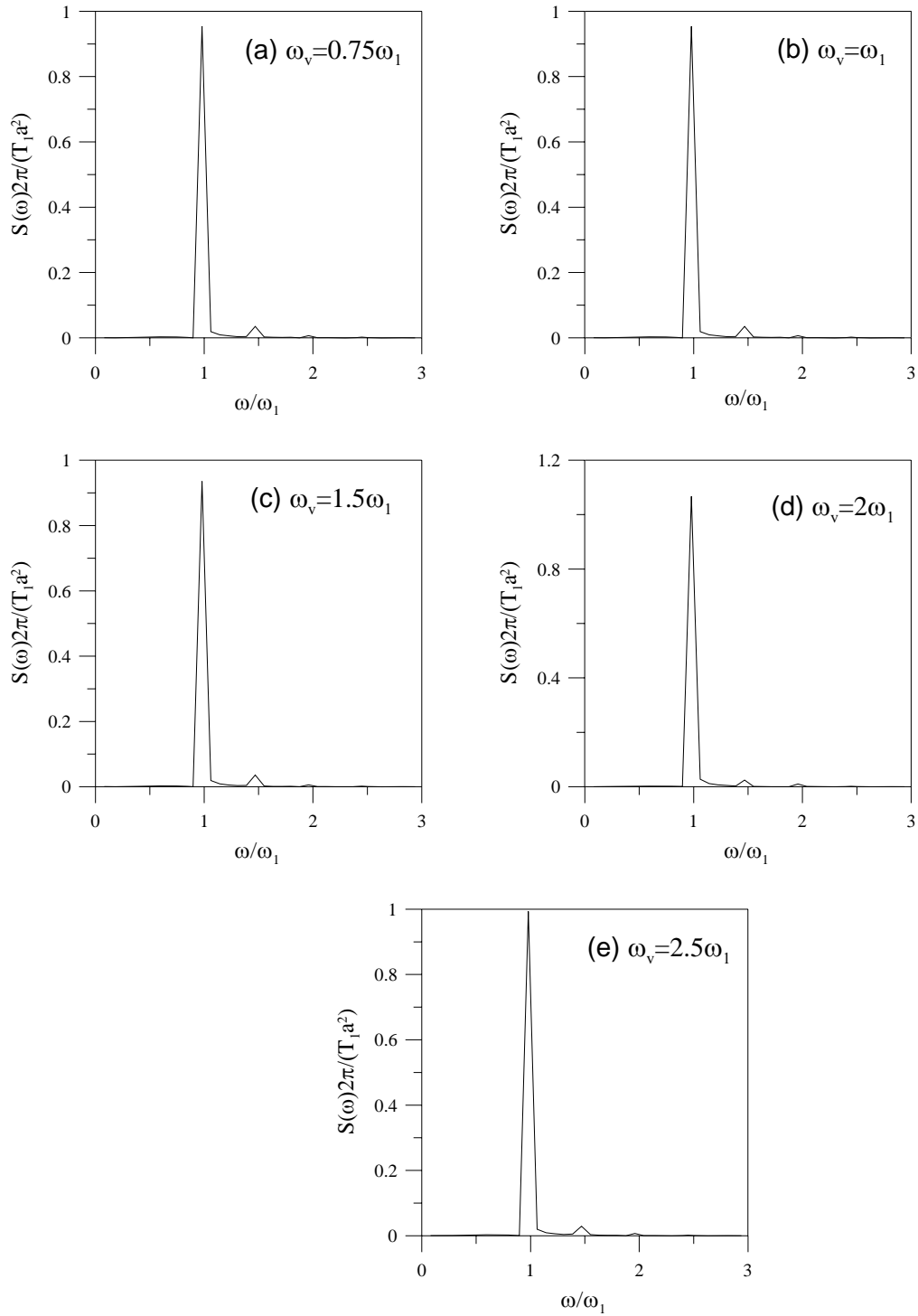


Fig. 5.36 Power Spectra of Free Surface Sloshing Waves at the Left Corner of the Wall due to Regular Vertical Excitation for an Initial Steepness of 0.288, $a_v = 0.005h$ [$T_1 = 2\pi/\omega_1$]

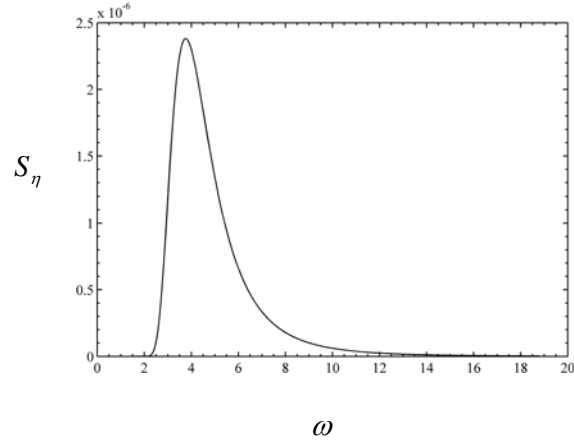


Fig. 5.37a Typical Excitation Spectrum with $H_s = 0.01h$ and $\omega_p = \omega_l$

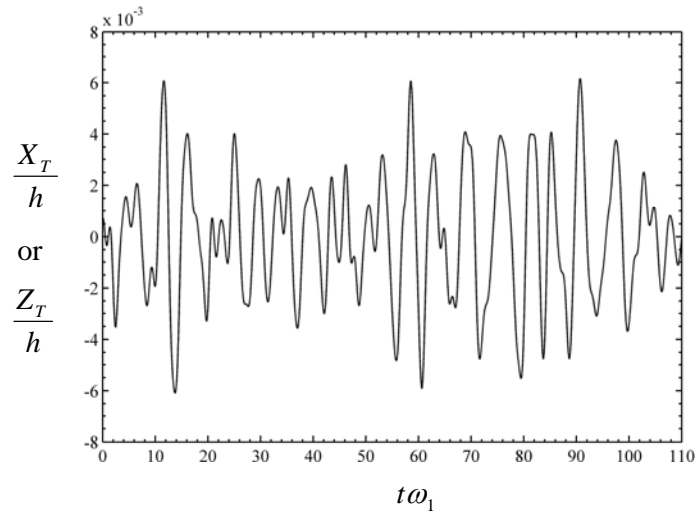


Fig. 5.37b Displacement Generated from the Spectrum Fig. 5.37a

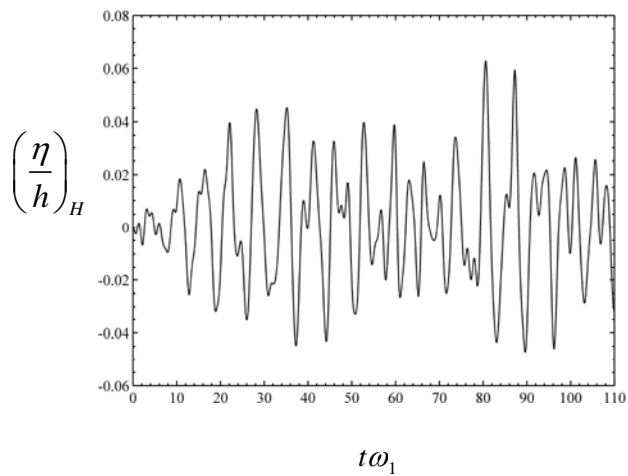


Fig. 5.37c Free Surface Elevation at the Left Corner of the Wall due to Horizontal Motions Prescribed by Fig. 5.37b

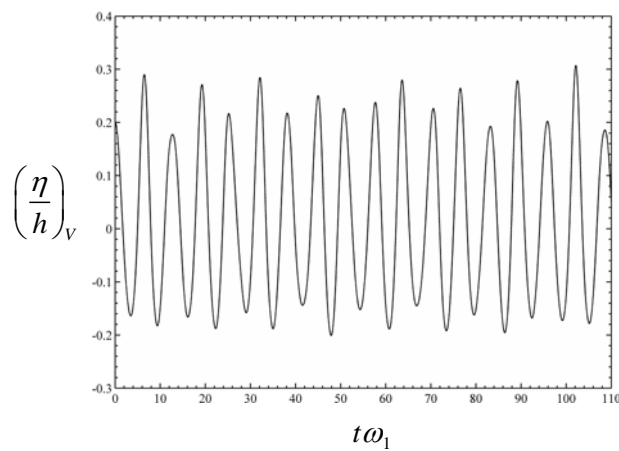


Fig. 5.37d Free Surface Elevation at the Left Corner of the Wall due to Vertical Motions Prescribed by Fig. 5.37b

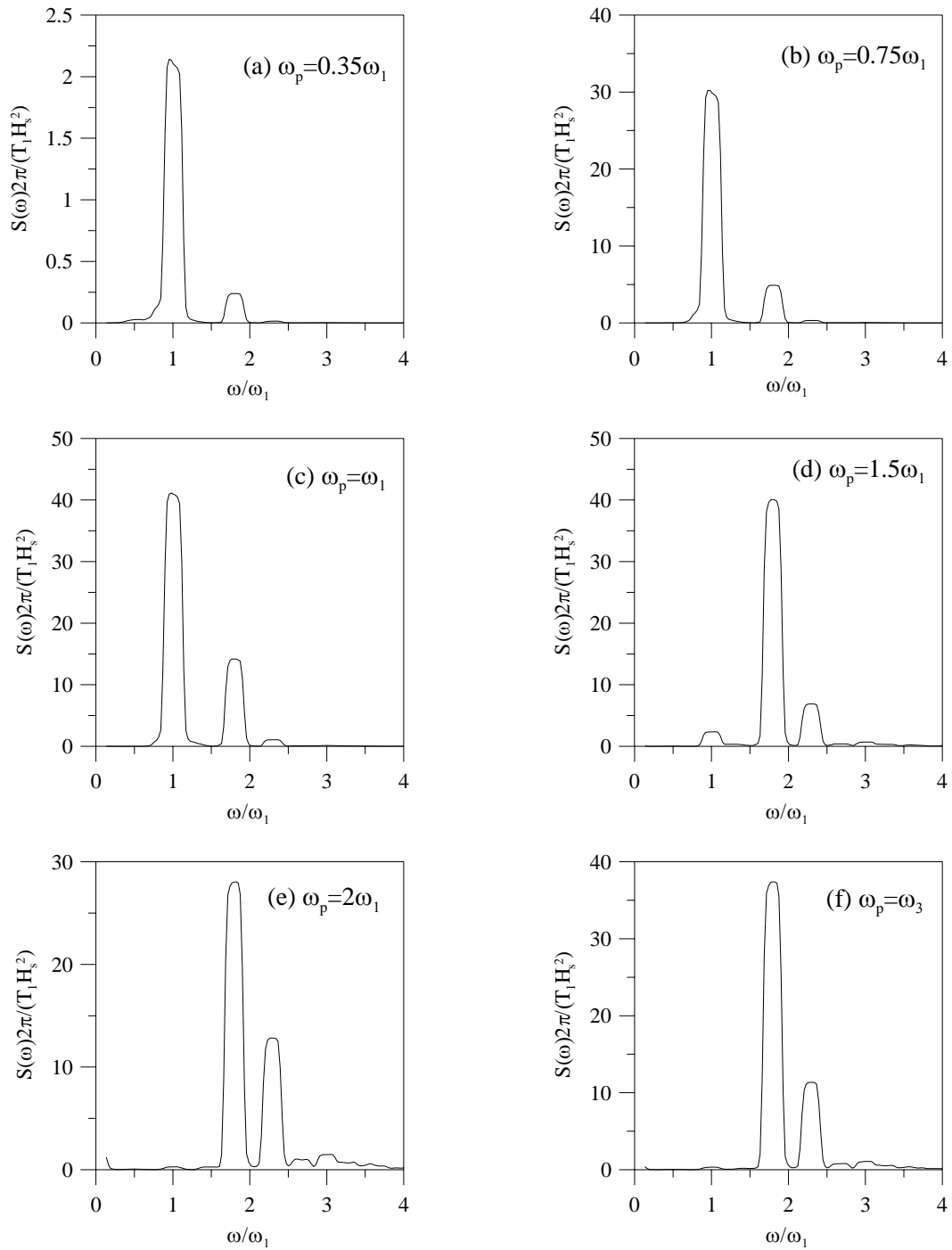


Fig. 5.38 Spectra of Free Surface Sloshing Waves at the Left Corner of the Wall due to Horizontal Random Excitation of $H_s = 0.006h$ [$T_1 = 2\pi / \omega_1$]

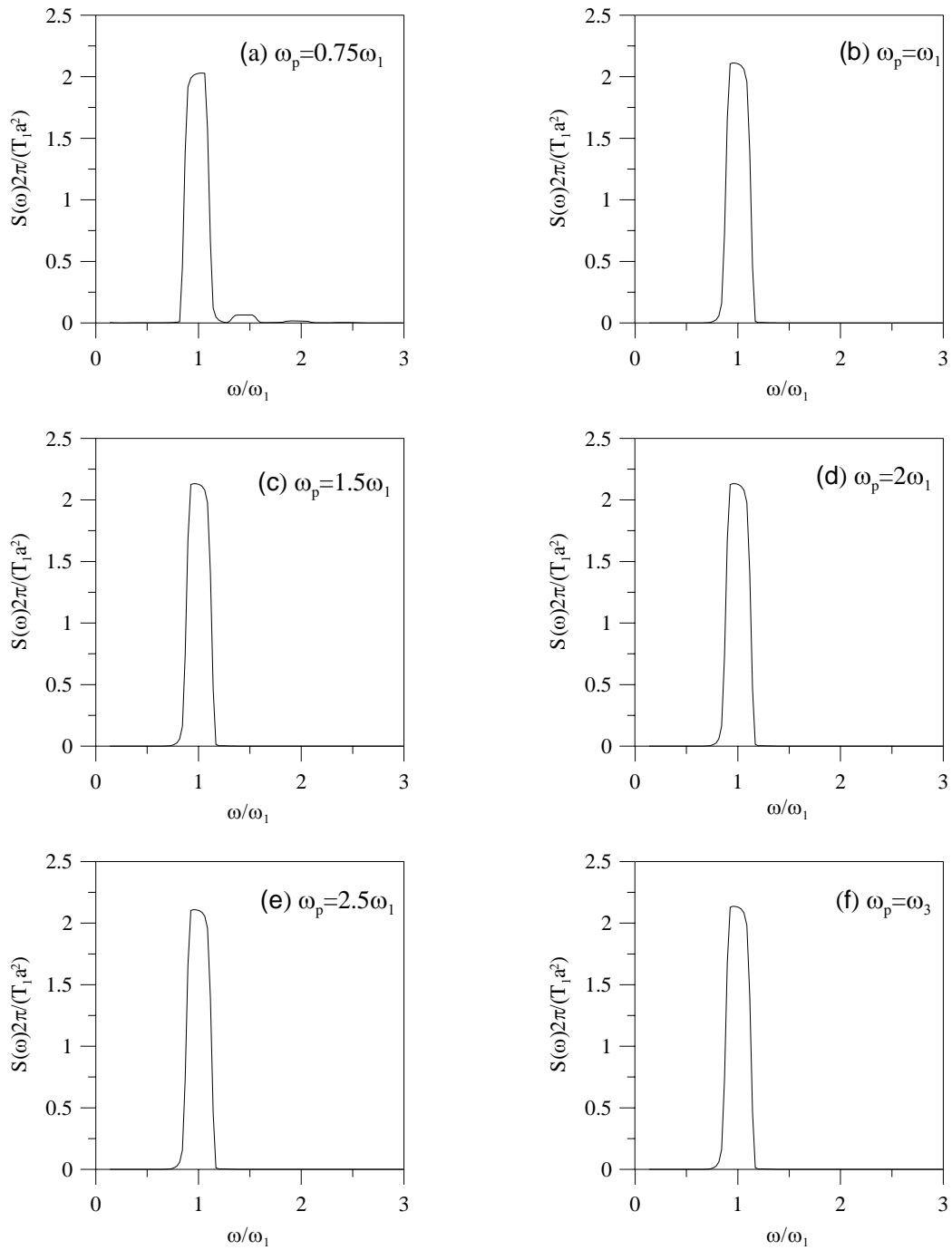


Fig. 5.39 Spectra of Free Surface Sloshing Waves at the Left Corner of the Wall due to Vertical Random Excitation for an Initial Steepness of 0.014 and $H_s = 0.006h$ [$T_1 = 2\pi / \omega_1$]

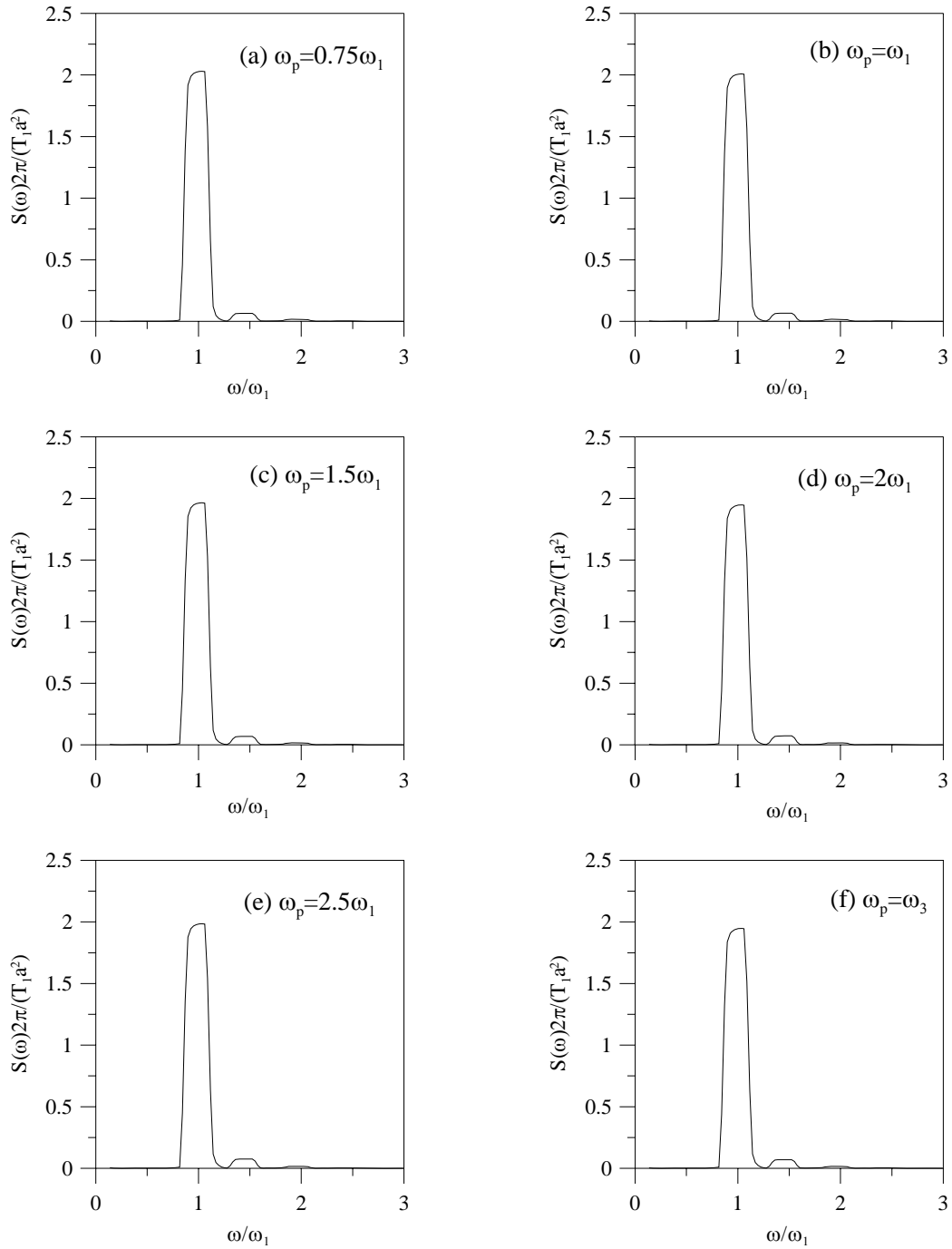


Fig. 5.40 Spectra of Free Surface Sloshing Waves at the Left Corner of the Wall due to Vertical Random Excitation for an Initial Steepness of 0.288 and $H_s = 0.006h$ [$T_1 = 2\pi / \omega_1$]

CHAPTER 6

3-DIMENSIONAL NUMERICAL WAVE TANK

6.1 GENERAL

The previous chapters focused in detail the implementation of 2-dimensional simulation in FEM and the estimation of different velocity calculation methods and its influence on smoothing/ regriding. The developed model has been applied to various wave structure problems and sloshing. In this chapter, the extension of the present code to the 3-D tank has been presented. In the previous chapters, width of the tank for the numerical simulation has not been considered, from herein, the width will be considered and hence named as 3-D tank following Ma *et al.* (2001). For the FEM discretization, four noded tetrahedron elements are used. As a preliminary investigation, only 2-D waves are generated in a 3-D tank.

6.2 MATHEMATICAL FORMULATION

The basic assumption, boundary conditions, FE formulation as described in chapter 3, remains same but with an additional horizontal dimension, y . A brief overview of the mathematical formulations is given in this section. The flow problem to be defined with the Laplace's equation involving velocity potential $\Phi(x, y, z, t)$ given by

$$\nabla^2\Phi=0 \tag{6.1}$$

A potential flow in a rectangular flume with a wavemaker at one end and the nonlinear free surface boundary condition at the free surface is considered. The schematic representation of the computational domain and the prescribed Neumann and Dirichlet boundary conditions on the five boundaries [bottom (A_B), left (A_P), right (A_∞), front (A_W) and back (A_W) wall] and at the free surface are shown in Fig. 6.1.

The tank bottom is assumed to be flat, rigid and no flow through it is given by,

$$\frac{\partial \Phi}{\partial n} = 0 @ z = -h, \text{ on } A_B \quad (6.2)$$

Fully reflecting wall at the far end and at side walls are represented by,

$$\frac{\partial \Phi}{\partial n} = 0 @ x = L, \text{ on } A_\infty \quad (6.3)$$

$$\frac{\partial \Phi}{\partial n} = 0 @ y = 0 / y = B, \text{ on } A_w \quad (6.4)$$

Wave paddle on the left end,

$$\frac{\partial \Phi}{\partial n} = \dot{x}_p(t) @ x = x_p(t), \text{ on } A_p \quad (6.5)$$

where, $x_p(t)$ is the time history of wave paddle motion. The boundary condition at the far end is dealt later.

The Lagrangian form of nonlinear free surface boundary condition is given by Longuet–Higgins and Cokelet (1976) as,

$$\frac{Dx}{Dt} = \frac{\partial \Phi}{\partial x} \quad (6.6a)$$

$$\frac{Dy}{Dt} = \frac{\partial \Phi}{\partial y} \quad (6.6b)$$

$$\frac{Dz}{Dt} = \frac{\partial \Phi}{\partial z} \quad (6.6c)$$

$$\frac{D\Phi}{Dt} = \frac{1}{2} \nabla \Phi \nabla \Phi - g\eta \quad (6.6d)$$

The finite element formulation in the 3-D tank without considering the Dirichlet condition is then written as (Eqn.3.14 in 2-D),

$$\iiint_V \nabla N_i \sum_{j=1}^m \phi_j \nabla N_j dV = - \iint_A N_i \dot{x}_p(t) dA \quad (6.7)$$

The above equation can be rewritten in the matrix form and the Dirichlet condition can be imposed as,

$$\mathbf{A}_{ij} \Phi = \mathbf{B}_i \quad (6.8a)$$

where,

$$\mathbf{A}_{ij} = \begin{cases} \iiint_V \nabla N_i \nabla N_j dV, & i, j \notin A_s \\ 1, & i = j \text{ \& } j \in A_s \\ 0, & (i \in A_s \text{ or } j \in A_s) \text{ \& } i \neq j \end{cases} \quad (6.8b)$$

$$\mathbf{B}_i = \begin{cases} - \iint_A N_i \dot{x}_p(t) dA \\ \phi_i, & i \in A_s \end{cases} \quad (6.8c)$$

Linear 4- noded tetrahedron element is adopted. Even though, the solution for the above system of linear equations is symmetric and banded, the number of nodes (equations) in the 3-D case is large and hence, in order to minimize the computational time, one has to resort to special solvers like direct solver with out-of-core or indirect matrix solver. For the present study, the Gauss elimination method as an in-core solver is used even though the computational time is large.

As described in the previous chapters, the calculation of velocity plays a major role in the time dependent simulation. In analyzing the different velocity calculations methods, the proposed cubic spline approach (Section 3.6.6) holds good only for 2-D, whereas, sigma transformation, least square method and global projection method are applicable for both the cases. The estimation using global projection method in the 3-D case is expensive, since one has to solve two equations based on the total number of nodes in the domain. The mapping of the physical domain to the computational

domain at every time step using sigma transformed FD is not feasible for unstructured mesh. The least square principle is flexible to adapt for any kind of mesh configuration and hence adopted in the present study.

Ma *et al.* (2001a) used the least square principle by making use of the free surface nodes alone (considering as grouping vectors) for the calculation of velocity and claimed that this led to inaccurate velocity evaluations. Hence, a recovery procedure has been implemented based on patch recovery techniques (Zienkiewicz and Zue , 1992) that are commonly adopted in the stress calculations in solid mechanics.

To overcome this difficulty, the least squares principle is adopted by considering the inner nodes also in the present investigation. The basic idea behind this method is to find the derivatives at any node by minimizing the sum of the squares of the error. Let k be neighbouring nodes for i th node (Fig. 6.2). For obtaining the derivative of function $\phi(x)$ at a point i , expand ϕ_i around ϕ_l that lead to,

$$\phi_i = \phi_l + (x_i - x_l)\phi_{,x} + (y_i - y_l)\phi_{,y} + (z_i - z_l)\phi_{,z} + O(\Delta x^2, \Delta y^2, \Delta z^2) \quad (6.9)$$

Defining,

$$\begin{aligned} x_{,l} &= (x_i - x_l) / dl ; \quad y_{,l} = (y_i - y_l) / dl ; \quad z_{,l} = (z_i - z_l) / dl ; \\ \phi_{,l} &= (\phi_i - \phi_l) / dl \\ dl &= \sqrt{(x_i - x_l)^2 + (y_i - y_l)^2 + (z_i - z_l)^2} \end{aligned} \quad (6.10)$$

Taking the RHS in Eqn. (6.9) to LHS and neglecting the higher order terms, then summing up the squares of the error around the point ϕ_i results in,

$$e = \sum_{n=1}^k (\phi_l^n - x_{,l}^n \phi_{,x} - y_{,l}^n \phi_{,y} - z_{,l}^n \phi_{,z})^2 \quad (6.11)$$

Minimizing the error e of Eqn. (6.11) with respect to ϕ_x, ϕ_y, ϕ_z (i.e., u, v, w) leads to the following system of linear equations.

$$\begin{pmatrix} \sum_{n=1}^k x_l^n x_l^n & \sum_{n=1}^k x_l^n y_l^n & \sum_{n=1}^k x_l^n z_l^n \\ \sum_{n=1}^k y_l^n x_l^n & \sum_{n=1}^k y_l^n y_l^n & \sum_{n=1}^k y_l^n z_l^n \\ \sum_{n=1}^k z_l^n x_l^n & \sum_{n=1}^k z_l^n y_l^n & \sum_{n=1}^k z_l^n z_l^n \end{pmatrix} \begin{Bmatrix} u \\ v \\ w \end{Bmatrix} = \begin{Bmatrix} \sum_{n=1}^k x_l^n \phi_l^n \\ \sum_{n=1}^k y_l^n \phi_l^n \\ \sum_{n=1}^k z_l^n \phi_l^n \end{Bmatrix} \quad (6.12)$$

If one knows the vertical velocity (w), the above equation can be solved to obtain the tangential velocities. The above system of equations reduce to the 2-D case as given in Eqn.(3.20a), when one eliminates v . For calculation of the vertical velocity (w), a standard 4 point backward finite difference scheme for unequal interval is used taking the advantage of node distribution in vertical direction, similar to 2-D case. A cubic polynomial is employed to represent the velocity potential at four different points that lies along a vertical straight line below the free surface node.

$$\begin{aligned} \phi_1 &= a + bz_1 + cz_1^2 + dz_1^3 \\ \phi_2 &= a + bz_2 + cz_2^2 + dz_2^3 \\ \phi_3 &= a + bz_3 + cz_3^2 + dz_3^3 \\ \phi_4 &= a + bz_4 + cz_4^2 + dz_4^3 \end{aligned} \quad (6.13)$$

The above system of equations can be solved a, b, c and d . The first order difference is found out by direct differentiation of first equation (ϕ_l , lies on the free surface) and plug-in the constant values to find the vertical velocity. This method of estimating the vertical velocity is found to be more accurate than that from Eqn.(3.1) for the 3-D case. The NODETAB algorithm detailed earlier for 2-D tank has been established for the 3-D tank, which is used for the least square method to calculate horizontal velocities.

6.3 MESH GENERATION

In the present study, the mesh generation has been kept simple. The free surface nodes are initially equally spaced as,

$$\begin{aligned} x_i &= ((i-1)*L)/NX \\ y_i &= ((j-1)*B)/NY \end{aligned} \quad (6.14)$$

where, NX and NY are the number of elements in the x and y direction, respectively. L and B are the length and breadth of the tank, respectively. One could use Eqn. (3.26), to find the nodes across the depth using exponential decay. However, during implementation it has been noticed that as the time progresses, the mesh configuration gets skewed. Hence, the positions of the nodal coordinates are generated depending upon the y - coordinates. Thus, Eqn. (3.26) has been modified as given below following Ma *et al.* (2001a).

$$z_{i,j} = (h + \eta_i) \frac{\exp(-\alpha_z(h + \eta_i)) - \exp(-\alpha_z(h + \eta_i)(j)/NZ)}{1 - \exp(-\alpha_z(h + \eta_i))} + \eta_i \quad (6.15)$$

for $i = 1, 2, \dots, (NX+1)$ and $j = 1, 2, \dots, NZ+1$

where, α_z is the parameter controlling the mesh size along the vertical direction, which is inversely proportional to λ/h ratio. That is, a larger value is adopted for smaller λ/h ratio, which leads to smaller elements near to the free surface. One should avoid high mesh aspect ratio, hence, the following criteria is used for the evaluation of α_z .

$$\alpha_z = -0.31 \frac{h}{g} \sigma^2 + 2.29 \sqrt{\frac{h}{g} \sigma^2} - 1.47 \quad (6.16)$$

As discussed earlier, the value of the parameter α_z also depends on the $y -$ coordinates, i.e., by considering the length of the element in the $x-y$ direction (l_{xy}) and hence, the following criteria is also checked,

$$\alpha_z < \min(\alpha_1, \alpha_2)$$

where α_1 and α_2 are determined by solving the following implicit equations.

$$\frac{\exp\left[\frac{\alpha_1(h + \eta_i)}{NZ}\right] - 1}{\exp[\alpha_1(h + \eta_i)] - 1} = \frac{l_{xy}}{10(h + \eta_i)} \quad (6.17a)$$

$$\frac{\exp\left[\frac{-\alpha_2(h + \eta_i)}{NZ}\right] - 1}{\exp[-\alpha_2(h + \eta_i)] - 1} = \frac{10l_{xy}}{(h + \eta_i)} \quad (6.17b)$$

After obtaining the nodal coordinates and node numbering, the element connectivity has been done. In order to generate the linear 4 - noded tetrahedron element, the following procedure is adopted. Initially, the hexahedron is formed, followed by dividing it into two prism elements. Each prism is divided into three tetrahedron elements. Thus, a hexahedron is divided into six linear 4 - noded tetrahedron elements. The physical interpretation of the above procedure is depicted in Fig. 6.3.

6.4 MESH ORIENTATION STUDY

The mesh structure plays an important role in FEM. In the case of 2-D mesh structure (Fig. 3.6), the mesh orientation suggested by Westhuis (2001) based on Eigen value test has been adopted, whereas, for the 3-D meshing, different investigators used different configuration (Ma *et al.* 2001b; Wu and Hu, 2004; Wang and Wu, 2007). Hence, an orientation study has been carried out based on numerical experiments for different 3-D mesh configuration. To quantify the effect of the mesh configuration,

the velocity potential has been compared with the results from 2-D simulation for a narrow tank. A 5m long tank with a water depth of 1m is considered in a 2-D simulation and a constant velocity of 3.132 m/s is given at the left side boundary. The velocity contour along the length of the tank is shown in Fig. 6.4. The velocity potential along the y - direction remains same. Four different 3-D mesh orientations have been considered. Considering the mesh type I, the velocity potential contours are shown in Fig. 6.5a. The breadth of the tank is assumed to be 0.5m. The comparison of the velocity potential at a particular depth ($z/h = -0.045$) along the y -direction is shown in Fig. 6.5b. For 2-D, the velocity potential values remain constant along the y -direction. Similarly, the velocity potential across the z - direction at the left side boundary obtained from 3-D simulation is compared with 2-D. The variation across the depth is found to oscillate as can be seen in Fig. 6.5c.

In mesh type II, the mesh orientation has been reversed and the corresponding simulated velocity potential contour is shown in Fig. 6.6. The variation of potential across the tank width (Fig. 6.6b) is observed to be reversed compared to Fig. 6.5b, corresponding to the reversal of mesh orientation. After observing mesh orientation, mesh type III has been attempted by using zigzag configuration. Fig. 6.7a shows the simulated potential contours and Fig. 6.7b shows the variation of potential across the width of the tank. The variation is also found to be zigzag. Even after increasing the number of nodes in the y – direction, the inaccuracies exist for all the above mesh types. To overcome the above difficulties, mesh type IV with crisscross links has been generated and the corresponding simulated potential contour is shown in Fig. 6.8a. It is found that the potential value across the width and depth are in good agreement

with the comparison of potential in 2-D simulation. Hence, mesh type IV has been considered for all the 3-D simulation in the present study.

6.5 WAVE ABSORBERS

6.5.1 General

The absorption of the nonlinear free surface waves has been a topic of intensive research both through experimental and numerical studies. In the case of experiments, the absorption of the nonlinear free surface waves has been attempted by using the porous systems. The numerical absorption using non-reflecting boundary condition is being adopted to let the waves purely outgoing as in open sea state. A comprehensive review of the numerical methods in the context of absorption of nonlinear free surface waves is given by Romate (1992). The commonly adopted absorber types are:

- *Matching boundary condition:* This technique consists in matching the inner solution at the truncation boundary with an outer one generated by Kelvin's Green function which satisfies intrinsically the free surface condition. In order to minimise the difference between the inner nonlinear solution and the outer linear one, the above linear approximation being imposed at a larger distance thus it requires larger computational domain. This method was being implemented by Lin *et al.* (1984) and Dommermuth and Yue (1987).
- *Sommerfeld radiation boundary condition:* This condition is often used in the frequency domain analysis, providing a simple relationship between the time and normal derivatives. Sommerfeld condition in the time domain has been given by Orlandi (1976) by replacing the frequency dependent phase velocity to the local

time dependent velocity, $C(t)$. This condition is local both in time and space and also applicable for the known time period steady waves. Grilli *et al.* (1989) developed an implicit iterative radiation condition, based on Sommerfeld's condition, which worked quite well for waves of permanent form like solitary waves. A more accurate explicit approach was proposed by Otta *et al.* (1992), combining Orlandi's condition with the incident wave kinematics calculated at internal nodes in the model, close to the radiation boundary. The method worked well for periodic waves but only exhibited limited success when applied to irregular waves.

- *Damping zone:* Based on the methodology of Le Mehaute (1972), Larsen and Darcy (1983) introduced a concept of 'absorbing beach' in which an external pressure was applied on the surface to create a negative work against the incident work. This concept has been implemented in the weakly nonlinear model based on Boussinesq equations. This concept acts as an artificial damping in the form of sponge layers or damping zone so that the outgoing waves are damped near the open boundary with little reflection. Two methods of implementation are possible for this concept: the first is to add a damping in the field equation and the other is to include the damping term in the surface boundary condition. In the case of fully nonlinear free surface waves based on potential flow method, it has been used by adding in dynamic condition and/or in kinematic condition. (Betts and Mohamad, 1982; Cointe *et al.* 1990; Cao *et al.* 1993; Ohya and Nadaoka, 1991; Subramanya and Grilli, 1994; and Clement, 1996). This concept is easier to implement and has good absorption capacity over a wide range of frequencies

requiring a large damping zone normally of the order of ten times the water depth or three times the wavelength.

- *Active wave absorber*: This technique is similar to the wave paddle absorption used in the laboratory by use of piston type boundary condition. Clement (1996) used this type of boundary condition and later was implemented by several investigators.

Instead of using a single absorber, combination of any two absorbers provides an efficient solution. A combination of a Sommerfeld condition and a numerical dissipation zone, originally suggested by Israeli and Orszag (1981) and later extended by several authors' (e.g., Ohyama and Nadaoka, 1991; Ma *et al.* 2001). However, a relatively long dissipative zone is needed to obtain sufficiently low reflection and hence the associated computational costs considerably increase for some of the applications. Westhuis (2001) used a combination of absorbing beach with a constant length and Sommerfeld radiation condition along with the grid stretching. Clement (1996) proposed a method by combining an absorbing beach with an active absorbing boundary condition at the tank extremity, and showed that this method performed well for unsteady finite amplitude waves. In the 2-D simulation, the inclusion of the damping zone is sufficient since, larger domains can be considered. In the 3-D simulation, this is not feasible. Hence, a combination of new type of mixed boundary condition consisting of absorbing beach along with the mesh stretching technique is adopted in the present study. A brief overview of the proposed methodology is given below.

6.5.2 Mixed Boundary Condition

The well known Orlanski condition can be written as,

$$\frac{\partial \Phi(z,t)}{\partial n} = \frac{1}{c(t)} \frac{\partial \Phi(z,t)}{\partial t} \quad (6.18)$$

where, the local normal velocity is considered proportional to the dynamic pressure and therefore, is a function of z . The coefficient $c(t)$ is kept constant with a limit of long wave theory \sqrt{gh} or assumed to be time dependent and continuously extrapolated at each time instant from the previous time steps during the simulation. Clement (1996) proposed a piston like boundary condition after the extensive investigation on the above method of implementation. This Neumann boundary condition is said to be piston like since the normal derivative does not depend upon z (dependency is being neglected, by averaging the dynamic pressure at the boundary), and is given in 2D as,

$$\frac{\partial \Phi(z,t)}{\partial n} = \frac{1}{c(t)} \int_r \rho \frac{\partial \Phi}{\partial t} \quad (6.19)$$

As per Clement (1996), this would act as an efficient filter in the lower frequency zone. In the present 3-D implementation it is denoted by replacing Eqn. (6.4) as,

$$\frac{\partial \Phi}{\partial x} = \frac{1}{\rho A \sqrt{gh}} \int_A \rho \frac{\partial \Phi}{\partial t} dA \quad @ x=L, A_\infty \quad (6.20)$$

The evaluation of the dynamic pressure plays a crucial role. In usual practice, it is calculated based on the potentials at the previous time step. To avoid numerical oscillation, Grilli and Horillo (1999) proposed a moving average scheme. In the present study, an implicit form has been attempted. This is similar to the source and sink approach that is widely used in ground water flow problems (Seegerlind, 1984).

The dynamic pressure term is written in the forward difference form and simplified as given below.

$$\frac{\partial \phi}{\partial x} = \frac{1}{A\sqrt{gh}} \sum_1^n (\phi(t+dt) - \phi(t) / dt) dA \quad (6.21)$$

This is simplified to the following mixed form as,

$$\frac{\partial \phi}{\partial x} = S - M \phi \quad (6.22)$$

where,

$$S = -\frac{1}{dtA\sqrt{gh}} \sum_1^n \phi(t) dA, \quad M = \frac{1}{dt\sqrt{gh}} \quad (6.23)$$

Here, M is analogous to the sink term and S is the known velocity potential at the previous time step.

The inclusion of the above formulated mixed boundary condition has been implicitly coupled with the global stiffness matrix (\mathbf{A}) and the right hand side matrix (\mathbf{B}) as given below. The final FE formulation [Eqn. (6.7)] after the inclusion of the mixed boundary condition is,

$$\iiint_V \nabla N_i \sum_{j=1}^m \phi_j \nabla N_j dv = \iint_{A_e} N_i \left(S - M \sum_{j=1}^m \phi_j \right) dA - \iint_{A_p} N_i \dot{x}_p(t) dA \quad (6.24a)$$

Separating known and unknown values in matrix form leads to,

$$\mathbf{A}_{ij} \Phi = \mathbf{B}_i \quad (6.24b)$$

Where,

$$\mathbf{A}_{ij} = [\mathbf{A}_1] + [\mathbf{A}_M]_{ij} \quad (6.24c)$$

$$[\mathbf{A}_1] = \begin{cases} \iiint_V \nabla N_i \nabla N_j dV + M \iint_{A_s} N_i N_j dA, & i, j \notin A_s \\ 1 & , i = j \text{ \& } j \in A_s \\ 0 & , (i \in A_s \text{ or } j \in A_s) \text{ \& } i \neq j \end{cases} \quad (6.24d)$$

$$\mathbf{B}_i = \begin{cases} \iint_{A_s} S N_i dA - \iint_A N_i \dot{x}_p(t) dA \\ \phi_i & , i \in A_s \end{cases} \quad (6.24e)$$

The element matrix $[\mathbf{A}_M]_{ij}$ for tetrahedron element is given by,

$$[A_M]_{ij}^{abc} = \frac{MA_{abc}}{12} \begin{bmatrix} 2 & 1 & 1 & 0 \\ 1 & 2 & 1 & 0 \\ 1 & 1 & 2 & 0 \\ 0 & 0 & 0 & 0 \end{bmatrix}, [A_M]_{ij}^{bcd} = \frac{MA_{bcd}}{12} \begin{bmatrix} 0 & 0 & 0 & 0 \\ 0 & 2 & 1 & 1 \\ 0 & 1 & 2 & 1 \\ 0 & 1 & 1 & 2 \end{bmatrix} \quad (6.25)$$

$$[A_M]_{ij}^{acd} = \frac{MA_{acd}}{12} \begin{bmatrix} 2 & 0 & 1 & 1 \\ 0 & 0 & 0 & 0 \\ 1 & 0 & 2 & 1 \\ 1 & 0 & 1 & 2 \end{bmatrix}, [A_M]_{ij}^{abd} = \frac{MA_{abd}}{12} \begin{bmatrix} 2 & 1 & 0 & 1 \\ 1 & 2 & 0 & 1 \\ 0 & 0 & 0 & 0 \\ 1 & 1 & 0 & 2 \end{bmatrix}$$

where, $abcd$ are the local numbering of the element. The superscript in the matrix $[\mathbf{A}_M]$ of the above equations represents the local numbers that lie on the boundary. Thus, the inclusion of the mixed boundary condition has been coupled with the global stiffness matrix.

6.5.3 Damping Zone

The inclusion of the absorbing beach is similar to the 2-D case as discussed in Chapter 3 by incorporating in the dynamic and kinematic free surface boundary conditions as,

$$\frac{Dx}{Dt} = \frac{\partial \Phi}{\partial x}$$

$$\frac{Dy}{Dt} = \frac{\partial \Phi}{\partial y}$$

$$\frac{Dz}{Dt} = \frac{\partial \Phi}{\partial z} - v(x)z \quad (6.26a)$$

$$\frac{D\Phi}{Dt} = \frac{1}{2} \nabla \Phi \nabla \Phi - g\eta - v(x)\Phi$$

where, $v(x)$ is a damping coefficient defined by

$$v(x) = \begin{cases} 0 & , x < L - L_{beach} \\ \sigma_b \left(\frac{x - (L - L_{beach})}{L_{beach}} \right)^3 & , L - L_{beach} \leq x \leq L \end{cases} \quad (6.26b)$$

The damping frequency (σ_b) is used to control the strength of the damping zone, while, the parameter L_{beach} (beach length) is used to control the length of the damping zone.

6.5.4 Mesh Stretching

The implementation of mesh stretching has two advantages. The number of nodes in the damping zone has been redistributed to a larger length than required, thus one could increase the length of the beach without increasing the computational effort. In addition, FEM solution provides an underestimation of potential values in the damping zone due to coarser mesh adopted along the length of the beach, thus leading to better damping mechanism.

The number of nodes along the length of the beach has been stretched or redistributed. The distance between the two successive nodes thus has been increased in the horizontal direction.

$$\Delta x_{i+1} = \gamma \Delta x_{i-1}, \quad \text{for } i = 1, 2, \dots, N_b \quad (6.27)$$

where $\Delta x_{i+1} = |x_{i+1} - x_i|$, $i+1$ is node indices in the direction of wave propagation and N_b is the number of nodes along the beach length (L_{beach}). If one adopts the above formula for the known L_{beach} , then the effective beach width (L_{eff}) can be arrived based on the following expression,

$$L_{eff} = L_{Beach} \frac{\gamma^{N_b} - 1}{N_b(\gamma - 1)} \quad (6.28)$$

Herein, γ play a major role in the mesh stretching technique and is called as mesh stretching coefficient. The mesh stretching coefficient can be adopted based on the simulation problem. Larger coefficient leads to a larger spacing along the horizontal direction leading to skewed mesh and hence the mesh aspect ratio should also be considered. The physical interpretation of the mesh stretching technique is shown in Fig. 6.9.

6.5.5 Proposed Wave Absorber for the Present Study

For the present 3-D implementation, the piston like boundary condition is replaced with a mixed form and specified at the far end. This form of implicit coupling leads to a stable simulation. The damping frequency, σ_b is assumed to be equal to three times the input frequency and L_{beach} is assumed to be equal to one wave length. In general, the beach length should be of the order of damping frequency. To achieve this, the mesh stretching technique has been included as described in the last section. The mesh stretching coefficient is assumed to be 1.03. This coefficient has been arrived based on the extensive numerical tests for the combination of the three different absorption conditions.

6.6 REGRIDDING METHOD

In the case of 2-D, regridding is simple to implement, whereas, for 3-D it is more complex, time consuming and loss of energy occurs. In the present study, a simple regridding procedure is adopted and the mesh stretching algorithm has also been considered before implementing. The first step in the regridding procedure is the generation of the x - and y - coordinates. This can be done by dividing the length of the domain (from the new wave maker position to the point before the mesh has been stretched) by initial number of nodes to generate x - coordinates. Similarly, y -coordinates are generated with equal spacing. Thus, a mesh structure is formed initially. The second step is to find the new vertical positions (z) and the corresponding velocity potential for the mesh structure. This can be evaluated using the TRIFIND algorithm described in the unstructured mesh and the interpolation is based on the shape function (3-point).

6.7 COMPARISON WITH 2-D TANK

In this section, the validation of the developed 3-D model has been made by comparing the simulated nonlinear wave with the simulation using 2-D model. The length of the tank for the present case is 15.1m. The wave height is 0.07m and the wave period is 0.8s in a water depth of 0.6m, so as to generate a steepness of 0.082. The comparison of the time histories at the 0.5m and 3.572m from the wave paddle are shown in Fig. 6.10 and Fig. 6.11. The relative errors for the above two time histories with respect to the 2-D simulations are 0.03 and 0.16 respectively. The wave profile along the length of the tank near the wave paddle is depicted in Fig. 6.12. Regridding has been applied after every 20 time steps. A good agreement with the 2D

tank simulation can be observed. A snap shot of the mesh configuration during the simulation is shown in Fig. 6.13.

6.8 LONG TIME SIMULATION: WAVE ABSORBER

6.8.1. Monochromatic Wave

To show the efficacy of the wave absorber, the length of the tank is reduced to 6.7m and the simulation is carried out for a long time. The snapshots of the free surface profile at various time intervals are shown in Fig. 6.14. The damping zone starts at 4m from the wave paddle in the figure after the black line. The capability of the adopted methodology in dampening the steep nonlinear free surface waves can be seen. The comparison is made after a long time (after the reflection from the end wall) with the simulation carried out in the longer tank (15.1m). The time histories of free surface elevation near the paddle and just before the damping zone are depicted in Fig. 6.15 and Fig. 6.16, respectively. The space profile at time before the wave starts damped by the combined absorber ($t = 10.995\text{s}$) and after the long time ($t = 14.995\text{s}$) are shown in Fig. 6.17 and Fig. 6.18.

In order to show the efficiency of the present absorber, the absorption coefficients are estimated based on the numerical experiments carried out for various wave frequencies in the short and long tank. In the short tank, the initial distance between the wave paddle and the left end of the damping zone is taken as 4λ and for the long tank, it is taken as 12λ . The computations are carried out for $12T$.

The coefficient of absorption (C_a) is evaluated by the following expression.

$$C_a = 1 - \sqrt{1 - \frac{\|E_s - E_l\|}{E_l}} \quad (6.29)$$

where, E_s is the energy in the short tank and E_l is the energy in the long tank. The energy has been evaluated from the fourier spectrum of the time history recorded at the location $[L - (L_{beach} + 0.2\lambda)]$, which is just before the absorbing zone in the short length of the tank. For the long tank, the same location as in short tank has been chosen.

The coefficient of absorption for wave steepness ranging from 0.01 to 0.082 and for various wave frequencies is shown in Fig. 6.19. For all the test cases, the absorption coefficient is found to be greater than 0.95.

6.8.2. Bi-chromatic Wave

In order to show the efficiency of the present methodology for the absorber, waves with more than one frequency components, bi-chromatic waves are simulated.

The velocity of the wave maker is given as,

$$u = a_1 \sigma_1 \sin(\sigma_1 t) + a_2 \sigma_2 \sin(\sigma_2 t) \quad (6.30)$$

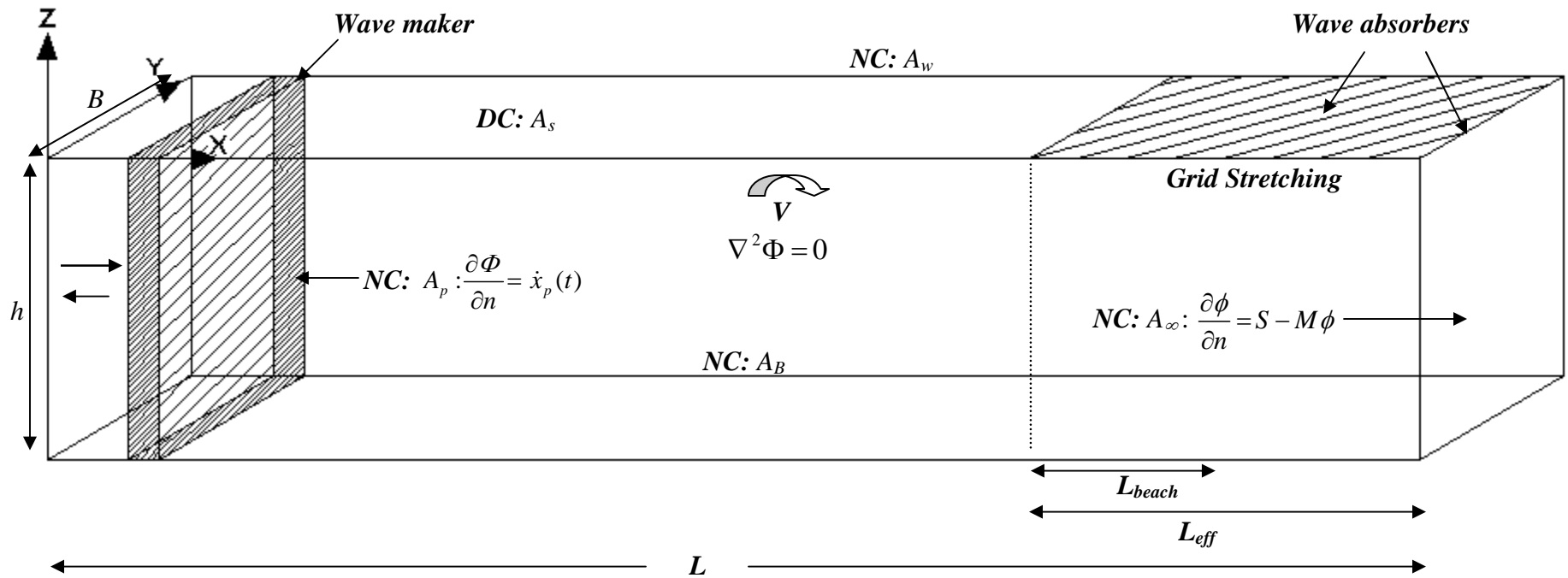
where a_1 and a_2 are the amplitudes corresponding to the wave frequency σ_1 and σ_2 .

The same damping mechanism as discussed earlier is used, but one has to properly choose the frequency (σ_b) and the length (L_{beach}) of the beach. In the present investigation, average frequency (σ_{avg}) in the domain is considered as input frequency (i.e, $\sigma_b = 3\sigma_{avg}$) and the average wave length is assumed to be the length of the beach. The simulation is carried out for short and long wave tanks and the time histories of free surface profile near to the paddle and before the absorber are compared. The

length of the short tank and long tank are 8.74m and 26.16m, respectively. The lengths of the tank due to mesh stretching are 11.503 and 28.75m. The wave amplitudes are taken as $a_1 = 0.016h$ and $a_2 = 0.5a_1$ and the corresponding angular wave frequencies are 5.86s and 8.08s. The free surface profile comparison before the absorber in the short tank is depicted in Fig. 6.20. The free surface profiles at two different time instants are shown in Fig. 6.21 and Fig. 6.22. The dampening efficient can clearly shows the capability of the proposed absorbing technique even for the bi-chromatic waves.

6.9 SUMMARY

This chapter deals with the implementation of the 3-D tank. The mesh orientation study has been carried out for the structured mesh simulation of the nonlinear free surface waves. Further, the implementation of the combined mixed boundary condition, damping zone along with the mesh stretching strategies are incorporated in the present model to deal with the highly nonlinear waves. The present absorber also works well for the bi-chromatic waves.



NC: Neumann Boundary condition,
 DC: Dirichlet Boundary condition,
 $A_B, A_w : \frac{\partial \Phi}{\partial n} = 0$

Fig. 6.1 Representation of 3-D Numerical Wave Tank with Prescribed Boundary Conditions

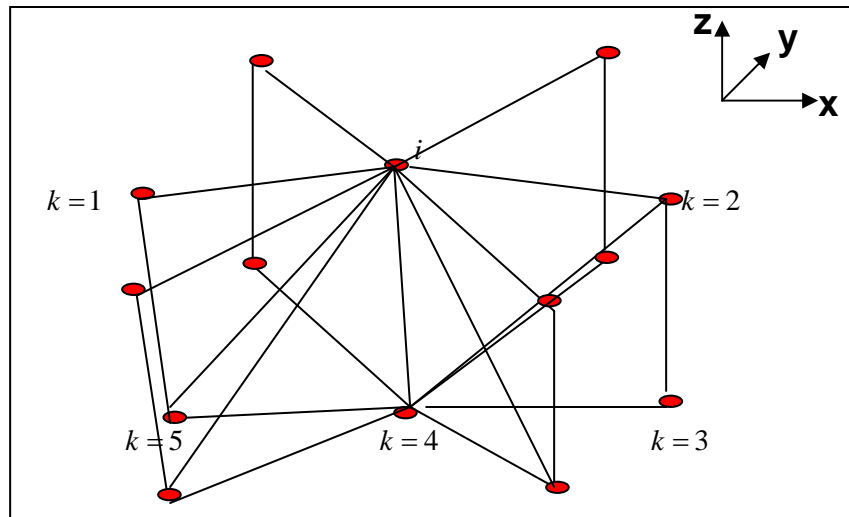
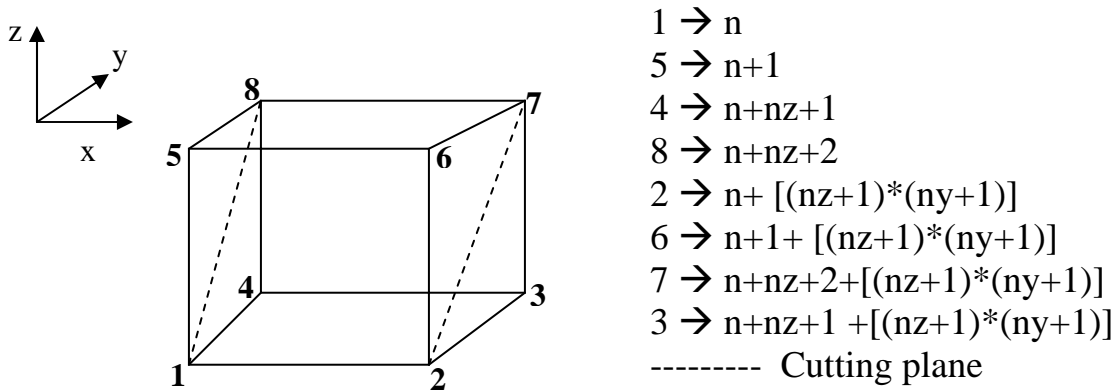
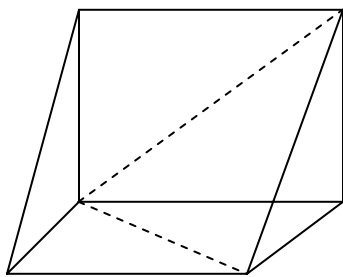


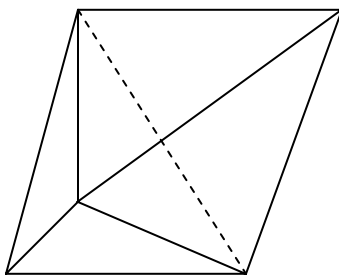
Fig. 6.2 Nodal Configuration for Least Squares Principle



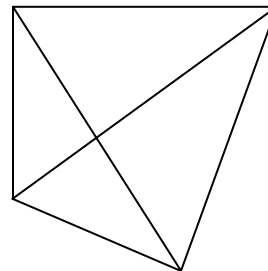
1st prism



2374

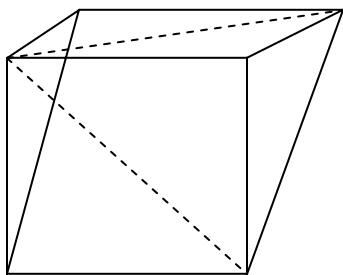


1482

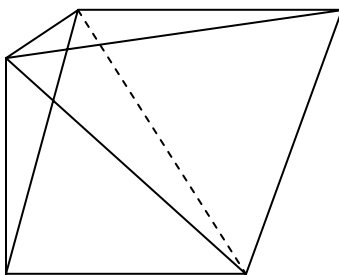


4782

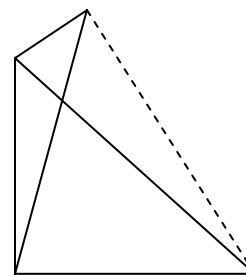
2nd prism



2765



5782



1258

Fig. 6.3 Division of Hexahedron to Six Tetrahedrons

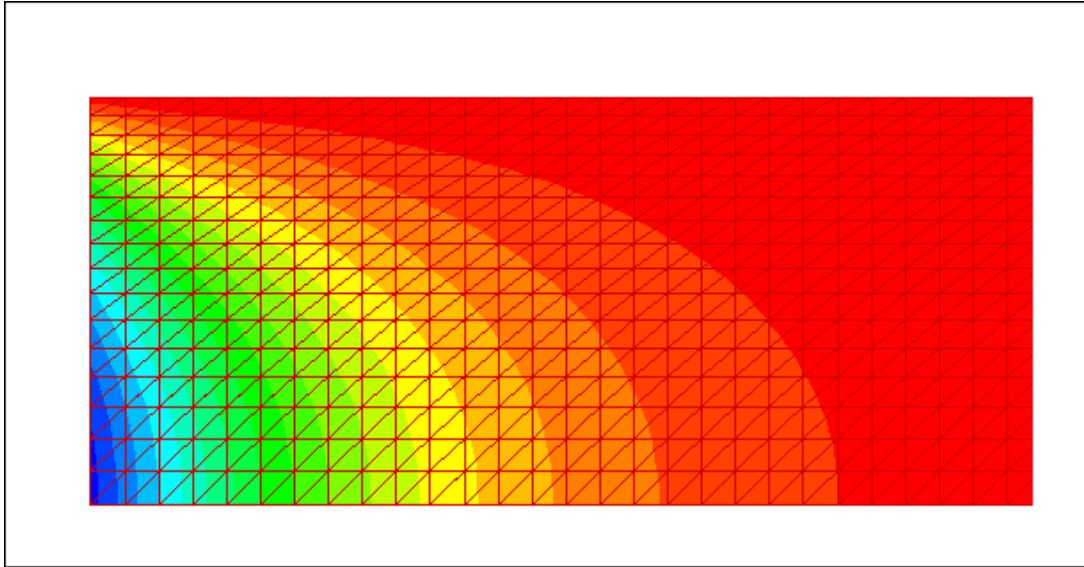


Fig. 6.4 Velocity Potential Contours along the Length of the 2-D Tank

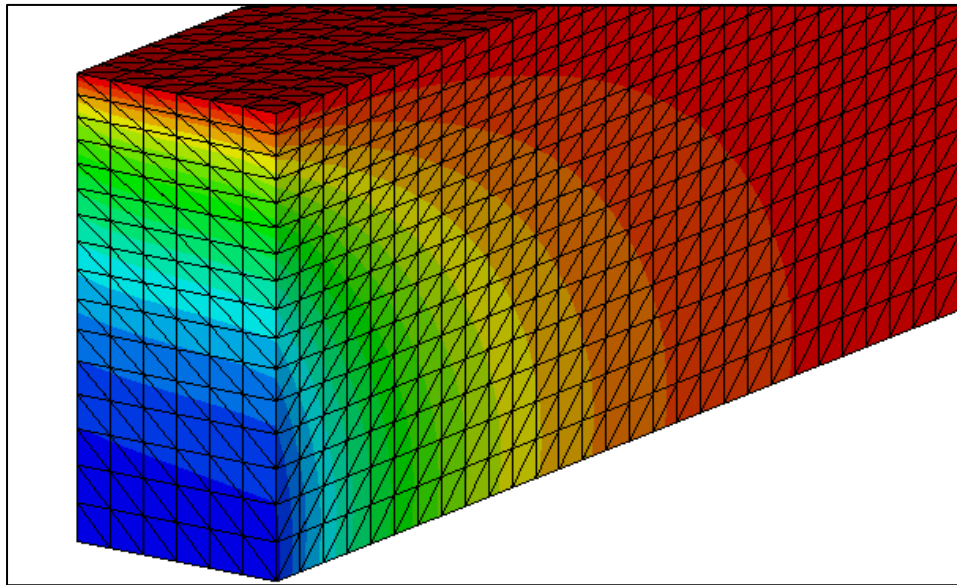


Fig. 6.5a Mesh Type I along with the Velocity Potential Contours in a 3-D Tank

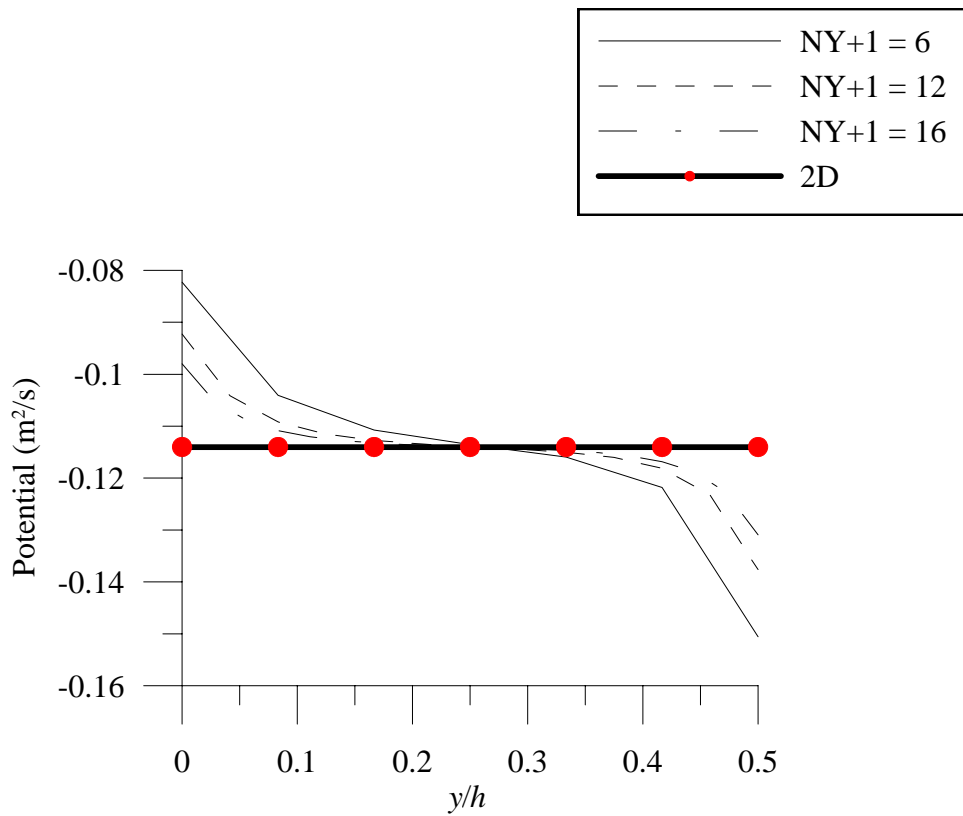


Fig. 6.5b Velocity Potential along y/h at $z/h = -0.045$ [Mesh Type I]

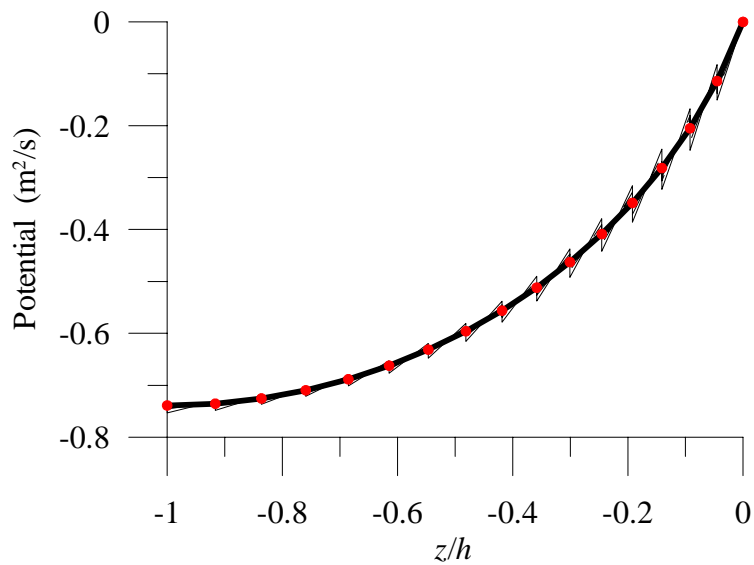


Fig. 6.5c Velocity Potential across z/h for all the y/h Values [Mesh Type I]

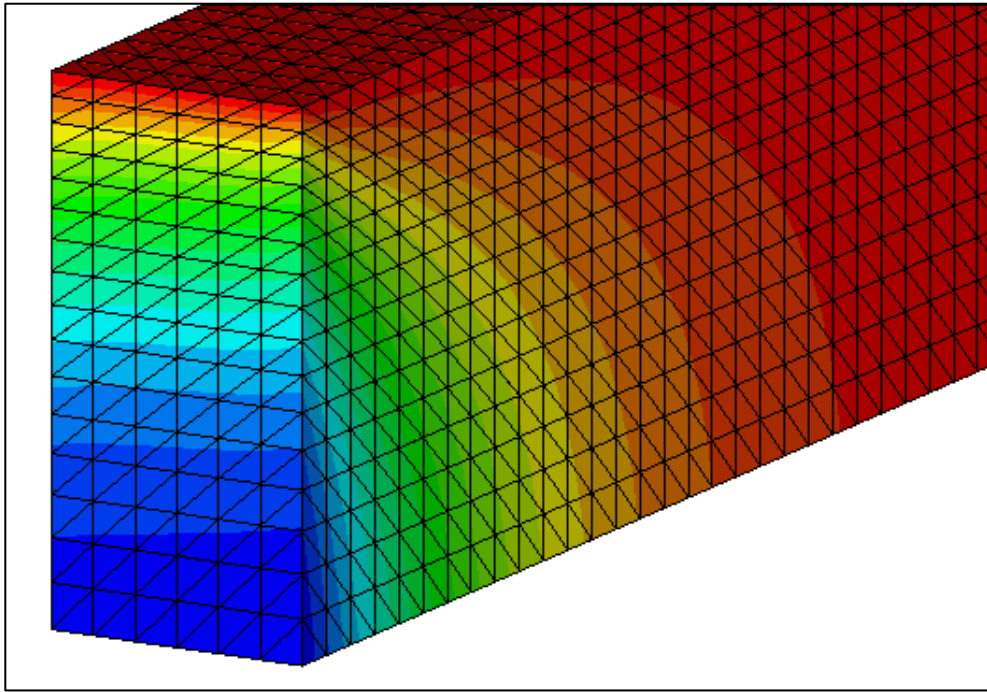


Fig. 6.6a Mesh Type II along with the Velocity Potential Contours

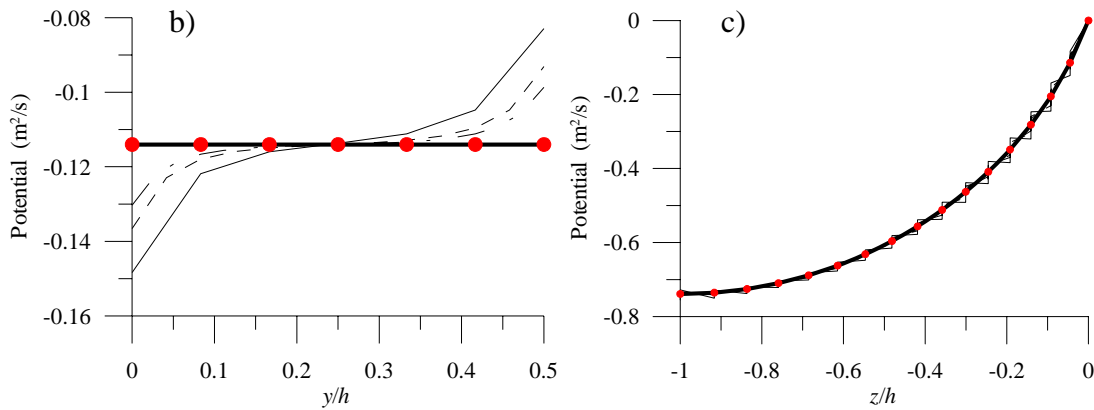


Fig. 6.6 (b) Velocity Potentials along y/h at $z/h = -0.045m$ (c) Velocity Potential across z/h for all y/h Values [Mesh Type II, — $NY+1= 6$; ----- $NY+1 = 12$; - . - .- $NY+1 = 16$; •-•-• 2-D]

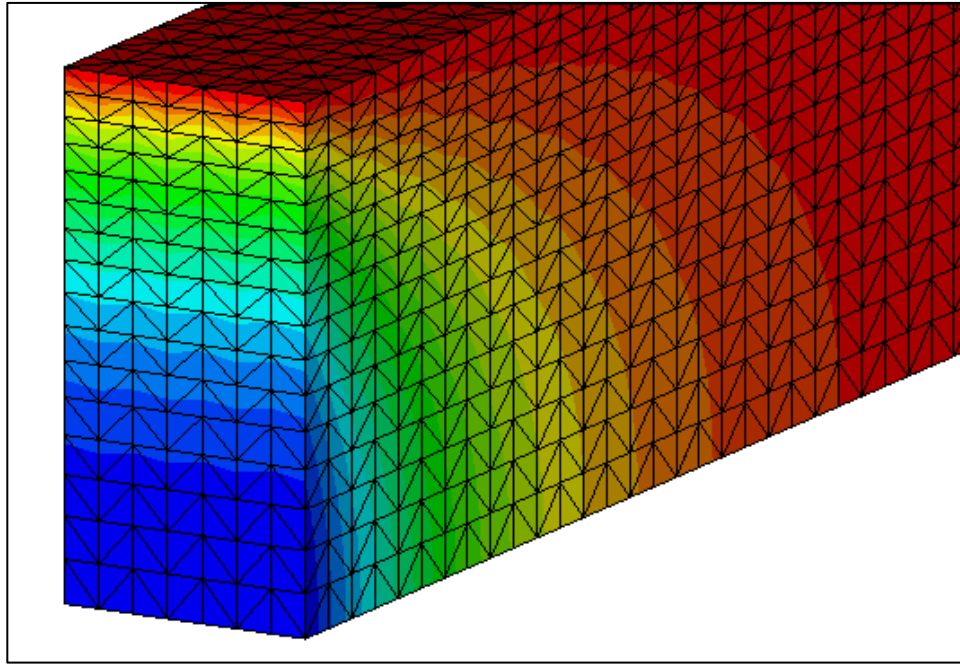


Fig. 6.7a Mesh Type III along with the Velocity Potential Contours

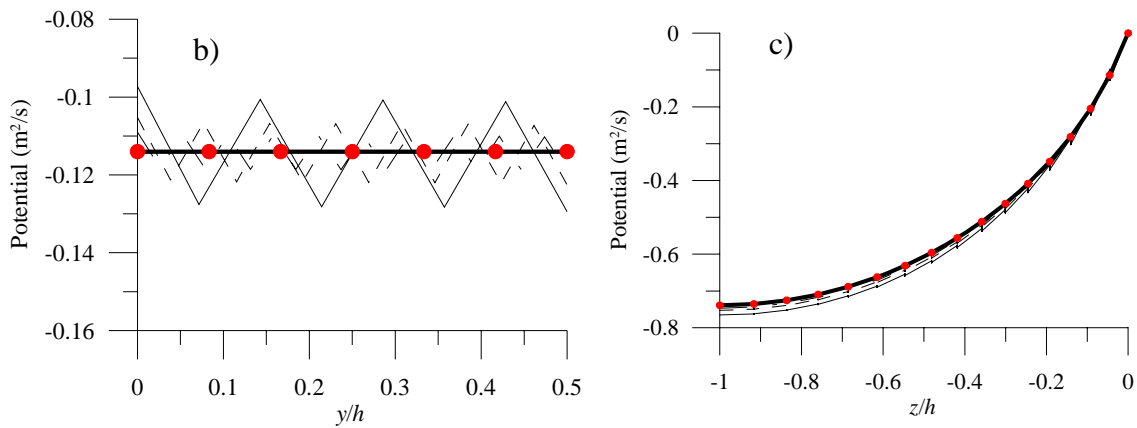


Fig. 6.7 (b) Velocity Potentials along y/h at $z/h = -0.045m$ (c) Velocity Potential across z/h for all y/h Values [Mesh Type III, — NY+1= 6; ----- NY+1 = 12; - . - . NY+1 = 16; •-•-• 2-D]

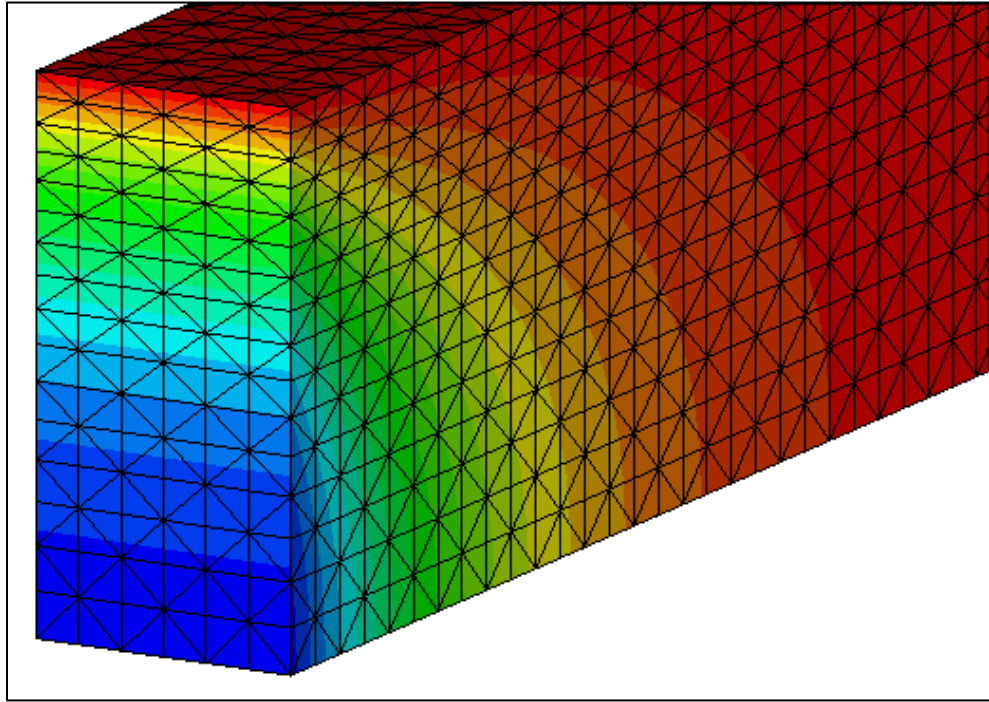


Fig. 6.8a Mesh Type IV along with the Velocity Potential Contours

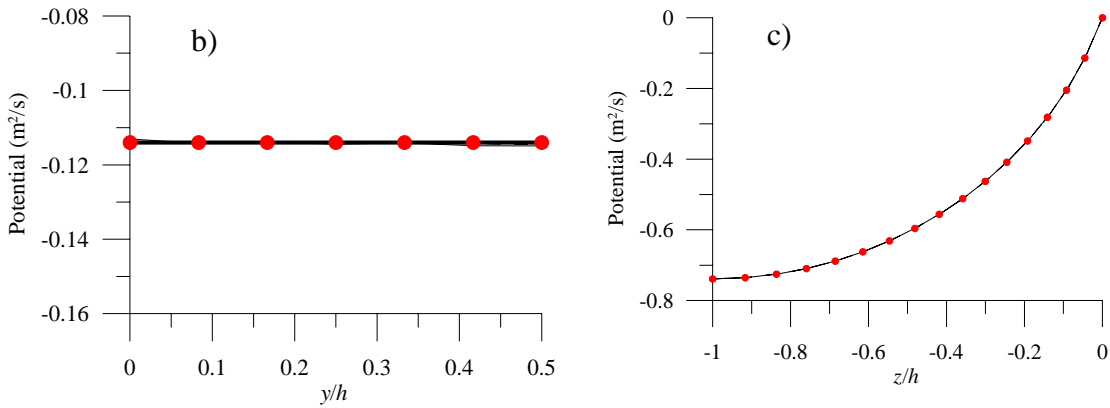


Fig. 6.8 (b) Velocity Potentials along y/h at $z/h = -0.045m$ (c) Velocity Potential across z/h for all y/h Values [Mesh Type IV, — NY+1= 6; ----- NY+1 = 12; - . - . NY+1 = 16; ●-●-● 2-D]

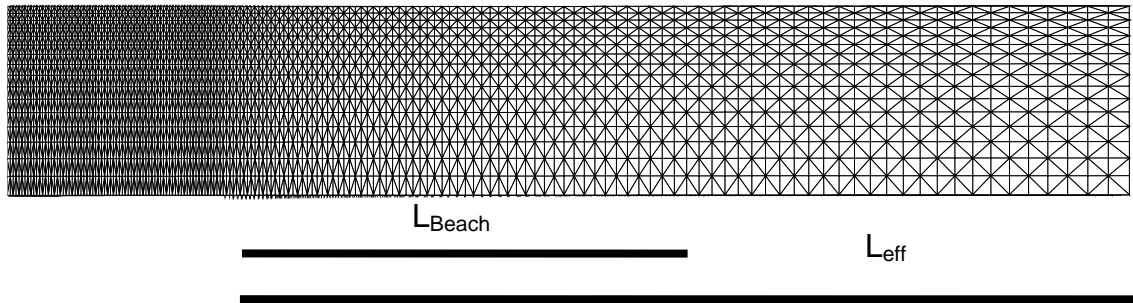


Fig. 6.9 Representation of Mesh Stretching in x - z Direction

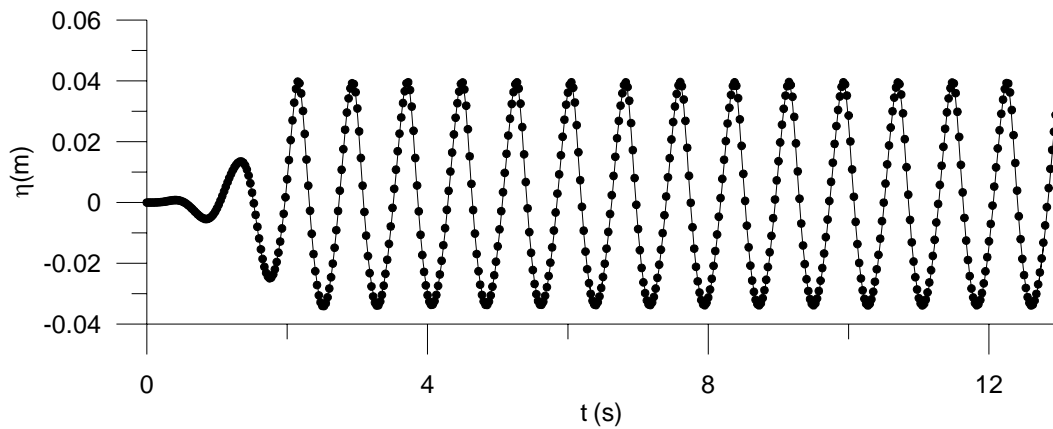


Fig. 6.10 Time History at 0.5m from the Wave Paddle [••• 2-D; — 3-D]

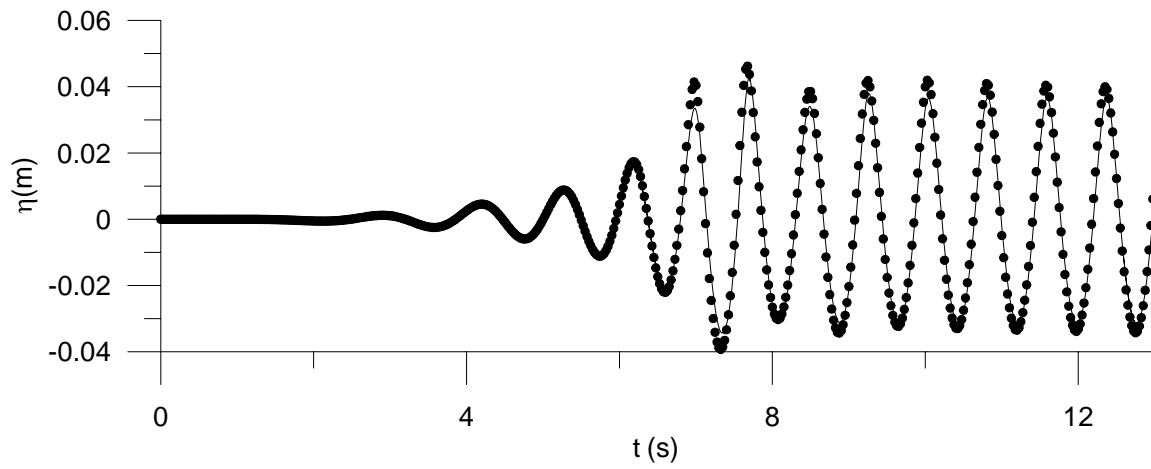


Fig. 6.11 Time History at 3.572m from the Wave Paddle [••• 2-D; — 3-D]

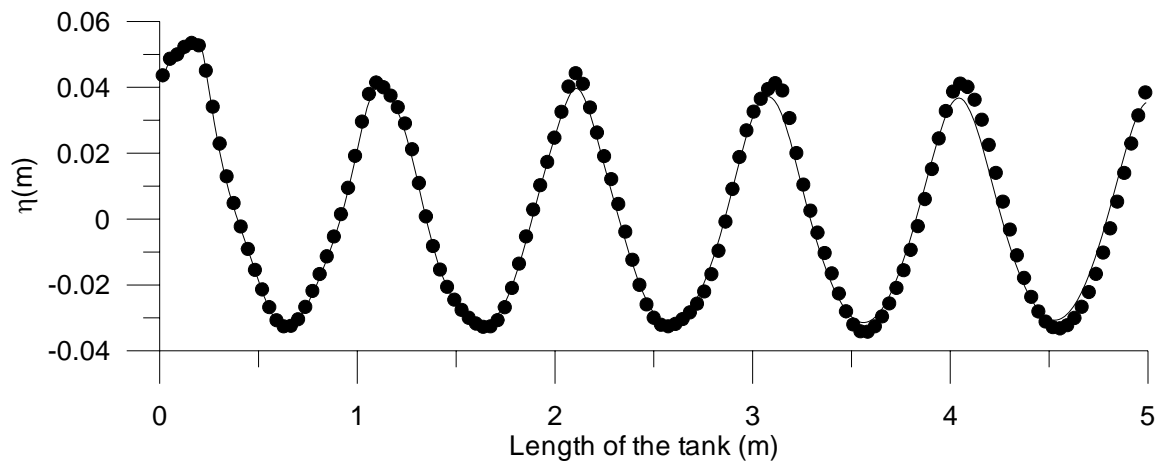


Fig. 6.12 Space Profile at Time 11.995s [••• 2-D; — 3-D]

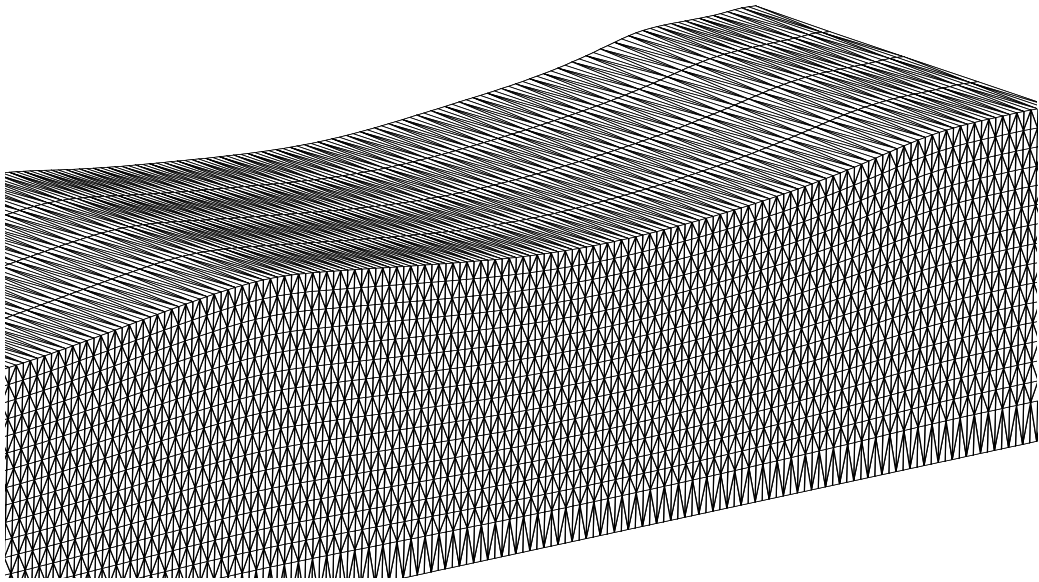


Fig. 6.13 Snapshot of the Mesh Configuration during the Wave Simulation

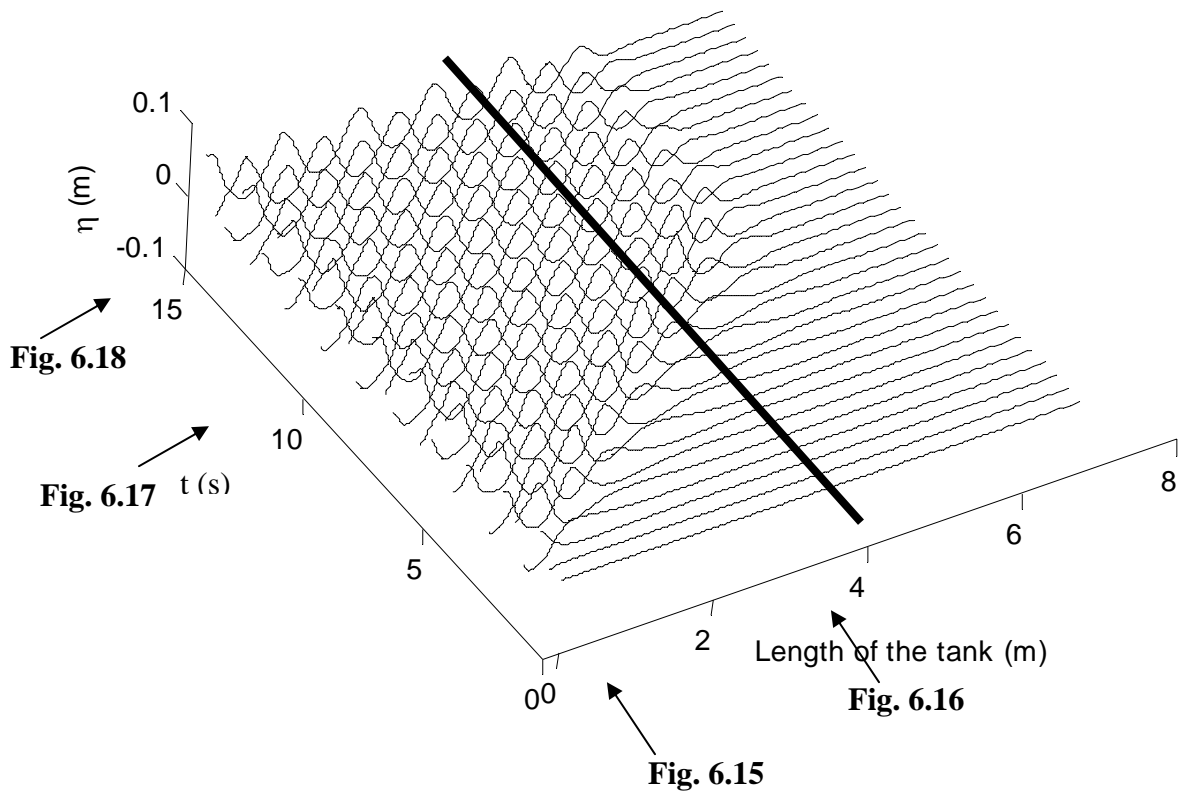


Fig. 6.14 Space – Time Profile showing the Absorption Efficiency for a Wave Steepness of 0.082 [Right Side of the Black Line is the Absorption Zone]

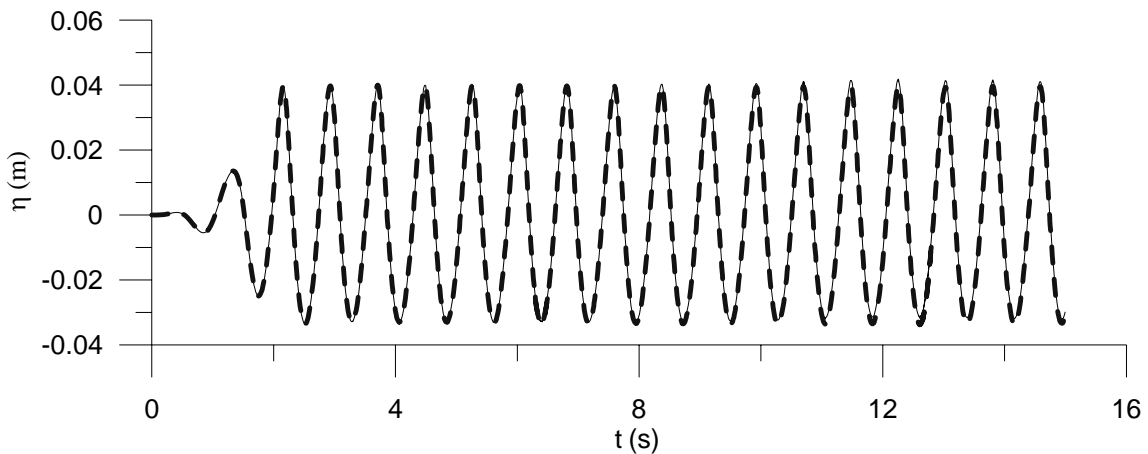


Fig. 6.15 Time History at 0.5m from the Wave Paddle [----- Long Tank, 15.1m; ———Short Tank, 6.69m]

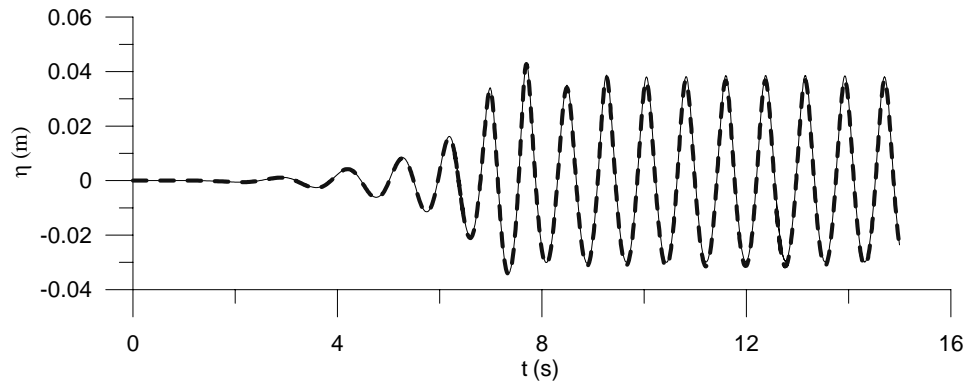


Fig. 6.16 Time History at 3.572m from the Wave Paddle [-----Long Tank, 15.1m; —— Short Tank, 6.69m]

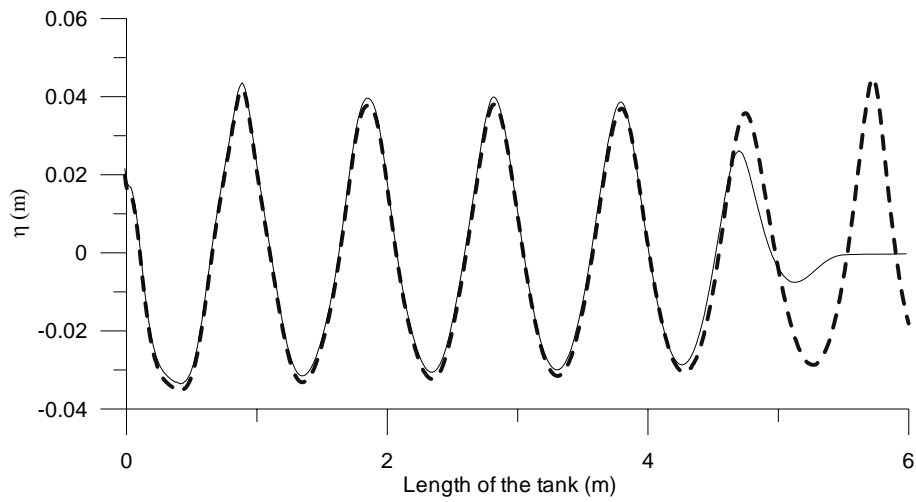


Fig. 6.17 Wave Profile at Time 10.995s [----- Long Tank, 15.1m; —— Short Tank, 6.69m]

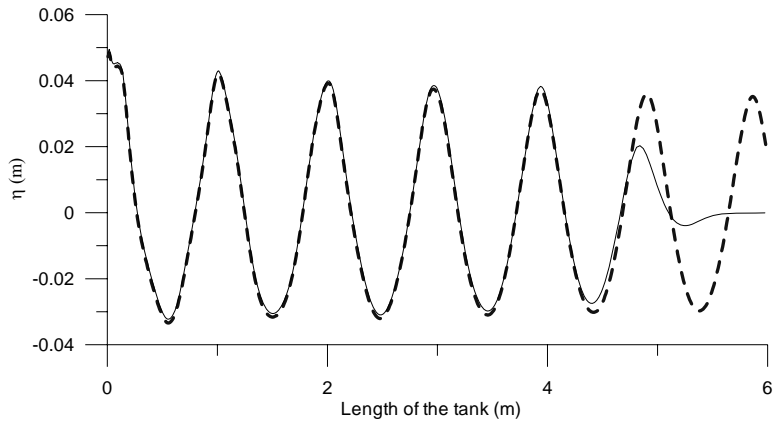


Fig. 6.18 Wave Profile at Time 14.995s [----- Long Tank, 15.1m; — Short Tank, 6.69m]

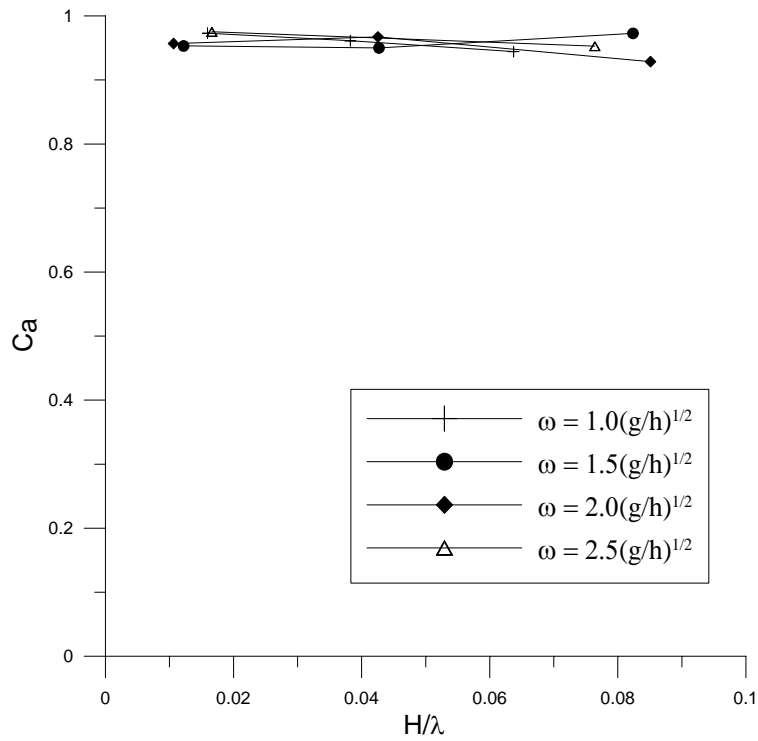


Fig. 6.19 Absorption Coefficient against Wave Steepness for various Wave Frequency [Beach Length = λ ; Mesh Stretching Coefficient = 1.03]

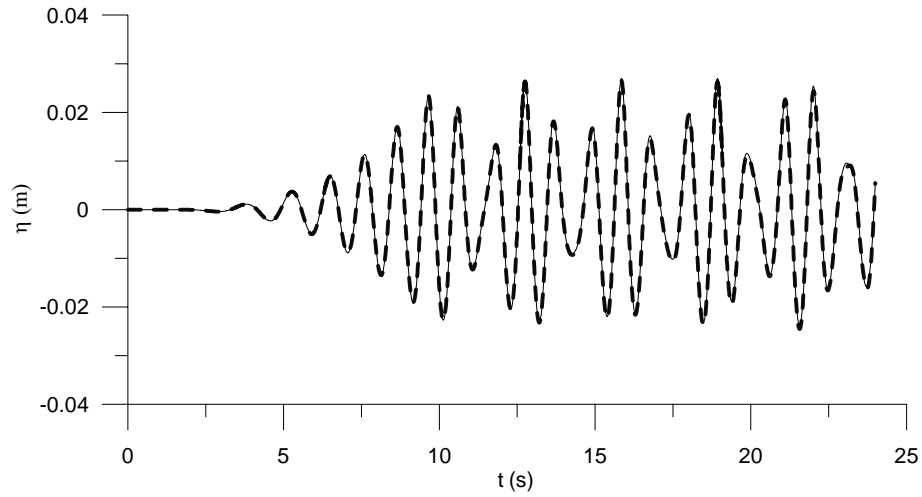


Fig. 6.20 Time History before the Beach [----- Long Tank; —— Short Tank]

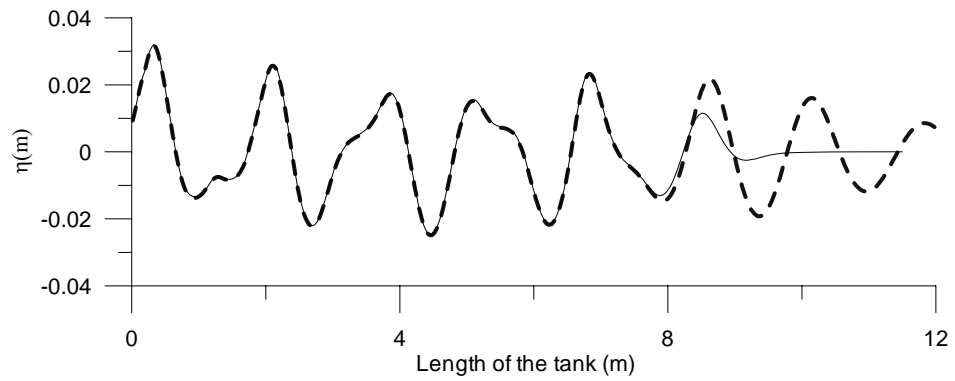


Fig. 6.21 Space Profile at 15s [----- Long Tank; —— Short Tank]

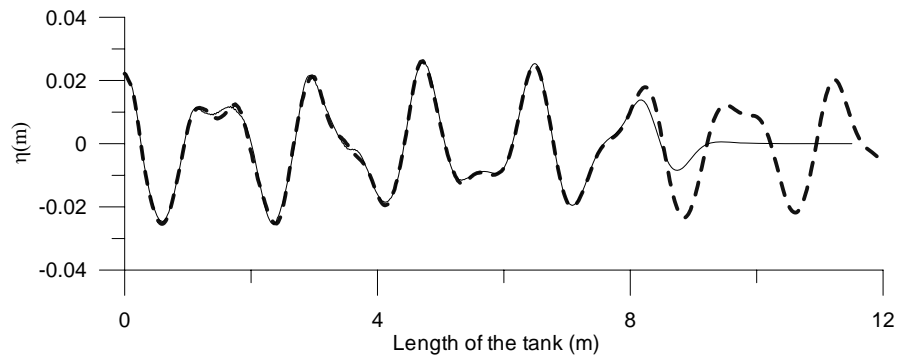


Fig. 6.22 Space Profile at 25s [----- Long Tank; —— Short Tank]

CHAPTER 7

SUMMARY AND CONCLUSIONS

7.1 SUMMARY

The simulation of nonlinear free surface waves have been carried out using the Finite Element (FE) formulation of potential flow approximation based on Mixed Eulerian and Lagrangian (MEL) approach. Different velocity calculation methods namely, Global Projection Method, Least Squares Method, Mapped Finite Differences and the proposed Cubic Spline method have been investigated in detail to understand their region of applications. The computational time for all the methods are also reported. Extension of the FE based MEL approach using the unstructured mesh is similar to Arbitrary Lagrangian and Eulerian method and hence, it has been called as Semi-Arbitrary Lagrangian and Eulerian (Semi-ALE/SALE) method. The developed numerical code with various velocity calculation methods was validated with the experimental measurements available from the literature as well as with the measurements made under the present investigation. The quantitative analysis of the phase difference between the measurements and numerical simulation has been reported using wavelet transformation. The time-frequency analysis gives better understanding of the phase shift both qualitatively and quantitatively compared to Fourier analysis. The cross wavelet transformation and wavelet coherence analysis are used to reveal the common high power and phase lock behaviours, respectively. The solitary wave measurements and the comparison with the numerical simulation are reported along with the crest particle velocity. The three wave split-up of solitary waves was successfully simulated by using the present numerical model based on FEM for the test case of Van Daalen *et al.* (1997). Further, the complex wave

interaction problems such as wave propagation over a continental shelf, submerged bar, and submerged cylinder, and wave interaction with a vertical wall and surface piercing objects are successfully simulated.

The numerical simulation of sloshing waves due to the individual excitation in horizontal and vertical directions of a container shows a good agreement with the numerical simulation of Frandsen (2004). An extensive investigation on the sloshing waves induced by different sea states has been carried out. Finally, the model is extended to three-dimensional tank by adopting an efficient absorber at the far end of the tank for long time simulation of nonlinear waves. The efficiency of the mesh orientation that influences the solution of the 3-D numerical wave tank has been discussed.

7.2 CONCLUSIONS

The following are the salient conclusions drawn from the present study.

7.2.1. Simulation of Nonlinear Waves using Wave Paddle

- The global projection method can be used efficiently when the quality of mesh has been taken care at every time step. While adopting regeneration of mesh using a simple formula, the simulation breaks down most of the time. This certainly needs smoothing and regridding after every 20 time steps.
- The proposed cubic spline method holds good for both structured and unstructured meshes in two-dimensional tanks for the simulation of medium steep waves (upto $H/\lambda = 0.045$) even for the sudden startup of the wave paddle. For a high steepness

wave, a phase lag is noticed. This method certainly needs improvement even though it requires less number of nodes with less smoothing/regridding strategies.

- Mapped finite difference and least squares method are promising velocity calculation approaches for the simulation of nonlinear free surface waves using FE. The former method holds good for the structured mesh, since transformation to the computational grid using unstructured grid is difficult to implement at every time step. The least squares method shows good results with a flexibility of adapting to all kinds of mesh structures.
- The main reason for the requirement of regridding/smoothing has been attributed to the fact of Lagrangian motion characteristics of the nodes near the moving wave paddle boundary for medium to high steep waves. The regridding/smoothing interval is highly depends on the wave frequency, method of velocity calculation and the problem in hand.
- A quantitative comparison with laboratory measurements reveals that there is a positive phase shift during the steep wave simulation using cubic spline. Even though, the least squares approach shows a positive phase lag, the phase difference is found to be less compared to the former approach of simulation. However, the phase difference occurs not at the primary period under investigation, but at higher modes. The phase difference is inconsistent along the length of the tank, thus requiring more accurate measurements in the future studies. As the errors are minimal, both these approaches are quite acceptable for engineering applications and the numerical simulation can be successfully used as a replacement for physical modeling when situation demands.

- In unstructured mesh implementation, the efficacy of the spring analogies namely, vertex and segment methods are tested. It has been shown that both the methods work well provided the stiffness of the segments are appropriately handled. It has been suggested that for vertex method, spring stiffness has to be increased only at the boundary nodes, whereas, for segment spring method, the stiffness need to be increased to the adjacent layers. Stiffening exponentially across the depth works well in most of the present numerical experiments by following the physical behaviour of the water waves.

7.2.2. Nonlinear Wave Propagation

- The dispersive wave characteristics during the propagation over a submerged bar has been simulated using the present numerical model. The simulation result reveals that the model based on cubic spline does not compare well with the experiments for the steep waves that exists in shallow water region compared to method of least squares. A slight phase shift in the computation and a deeper trough are found to exist from the results obtained by cubic spline method.

7.2.3. Solitary Wave Propagation and its Interaction

- The propagation of the solitary waves over a step has been modelled which shows a good comparison with the experimental measurements (Seabra-Santos *et al.* 1987) for three different relative obstacle height ($b/h = 0.33, 0.4$ and 0.5) within the capability of the model. It has been noticed that both in measurements and numerical simulation, the transmission coefficient is lower and the reflection coefficient is higher than the first order shallow water wave theory. It is noted that the reflection coefficient tends to decrease as the wave steepness increases. The

simulation carried out for different smooth slopes (based on sine curve) reveals that as the slope becomes flatter, the reflection is less compared to that for steeper slopes.

- The interaction of the solitary wave with a vertical wall has also been modelled and the force time history shows the existence of nonlinearity in terms of double peaks. The reflected wave profile is in agreement with the observations made by Fenton and Rienecker (1982). It has been quoted that the reason for increase in celerity of the reflected wave profile for high steep waves is mainly due to the formation of trough, whereas, the reason for low steep waves is unclear. This phenomenon has been re-analysed in the present study with the help of continuity equation, showing that the wave elevation is inversely proportional to celerity and hence, in order to conserve the mass, the celerity increases with the decrease in wave elevation.

7.2.4. Simulation of Sloshing Waves

- Due to regular excitation in the horizontal direction, the spectral peak dominates at the excitation mode, when the excitation frequency is less than the first sloshing mode. For the excitation frequency greater than the first sloshing mode, the dominant spectral peak occurs at the natural sloshing frequency of the container. The critical sloshing motion occurs at the well known resonance condition, while the excitation frequency is equal to the first mode.
- Due to regular excitation in the vertical direction, the spectral peak occurs at the first mode for small initial perturbation and; at first, second and two times of the first mode for higher initial perturbation for constant excitation amplitude. The

dominating spectral peaks in both the cases are at the first mode. The critical sloshing occurs at the parametric resonance (excitation frequency equal to twice the first mode).

- For the random excitation in the horizontal direction, the spectral peaks occur only at the natural sloshing frequencies of the container. The dominating peaks appear close to i^{th} mode, when the excitation peak frequency is at i^{th} mode. The maximum sloshing is induced while the excitation peak frequency is equal to first mode, that is, resonance condition.
- In the case of random excitation in the vertical direction, the dominating peak appears only at the first mode. The magnitude of peak is almost the same irrespective of the excitation peak frequency and initial perturbation, contrary to the regular excitation, wherein, the magnitude is large only if the excitation frequency is equal to twice the first mode (parametric resonance) irrespective of initial perturbation.

7.2.5. 3-D Numerical Wave Tank

- In 3-D structured mesh implementation, the linear tetrahedron elements are used. The mesh structure plays a major role in choosing tetrahedron elements and the orientation study reveals that crisscross link yields better results when compared to zig-zag and one side orientation of the mesh structure.
- The combination of mixed boundary condition at the far end and damping zone along with mesh stretching technique is found to be efficient damping strategy with 93% of absorption coefficient (99.5% in terms of energy) for the worst case.

- Mesh stretching technique reduces the number of nodes in the domain and increases the length of the domain, thus minimizing the computational time and increasing the absorption efficiency.

7.3 SUGGESTIONS FOR FUTURE STUDIES

Much of the work on 2-D has been done in the past and the present study based on FEM shows that the velocity calculation plays a major role unlike BEM studies. SALE method solves the moving boundary problems like floating body but the acceleration has to be calculated accurately like the velocities. The vertical velocity estimation using backward finite difference has to be modified to have a more generalized code to accommodate unstructured mesh computation easily and to simulate over turning wave.

Frandsen (2004) showed that the combined effect of vertical and horizontal regular excitations of the container lead to infinite number of additional resonant frequency components in sloshing waves. The magnitude of peak is almost same irrespective of excitation peak frequency and initial perturbation for vertical random excitation in the present study. This requires further investigation to examine the effect of the additional frequency resonance for combined random excitation.

The development of 3-D NWT is still an active area of research (Ma, 2008) due to the investigation of any offshore/ coastal structures under the action of multi-directional waves. The present developed code for 3-D NWT forms the base work for the above extensions. The in-core gauss elimination solver has to be replaced by an out-of-core solver or iterative solvers (like Preconditioned Conjugate gradient, Bi-Conjugate

Gradient Stabilized Method, etc.) to deal with larger domains as in the case of multi-directional waves.

APPENDIX A

MOVING LEAST SQUARES

Moving Least Squares (MLS), originated by mathematicians for data fitting and surface construction, is often termed as local regression and loss. It can be categorized as a method of finite series representation of functions. The MLS approximation has two major features that make it more popular:

1. The approximated field function is continuous and smooth in the entire problem domain.
2. It is capable of producing an approximation with the desired order of consistency.

Let $\phi(x)$ be the function of the field variable defined in the domain, Ω . The approximation of $\phi(\mathbf{x})$ at point \mathbf{x} is denoted by $\phi^h(\mathbf{x})$. MLS approximation first writes the field function in the form:

$$\phi^h(\mathbf{x}) = \sum_j^m p_j(\mathbf{x}) a_j(\mathbf{x}) \equiv \mathbf{P}^T(\mathbf{x}) \mathbf{a}(\mathbf{x}) \quad (\text{A.1})$$

where, m is the number of terms of monomials (polynomial basis), and $\mathbf{a}(\mathbf{x})$ is a vector of coefficients given by

$$\mathbf{a}^T(\mathbf{x}) = \{a_0(\mathbf{x}) a_1(\mathbf{x}) \dots \dots \dots a_m(\mathbf{x})\} \quad (\text{A.2})$$

Which are functions of x .

In Eqn. (A.1), $\mathbf{P}(\mathbf{x})$ is a vector basis functions that consists of the monomials of the lowest orders to ensure minimum completeness. In 2-D, it is taken as, (based on pascal triangle as in choosing FEM basis function)

$$\mathbf{P}^T(\mathbf{x}) = \{1, x, y, xy, x^2, y^2, \dots, x^m, y^m\} \quad (\text{A.3})$$

The vector coefficients $\mathbf{a}(\mathbf{x})$ in Eqn. A.1 is determined using the function values at a set of nodes that are included in the support domain of \mathbf{x} . A support domain of a point \mathbf{x} determines the number of nodes that are used locally to approximate the function value at \mathbf{x} .

Given a set of n nodal values for the field function $\phi_1, \phi_2, \phi_3, \dots, \phi_n$ at n nodes x_1, x_2, \dots, x_n that are in the support domain, then the Eqn. (A.1) can be used to calculate the approximated values of the field function at these nodes:

$$\phi^h(\mathbf{x}, \mathbf{x}_I) = \mathbf{P}^T(\mathbf{x}_I) \mathbf{a}(\mathbf{x}), \quad I = 1, 2, \dots, n \quad (\text{A.4})$$

In which $\mathbf{a}(\mathbf{x})$ here is an arbitrary function of \mathbf{x} . A functional of weighted residual is constructed using the approximated values of the field function and the nodal parameters, $\phi_I = \phi(\mathbf{x}_I)$,

$$\begin{aligned} J &= \sum_I^n \widehat{W}(x - x_I) [\phi^h(x, x_I) - \phi(x)]^2 \\ &= \sum_I^n \widehat{W}(x - x_I) [\mathbf{P}^T(x_I) \mathbf{a}(x) - \phi_I]^2 \end{aligned} \quad (\text{A.5})$$

Where $\widehat{W}(x - x_I)$ is a weight function, and ϕ_I is the nodal parameter of the field variable at node I .

The weight function in this context is different from the finite element weight function. The reader can refer Liu (2002) for further details.

At an arbitrary point \mathbf{x} , $\mathbf{a}(\mathbf{x})$ has been chosen to minimize the weighted residuals. The minimization condition requires,

$$\frac{\partial J}{\partial \mathbf{a}} = 0 \quad (\text{A.6})$$

which results in the set of linear equations, and can be written in the matrix form as,

$$\mathbf{A}(\mathbf{x}) \mathbf{a}(\mathbf{x}) = \mathbf{B}(\mathbf{x}) \boldsymbol{\phi}_s \quad (\text{A.7})$$

Where \mathbf{A} is called the weighted moment matrix,

$$\mathbf{A}(\mathbf{x}) = \sum_I^n \widehat{\mathbf{W}}_I(\mathbf{x}) \mathbf{P}(\mathbf{x}_I) \mathbf{P}^T(\mathbf{x}_I) \quad \text{where } \widehat{\mathbf{W}}_I(\mathbf{r}) = \widehat{\mathbf{W}}(\mathbf{x} - \mathbf{x}_I) \quad (\text{A.8})$$

Matrix \mathbf{B} is,

$$\mathbf{B}(\mathbf{x}) = [\mathbf{B}_1, \mathbf{B}_2, \dots, \mathbf{B}_n] \quad (\text{A.9})$$

$$\mathbf{B}_I = \widehat{\mathbf{W}}_I(\mathbf{r}) \mathbf{P}(\mathbf{x}_I) \quad (\text{A.10})$$

And $\boldsymbol{\phi}_s$ is the nodal parameters of the field variables for all the nodes in the support domain

$$\boldsymbol{\phi}_s = \{\phi_1, \phi_2, \phi_3, \dots, \phi_n\}^T \quad (\text{A.11})$$

Solving the Eq. A.7 for $\mathbf{a}(\mathbf{x})$, leads to,

$$\mathbf{a}(\mathbf{x}) = \mathbf{A}^{-1}(\mathbf{x}) \mathbf{B}(\mathbf{x}) \boldsymbol{\phi}_s \quad (\text{A.12})$$

Substituting the above equation back into Eq. A.5 leads to

$$\phi^h(\mathbf{x}) = \sum_I^n \sum_j^m p_j(\mathbf{x}) \left(\mathbf{A}^{-1}(\mathbf{x}) \mathbf{B}(\mathbf{x}) \right)_{ji} \phi_i \quad (\text{A.13})$$

$$\text{i.e., } \phi^h(\mathbf{x}) = \sum_I^n \mathfrak{R}_I(\mathbf{x}) \phi_i \quad (\text{A.14})$$

Where the MLS shape function $\mathfrak{R}_I(\mathbf{x})$ is defined by

$$\mathfrak{R}_I(\mathbf{x}) = \sum_j^m p_j(\mathbf{x}) \left(\mathbf{A}^{-1}(\mathbf{x}) \mathbf{B}(\mathbf{x}) \right)_{ji} = \mathbf{P}^T \mathbf{A}^{-1} \mathbf{B}_I \quad (\text{A.15})$$

Note that m is the number of terms of polynomial basis $p(\mathbf{x})$, which is usually much smaller than n , which is the number of nodes in the support domain for constructing the shape function. The requirement of $n \gg m$ prevents the singularity of the weighted moment matrix, so that A^{-1} exist.

In the present application, the weight function $\widehat{W}_1(r)$ is taken as a quartic spline function as,

$$\widehat{W}(r) = \begin{cases} \frac{2}{3} - 4r^2 + 4r^3 & \text{for } r \leq \frac{1}{2} \\ \frac{4}{3} - 4r + 4r^2 - \frac{4}{3}r^3 & \text{for } \frac{1}{2} < r \leq 1 \\ 0 & \text{for } r > 1 \end{cases} \quad (\text{A.16})$$

APPENDIX B

ANALYTICAL SOLUTION FOR FREE SLOSHING

The derivation for the second order analytical solution for a rectangular container having an initial free surface has been reported in this appendix. Let us consider the 2-D tank of length, L and water depth h , the origin of the tank is at the top left corner of the free surface. The governing equation and the corresponding boundary condition for a first order potential theory is given as,

$$\nabla^2 \phi = 0 \quad (B.1)$$

$$\frac{\partial^2 \phi}{\partial t^2} + g \frac{\partial \phi}{\partial z} = 0 \quad z=0 \quad (B.2)$$

$$\frac{\partial \phi}{\partial z} = 0 \quad z = -h \quad (B.3)$$

$$\frac{\partial \phi}{\partial x} = 0 \quad x=0 \text{ or } x=L \quad (B.4)$$

The initial condition is given by,

$$\begin{aligned} \phi(x, z=0, t=0) &= \varphi(x) \\ \eta(x, t=0) &= - \left. \frac{\partial \phi}{g \partial t} \right|_{z=0, t=0} = \zeta(x) \end{aligned} \quad (B.5)$$

One can easily write the solution for the above set of equations in the series form as,

$$\phi = \sum_{n=0}^{\infty} F_n(t) \frac{\cosh k_n(z+h)}{\cosh k_n h} \cos k_n x \quad (B.6)$$

where, $k_n = n\pi/L$. From Eqn. (B.2), one could define,

$$F_n(t) = A_n \cos \sigma_n t + B_n \sin \sigma_n t \quad (B.7)$$

$$\text{Where, } \sigma_n = \sqrt{k_n g \tanh(k_n h)} \quad (B.8)$$

Substituting, Eqns. (B.6) and (B.7) into (B.5),

$$\begin{aligned} A_n &= \frac{2}{L} \int_0^L \varphi(x) \cos k_n x dx \\ B_n &= -\frac{2g}{L\sigma_n} \int_0^L \zeta(x) \cos k_n x dx \end{aligned} \quad (\text{B.9})$$

Assuming the initial condition as,

$$\varphi(x) = 0 \text{ and } \zeta(x) = a \cos(2\pi x/L) \quad (\text{B.10})$$

Eqn. (B.9) becomes,

$$A_n = 0, \quad B_2 = -ag/\sigma_2 \text{ and } B_n = 0 \quad (\text{B.11})$$

Finally, this leads to

$$\phi_1 = -\frac{ag}{\sigma_2} \sin \sigma_2 t \frac{\cosh k_2(z+h)}{\cosh k_2 h} \cos k_2 x \quad (\text{B.12})$$

$$\eta_1(x,t) = a \cos \sigma_2 t \cos k_2 x \quad (\text{B.13})$$

Considering the Stokes perturbation expansion of velocity potential, one could derive the second order analytical expression also. The free surface boundary condition will be written as,

$$\frac{\partial^2 \phi_2}{\partial t^2} + g \frac{\partial \phi_2}{\partial z} = -\eta_1 \frac{\partial}{\partial z} \left(\frac{\partial^2 \phi_1}{\partial t^2} + g \frac{\partial \phi_1}{\partial z} \right) - \frac{\partial}{\partial t} (\nabla \phi_1)^2 \quad z=0 \quad (\text{B.14})$$

$$\eta_2 = -\frac{1}{g} \left[\frac{\partial \phi_2}{\partial t} + \eta_1 \frac{\partial^2 \phi_1}{\partial y \partial t} + \frac{1}{2} (\nabla \phi_1)^2 \right] \quad (\text{B.15})$$

The initial condition is,

$$\begin{aligned} \phi_2(x, z=0, t=0) &= 0 \\ \eta_2(x, t=0) &= 0 \end{aligned} \quad (\text{B.16})$$

Using the solution of ϕ_1 and η_1 , one could obtain the following Eqns.,

$$\frac{\partial^2 \phi_2}{\partial t^2} + g \frac{\partial \phi_2}{\partial z} = -\frac{1}{4} \frac{a^2}{\sigma_2} \sin 2\sigma_2 t \left[3\sigma_2^4 + k_2^2 g^2 + 3(\sigma_2^4 - k_2^2 g^2) \cos 2k_2 x \right] \quad z=0 \quad (\text{B.17})$$

$$\frac{\partial \phi_1}{\partial t} = -ag \cos \sigma_2 t \frac{\cosh k_2 (z+h)}{\cosh k_2 h} \cos k_2 x \quad (\text{B.18})$$

$$\frac{\partial^2 \phi_1}{\partial z \partial t} = -agk_2 \frac{\sinh k_2 (z+h)}{\cosh k_2 h} \cos k_2 x \cos \sigma_2 t \quad (\text{B.19})$$

$$\eta_1 \frac{\partial^2 \phi_1}{\partial z \partial t} = -a^2 \sigma_2^2 \cos^2 k_2 x \cos^2 \sigma_2 t \quad (\text{B.20})$$

$$\frac{1}{2} \left[\frac{\partial^2 \phi}{\partial x^2} + \frac{\partial^2 \phi}{\partial z^2} \right] = \frac{1}{2} a^2 \sin^2 \sigma_2 t \left[\frac{g}{\sigma_2^2} k_2^2 \sin^2 k_2 x + \sigma_2^2 \cos^2 k_2 x \right] \quad (\text{B.21})$$

Second order velocity potential after simplification using the initial condition is given

by,

$$\begin{aligned} \phi_2 = & \frac{1}{16} \frac{a^2}{\sigma_2^3} (3\sigma_2^4 + k_2^2 g^2) \sin 2\sigma_2 t \\ & + \frac{1}{16} \frac{a^2}{\sigma_2^3} (\sigma_2^4 - k_2^2 g^2) \frac{\cosh 2k_2 (z+h)}{\cosh 2k_2 h} \cos 2k_2 x \sin 2\sigma_2 t - \frac{1}{8} \frac{a^2}{\sigma_2^2} (k_2^2 g^2 - \sigma_2^4) t \\ & + \frac{1}{8\sigma_4} \frac{a^2}{\sigma_2^2} (k_2^2 g^2 + 3\sigma_2^4) \sin \sigma_4 t \frac{\cosh k_4 (z+h)}{\cosh k_4 h} \cos k_4 x \end{aligned} \quad (\text{B.22})$$

The second order velocity potential derivative w.r.t. t is given by,

$$\frac{\partial \phi_2}{\partial t} = \frac{1}{8} \frac{a^2}{\sigma_2^2} \left[(3\sigma_2^4 + k_2^2 g^2) \cos 2\sigma_2 t + (\sigma_2^4 - k_2^2 g^2) \cos 2k_2 x \cos 2\sigma_2 t - (k_2^2 g^2 - \sigma_2^4) \right] \\ + (k_2^2 g^2 + 3\sigma_2^4) \cos \sigma_4 t \cos k_4 x \quad (\text{B.23})$$

Second order wave elevation can be obtained from Eqn. (B.15). Which is simplified

as,

$$\eta_2 = -\frac{1}{g} \text{Eqn}[B.23 + B.20 + B.21]$$

Substituting Eqn. (B.23), Eqn. (B.20) and Eqn. (B.21) in the above equation leads to

the following expression,

$$\begin{aligned}
\eta_2 = -\frac{1}{g} & \left[-a^2 \sigma_2^2 \cos^2 k_2 x \cos^2 \sigma_2 t + \frac{a^2}{2} \sin^2 \sigma_2 t \left(\frac{g^2}{\sigma_2^2} k_2^2 \sin^2 k_2 x + \sigma_2^2 \cos^2 k_2 x \right) \right. \\
& + \frac{a^2}{8\sigma_2^2} (3\sigma_2^4 + k_2^2 g^2) \cos 2\sigma_2 t + \frac{a^2}{8\sigma_2^2} (\sigma_2^4 - k_2^2 g^2) \cos 2\sigma_2 t \cos 2k_2 x \\
& \left. - \frac{a^2}{8\sigma_2^2} (-\sigma_2^4 + k_2^2 g^2) + \frac{a^2}{8\sigma_2^2} (3\sigma_2^4 + k_2^2 g^2) \cos \sigma_4 t \cos k_4 x \right] \quad (\text{B.24})
\end{aligned}$$

If one need to find the time history at the center of the container, the above equations simplifies to the following by plugging in $x = -L/2$. [as reported in Wu and Eatock Taylor, 1994]

$$\begin{aligned}
\eta_2 = -\frac{1}{g} & \left[\frac{a^2}{8\sigma_2^2} (2\sigma_2^4 + 6\sigma_2^4 \cos 2\sigma_2 t) + \frac{a^2}{8\sigma_2^2} (4\sigma_2^4) \cos 2\sigma_2 t \right. \\
& \left. - \frac{a^2}{8\sigma_2^2} (-\sigma_2^4 + k_2^2 g^2) + \frac{a^2}{8\sigma_2^2} (3\sigma_2^4 + k_2^2 g^2) \cos \sigma_4 t \right] \quad (\text{B.25})
\end{aligned}$$

Eqn. (B.22) and Eqn. (B.24) has been used in Chapter 4, Section 4.2.2 to find out the second order energy $[E_2(t)]$.

APPENDIX C

SOLITARY AND CNOIDAL WAVE SIMULATION

C.1 SOLITARY WAVE

The simulation of solitary waves by prescribing the ‘piston’ type wave paddle motion is determined from the first order Boussinesq wave theory used by Goring (1979).

The velocity of the wave paddle is given by,

$$\dot{x}_p = \frac{cH}{h} \frac{1}{\cosh^2 \chi(t) + \frac{H}{h}} \quad (C.1)$$

and the paddle displacement is

$$x_p(t) = \frac{H}{k} \left[\tanh \chi(t) + \tanh \frac{k}{h} \lambda \right] \quad (C.2)$$

where,

$$\chi(t) = \frac{k}{h} (ct - x_p(t) - \lambda) \quad (C.3)$$

and

$$k = \sqrt{3H/4h} \quad , \quad c = \sqrt{g(h+H)}$$

The implicit Eqn. (C.2) is solved using the Newton –Rapsion method. For the truncation of the initial motion [λ in Eqn.(C.2)], Grilli and Svendsen (1990) suggested a small truncation parameter namely, $\varepsilon_z = 0.002$, which is a function of

$$\lambda \simeq \frac{1}{k} \left[\log \frac{4 - \varepsilon_z}{2\varepsilon_z^{0.5}} \right], \text{ thus giving an approximate value of } 3.80/k. \text{ This analytical}$$

formulation is given in both the experimental work carried out at University of Wuppertal, Germany and in all the present numerical modelling. Whereas, the solitary

wave measurements carried out at IITMadras, India is governed by the built-in functions of the DHI wave synthesizer.

C.2 CNOIDAL WAVE

The simulation of Cnoidal wave in the experiments carried out at University of Hannover, Germany is based on the First order Cnoidal wave theory. The paddle displacements are established by the transfer functions of the wave maker, by giving the input wave elevations. As it is well known, that the first order surface elevation of the Cnoidal wave theory is based on the implicit equations (Goring, 1979). An Adhoc trial and error method scheme is used to solve the equations. The code is written in MATLAB. The source code is given below for future references.

```

% Cnoidal.m
%
% % E-Mailed in coastal_list on 22nd Feb.2007
% Modified to obtained the time series at the wave paddle on 27th August'07
% -----
% This Program will generate the modulus of elliptic integrals for a Cnoidal wave
% with wave-height, wave-period and water depth as input using
% AGM for 3 significant figures

% Reference:
% Goring, D.G., 1978. Tsunamis—the propagation of long waves onto a shelf,
% Ph.D. thesis, Univ. of California, Berkley.
% Note: Eq.(A.4) in the above said reference is wrong.
% for computation of K and E use  $k = \sqrt{m} = \sqrt{1-m}$ 
% *****
% default the program gives the result at  $x = 0$ , if you want u
% can modify for space also.
clear
clc
H= input('Enter the value of wave-height: ');
d= input('Enter the value of water depth: ');
T= input('Enter the value of time-period: ');
% NW = input('Enter the number of data points in a waves: ');
% %dt = input('Enter the value of time step: ');
% AW = input('Enter the number of waves: ');
% ramp = input('Enter the ramp for data points:');
% filename=input('enter the filename:'); % 'rw070960.dat'
dt = 0.01;
%N = 60;
%dt = T/NW;
% N = NW*AW;
endt = input('End of simulation time: ');
g = 9.806;
%first step is computing 'j'
j=0;
while (1)
m= 10^-j;
n= 10^-(j+1);
[K1,E1]=ellipke((1-m)^.5);
[K2,E2]=ellipke((1-n)^.5);
T1= ((4/1.732)*(d^1.5)*K1*(1-m))/((9.8*H*((1-m)*d+H*(2-(1-m)-3*(E1/K1))))^.5);
T2= ((4/1.732)*(d^1.5)*K2*(1-n))/((9.8*H*((1-n)*d+H*(2-(1-n)-3*(E2/K2))))^.5);
if ((T-T1)*(T-T2)<0)
    break
else
    j=j+1;
end
end
%j

```

```

% second step involves computing 'k1'(here p)
p=1;
while (1)
a= p*(10^-(j+1));
b=(p+1)*(10^-(j+1));
[K1,E1]=ellipke((1-a)^.5);
[K2,E2]=ellipke((1-b)^.5);
T1= ((4/1.732)*(d^1.5)*K1*(1-a))/((9.8*H*((1-a)*d+H*(2-(1-a)-3*(E1/K1))))^1.5);
T2= ((4/1.732)*(d^1.5)*K2*(1-b))/((9.8*H*((1-b)*d+H*(2-(1-b)-3*(E2/K2))))^1.5);
if ((T-T1)*(T-T2)<0)
    break
else
    p=p+1;
end
end
%p
%third step involves computing k2(here its q)
q=1;
while (1)

    a= (p+q*.1)*(10^-(j+1));
    b=(p+(q+1)*.1)*(10^-(j+1));
    [K1,E1]=ellipke((1-a)^.5);
    [K2,E2]=ellipke((1-b)^.5);
    T1= ((4/1.732)*(d^1.5)*K1*(1-a))/((9.8*H*((1-a)*d+H*(2-(1-a)-3*(E1/K1))))^1.5);
    T2= ((4/1.732)*(d^1.5)*K2*(1-b))/((9.8*H*((1-b)*d+H*(2-(1-b)-3*(E2/K2))))^1.5);
    if ((T-T1)*(T-T2)<0)
        break
    else
        q=q+1;
    end
end
%q

%fourth step involves computing k3(here its r)
r=1;
while (1)

    a= (p+q*.1+r*.01)*(10^-(j+1));
    b=(p+q*.1+(r+1)*.01)*(10^-(j+1));
    [K1,E1]=ellipke((1-a)^.5);
    [K2,E2]=ellipke((1-b)^.5);
    T1= ((4/1.732)*(d^1.5)*K1*(1-a))/((9.8*H*((1-a)*d+H*(2-(1-a)-3*(E1/K1))))^1.5);
    T2= ((4/1.732)*(d^1.5)*K2*(1-b))/((9.8*H*((1-b)*d+H*(2-(1-b)-3*(E2/K2))))^1.5);
    if ((T-T1)*(T-T2)<0)
        break
    else
        r=r+1;
    end
end

```

```

end
%r
s= (p+q*.1+r*.01)*10^-(j+1); % s = m'
disp('Modulus of the elliptic functions(k) is')
%disp(s)
sr = sqrt(1-s); %sr is nothing but m=k^2=(1-m') for computing use k'
disp(sr)
[K,E]= ellipke(sr);
L = sqrt(g*d*T^2*(1+((H/(d*sr^2))*(2-sr^2-3*E/K))));
disp('Wave length is ');
disp(L);
disp('ursell parameter');
disp(H*L^2/d^3);
%L1 = sqrt(16*d^3/(3*H))*K*sr;
yt = ((H*(K-E))/(K*(sr^2)))+(d-H);
%x = 0:0.01:30;
x = 0;
% for it=1:N;
% t(it)=(it-1)*dt;
% end;
t= 0:dt:endt;
eta(1:length(t)) = 0;
for i= 1:1:length(t)
U= (2*K*((x/L)-(t(i)/T)));
[SN,CN,DN] = ellipj(U,sr);
eta(i)=yt-d+ (H*(CN^2));
end
plot(t,eta)

```

APPENDIX D

WAVELET TRANSFORMATION

D.1 GENERAL

Fourier Transform (FT) is an important tool for the analysis and processing of many time varying signals. FT has certain limitations to characterize non-stationary signals. Though a time varying, overlapping window based FT known as Short-Time FT (STFT) is capable of processing the non-stationary signals, the selection of size and shape (rectangular, Gaussian and elliptic) of the window function is highly difficult, as it significantly affect the spectral resolutions. For example, a narrow window would give better time resolution, whereas, a wider one yield could result in a better frequency resolution. In addition, the window size and shape could not be changed during analysis, once selected the resolution is also set. Thus, analysis of time series through STFT is completely dictated by the selection of window function. Hence, its application on the analysis of the non-stationary and signals with sharp changes in its spectral characteristics along the time scale is highly questionable. The aforementioned drawbacks could well be overcome by the use of a window function of varying length or width. Such an analysis function would certainly be useful for analysis of signals with slowly varying characteristics with occasional sudden bursts. Wavelets are analysis mathematical functions that solve the above said problems. In this appendix, a brief overview about Wavelet is given. The description about Wavelets are given by Weng and Lau (1995), Torrence and Compo (1997) and the theoretical background of wavelet analysis are described in Daubechies (1990). This is a suitable tool for the analysis of the transient, non-stationary or time-varying phenomena. In the context of ocean Engineering, the wavelet transform has been

successfully used in the dispersion of ocean waves by Meyers *et al.* (1993), wave growth and breaking by Liu (1994) and more recently by Balaji *et al.* (2007) on the prediction of the ocean waves using data buoy. Wavelets are similar to but an extension of Fourier analysis and computational wise the wavelet transformation are similar to the fast fourier transformation and hence its an alternative to classical windowed fourier transformation. The major difference when compared to the windowed fourier transformation is that the window in wavelet is already oscillating and is called mother wavelet, which are not multiplied by sine or cosine functions.

D.2 DEFINITION OF WAVELET

A ‘wavelet’ is a small wave which has its energy concentrated in time. It has an oscillating wave characteristic but also has the ability to allow simultaneous time and frequency analysis which is a suitable tool for the analysis of the transient, non-stationary or time-varying phenomena. In order a function to be called a wavelet, it must satisfy the following conditions.

(1) The wavelet must have zero mean. This condition, known as the admissibility condition, ensures the invertibility of the wavelet transform. Thus, the original signal can be obtained from the wavelet coefficients through the inverse transform.

(2) The integral of the wavelet function, usually denoted by ψ , must be zero.

$$\int_{-\infty}^{\infty} \psi(t) dt = 0 \tag{D.1}$$

This assures that the wavelet function has a wave shape and is known as the admissibility condition.

(3) The wavelet function must have unitary energy, i.e.,

$$\int_{-\infty}^{\infty} |\psi(t)|^2 dt = 1 \quad (\text{D.2})$$

This assures that the wavelet function has compact support or has a fast amplitude decay enabling physical domain localization.

These wavelets split up a time varying data into different frequency components, and then study each component with a resolution matched to its scale. They have advantages over traditional Fourier methods of analyzing physical situations, where, the signal contains discontinuities and sharp spikes. The basic difference between waves and wavelets is that waves are smooth, predictable and everlasting, whereas, wavelets are of limited duration, irregular and may be asymmetric. Waves are used as deterministic basis functions in FT for the expansion of signals, which are time-invariant, or stationary. The important characteristic of wavelets is that they can serve as deterministic or non-deterministic basis for generation and analysis of the most natural signals to provide better time-frequency representation, which is not possible with waves using conventional FT.

D.3 MOTHER WAVELET

The wavelet analysis procedure is to adopt a wavelet prototype function, called an ‘analysing wavelet’ or ‘mother wavelet’. Temporal analysis is performed with a contracted, high frequency version of the prototype wavelet, while, frequency analysis is performed with a dilated, low frequency version of the same wavelet. In simple terms, the kernel functions used in the transformations are obtained by scaling and translating the prototype function. The kernels are obtained as,

$$\Psi_{\gamma, \tau}^*(t) = \frac{1}{\sqrt{\gamma}} \Psi\left(\frac{t-\tau}{\gamma}\right) \quad (D.3)$$

In which, γ is the scaling factor and τ is the translating or shifting factor and $1/\sqrt{\gamma}$ is the normalization factor to ensure that all wavelets have the same energy.

Among the few mother wavelets, such as the orthogonal wavelets, Paul's wavelet or DOG wavelet (derivative of a Gaussian), the Morlet wavelet is widely adopted for oceanographic applications. The Morlet wavelet function is a Gaussian modulated complex-valued plane wave and hence, for the transformation of ocean wave signals, it is widely adopted. The Morlet wavelet function is defined as,

$$\psi(t) = \pi^{-(1/4)} e^{i\omega_0 t} e^{-(t^2/2)} \quad (D.4)$$

Where, ω_0 is the non-dimensional frequency, which is taken as 6.0 in the present study for satisfying the admissibility conditions (Farge, 1992). Typical Morlet real and imaginary parts are shown in Fig. D.1.

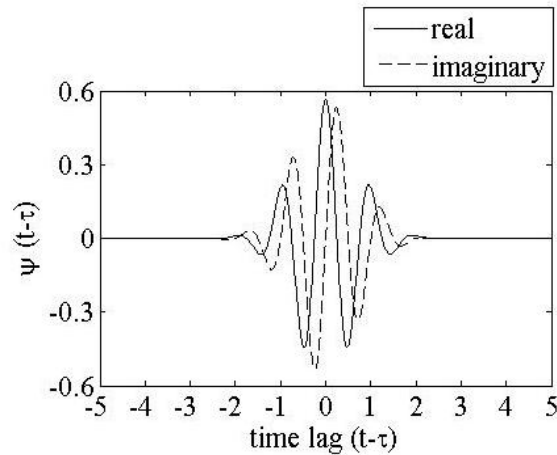


Fig. D.1 The Morlet Wavelet

Using the above basis function, the time histories were multiplied by ψ^* , in which the parameters γ and τ are continuously varying, thus leading to a two-dimensional representation of the one-dimensional signal. For the Morlet wavelet with ω_0 of 6.0, the Fourier period (or inverse of frequency) corresponding to the wavelet scale is 1.03a (Torrence and Compo, 1998).

D.4 CONTINUOUS WAVELET TRANSFORMATIONS

The Continuous Wavelet Transformation [CWT, $W_x(\gamma, \tau)$] of a one-dimensional signal $x(t)$ is given as,

$$W_x(\gamma, \tau) = \frac{1}{\sqrt{|\gamma|}} \int_{-\infty}^{\infty} x(t) \cdot \psi^* \left(\frac{t - \tau}{\gamma} \right) dt \quad (D.5)$$

in which, ψ^* is scaled and translated version of basis function, ψ , given in Eqn. (D.3).

The variation of the size of the analysis function with respect to the time and frequency for the CWT is shown in Fig. D.2.

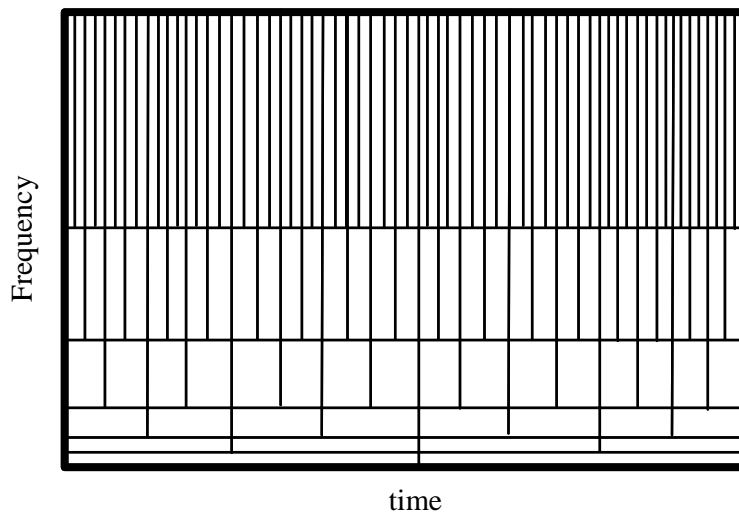


Fig. D.2 Size and Shape of the Analyzing Function

The data $x(t)$ is bounded in time so the wavelet transform is affected by edge effects, this effect has been called as the Cone of Influence (COI) by Torrence and Compo (1998). Statistical significance was also estimated against a red noise model as proposed by them.

D.4 CROSS WAVELET TRANSFORM (XWT)

The analysis of the covariance of the two time series has been carried out using the cross wavelet transformation. The cross wavelet transform of the two time series $X(t)$ and $Y(t)$ with wavelet transform W_x and W_y is defined as,

$$W_{xy}(\gamma, t) = W_x(\gamma, t) W_y^*(\gamma, t) \quad (\text{D.6})$$

Where, the asterisk denotes complex conjugate. The phase angle of W_{xy} describes the phase relationship between X and Y , Whereas, the power is obtained from $\text{abs}(W_{xy})$ in the time-frequency space. The main interest is the phase difference between the components of the two time series, the mean and confidence interval of the phase difference were estimated. The circular mean of a set of angles within the 5% statistical significant region (or 95% confidence) is estimated following Zar (1999). Whereas, the confidence interval is difficult to interpret, hence it is find out using the circular standard deviation reported in Grinsted *et al.* (2004).

D.5 THE WAVELET COHERENCE (WTC)

This is an estimation of the intensity of the covariance of the two given time series in time-frequency space, unlike the XWT power, which is the estimation of common powers. Coherence has been defined as (Torrence and Webster, 1999),

$$R^2(\gamma, t) = \frac{\left| S\left(s^{-1}W_{xy}(\gamma, t)\right) \right|^2}{S\left(s^{-1}|W_x(\gamma, t)|^2\right) \cdot S\left(s^{-1}|W_y(\gamma, t)|^2\right)} \quad (D.7)$$

Where S is a smoothing operator, defined as, $S(W) = S_{scale}(S_{time}(W(\gamma, t)))$. The scales in time and frequency over which S is smoothing define the scales at which the coherence measures the covariance. Torrence and Webster (1998) reported the natural way to design the smoothing operator for the Morlet wavelet. The coherence significant levels was estimated using Monte Carlo methods with red noise to determine the 5% statistical significance level (Grinsted *et al.* 2004). The circular mean as well as the confidence interval are calculated similar to XWT. The reason for the difference between the phase angles reported for the cross wavelet and coherence methods is because of the smoothing operator used in Coherence method.

REFERENCES

1. **Abbott, M.B., H.M. Peterson, and O. Skovgaard** (1978) On the numerical modelling of short waves in shallow water. *Journal of Hydraulic Research*, **16**, 173-203.
2. **Armenio, V. and M. La Rocca** (1996) On the analysis of sloshing of water in rectangular containers: numerical study and experimental validation. *Ocean Engineering*, **23(8)**, 705-739.
3. **Atluri, S.N. and T. Zhu** (1998) A new meshless local Petrov–Galerkin (MLPG) approach in computational mechanics. *Computational Mechanics*, **22**, 117–127.
4. **Bai, K.J. and J.W. Kim** *FEM on nonlinear free surface flow*. pp. 83-134. In S. Chakrabarti (ed.) *Numerical Models in Fluid-Structure Interaction*. WIT Press, Boston, 2005.
5. **Balaji, R., S.A. Sannasiraj, and V. Sundar** (2007) Detection of wave groups from the motion behaviour of a discus buoy. *Journal of Hydro-Environment Research*, **1(3-4)**, 195-205.
6. **Batina, J.T.** (1990) Unsteady Euler airfoil solutions using unstructured dynamic meshes. *AIAA Journal*, **28(8)**, 1381-1388.
7. **Beji, S. and J.A. Battjes** (1993) Experimental investigation of wave propagation over a bar. *Coastal Engineering*, **19**, 151-162.
8. **Beji, S. and J.A. Battjes** (1994) Numerical simulation of nonlinear wave propagation over a bar. *Coastal Engineering*, **23**, 1-16.
9. **Benjamin, T.B. and F. Ursell** (1954) The stability of the plane free surface of a liquid in a vertical periodic motion. *Proceedings of Royal Society London Series Part A*, **225**, 505-515.
10. **Betts, P.L. and T.T. Mohamad** (1982) Water waves: a time-varying unlinearized boundary element approach. Proceedings of *4th International Symposium on Finite Element Methods in Flow Problems*, Tokyo, 923-929.
11. **Bloom, F.J.** (2000) Considerations on the spring analogy. *International Journal for Numerical Methods in Fluids*, **32(6)**, 647-668.
12. **Boo, S.Y.** (2002) Linear and Nonlinear Irregular Waves and Forces in a numerical wave tank. *Ocean Engineering*, **29**, 475-493.
13. **Boussinesq, J.** (1871) Théorie de l'intumescence liquide appelée onde solitaire ou de translation, se propageant dans un canal rectangulaire. *Comptes Rendues*, **72**, 755-759.
14. **Bredmose, H., M. Brocchini, D.H. Peregrine, and L. Thais** (2003) Experimental investigation and numerical modelling of steep forced water waves. *Journal of Fluid Mechanics*, **490**, 217-249.
15. **Byatt-Smith, J.G.** (1971) An integral equation for unsteady surface waves and a comment on the boussinesq equation. *Journal of Fluid Mechanics*, **49**, 625-633.

16. **Cai, X., H.P. Langtangen, B.F. Nielsen, and A. Tyeito** (1998) A finite element method for fully nonlinear water waves. *Journal of Computational Physics*, **143**, 544-568.
17. **Cao, Y., R.F. Beck, and W.W. Schultz** (1993) An Absorbing Beach for Numerical simulations of nonlinear waves in a wave tank. Proceedings of *8th International Workshop Water Waves and Floating Bodies*, Newfoundland, May, 17-20.
18. **Casulli, V.** (1999) A Semi-implicit finite difference method for non-hydrostatic, free surface flows. *International Journal for Numerical Methods in Fluids*, **30**, 425-440.
19. **Chakrabarti, S.K.** *Hydrodynamics of Offshore Structures*, Springer-Verlag, Berlin, Heidelberg, 1987.
20. **Chan, R.K.C. and R.L. Street** (1970) A computer study of finite- amplitude water waves. *Journal of Computational Physics*, **6**, 68-94.
21. **Chang, K.A., T.J. Hsu, and P.L.F. Liu** (2001) Vortex generation and evolution in water waves propagating over a submerged rectangular obstacle: Part I. Solitary waves. *Coastal Engineering*, **44**, 13-26.
22. **Chaplin, J.R.** (1984) Nonlinear forces on a horizontal cylinder beneath waves. *Journal of Fluid Mechanics*, **147**, 449-464.
23. **Chern, M.J., A.G.L. Borthwick , and R. Eatock Taylor** (1999) A pseudospectral s-transformation model of 2-D non-linear waves. *Journal of Fluids and Structures*, **13**, 607-630.
24. **Clauss, G. and R. Habel** (2000) Artificial Reefs for Coastal Protection - Transient Viscous Computation and Experimental Evaluation. Proceedings of *27th International Conference on Coastal Engineering*, Sydney, Australia, 22-30.
25. **Clauss, G.F. and U. Steinhagen** (1999) Numerical simulation of nonlinear transient waves and its validation by laboratory data. Proceedings of *9th International offshore and polar engineering conference*, Brest, France, 368-375.
26. **Clauss, G.F., J. Hennig, and C. Schmittner** (2004) Modelling extreme wave sequences for the hydrodynamic analysis of ships and offshore structures. Proceedings of *9th Symposium on Practical Design of Ship and other Floating Structures*, Lübeck-Travemünde, Germany, September 12-17, 1-9.
27. **Clement, A.H.** (1996) Coupling of two absorbing boundary conditions for 2D time-domain simulations of free surface gravity waves. *Journal of Computational Physics*, **126**, 139-151.
28. **Cointe, R., P. Geyer, B. King, B. Molin, and M. Tramoni** (1990) Nonlinear and linear motions of a rectangular barge in a perfect fluid. Proceedings of *the 18th Symposium on Naval Hydrodynamics*, 85-99.

29. **Contento, G.** (2000) Numerical wave tank computations of nonlinear motions of two-dimensional arbitrarily shaped free floating bodies. *Ocean Engineering*, **27**, 531-556.
30. **Dattatri, J., H. Raman, and N. Jothi Shankar** (1978) Performance characteristics of submerged breakwaters. Proceedings of *16th Coastal Engineering Conference*, Hamburg, Germany, 2153–2171.
31. **Daubechies, I.** (1990) The wavelet transform time-frequency localization and signal analysis. *IEEE Trans. Inform. Theory*, **36**, 961-1004.
32. **Dean, W.R.** (1948) On the reflection of surface waves by a submerged cylinder. *Proceedings of Cambridge Philosophical Society*, **44**, 483-491.
33. **Dold, J.W. and D.H. Peregrine** (1984) Steep unsteady waves: an efficient computational scheme. Proceedings of *19th Coastal Engineering Conference*, Houston, 955-965.
34. **Dommermuth, D.G. and D.K.P Yue** (1987) Numerical simulation of nonlinear axisymmetric flows with a free surface. *Journal of Fluid Mechanics*, **178**, 195-219.
35. **Dommermuth, D.G., D.K.P. Yue, W.M. Lin, R. J. Rapp, E.S. Chan, and W.K. Melville** (1988) Deep-water plunging breakers: A comparison between potential theory and experiments. *Journal of Fluid Mechanics*, **189**, 423-442.
36. **Faltinsen, O.M.** (1974) A nonlinear theory of sloshing in rectangular tanks. *Journal of Ship Research*, **18(4)**, 224-241.
37. **Faltinsen, O.M.** (1978) A numerical nonlinear method of sloshing in tanks with two dimensional flow. *Journal of Ship Research*, **22(3)**, 193–202.
38. **Faltinsen, O.M., O.F Rognebakke, I.A Lukovsky, and A.N Timokha** (2000) Multidimensional modal analysis of nonlinear sloshing in a rectangular tank with finite water depth. *Journal of Fluid Mechanics*, **407**, 201-234.
39. **Faltinsen, O.M., O.F. Rognebakke, and A.N Timokha** (2005) Classification of three-dimensional nonlinear sloshing in a square-base tank with finite depth. *Journal of Fluids and Structures*, **20**, 81-103.
40. **Faltinsen, O.M., O.F. Rognebakke, I.A. Lukovsky, and A.N. Timokha** (2000) Multidimensional modal analysis of nonlinear sloshing in a rectangular tank with finite water depth. *Journal of Fluid Mechanics*, **407**, 201-234.
41. **Faraday, M.** (1831) On a peculiar class of acoustical figures, and on certain forms assumed by groups of particles upon vibrating elastic surfaces. *Philosophical Transaction of Royal Society, London*, **121**, 299-340.
42. **Farge, M.** (1992) Wavelet transforms and their applications to turbulence. *Annual Review of Fluid Mechanics*, **24**, 395-457.

43. **Fenton, J.D. and M.M. Rienecker** (1982) A fourier method for solving nonlinear water-wave problems: application to solitary wave interaction. *Journal of Fluid Mechanics*, **118**, 411-443.
44. **Ferrant, P.** (1996) Simulation of strongly nonlinear wave generation and wave-body interactions using a 3-D MEL method. Proceedings of *21st ONR symposium on Naval Hydrodynamics*, Trondheim, 93-109.
45. **Fontaine, E., M. Landrini, and M.P. Tulin** (2000) On modelling the post breaking phase: splashing. Proceedings of *15th International Workshop on Water Waves and Floating Bodies*, Israel, March, 51-54.
46. **Frandsen, J.B.** (2004) Sloshing motions in the excited tanks. *Journal of Computational Physics*, **196**, 53-87.
47. **Freilich, M.H. and R.T. Guza** (1984) Nonlinear effects on shoaling surface gravity waves. *Philosophical Transaction of Royal Society London, Part A*, **311**, 1-41.
48. **Germain, J.P.** *Coefficients de reflexion et de transmission en eau peu profonde*, Rozprawy Hydrotechniczne Report, 46, Instytut Budownictwa Wodnego, Ghansk, 1984.
49. **Goring, D.G. and F. Raichlen** (1992) Propagation of long waves onto shelf. *Journal of Waterwaves, Port, Coastal and Ocean Engineering*, **118(1)**, 43-61.
50. **Goring, D.G.** *Tsunamis - The propagation of long waves onto a shelf*, Ph.D. Thesis, California Institute of Technology, Pasadena, California, 1979.
51. **Greaves, D.M., A.G.L Borthwick, G.X Wu, and R. Eatock Taylor** (1997) A moving boundary finite element method for fully non-linear wave simulations. *Journal of Ship Research*, **41(3)**, 181-194.
52. **Grilli, S.T. and I.A. Svendsen** *Computation of Nonlinear Wave Kinematics during Propagation and Runup on a Slope*. pp.178, 387-412. In **Torum, A. and O.T. Gudmestad** (eds.) *Water Wave Kinematics, NATO ASI Series E: Applied Sciences*. Kluwer Academic Publishers, 1990.
53. **Grilli, S.T. and J. Horrillo** (1999) Shoaling of periodic waves over barred-beaches in a fully nonlinear numerical wave tank. *International Journal of Offshore and Polar Engineering*, **9(4)**, 257-263.
54. **Grilli, S.T., F. Dias, P. Guyenne, C. Fochesato, and F. Enet** *Progress in fully nonlinear potential flow modelling of 3D extreme ocean waves*. pp.55. In (eds.) Ma, Q.W. *Advances in Numerical Simulation of Nonlinear Water Waves*. World Scientific Publishing, 2008.
55. **Grilli, S.T., J. Skourup, and I.A. Svendsen** (1989) An efficient boundary element method for nonlinear water waves. *Engineering Analysis with Boundary Elements*, **6(2)**, 97-107.

56. **Grilli, S.T., M.A. Losada, and F. Martin** (1994) Characteristics of solitary wave breaking induced by breakwaters. *Journal of Waterwaves, Port, Coastal and Ocean Engineering*, **120(1)**, 74-92.
57. **Grilli, S.T., R.W. Gilbert, P. Lubin, S. Vincent, D. Astruc, D. Legendre, M. Duval, O. Kimmoun, H. Branger, D. Devrard, P. Fraunie, and S. Abadie** (2004) Numerical modeling and experiments for solitary wave shoaling and breaking over a sloping beach. Proceedings of *14th International Offshore and Polar Engineering Conference*, Toulon, France, May 23-28.
58. **Grimshaw, R.** (1970) The solitary wave in water of variable depth. *Journal of Fluid Mechanics*, **42**, 639-656.
59. **Grinsted, A., J.C. Moore, and S. Jevrejeva** (2004) Application of the cross wavelet transform and wavelet coherence to geophysical time series. *Nonlinear Processes in Geophysics*, **11**, 561-566.
60. **Harlow, F.** (1964) The particle-in-cell computing method for fluid dynamics. *Methods of Computational Science*, **3**, 313-343.
61. **Hirt, C., A. Amsden, and J. Cook** (1974) An Arbitrary Lagrangian Eulerian computing method for all speeds. *Journal of Computational Physics*, **14**, 227-253.
62. **Hirt, C.W. and B.D. Nichols** (1981) Volume of fluid (VOF) method for the dynamics of free boundaries. *Journal of Computational Physics*, **39(1)**, 201-225.
63. **Huang, Z.J. and C.C. Hsiung** (1996) Nonlinear shallow-water flow on deck. *Journal of Ship Research*, **40(4)**, 303-315.
64. **Hulsbergen, C.H.** (1974) Origin, effect and suppression of secondary waves. Proceedings of *14th International Coastal Engineering Conference*, New York, 392-411.
65. **Ibrahim, R.A., V.N. Pilipchuk, and T. Ikeda** (2001) Recent advances in liquid sloshing dynamics. *ASME Applied Mechanics Review*, **54(2)**, 133-199.
66. **Israeli, M. and S.A. Orszag** (1981) Approximation of radiation boundary conditions. *Journal of Computational Physics*, **41**, 115-135.
67. **Jain, M.K., S.R.K. Iyengar, and R.K. Jain** *Numerical methods for scientific and engineering computation*, New Age International Publishers, New Delhi, 2003.
68. **Jensen, A. and J. Grue** (2002) A note on the difference in the speed of gravity waves in a physical and numerical wave tank. *Wave motion*, **36**, 41-48.
69. **Jeong, S.J.** *Ein Beitrag zur Erzeugung nichtlinearer Entwurfsseegaenge im numerischen Wellenkanal*, Ph.D. Thesis, Technische Universitaet Berlin, Germany, 2003.

70. **Jiang, L., C.L. Ting, M. Perlin, and W.W. Schultz** (1996) Moderate and steep faraday waves: instabilities, modulation and temporal asymmetries. *Journal of Fluid Mechanics*, **329**, 275-307.
71. **Johnson, J.W., R.A. Fuchs, and J.R. Morison** (1951) The damping action of submerged breakwaters. *Transaction of American Geophysical Union*, **32(5)**, 704-718.
72. **Johnson, R.S.** (1973) On the development of a solitary wave moving over an uneven bottom. *Proceedings of Cambridge Philosophical Society*, **73**, 183-203.
73. **Kabbaj, A.** *Contribution a l'etude du passage des ondes de gravite et de la generation des ondes internes sur un talus, dans le cadre de la theorie de l'eau peu profonde*, These, Universite Scientifique et Medicale de Grenoble, 1985.
74. **Kim, C.H., A.H. Clement, and K. Tanizawa** (1999) Recent Research and Development of Numerical wave tanks - A Review. *International Journal of Offshore and Polar Engineering*, **9(4)**, 241-256.
75. **Kinsman, B.** *Wind Waves: Their Generation and Propagation on the Ocean Surface*, Prentice-Hall Inc., New Jersey, 1965.
76. **Kojima, H., T. Ijima, and A. Yoshida** (1990) Decomposition and interception of long waves by a submerged horizontal plate. *Proceedings of 22nd Coastal Engineering Conference*, 1228-1241.
77. **Koo, W.** *Fully nonlinear wave- body interactions by a 2D potential numerical wave tank*, Ph.D. Thesis, Texas A&M University, USA, 2003.
78. **Larsen, J. and H. Darcy** (1983) Open Boundaries in ShortWaves Simulations—A New Approach.. *Coastal Engineering*, **7**, 285-297.
79. **Le Mehaute, B .** (1972) Progressive wave absorber. *Journal of Hydraulic Research*, **10(2)**, 153-169.
80. **Lin, P.** (2004) A numerical study of solitary wave interaction with rectangular obstacles. *Coastal Engineering*, **51**, 35-51.
81. **Lin, W.M., J.N. Newman, and D.K. Yue** (1984) Nonlinear Forced Motion of Floating Bodies. *Proceedings of 15th International Symposium on Naval Hydrodynamics*, Hamburg, Germany.
82. **Liu, G.R.** *Mesh free methods: moving beyond the finite element method*, CRC Press, Florida, 2002.
83. **Liu, P.C.** *Wavelet spectrum analysis and ocean wind waves.* pp.151-166. In **Foufoula-Georgiou, E. and P. Kumar** (eds.) *Wavelets in Geophysics*. Academic Press, USA, 1994.
84. **Liu, P.L.-F., S.B. Yoon, and J.T. Kirby** (1985) Nonlinear refraction-diffraction of waves in shallow water. *Journal of Fluid Mechanics*, **153**, 185-201.

85. **Longuet-Higgins, M.S.** and **E.D. Cokelet** (1976) The deformation of steep surface waves on water: I. A numerical method of computation. *Proceedings of Royal Society London Part A*, **350**, 1-26.
86. **Lynett, P.J.** and **P.L.F. Liu** (2004) A two-layer approach to wave modeling. *Proceedings of Royal Society London Part A*, **460**, 2637-2669.
87. **Ma, Q.W.** (2005) Meshless local Petrov–Galerkin method for two-dimensional nonlinear water wave problems. *Journal of Computational Physics*, **205**, 611-625.
88. **Ma, Q.W.** *Advances in numerical simulation of nonlinear water waves*, World Scientific Publishing, 2008.
89. **Ma, Q.W.** and **S. Yan** (2006) Quasi ALE finite element method for nonlinear water waves. *Journal of Computational Physics*, **212(1)**, 52-72.
90. **Ma, Q.W., G.X. Wu,** and **R. Eatock Taylor** (2001a) Finite element simulation of fully nonlinear interaction between vertical cylinders and steep waves- Part 1: Methodology and Numerical procedure. *Journal for Numerical Methods in Fluids*, **36**, 265-285.
91. **Ma, Q.W., G.X. Wu,** and **R. Eatock Taylor** (2001b) Finite element simulation of fully nonlinear interaction between vertical cylinders and steep waves- Part 2: Numerical results and validation. *Journal for Numerical Methods in Fluids*, **36**, 287-308.
92. **Madsen, P.A.** and **O.R. Sørensen** (1992) A new form of the Boussinesq equations with improved linear dispersion characteristics. Part 2: a slowly-varying bathymetry. *Coastal Engineering*, **18**, 183-205.
93. **Madsen, P.A., D.R. Fuhrman,** and **B. Wang** (2006) A Boussinesq-type method for fully nonlinear waves interacting with a rapidly varying bathymetry. *Coastal Engineering*, **53**, 487-504.
94. **Madsen, P.A., H.B. Bingham,** and **H. Liu** (2002) A new Boussinesq method for fully nonlinear waves from shallow to deep water. *Journal of Fluid Mechanics*, **462**, 1-30.
95. **Madsen, P.A., R. Murray,** and **O.R. Sørensen** (1991) A new form of the Boussinesq equations with improved linear dispersion characteristics. *Coastal Engineering*, **15**, 371-388.
96. **Maiti, S.** *A Numerical study of fully nonlinear two-dimensional free surface flows and wave body interactions*, Ph.D. thesis, IIT Kharagpur, India, 1999.
97. **Massel, S.R.** (1983) Harmonic generation by waves propagating over a submerged step. *Coastal Engineering*, **7**, 357-380.
98. **Maxworthy, T.** (1976) Experiments on collisions between solitary waves. *Journal of Fluid Mechanics*, **76**, 177-185.

99. **Meyers, S. D., B.G. Kelly, and J.J. O'Brien** (1993) An introduction to wavelet analysis in oceanography and meteorology: With application to the dispersion of Yanai waves. *Monthly Weather Review*, **121**, 2858-2866.
100. **Miles, J. and D. Henderson** (1990) Parametrically forced surface waves. *Annual Review of Fluid Mechanics*, **22**, 143-165.
101. **Miles, J.W.** (1979) On the Kortweg-de Vries equation for a gradually varying channel. *Journal of Fluid mechanics*, **91**, 181-190.
102. **Monaghan, J.** (1994) Simulating free surface flows with SPH. *Journal of Computational Physics*, **110**, 399-406.
103. **Murty, T. S.** (1979) Submarine slide-generated water waves in Kitimat Inlet, British Columbia. *Journal of Geophysical Research*, **84(12)**, 7777-7779.
104. **Nakayama, T. and K. Washizu** (1980) Nonlinear analysis of liquid motion in a container subjected to forced pitching oscillation. *International Journal of Numerical Methods in Engineering*, **15**, 1207-1220.
105. **Nasar, T., S.A. Sannasiraj, and V. Sundar** (2008) Experimental study of liquid sloshing dynamics in a barge carrying tank. *Fluid Dynamics Research* (In press).
106. **Nitikipaiboon, C. and K.J. Bathe** (1993) An arbitrary lagrangian-eulerian velocity potential formulation for fluid-structure interaction. *Computers and Structures*, **47**, 871-891.
107. **Nwogu, O.** (1993) Alternative form of Boussinesq equations for nearshore wave propagation. *Journal of Waterways, Ports, Coastal and Ocean Engineering*, **119**, 618-638.
108. **Ogilvie, F.** (1963) First and second order forces on a cylinder submerged under waves. *Journal of Fluid Mechanics*, **16**, 451-472.
109. **Ohyama, T.** (1991) Development of a numerical wave tank for analysis of nonlinear and irregular wave field. *Fluid Dynamics Research*, **8**, 231-251.
110. **Ohyama, T. and K. Nadaoka** (1991) Development of a numerical wave tank for analysis of nonlinear and irregular wave field. *Fluid Dynamic Research*, **8**, 231-251.
111. **Ohyama, T. and K. Nadaoka** (1992) Modeling the transformation of nonlinear waves passing over a submerged dike. *Proceedings of 23rd International Conference on Coastal Engineering, Venice*, 526-539.
112. **Ohyama, T. and K. Nadaoka** (1994) Transformation of nonlinear wave train passing over submerged shelf without breaking. *Coastal Engineering*, **24**, 1-22.
113. **Ohyama, T., W. Kioka, and A. Tada** (1995) Applicability of numerical models to nonlinear dispersive waves. *Coastal Engineering*, **24**, 297-313.

114. **Okamoto, T.** and **M. Kawahara** (1990) Two-dimensional sloshing analysis by Lagrangian finite element method. *International Journal of Numerical Methods in Fluids*, **11**, 453-477.
115. **Orlanski, I.** (1976) A simple boundary condition for unbounded hyperbolic flows. *Journal of Computational Physics*, **21**, 251-269.
116. **Osborne, A.R.** (1994) Shallow water cnoidal wave interactions. *Nonlinear process in Geophysics*, **1(14)**, 241-251.
117. **Otta, A.K., I.A. Svendsen,** and **S.T. Grilli** *Unsteady free surface waves in region of arbitrary shape*, CACR, Univ. of Delaware, Research Report 10, 153, USA, 1992.
118. **P.J. Bryant.** (1973) Periodic waves in shallow water. *Journal of Fluid Mechanics*, **59**, 625-644.
119. **Park, J.C., M.H Kim, H. Miyata,** and **H.H. Chun** (2003) Fully nonlinear numerical wave tank (NWT) simulations and wave run-up prediction around 3-D structures. *Ocean Engineering*, **30**, 1969–1996.
120. **Peregrine, D.H.** (1967) Long waves on a beach. *Journal of Fluid Mechanics*, **27**, 815-827.
121. **Pudjaprasetya, S.R., E. Van Groesen,** and **E. Soewono** (1999) The splitting of solitary waves running over a shallower water. *Wave Motion*, **29**, 375-389.
122. **Raichlen, F.** (2008) Considerations of nonlinear wave propagation in a distorted physical model. (Unpublished note).
123. **Ramaswamy, B.** and **M. Kawahara** (1987) Lagrangian Finite Element analysis applied to viscous free surface fluid flow. *International Journal for Numerical Methods in Fluids*, **7**, 953-984.
124. **Rey, V., M. Belrous,** and **E. Guaselli** (1992) Propagation of surface gravity waves over a rectangular submerged bar. *Journal of Fluid Mechanics*, **235**, 453-479.
125. **Robertson, I.** and **S. Sherwin** (1999) Free-surface flow simulation using hp/spectral elements. *Journal of Computational Physics*, **155**, 26-53.
126. **Romate, J. E.** (1992) Absorbing boundary conditions for free surface waves. *Journal of Computational Physics*, **99**, 135-145.
127. **Scardovelli, R.** and **S. Zaleski** (1999) Direct numerical simulation of free-surface and interfacial flow. *Annual Review of Fluid Mechanics*, **31**, 567-603.
128. **Schlurmann, T.** *Time frequency Analysis methods in Hydrology and Hydraulic Engineering*, Habilitationsschrift, Bergische Universität Wuppertal, Germany, 2004.
129. **Schwartz, L.** and **J. Fenton** (1982) Strongly non-linear waves. *Annual Review of Fluid Mechanics*, **14**, 39-60.

130. **Seabra-Santos, F.J., D. Renouard, and A. Temperville** (1987) Numerical and experimental study of the transformation of a solitary wave over a shelf or isolated obstacle. *Journal of Fluid Mechanics*, **176**, 117-134.
131. **Seegerlind, L.J.** *Applied Finite Element Analysis*, J. Wiley & Sons, New York, 1984.
132. **Sen, D.** (1993) Numerical simulation of motions of two-dimensional floating bodies. *Journal of Ship Research*, **37(4)**, 307-330.
133. **Sen, D. and J.S. Pawlowski, J. Lever** (1989) Two dimensional numerical modelling of large motions of floating bodies in waves. Proceedings of *5th International Conference on Numerical modeling of Ship Hydrodynamics*, Hiroshima, Japan, 351-373.
134. **Sen, D. and S. Maiti** (1996) Numerical modelling of extreme and breaking waves. Proceedings of *International conference on ocean Engineering*, IITMadras, Chennai, India, 165-170.
135. **Shen, Y.M., C.O. Ng, and Y.H. Zheng** (2004) Simulation of wave propagation over a submerged bar using the VOF method with a two-equation $k-\epsilon$ turbulence modeling. *Ocean Engineering*, **31(1)**, 87-95.
136. **Skourup, J. and I.G. Jonsson** (1992) Computations of forces on, and particle orbits around, horizontal cylinders under steep waves. *Ocean Engineering*, **19(6)**, 527-553.
137. **Sommerfeld, A.** *Partial Differential Equations in Physics*, Academic Press, New York, USA, 1949.
138. **Steinhagen, U.** *Synthesizing Nonlinear Transient Gravity Waves in Random Seas*, Ph. D., Thesis, Technische Universit`at Berlin, Germany, 2001.
139. **Su, C.H. and R.M. Mirie** (1980) On head on collisions between two solitary waves. *Journal of Fluid Mechanics*, **98**, 509-525.
140. **Subramanya, R. and S.T. Grilli** (1994) Kinematics and Properties of Fully Nonlinear Waves Shoaling and Breaking over a Gentle Slope. Proceedings of *International Symposium on Waves - Physical and Numerical Modelling*, Vancouver BC, Canada, August, 1106-1115.
141. **Sudharsan, N.M., R. Ajaykumar, K. Murali, and K. Kurichi** (2004) A comparative study of dynamic mesh updating methods used in the simulation of fluid-structure interaction problems with non-linear free-surface. *Journal of Mechanical Engineering Science, Proceedings of the Institution of Mechanical Engineers, Part C*, **218(3)**, 283-300.
142. **Sugimoto, N., N. Nakajima, and T. Kakutani** (1987) Edge-layer theory for shallow water waves over a step - reflection and transmission of a soliton. *Journal of Physical Society of Japan*, **56(5)**, 1717-1730.

143. **Sveen, J.K.** *An introduction to MatPIV V 1.6.1*, Mechanics and Applied Mathematics, Dept. of Math. University of Oslo, USA, 2004.
144. **Tang, C.J.** and **J.H. Chang** (1998) Flow separation during solitary wave passing over submerged obstacles. *Journal of Hydraulic Engineering*, **124(7)**, 742-749.
145. **Torrence, C.** and **G.P. Compo** (1998) A practical guide to wavelet analysis. *Bulletin of American Meteorological Society*, **79**, 61-78.
146. **Torrence, C.** and **P. Webster** (1999) Interdecadal Changes in the ENSO Monsoon System. *Journal of Climate*, **12**, 2679-2690.
147. **Tsai, W.** and **D. Yue** (1996) Computation of non linear free surface flows. *Annual Review of Fluid Mechanics*, **28**, 249-278.
148. **Turnbull, M.S., A.G.L. Borthwick,** and **R. Eatock Taylor** (2003a) Numerical wave tank based on sigma-transformed finite element inviscid flow solver. *International Journal of Numerical Methods in Fluids*, **42**, 641-663.
149. **Turnbull, M.S., A.G.L. Borthwick,** and **R. Eatock Taylor** (2003b) Wave-structure interaction using coupled structured-unstructured finite element meshes. *Applied Ocean Research*, **25**, 63-77.
150. **Unverdi, S.** and **G. Tryggvason** (1992) Computation of multifluid flow. *Physica D*, **60**, 70-83.
151. **Van Daalen, E.F.G., E. Van Groesen,** and **S.R. Pudjaprasetya** (1997) BEM- Numerics and Kdv- model analysis for solitary wave split-up. *Computational Mechanics*, **19**, 179-187.
152. **Vinje, T.** and **P. Brevig** (1981) Numerical simulation of breaking wave. *Advances in Water Resources*, **4**, 77-82.
153. **Wang, C.Z.** and **B.C. Khoo** (2005) Finite Element analysis of two-dimensional nonlinear sloshing problems in random excitation. *Ocean Engineering*, **32**, 107-133.
154. **Wang, C.Z.** and **G.X. Wu** (2006) An unstructured mesh based finite element simulation of wave interactions with non-wall-sided bodies. *Journal of Fluids and Structures*, **22**, 441-461.
155. **Wang, C.Z.** and **G.X. Wu** (2007) Time domain analysis of second-order wave diffraction by an array of vertical cylinders. *Journal of Fluids and Structures*, **23(4)**, 605-631.
156. **Washizu, K.** (1982) Some applications of finite element techniques to nonlinear free surface fluid flow problems. Proceedings of *4th International Symposium on FEM in Flow Problems*, Finite Element Flow Analysis, 3-15.
157. **Weng, H.** and **K.M. Lau** (1994) Wavelets, period doubling, and time-frequency localization with application to organization of convection over the tropical western Pacific. *Journal of Atmospheric Sciences*, **51**, 2523-2541.

158. **Westhuis, J.H.** and **A.J. Andonowati** (1998) Applying the finite element method in numerically solving the two dimensional free-surface water wave equations. *Proceedings of 13th International Workshop on Water Waves and Floating Bodies*, Alphen an den Rijn, The Netherlands, 171-174.
159. **Westhuis, J.H.** *The Numerical Simulation of Nonlinear Waves in the Hydrodynamic Model Test Basin*, Ph.D. Thesis, Universiteit Twente, The Netherlands, 2001.
160. **Wu, G.X.** and **R. Eatock Taylor** (1994) Finite element analysis of two-dimensional non-linear transient water waves. *Applied Ocean Research*, **16**, 363-372.
161. **Wu, G.X.** and **R. Eatock Taylor** (1995) Time stepping solutions of the two-dimensional nonlinear wave radiation problem. *Ocean Engineering*, **22**, 785-798.
162. **Wu, G.X.** and **Z.Z. Hu** (2004) Simulation of nonlinear interactions between waves and floating bodies through a finite-element-based numerical tank. *Proceedings of Royal Society London, Part A*, **460**, 2797-2817.
163. **Wu, G.X., Q.W. Ma,** and **R. Eatock Taylor** (1998) Numerical simulation of sloshing waves in a 3D tank based on a finite element method. *Applied Ocean Research*, **20**, 337-355.
164. **Yeung, R.W.** (1982) Numerical methods in free-surface flows. *Annual Review of Fluid Mechanics*, **14**, 395-442.
165. **Yeung, R.W.** and **M. Vaidhyanathan** (1992) Non-linear interaction of water waves with submerged obstacles. *International Journal for Numerical Methods in Fluids*, **14(9)**, 1111-1130.
166. **Yim, S.C., H. Yeh,** and **D. Cox** (2004) International collaborative tsunami, storm surge, and wave structure interaction research opportunities using the Oregon State multidirectional wave basin and large wave flume. *Proceedings of 36th Joint Panel Meeting on Wind and Seismic Effects*, Chicago, May, 1-11.
167. **Young, I.R.** (1989) Wave transformation over coral reefs. *Journal of Geophysical Research*, **94**, 9779-9789.
168. **Zar, J.H.** *Biostatistical Analysis*, Prentice hall, New Jersey, 1999.
169. **Zienkiewicz, O.C.** and **J.Z. Zhu** (1992) The superconvergent patch recovery and a posteriori error estimates. Part 1: The recovery technique. *International Journal for Numerical Methods in Engineering*, **33**, 1331-1364.

PUBLICATIONS BASED ON THIS THESIS

I Fellowships / Awards

1. Won the **Best paper award** in 15th Asia Pacific Division- International Association of Hydraulic Research (APD-IAHR) held at Chennai, India for the paper entitled '*Simulation of nonlinear free surface waves*' (2006).
2. Won the Institute **CFD Award for the best Computational Fluid Dynamics** research work at Indian Institute of Technology, Madras for the year 2006-2007.
3. Recipient of the **DAAD short term Fellowship** for the year 2006-2007 to carry out research at University of Wuppertal, Wuppertal, Germany.

II Chapters in Book

1. **V. Sriram, S.A. Sannasiraj, and V. Sundar** (2008) Velocity calculation methods in Finite Element based MEL formulation. Advances in Numerical Simulation of Nonlinear Waves, Ed. Ma. Q.W., *Advances in Coastal and Ocean Engineering Series*, World Scientific. (In press)

III Refereed International Journals

1. **V. Sriram, S.A. Sannasiraj, and V. Sundar** (2006) Numerical simulation of 2D nonlinear waves using Finite Element with Cubic Spline Approximation. *Journal of Fluids and Structures*, **22(5)**, 663-681.
2. **V. Sriram, S.A. Sannasiraj, and V. Sundar** (2006) Numerical simulation of 2D sloshing waves due to horizontal and vertical random excitations. *Applied Ocean Research*, **28(1)**, 19-32.
3. **V. Sriram, S.A. Sannasiraj, and V. Sundar** (2006) NWF: Propagation of Tsunami and its interaction with continental shelf and vertical wall. *Marine Geodesy*, Special Issue on Tsunamis, Part-I. **29(3)**, 201-222.
4. **V. Sriram, S.A. Sannasiraj, and V. Sundar** (2007) Simulation of nonlinear free surface dispersive waves. *Journal of Hydro-Environment Research*, **1**, 126-132.

5. **V. Sriram, S.A. Sannasiraj, and V. Sundar** (2007) 2D Nonlinear wave body interaction using Semi-ALE. *Journal of Coastal Research*, SI **50**, 21-24,394-399.
6. **V. Sriram, S.A. Sannasiraj, V. Sundar.** Numerical absorption of steep nonlinear free surface waves based on Finite Elements in a 3-D tank. *Journal of Computational Physics*. (Communicated).

IV National Journals

1. **V. Sriram, R. Balaji, S.A. Sannasiraj, and V. Sundar** (2007) Experimental and numerical studies on the Tsunami wave characteristics. *ISH Journal of Hydraulics*, **12(1)**, 123-134.

V International Conferences

1. **V. Sriram, S.A. Sannasiraj, and V. Sundar.** Numerical Wave tank: Simulation of Shallow water waves. Proceedings of *1st International Conference in coastal zone Management and Engineering*, Arabiancoast, Dubai, 115-117, 2005.
2. **V. Sriram, S.A. Sannasiraj, and V. Sundar.** Simulation of nonlinear free surface waves. Proceedings of *15th Asia Pacific Division-International Association of Hydraulic Research (APD-IAHR) Congress*, Indian Institute of Technology Madras, India, Vol. II, 1105-1110, 2006.
3. **V. Sriram, S.A. Sannasiraj, and V. Sundar.** Numerical simulation of sloshing waves in horizontal direction due to regular and random waves. Proceedings of *1st international conference on marine hydrodynamics, MAHY*, 911-921, 2006.
4. **V. Sriram, S.A. Sannasiraj, and V. Sundar.** Propagation of Solitary wave over submerged trapezoidal bar in front of the vertical wall. Proceedings of *2nd International short course and workshop on coastal processes and port engineering, IAHR*, Italy (In CDROM), 2006.
5. **V. Sriram, S.A. Sannasiraj, and V. Sundar.** 2D Nonlinear wave body interaction using Semi-ALE. Proceedings of *International Coastal Symposium*, Australia (In CDROM), 2007.

6. **V. Sriram, S.A. Sannasiraj, and V. Sundar.** Semi ALE: Simulation of nonlinear free surface waves. Proceedings of *7th International conference on coastal and port engineering in developing countries*, PIANC- COPEDEC VII, Dubai, (In CDROM), 2008.

VI National Conference/Workshop/Symposium

1. **V. Sriram, R. Balaji, S.A. Sannasiraj, and V. Sundar.** Tsunami wave simulation through experimental and numerical studies. Proceedings of *National workshop on Tsunami effects and mitigation measures*, Dept of Ocean Engg., IIT Madras, Chennai, 79-84, December 2005.
2. **V. Sriram, S.A. Sannasiraj, and V. Sundar.** Wave-Structure interaction using unstructured FEM. Proceedings of *Indian National Conference on Harbour and Ocean Engineering, INCHOE*, National Institute of Technology Karnataka, Surathkal, India, Vol. I, 99-106, 2007.